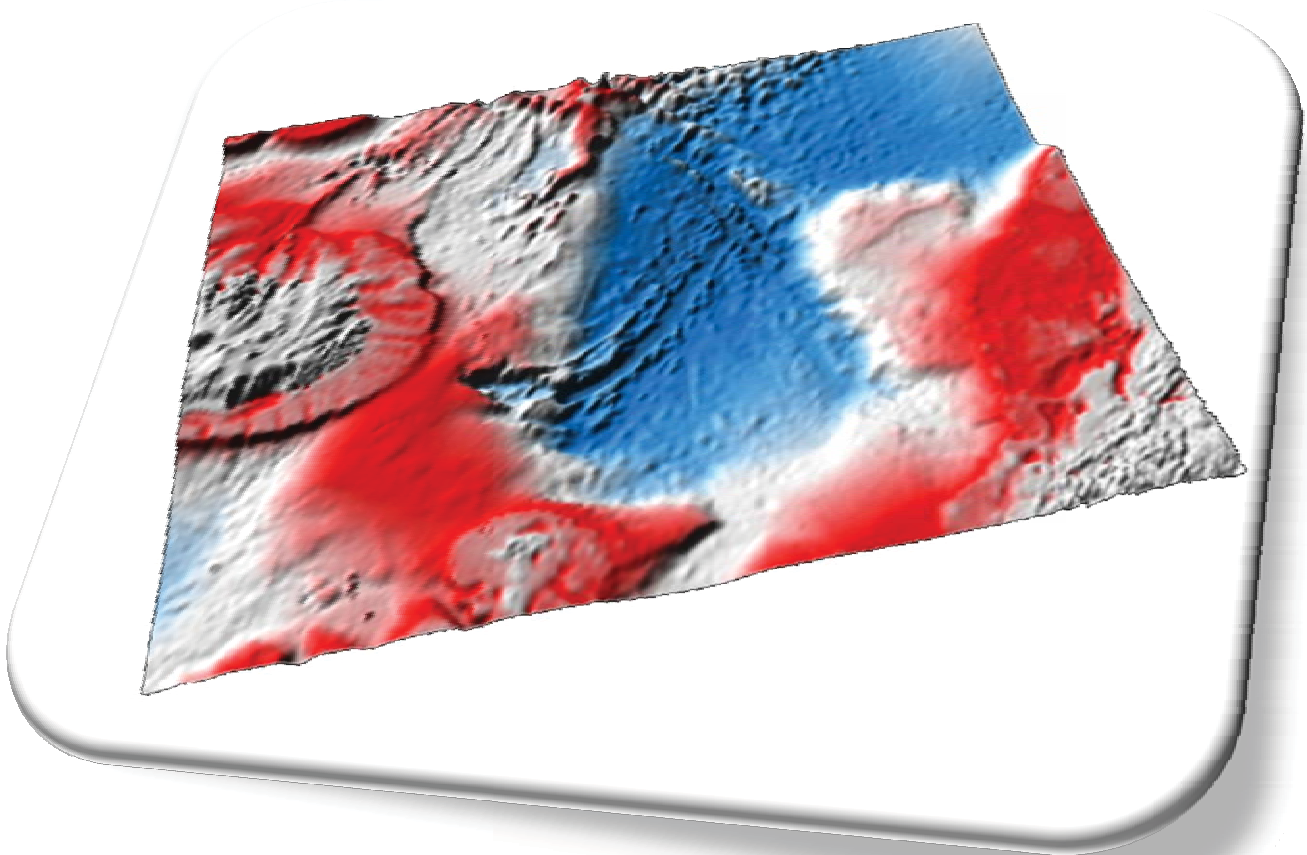


# NORWAY BASIN

Aeromagnetic Survey 2007 - NB-07

Acquisition, processing and interpretation

L. Gernigon, O. Olesen, J. Koziel and R. Lynum




NGU Report 2008.52

Norway Basin Aeromagnetic Survey NB-07 - Acquisition, processing and interpretation report.

NGU Report. 2008.052. Norway Basin Aeromagnetic Survey NB-07 - Acquisition, processing and interpretation report.

**REPORT**

Report no: 2008.052		ISSN 0800-3416	Grading: <b>Confidential to December 2012</b>	
Title: Norway Basin Aeromagnetic Survey NB-07 – Acquisition, processing and interpretation <i>(Version for Conoco-Phillips, Norwegian Petroleum Directorate, Norske Shell and StatoilHydro)</i>				
Authors: Laurent Gernigon, Odleiv Olesen, Janusz Koziel and Rolf Lynum		Clients: Faroes Earth and Energy Directorate, Conoco-Phillips, Norwegian Petroleum Directorate, Norske Shell, StatoilHydro and Total Norge		
Map-sheet name (M=1:250.000)		Map-sheet no. and -name (M=1:50.000)		
Deposit name and grid-reference:		Number of pages. 217	Price (NOK). 815,-	
Map enclosures. x				
Fieldwork carried out: May-September 2007	Date of report: 18.05.2008	Project no.: 318500	Person responsible: 	
Summary: A high sensitivity aeromagnetic survey, NB-07, was carried out in an area of 155.000 km <sup>2</sup> from the outer Vøring Basin to the Faroes Plateau in the Norway Basin. Data processing comprised spike-removal and data editing, systematic (IGRF and lag) corrections, statistical, differential median levelling and decorrugation micro-levelling. Several potential field maps were produced from the survey area. Examples of various filters applied to the magnetic field have been illustrated. One of the major results of this survey was a demonstration of modern, high-resolution aeromagnetic data providing an efficient geophysical tool for better re-mapping of the Norway Basin. Trend enhancement and a preliminary interpretation of the survey have been carried out. The magnetic chrons and other new oceanic features have been investigated. The NB-07 dataset documents the Continent-Ocean transition (COT) of the Faroes and Møre volcanic margins and the subsequent spreading history of the Norway Basin. The onset of the continental breakup and the subsequent segmentation of the early spreading system have been described and discussed. It involves complex tectono-magmatic processes which could explain the different magnetic patterns observed in the NB-07 survey area. The survey also documents an important kinematic phase of the spreading system after chron C22n (middle Eocene); never clearly documented before. The survey provides new elements to the discussion of the geodynamic evolution of the Norwegian-Greenland Sea and surrounding volcanic margins.				
Keywords. Geofysikk		Berggrunnsgeologi	Magnetometri	
Kontinentalsokkel			Fagrapport	

## CONTENTS

1	INTRODUCTION .....	7
1.1	Aeromagnetic data and exploration .....	7
1.2	Remapping the Norwegian oceanic domain.....	8
1.3	Objective: Norway Basin aeromagnetic survey 2007 (NB-07).....	10
2	SURVEY CHARACTERISTICS and ACQUISITION.....	14
2.1	Survey area and equipment .....	14
2.2	Personnel on board.....	16
2.3	Equipment and technical specification.....	17
2.4	Acquisition.....	19
2.5	Magnetic conditions .....	20
2.6	Map production, projection and archive CD .....	23
3	DATA PROCESSING AND PROFILES LEVELLING.....	25
3.1	Preliminary noise filtering and basic corrections .....	25
3.1.1	Noise filtering .....	25
3.1.2	Systematic lag corrections .....	25
3.1.3	International Geomagnetic Reference Field (IGRF correction) .....	25
3.2	Levelling and micro-levelling of the magnetic profiles.....	27
3.2.1	Diurnal variation and use of base magnetometer readings.....	27
3.2.2	Statistical levelling .....	29
3.2.3	Micro-levelling .....	31
3.3	Gridding of the NB-07 dataset: important comments for interpreters .....	34
4	CONVENTIONNAL FILTERING TECHNIQUES .....	38
4.1	Potential field and integrated study.....	38
4.2	Wavelength filtering, frequency content and power spectrum.....	38
4.3	Magnetic sources .....	40
4.4	Reduction to the pole (RTP).....	42
4.5	Upward continuation.....	49
4.6	High-pass, low-pass and band-pass filtering .....	51
5	ENHANCEMENT OF TREND USING STRUCTURAL FILTERS .....	57
5.1	Automatic gain control (AGC) .....	57
5.2	Derivative filters .....	58
5.2.1	Vertical derivatives .....	58
5.2.2	The horizontal derivatives .....	60
5.2.3	The terrain slope filter or maximum horizontal derivative filter .....	64
5.3	Analytic signal - 3D total gradient.....	66
5.4	Tilt derivative (TDR) .....	68

5.5	TDX filtering .....	72
5.6	Pseudogravity .....	76
6	FINAL MERGE AND COMPARISON WITH PREVIOUS COMPILATION.....	79
6.1	Merge of the NB-07 grid with the former regional grid .....	79
6.2	Comparison with other compilations .....	79
7	OTHER DATASETS.....	84
7.1	Bathymetry .....	84
	Multibeam echosounding (MBES) data .....	84
7.2	Gravity.....	84
7.3	Seismic reflection.....	85
8	ESTIMATION OF MAGNETIC DEPTHS .....	87
8.1	Implications .....	87
8.2	Euler deconvolution .....	87
8.3	Interpretation of the structural indices .....	88
8.4	Located 3D Euler method.....	90
8.5	Euler deconvolution of the tilt-angle derivative .....	94
8.6	Source parameter imaging (SPI).....	98
8.7	Werner deconvolution .....	100
9	INTERPRETATION .....	102
9.1	Introduction .....	102
9.2	Geodynamic and geological background of the Norway Basin: Review of previous works.....	104
9.2.1	Breakup and magmatism .....	104
9.2.2	Spreading and geodynamic setting of the Norway Basin.....	108
9.3	Refined magnetic chron interpretation, structure and spreading history of the Norway Basin ....	109
9.3.1	Potential field data.....	109
9.3.2	Methodology .....	111
9.3.3	Description of the magnetic pattern of the NB-07 survey and chron interpretation.....	114
9.3.4	Segmentation the Norway Basin.....	135
10	GRAVITY AND MAGNETIC MODELLING .....	140
10.1	Modelling methods and assumptions .....	140
10.1.1	Forward modelling approach .....	140
10.1.2	Magnetic .....	143
10.2	Flexural models.....	148
10.3	Description of the modelling along Section 1, LOS99-002 profile.....	149
10.3.1	Model setup.....	149
10.3.2	Gravity signature along the LOS99-002.....	152
10.3.1	Magnetic signature over the LOS99-002.....	156
10.4	Description of the modelling along of the Section 1, LOS00-13 profile .....	157

10.4.1	Gravity signature over the LOS00-13 .....	158
10.4.1	Magnetic interpretation along the LOS00-13 .....	158
10.5	Description of the modelling along Section 1, Faroes transect OF94-97 .....	161
10.5.1	Gravity signature of the Faroes section OF94-97 .....	161
10.5.2	Magnetic signature of the Faroes section OF94-97 .....	161
11	GEODYNAMIC AND TECTONIC IMPLICATIONS.....	165
11.1	Understanding the breakup.....	165
11.2	Early spreading dynamics: hot and warm lithosphere .....	170
11.3	Late spreading dynamics: colder lithosphere and fan-shaped development of the ridge system..	171
12	CONCLUSION AND PERSPECTIVES .....	178
12.1	Main results .....	178
12.2	Perspectives .....	179
12.3	Petroleum implications-discussion .....	180
13	ACKNOWLEDGEMENTS .....	181
14	BIBLIOGRAPHY.....	182
15	LIST OF FIGURES: .....	193
16	APPENDIX 1: .....	201
17	APPENDIX 2 .....	214

## 1 INTRODUCTION

*Laurent Gernigon and Odleiv Olesen*

Like several countries (e.g. Australia, Canada, Finland, Sweden, U.S), Norway was one of the first to support a vigorous government program to develop a countrywide, modern, high-resolution aeromagnetic database. This program includes continuous data acquisition, merging and re-processing of data from individual surveys. In this context, the Geological Survey of Norway (NGU) plays a crucial role in maintaining and continuously updating this national database. NGU's most recent aeromagnetic acquisitions proved the requisite for modern data in order to validate the first order geophysical and geologic features of the Norwegian continental shelf and contiguous oceanic domain. Comparing vintage and modern aeromagnetic surveys is like comparing 2D seismic lines from the 70ies with the most advanced 3D surveys and everybody usually agree that modern data provide much more details and significantly improve our geological knowledge. Consequently, NGU has launched a set of re-mapping projects of the Norwegian continental shelf and adjacent oceanic basins with funding from the petroleum industry and governmental institutions. The need for a new generation of high-quality data becomes now a reality for both academy and industry.

### 1.1 Aeromagnetic data and exploration

The delineation of gravity and magnetic anomalies should normally be the first geophysical method to be applied to a new basin or region being evaluated or re-evaluated. In frontier and under-explored areas, where seismic data are sparse or non-existent, aeromagnetic acquisition still remains the cheapest and easiest way to get and/or refine the structural setting of the study area. Aeromagnetic data can also be useful to plan strategically new seismic and electromagnetic acquisitions and define potential prospects. Large aeromagnetic surveys can be carried out efficiently and safely almost everywhere, in a short period of time and at a reasonable cost.

Also, when integrated with seismic interpretations, gravity, modern aeromagnetic information can reduce the risks of making faulty geological interpretations. Both gravity and magnetic data are independent of seismic data, both physically and from a measurement point of view. A joint interpretation that combines seismic and other potential field data thus produces a synergy that helps to significantly improve and validate the geological and structural interpretation of potential prospects.

Modern aeromagnetic data are usually applied as a relevant complement for basin and geodynamic interpretation in Norway. If the seismic coverage is poor, it can be jointly combined with gravity data to confirm and/or estimate the lateral extent of basement features, lava flows, magmatic intrusions, salt structures or sand channels observed throughout sparse seismic sections (Fig. 1.1).

High-resolution aeromagnetic surveys also represent relatively inexpensive tools for 3D mapping of faults and fracture systems propagating through hydrocarbon-bearing sedimentary levels.

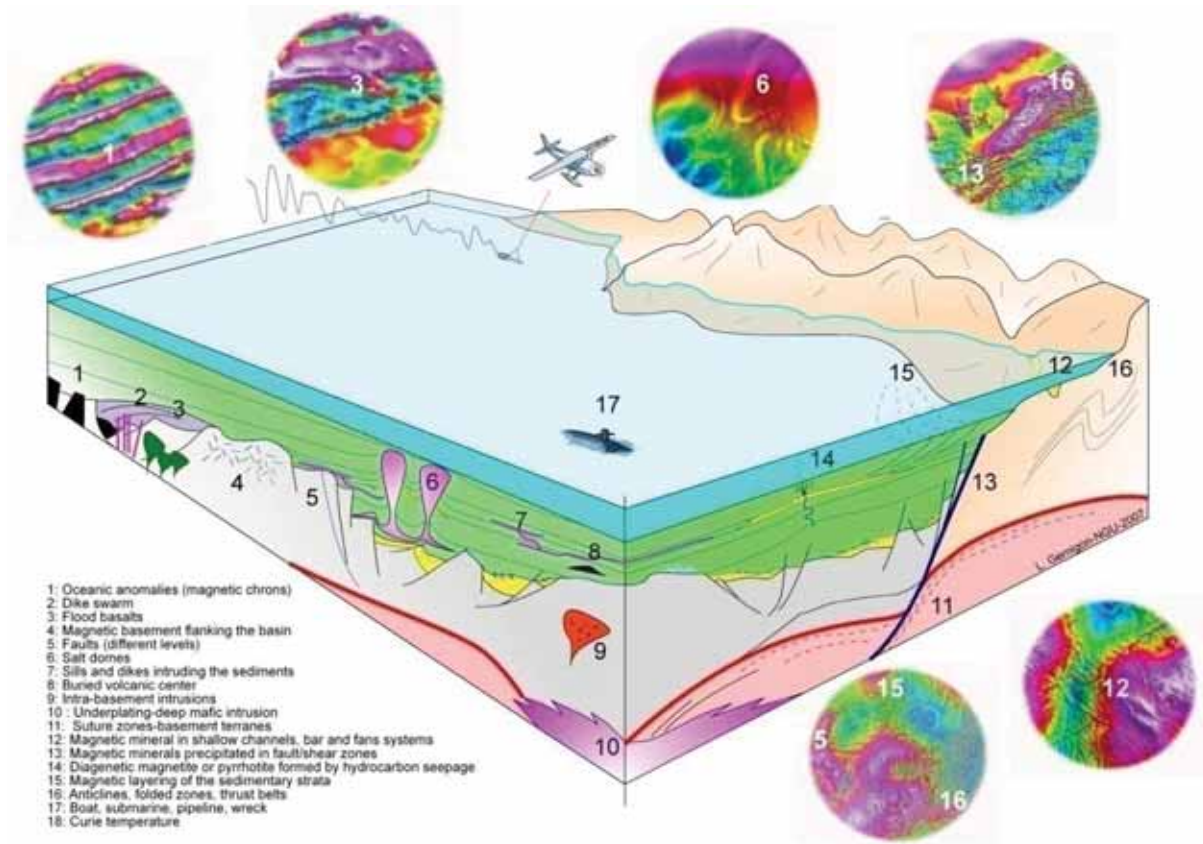


Figure 1.1. 3D cartoon and examples of the application of modern NGU aeromagnetic surveys to basin or geodynamic studies. The cartoon illustrates structures and geological units that can cause observable magnetic responses (Gernigon et al. 2007).

A variety of modern techniques to process, display and model the magnetic anomalies are offered for basin analysis. Several magnetic techniques can support the basin analysis and permit to: 1) identify and delineate in depth mafic intrusions and others volcanics, 2) to quantify and evaluate the top of the magnetic basement and infer the location of the thickest sedimentary section, 3) detect subtle intra-sedimentary "micro-magnetic" anomalies and 4) evaluate, to some extent the temperature of the crust (Curie temperature).

## 1.2 Remapping the Norwegian oceanic domain

Compared to the Norwegian continental shelf or the Barents Sea, the Norwegian oceanic domain is still poorly understood and like other distal margins and frontier areas, scientific interrogations remain. After almost 20 years of under-exploration of the Norwegian oceanic domain, NGU started



to re-investigate most of the oceanic domain and the continent-ocean transition in order to get an improved geophysical and geodynamic picture of the Norwegian-Greenland Sea. More precise plate reconstruction and/or advanced basin modelling require such an improved dataset and a complete and modern re-mapping of the oceanic domain is definitively a challenging task for NGU.

A detailed account of the spreading history provides crucial information about magmatic production, structures and geodynamics of the oceanic domain. A key element provided by the mapping of the oceanic systems such as the Norway Basin with modern aeromagnetic data is the time. Beginning in the 1950's, geophysicists recognized linear magnetic anomalies (magnetic chrons) across the ocean floor. The discovery of symmetric magnetic anomalies on both sides of mid-oceanic spreading ridges, and the subsequent development of the theory of sea floor spreading (1962), confirmed the continental drift theory proposed earlier by Wegner (1915) and revolutionized our understanding of the Earth leading to the theory of plate tectonics established in the late 1960's.

The correlation between oceanic magnetic anomalies (chrons) and a proper chronostratigraphic scale allows us to constrain accurately the timing of the oceanic accretion. Consequently, we can obtain good age constraints for the oceanic basement and overlying sedimentary sequences. The age of the ocean floor deduced from the magnetic chrons can be used to create a series of palaeotectonic and/or paleogeographic reconstructions. Placed in a time-referenced framework, deformation and movements of first order structures identified from new magnetic data-sets can be evaluated on the basis of several fundamental constraints which provide a means of explaining the tectonic, geological and petroleum evolution of a study area.

Most important, the magnetic pattern can help to locate the ultimate Continental-Oceanic boundary (COB) and delimit the distribution of the pre-breakup sedimentary sequences. In most continental margins, like the mid-Norwegian margin, this issue allows us to define the regional and maximum extend of interesting play concepts. Rift and lithospheric processes in the most distal part of the rifted margin start to be a serious problem as many contributions show that it cannot agree with conventional rift and subsidence prediction models (e.g. McKenzie approach). Advanced modelling suggests that stress and temperature influenced by poorly understood breakup processes and subsequent oceanic spreading can influence the adjacent rifted margin and indirectly its petroleum system. Constraints from the oceanic domain should provide serious constraints for understanding the thermo-kinematic evolution of rifted margin systems.

First re-investigation of the Norwegian oceanic domain started with the RAS-03 survey along the Lofoten Margin and later with the JAS-05 survey acquired between the Vøring Marginal High and Jan Mayen in 2005 (Figs. 1.2, 1.3). These surveys already support our idea that most of the fundamental structures of the Norwegian oceanic basins and adjacent margins are far from being well constrained and can significantly change our long-believed convictions. After analysis of the new datasets, we came up with new challenging hypotheses for the breakup and post-breakup evolution of the mid-Norwegian margin.

One of the first surprising results was probably that some of the "long-believe oceanic fracture zones" simply disappear with such modern datasets. For example, "the Bivrost Fracture Zone" that apparently offset magnetic chrons by 50 km, is just an artefact due to poor quality data (Olesen et al. 2007). When you realise that this trend was used for the last 30 years to guide structural and paleogeographic models offshore Mid-Norway, you may easily imagine the implications of new aeromagnetic acquisitions. Based on the new magnetic compilation and our tectonic analysis of the JAS-05 survey, we also proposed, for example, that a triple junction (ridge-ridge-fracture zone) initiated soon after the breakup between the Vøring Marginal High and the Traill Ø-Vøring igneous complex, now located offshore Greenland (Olesen et al. 2007). In places where a component of opening motion occurs along or close to a pre-existing oceanic transform, magmatic activity could have increased locally along such a "leaky transform" acting as a third branch. This early tectono-magmatic process could be compared to the active and more exotic Azores system, which can be used as a modern analogue of the vintage Norwegian spreading system, initiated 55 Ma ago (Gernigon et al. 2008).

### 1.3 Objective: Norway Basin aeromagnetic survey 2007 (NB-07)

The next and natural step of our investigation of the Norwegian oceanic domain is the survey NB-07 situated in the Norway Basin between the Faroes Plateau and the outer Vøring Basin (Figs. 1.2). Industry and governmental institutions welcomed this initiative and the NB-07 acquisition was co-funded by ConnocoPhillips, the Faroese Earth and Energy Directorate, the Norwegian Petroleum Directorate, Norske Shell, Statoil and Total Norge. The final compilation will certainly be welcomed by most researchers and explorationists working within the fields of geodynamics and geophysics and should provide a step further to our geodynamic knowledge of the Nordic Seas.

NGU initiated the NB-07 project in 2007 to acquire, process and interpret a new airborne magnetic dataset covering the Norway Basin where magnetic data remain extremely sparse and of poor-quality as suggested by the "gaps" observed in the regional compilation. Figure 1.3 underlines the location of the new survey area and illustrates the outline of the previous magnetic acquisition in the study area. Except for the NRL-90 survey acquired along the Aegir Ridge in 1990 (Jung and Vogt 1997), most of the magnetic profiles along the oceanic domain of the Norwegian-Greenland Sea remain old (70ies–80ies) and inaccurate. In the meantime, modern and more accurate magnetometers, navigation systems and recent advances in processing techniques allow us to seriously improve the quality of aeromagnetic mapping (Luyendyk 1997). Modern magnetometers, as used for the NB-07 survey, provide new total field measurements of high sensitivity, with virtually no drift and for all intents and purposes can be regarded as giving a reliable reading with a typical noise envelopes of  $\pm 0.1$  nT. The same cannot be said about the old magnetometers from the vintage surveys across the Norwegian-Greenland Sea. They were not absolute and had to be manually calibrated and were sensitive at best to about  $\pm 1$  nT.

Advances in data acquisition techniques (more sensitive magnetometers, full release of modern Global Positioning Systems, pre-planned drape surveys, etc.), as well as data processing and displaying procedures (such as micro-levelling and advanced gridding techniques), have also

significantly improved data quality and resolution, providing levels of detail that are compatible to those derived from seismic recording, well logging and surface geological mapping. Being aware of such major geophysical improvements, the primary objectives of the NB-07 project were multiple:

- 1) Provide a better and more reliable magnetic coverage of the study area.
- 2) Refine the tectonic and geodynamic setting of this oceanic basin, far from being well understood and often being neglected in the past.
- 3) Interpret the tectonic framework, basement structure, and lithology from aeromagnetic geophysical results.
- 4) Correlate and combine these results with the known geology of the study area to aid identification of new structural features.
- 5) Understand the Continent-Ocean transition (COT) and its implication for continental margins and oceanic segmentation.

The interpretation initiative involves the application of improved processing techniques and cultural source removal from the total magnetic field. In order to enhance the signatures of the basement structures and lithological units, as well as local volcanics lying above the older basement, a number of processed images and interpretations have been produced during this project.

The first part of this report describes acquisition, processing, levelling and map production of the NB-07. Filtering techniques and data enhancement methods were described leading subsequently to an integrated study of the survey and a discussion of the most interesting features revealed by this new dataset.

The second main part focuses on the geophysical and geological interpretation of the new survey, including also gravity and available and released seismic lines, kindly provided by the Norwegian Petroleum Directory (NPD). It led to a preliminary interpretation of the survey area and open discussion dealing about continental breakup and spreading history of the Norway Basin.

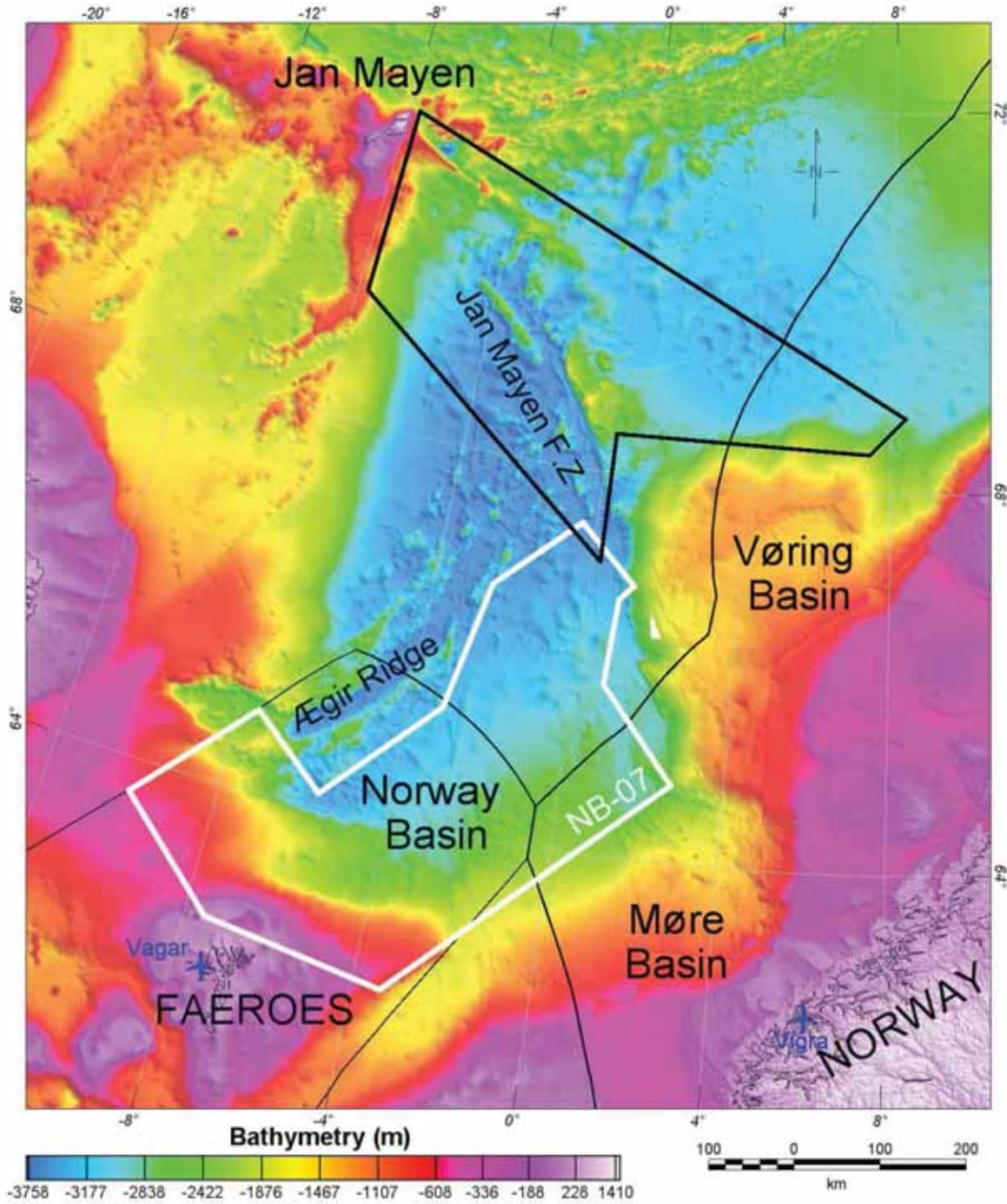


Figure 1.2. Geographic location of the NB-07 survey area. Vigra and Vagar airports were used during the survey acquisition.

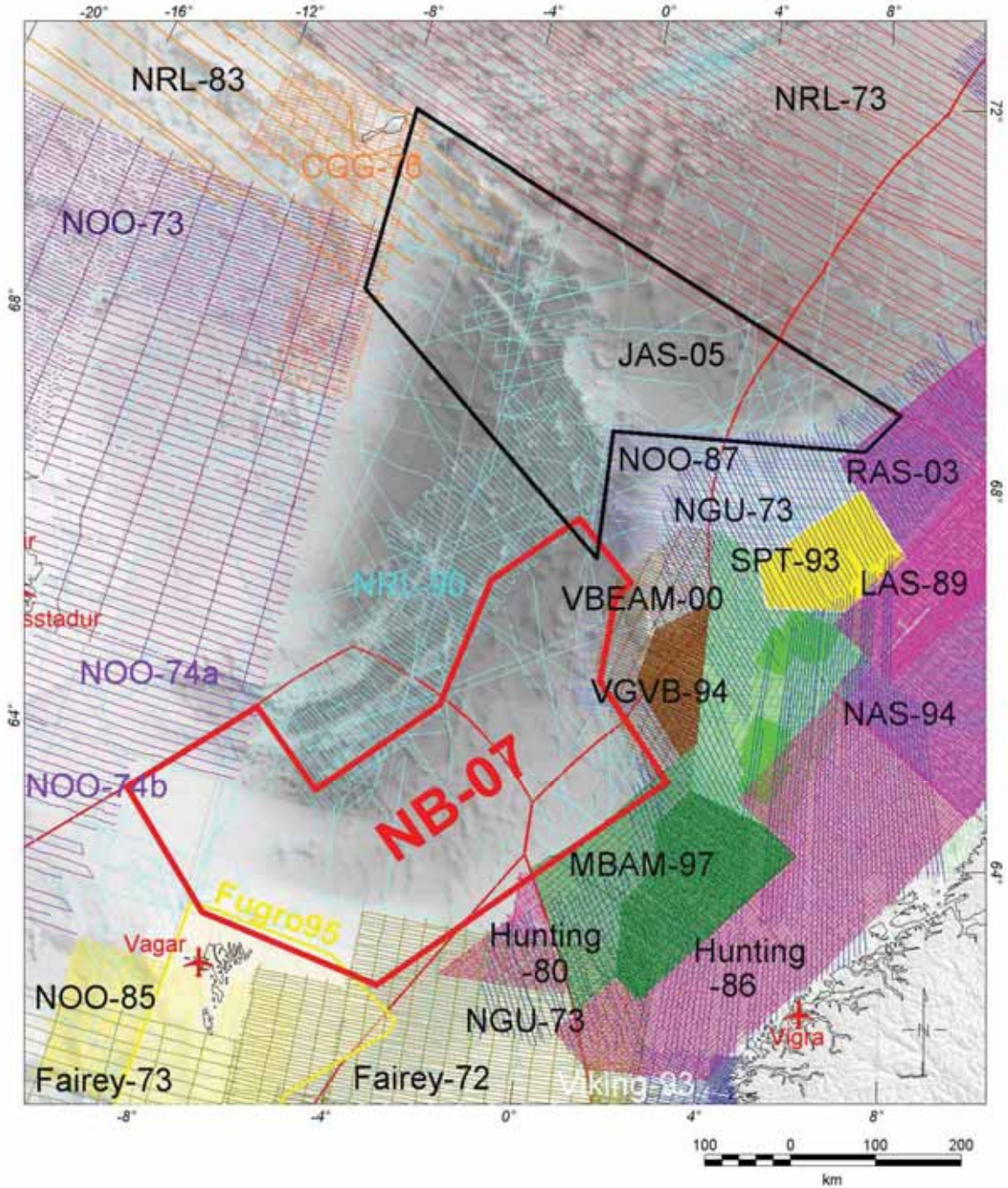


Figure 1.3 Location of the NB-07 survey area and outline of the previous aeromagnetic surveys surrounding the Norway Basin (Olesen et al. 2006; Olesen et al. 2007). The Norway Basin was mostly covered by sparse magnetic profiles acquired by the U.S. Naval Research Laboratory (NRL) in the 70ies and 80ies (Verhoef et al. 1997). The aim of the NB-07 was to fill the profile gaps between the Faroes and the outer Vøring Basin.

## 2 SURVEY CHARACTERISTICS AND ACQUISITION

*Odleiv Olesen, Laurent Gernigon and Janusz Koziel*

### 2.1 Survey area and equipment

The NB-07 is the most recent high-resolution aeromagnetic survey acquired in the Norway Basin after more than 15 years of non-magnetic acquisition in that area. As part of the NGU mapping program, the NB-07 acquisition was carried out during the two periods 14 May – 10 August and 21 August-24 September. The area is approximately 470 km long by 99 km wide and runs from the outer Vøring Basin onto the Faroes Plateau to the southwest (Figs. 1.2). The survey extends from the Continental-Ocean transition of the Møre volcanic margin to the southeast to the the aborted Aegir Ridge to the northwest (Fig. 1.1). The aeromagnetic survey was carried out using an aeroplane with a cesium magnetometer installed in a so-called "bird", towed at a sufficient distance from the plane (70 m) to make the plane's magnetic effects negligible (Fig. 2.1).



*Figure 2.1 Piper Chieftain from Fly Taxi Nord with the docking cradle for the bird containing a Scintrex Cesium Vapour MEP 410 high-sensitivity magnetometer.*

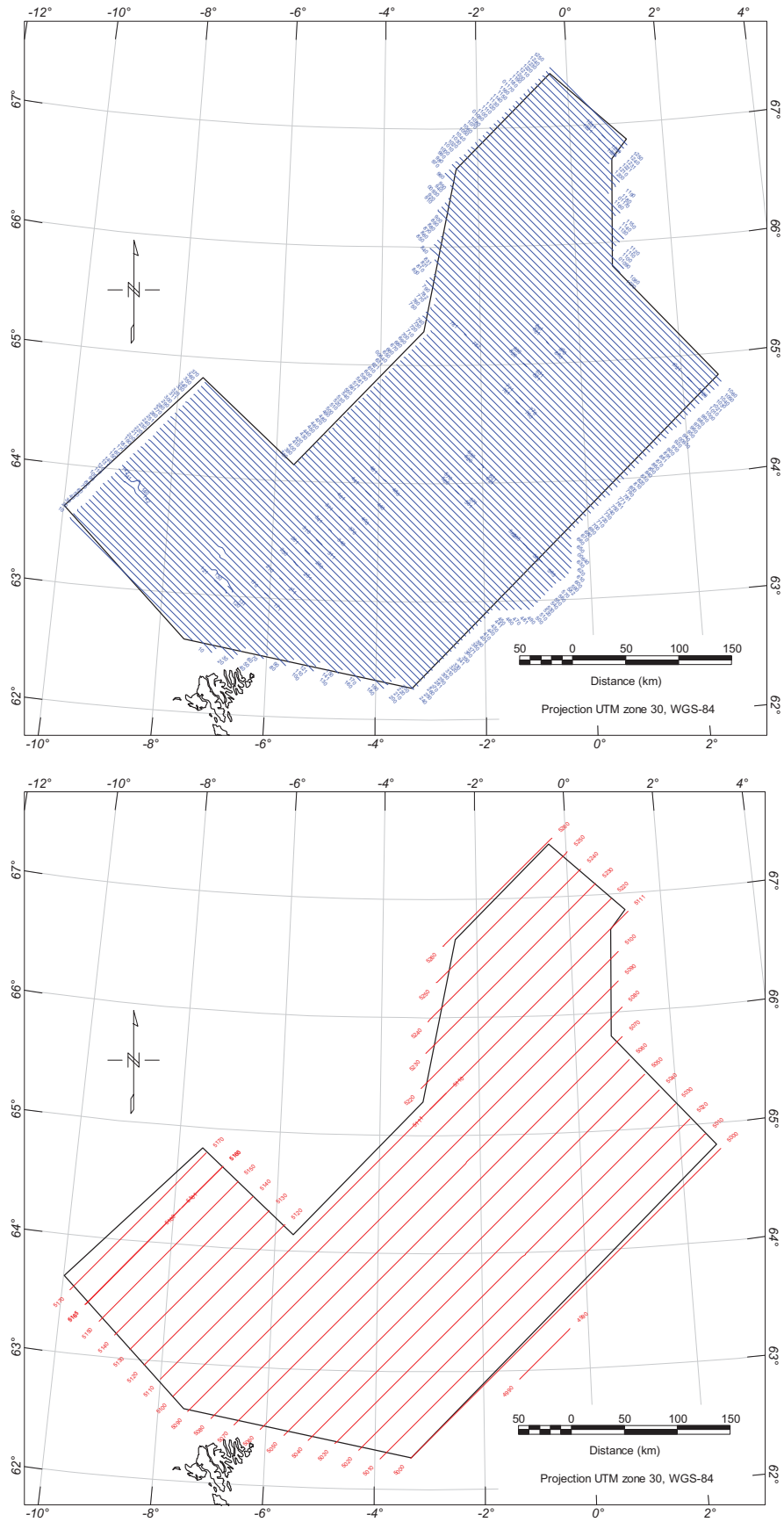


Figure 2.2: Flight pattern (blue lines and red tie-lines) of the NB-07 survey.

The airborne magnetic survey was conducted with constant flight-line orientations, usually perpendicular to the regional geological strike, and with a constant line spacing of 5 km x 20 km similar to the JAS-05's configuration (Fig. 2.2). Table 2.1 defines the coordinates of the original survey area.

<i>Longitude</i>	<i>Latitude</i>	<i>X-UTM30</i>	<i>Y-UTM30</i>
62.16.18.1427	-3.20.10.47918	482545.5373	6904494.436
62.36.54.7341	-7.31.55.49764	267562.1043	6950886.325
63.38.59.2506	-9.59.12.79296	154506.3618	7076899.874
64.49.51.5699	-7.31.25.67073	285468.372	7197289.683
64.08.18.3753	-5.39.24.57590	370720.8707	7115138.638
65.17.18.0541	-3.08.24.01254	493469.1596	7240598.306
66.39.36.7381	-2.27.35.49435	523879.4822	7393604.88
67.26.54.9626	-0.22.25.61613	612368.1666	7483769.162
66.51.29.4028	1.12.53.81934	684736.8935	7421821.139
66.42.00.6248	0.52.27.00578	670911.5976	7403266.617
65.47.58.8517	0.44.57.69535	671423.0271	7302700.591
64.49.11.1711	2.43.05.24113	771175.1778	7200628.185
62.16.18.1427	-3.20.10.47918	482545.5373	6904494.436

Table 2.1: Coordinates of the NB-07 survey area.

The following summary details the essence of the survey program:

Base of operation	Vagar, Faroe Islands and Vigra, Ålesund
Traverse line spacing and trend	5 km, north – south
Tie line spacing and trend	20 km, east – west
Flying height /sensor altitude	300m/230 m.
Speed	~225 km/h
Total line kilometres (original plan)	36.000
Total line kilometres (in contract)	38.800
Total line kilometres (acquired)	39.900
Data recorded	Magnetic field intensity, radar altitude and GPS positioning data

Table 3.2: Main characteristics of the NB-07 survey.

## 2.2 Personnel on board

From NGU participated:

Senior engineer. Janusz Koziel (leader of field operations)

Engineer: Rolf Lynum

Engineer: Einar Dalsegg

Engineer: Jomar Gellein



From Jardfeingi participated:

Geophysicist: Thomas Varming

From Fly Taxi Nord participated:

Captain: Ronny Thorbjørnsen

Captain: Ole Thorbjørnsen

Copilot: Ola Magnus Giæver

Copilot: Gard Pettersen

Copilot: John Harald Somby

### 2.3 Equipment and technical specification

The following equipment was used in the survey:

- Aircraft: Piper Chieftain PA31 with long range fuel tanks (registration. LN-ABZ) from FlyTaxi Nord in Tromsø (Fig. 2.1).
- Navigation: An Ashtech G12, 12 channel GPS receiver combined with a Trimble Navbeacon DGPS correctional receiver (SATREF) with flight guidance system from Seatex ASA was used for real time differential navigation. The navigation accuracy was better than  $\pm 5$  m throughout the survey.
- Altimeter: A KING KRA 405 radar altimeter is an integrated instrument of the aircraft and the data were both recorded and shown on the pilot's display. Accuracy of 0.25% with a resolution of 1 foot (0.3058 m) (Fig. 2.3).
- Magnetometer: A Scintrex Cesium Vapour MEP 410 high sensitivity magnetometer with a CS-2 sensor was applied in the data acquisition. The noise envelope of the onboard magnetometer was 0.1 nT. Most of the data fell within the limits of  $\pm 0.04$  nT.
- Base magnetometer: A Scintrex MP-3 and an EnviMag proton magnetometer were used for recording diurnals at the base station at the Vagar airport on the Faroes and later at Vigra airport on the mainland during the last phase of the survey (Fig. 2.4). Data from the base magnetometer were used in planning of flights and to decide on which lines eventually to re-fly.
- Data logging: A DAS8 datalogger, GR33 chart recorder and a HDR150 tape station from RMS Instruments were used to record the different data from the survey.

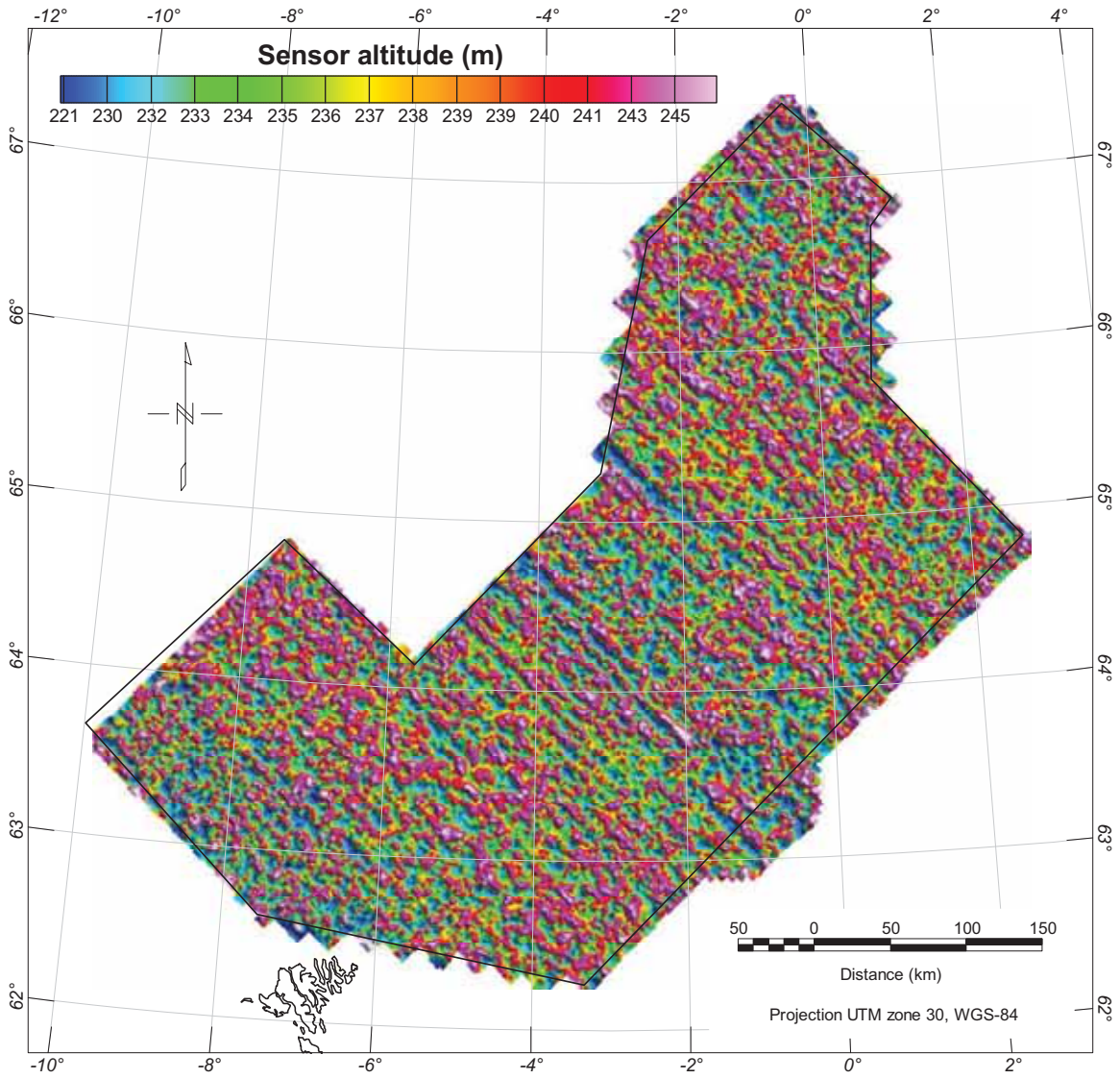


Figure 2.3 Sensor altitude (plane radar altitude – 70 m). Variation of sensor altitude can partly explain minor variation in the raw magnetic field, later corrected by advanced levelling techniques.



*Figure 2.4 Janusz Koziel next to the base station magnetometer deployed in the Faroe Islands during the NB-07 acquisition.*

## 2.4 Acquisition

The whole area was covered with both tie-lines and traverse lines (Fig. 2.2). The total survey area constituted c. 155.000 km<sup>2</sup> and consisted of 8.500 km tie lines and 31.400 km ordinary profiles. The aircraft altitude was 300 m in average (1000 feet) (Fig. 2.3). The magnetic sensor was towed approximately 70 m below and behind the aircraft, giving a sensor altitude of app. 230±5 m. The flying speed was 225 km/h and magnetic data were sampled at a rate of 5 Hz, giving a spatial sampling interval of 12-14 m along the lines.

The acquisition period was initially planned for approximately 15 weeks but due to poor weather conditions and some shorter periods with magnetic disturbances and finally the loss of the bird during the last acquisition phase, the acquisition has been seriously delayed with regard to the initial schedule.

## 2.5 Magnetic conditions

The most complex problem during magnetic acquisition is probably the diurnal variation of the Earth's magnetic field influenced by solar storms, particularly active at high latitudes (i.e. aurora borealis). It usually causes tie line and regular survey lines to have different readings at the same geographical point (crossover point). Such misfits can produce artefacts during interpolation and consequently erroneous interpretations if no suitable corrections have been applied.

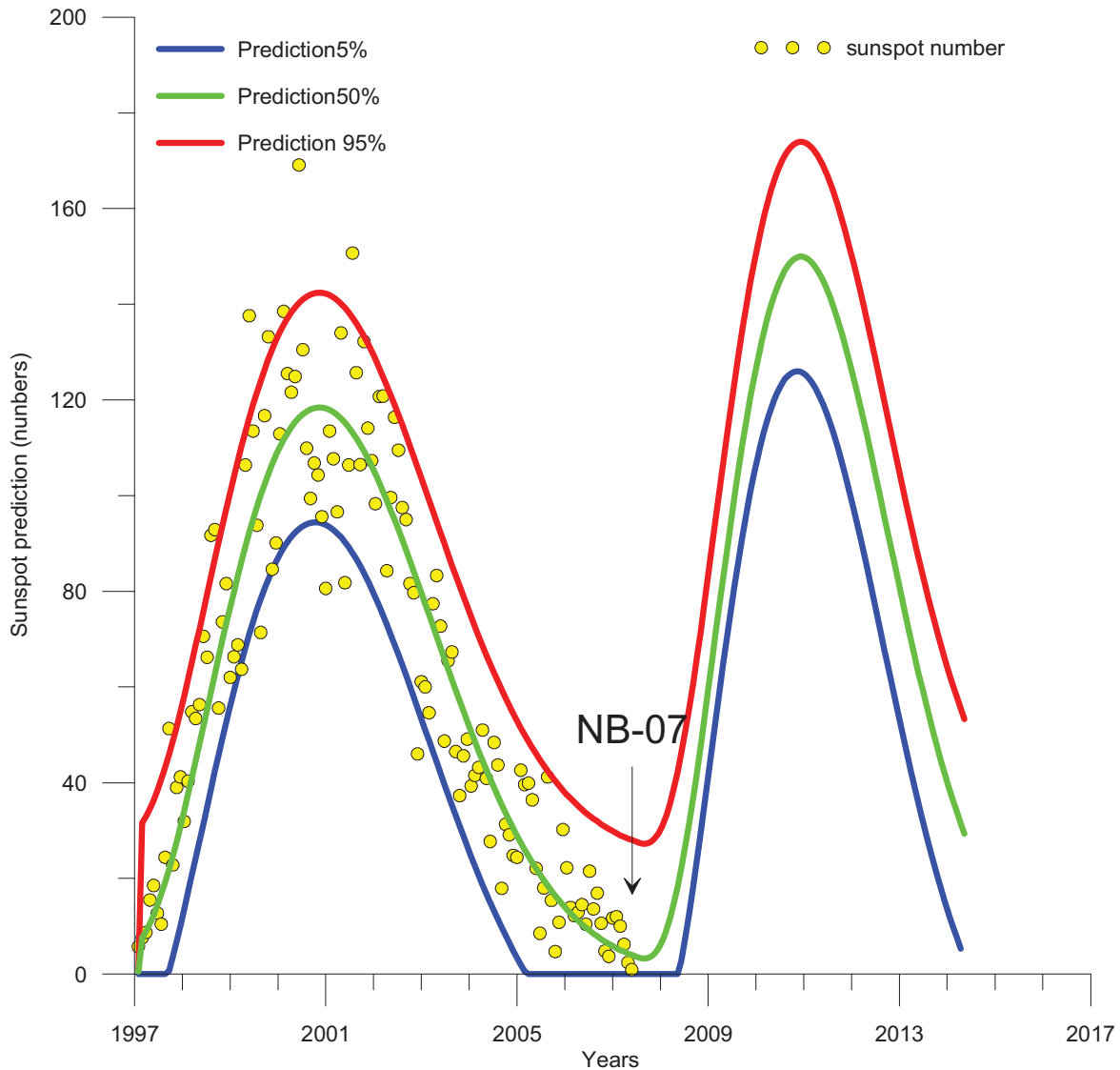


Figure 2.5 Observations and prediction models of sunspot numbers from the US National Oceanic and Asthenospheric Administration (NOOA)(Hathaway et al. 1999). Monthly averages (updated monthly) of the sunspot numbers show that the number of sunspots visible on the sun waxes and wanes with an approximate 11-year mega cycle. The NB-07 was carried out during a period of extremely low solar activity, which represented excellent conditions for the aeromagnetic acquisition.

If the survey is located close to a base station site, the lines can be directly corrected for diurnal variation. However, most of the offshore acquisition extends far away from land stations and can by experience suffer from different diurnal variation. Efficient statistical algorithms and filtering are

usually required to solve this issue and "level" in a proper way all the magnetic profiles (see Chapter 3). Sunspot cycle strongly influence the geomagnetic field and diurnals. The NB-07 was luckily acquired during a relatively quiet period. Solar cycle predictions suggest that 2007 was close to the lowest period of sun spot activity (Figs. 2.5, 2.6), providing really good magnetic conditions for the acquisition.

The magnetic signature of the airplane also includes 1) its permanent magnetization induced by its motion through the Earth's magnetic field and 2) a component due to the flow of electric current within the plane. The permanent magnetization of the plane varies as the plane changes its orientation leading to heading errors. A magnetic heading test (clover-leaf test) was carried out in October 2006 in the Hammerfest region for the SNAS-06 and BAS-06 projects. The maximum difference of magnetometer readings in the four different directions was small: 1.2 nT. We decided not to carry out any new clover-leaf test in 2007.

The diurnals for all flights are displayed in the database file delivered on the NB-97 archive CD. The data from the base magnetometer (EnviMag) located at Vagar airport were transferred to a laptop computer and plotted out flight by flight (Appendix I). The start and termination of each profile (traverse and tie) are indicated by red vertical lines (with annotated profile numbers) on the diurnal plots. The curve is coloured red for profiles and blue elsewhere. These plots ease the quality control of the acquired profiles. The data were classified into two quality groups according to magnetic diurnals:

Class	Criteria	Profile length
1	< 10 nT/10 min. linear	39.750 km
2	10 – 30 nT/10 min. linear	126 km
Total		39.876 km

A total of 126 line km was of intermediate quality (Fig. 2.7 and 2.8) and constitutes 0.3 % of the total survey. We were able to remove the diurnal effect during the levelling process and decided therefore not to re-fly any line. The base-magnetometer recordings are shown in Appendix 1.

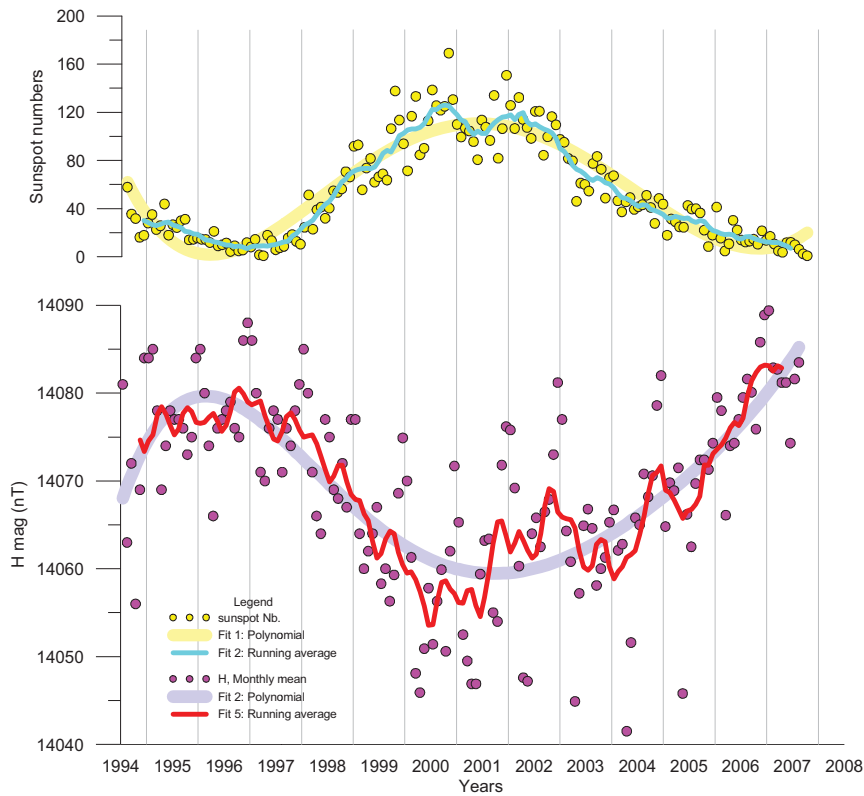


Figure 2.6 Diagram of the monthly mean values of the horizontal intensity of the geomagnetic field (H) observed at the Tromsø observatory from 1994 to 2008. This graph illustrates the good correlation between the periodic and semi-periodic evolution of the field and sunspot activity. Similar variation between the polynomial average of H and its running average illustrates the average good magnetic conditions for aeromagnetic surveying during the two periods in June-July and June-September 2007. Geomagnetic Data from Tromsø Geophysical Observatory (<http://www.tgo.uit.no/aix>). Sunspot number from the U.S National Oceanic and Asthenospheric Administration (NOOA) compilation.

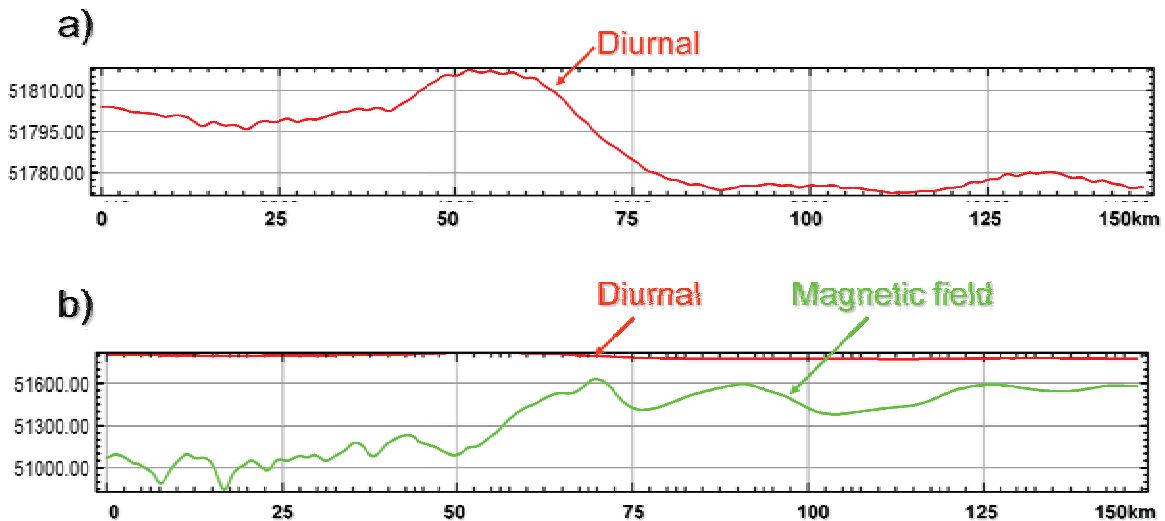


Figure 2.7: Magnetic diurnal along profile 210:6 (line with the most noise in the NB-07 survey). a) Base magnetometer reading. b) Base magnetometer and uncorrected magnetic field from the aeroplane plotted at the same scale.

**NB-07  
Diurnals  
10-30nT/10min  
126 km (i.e. 0.3%)**

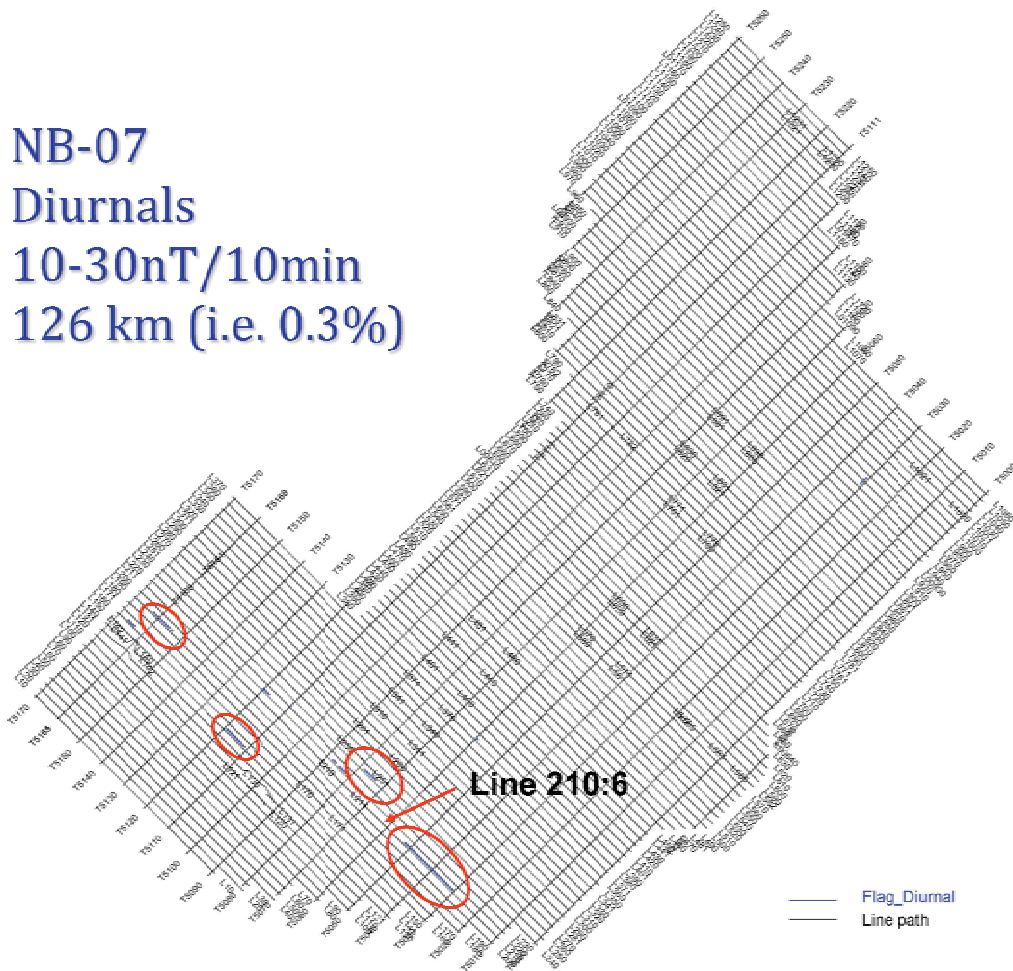


Figure 2.8 Profiles of intermediate quality (i.e. diurnal variation between 10 and 30 nT per 10 minutes) marked as blue lines. The total length of intermediate quality data is 126 km (i.e. 0.3 % of the total survey). Both base station and aeroplane readings along line 210:6 are shown in Fig. 2.7.

**2.6 Map production, projection and archive CD**

The Oasis Montaj software (Geosoft 2004) was intensively used for the map production. This software package has become a standard for many potential field experts in the mineral and petroleum industry. All database and grids in Geosoft format are provided on the archive CD. The grids are usually presented with a shaded relief technique (illumination from the northeast) and a non-linear color scale. Presentation of the maps with the shaded relief technique enhances lineaments that trend oblique to the illumination direction. Colour scale and colour distribution for the datasets have been computed using a histogram equalisation technique. We used most of the time the Geosoft minimum curvature gridding to produce the grids displayed in the present report. These maps have been produced in the Universal Transverse Mercator projection UTM zone 30 using the WGS 84 datum. We also used the UTM 32 projection for the regional interpretation.

We provide Oasis Montaj Viewer and its tutorial on the CD for companies that do not use Oasis Montaj specifically. Oasis Montaj Viewer is a free, easy-to-use software that allows anyone to view, share and print published Geosoft grid (.grd) and database (.gdb) files. The viewer can also be used to convert grids and images to a variety of supported data formats, including AutoCAD, ArcView, ER Mapper, TIF and many more. The free software can also be shared and downloaded from <http://www.geosoft.com/pinfo/oasismontaj/free/montajviewer.asp>.

For specific question of specific need do not hesitate to contact NGU ([Laurent.gernigon@ngu.no](mailto:Laurent.gernigon@ngu.no) or Odleiv. [Olesen@ngu.no](mailto:Olesen@ngu.no)).



### **3 DATA PROCESSING AND PROFILES LEVELLING**

**Laurent Gernigon**

The raw magnetic profiles (Fig. 3.1) could not be used directly for gridding and required a number of processing steps before production of the final aeromagnetic grid for interpretation use. Noise filtering and statistical levelling processing were carried out using the professional OASIS Montaj software (Geosoft 2005b). Micro levelling was performed using both the MAGMAP FFT package from OASIS Montaj (Geosoft 2005a) and the median filtering software developed at NGU (Mauring and Kihle 2006). The raw data have been processed using standard procedures and methodologies used in many other geological surveys (Luyendyk 1997). The various processing steps and standard procedures are outlined below.

#### **3.1 Preliminary noise filtering and basic corrections**

##### **3.1.1 Noise filtering**

High-frequency noise is usually created as the aeroplane is manoeuvring. After acquisition, initial raw data were imported directly into an Oasis Montaj database and subsequently interpolated to a regular grid of 500x500 m cells, to check the quality of lines and tie lines (Fig. 3.1). Spikes due to minor noise and artefacts were first removed by non-linear (Naudy) filtering and subsequently smoothed with a light low-pass filter (10 fiducials=500 m) in order to keep the signal intact.

##### **3.1.2 Systematic lag corrections**

Original magnetic profiles were lag-corrected, utilizing the Oasis Montaj processing package (Geosoft 2005a) with 5 fiducials (=250 m). As part of the processing sequence, lag correction was applied to the NB-07 data but did not change the data significantly due to negligible variations in values as a function of survey direction.

##### **3.1.3 International Geomagnetic Reference Field (IGRF correction)**

As part of the processing, the total magnetic field is computed from the recorded magnetic field after subtraction of the International Geomagnetic Reference Field (IGRF) model (Fig. 3.2). The IGRF is a mathematical representation of the undisturbed Earth's geomagnetic field. The International Geomagnetic Reference Field for 2006 (IGRF-2006) was calculated using the Oasis Montaj IGRF tool (Geosoft 2005a). The result of this subtraction isolates the component of the magnetic total field, which is dominated by the magnetic effects from the underlying crustal rocks.

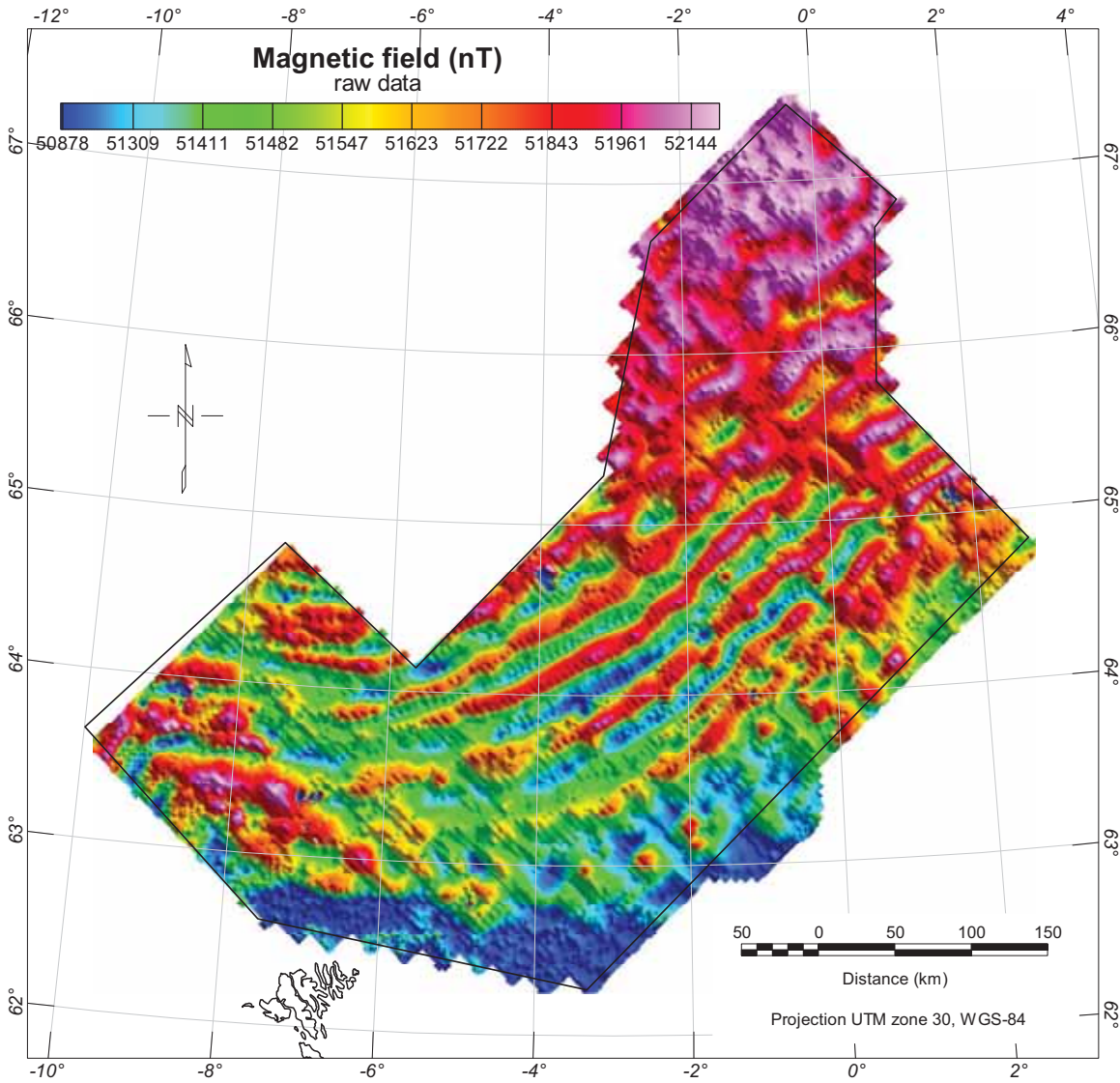


Figure 3.1 Raw magnetic profiles (without levelling) gridded by means of the minimum curvature algorithm (grid cell size at 500x500 m). Note that the artefacts are mostly parallel to the line profiles due to diurnals. Projection UTM 30, WGS 84.

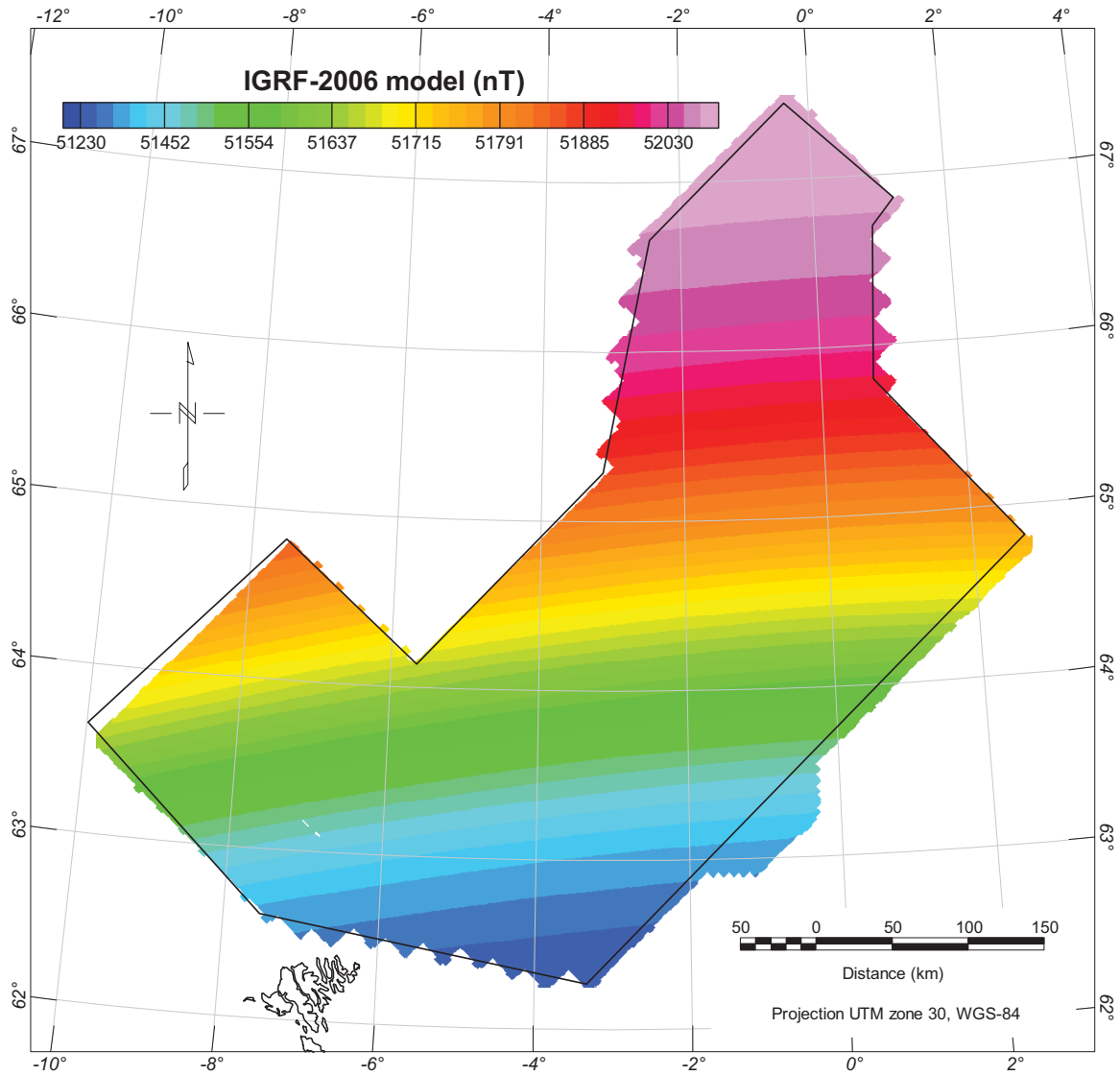


Figure 3.2: The IGRF-2006 (formally 2005) model along the NB-07 survey.

### 3.2 Levelling and micro-levelling of the magnetic profiles

#### 3.2.1 Diurnal variation and use of base magnetometer readings

A variety of external, time varying field factors usually influences and causes errors during aeromagnetic acquisition. This includes time variation in the magnetic field, ground clearance variation, altitude variation, magnetic effects of seawater waves and diurnal effects. This usually explains the errors at crossover points between line and tie-lines. The most complex and significant problem is probably the diurnal variation of the Earth's magnetic field influenced by the solar wind (Figs. 2.6, 3.3). In polar latitudes, the most famous and spectacular expression of these diurnal effects are the aurora borealis, known to be caused by the collision of charged particles (e.g.

electrons), in the magnetosphere with atoms in the Earth's upper atmosphere. Diurnal variations in the magnetic field can cause tie line and regular survey lines to have different readings at the same intersection. Even if they are small these long-wavelength effects can be visually distracting particularly on image-enhanced displays. Such misfits can produce artefacts during interpolation and consequently erroneous interpretation if no suitable corrections have been applied properly.

The most important reason for this is the time shift in the Earth's magnetic field variations between the large survey area and the onshore base station. There is normally a spatial difference in amplitude and frequency of these diurnals. Data from the base magnetometer have therefore only been used to assess the quality of individual lines and to make decisions on which lines eventually to re-fly. Due to good magnetic conditions, no lines have been re-flown (see Chapter 2.5, Fig. 8).

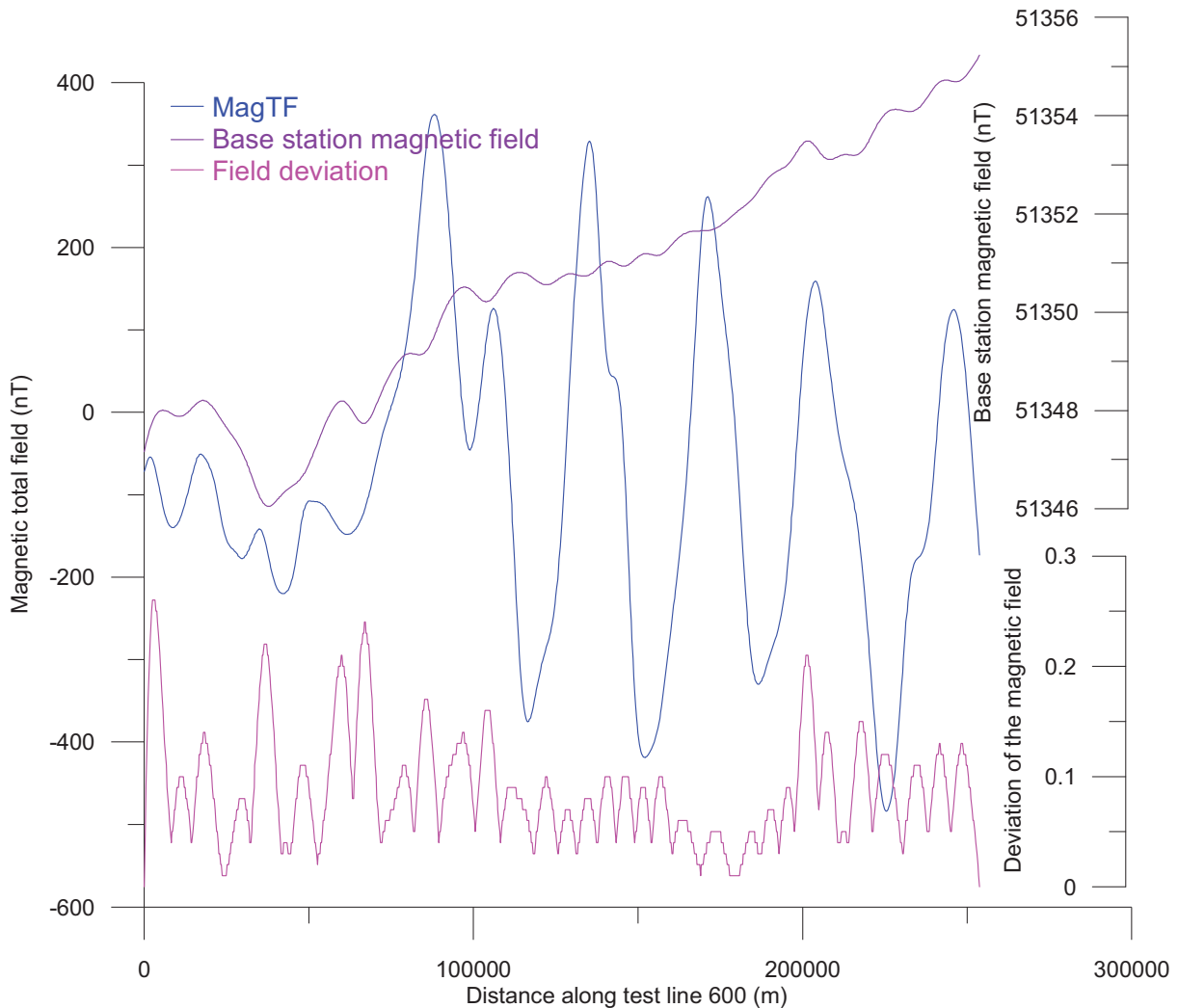


**Figure 3.3** Example of variation of the geomagnetic field recorded by the base station during the acquisition of Line 600. The standard variation of the total field (in pink) illustrates the diurnal variations observed onshore.

### 3.2.2 Statistical levelling

The purpose of "levelling science" is to minimize these residual differences in a coherent way by proportioning them between lines and tie lines. Proper levelling or micro-levelling algorithms usually require close and proper line spacing and the quality of the final result is most of the time a function of this crucial parameter. The large line spacing of previous surveys did not allow proper micro-levelling and interpolation of raw data produced erroneous or factitious anomalies.

Compared to the previous dataset, the NB-07 configuration and resolution allowed us to process and level the data in a proper way to get a reliable and updated magnetic picture of the Norway Basin and surroundings. After noise removal, head- and lag-corrections, the new aeromagnetic survey was processed using a statistical levelling method by which the discrepancies between the readings at each crossover points were reduced by systematically proportioning them between the tie and line profiles. 'Suspicious' cross-over differences (outliers) were first removed manually before levelling and full-levelling of the tie-lines and line profiles. The levelling method used for our study involved fitting a polynomial to the intersection errors by the methods of least squares (Mauring et al. 2002). We used a first order (linear) trend removal for the levelling of the NE-SW tie-line profiles. The linearly trended tie-lines profiles were then used for full statistical levelling of the survey lines after smoothing of the polynomial fitted mis-lines using a spline algorithm to avoid unwanted distortion of the anomalies (e.g. Mauring et al. 2002).

Levelling was undertaken using the standard statistical levelling method of the tie-lines followed by a statistical levelling of the profiles utilising the levelled tie-lines (Geosoft 2005b). We used first a first-order (linear) trend removal in the levelling of the tie-lines. Before running the trend-levelling algorithm, 'suspicious' mis-tie values (outliers) were removed manually before levelling of the tie-lines (Fig. 3.4). The linearly detrended tie-lines surface was finally used similarly for the final full levelling of the survey lines (Fig. 3.5). For each outlier removal, gridding has been systematically realised to check the validity of each trial, until we got a reasonable grid. Instead of smoothing, we re-ran several times the full levelling of the lines to further improve the levelling correction. Extreme mis-tie values (outliers) were checked and removed again manually before calculating the next full levelling correction, until convergence was achieved.

We also tried to apply different spline algorithms during the conventional levelling to remove the residual noise, but there were no observable improvements in the resulting grids. Spline and Akima algorithms smoothed the data too much and removed some interesting trends and features, with often small nT variation. The final results were the best compromise between the removal of levelling errors and anomalies preservation.

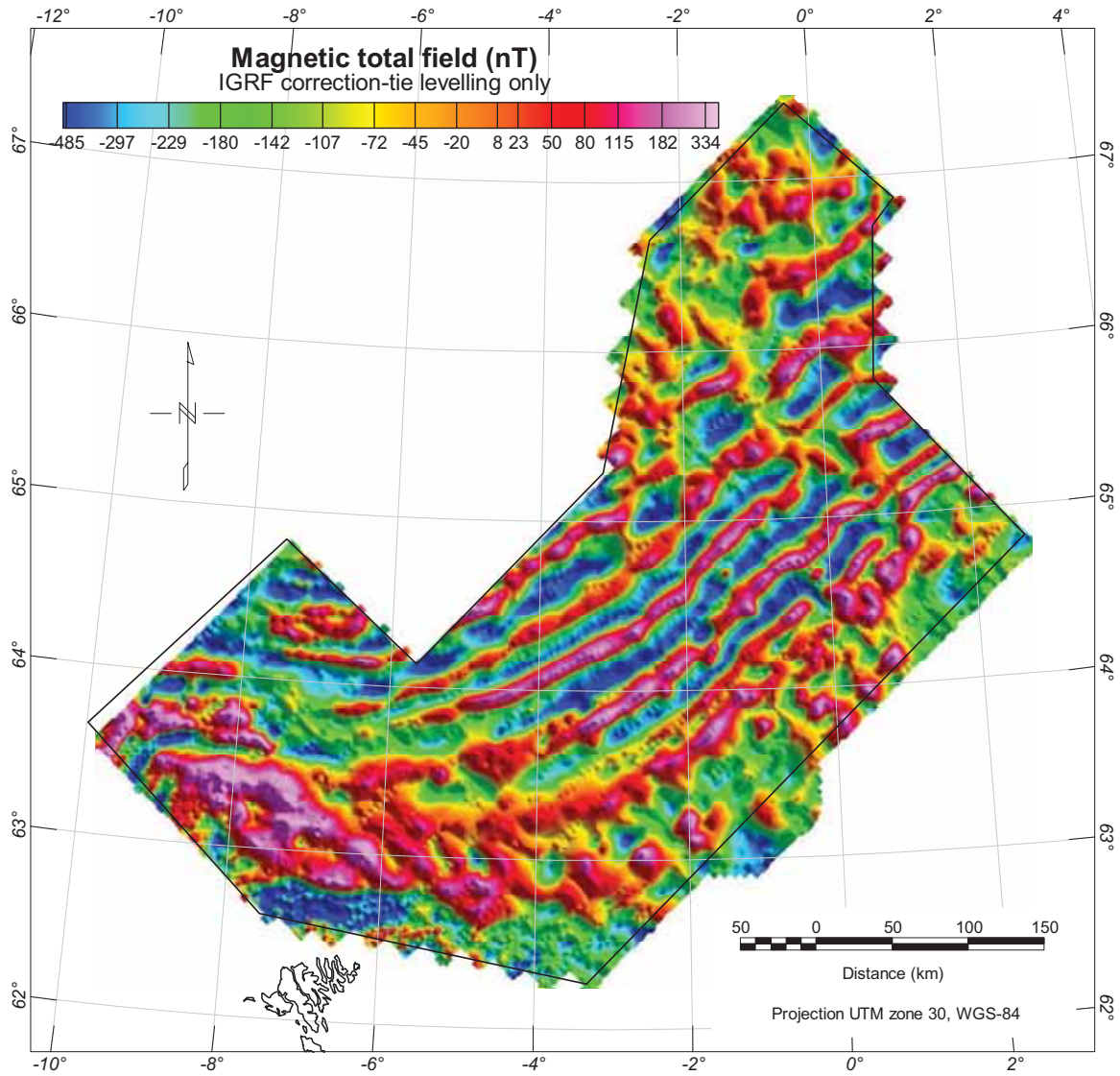


Figure 3.4 Statistical tie levelling of the magnetic profiles, lag corrected and referred to the International Geomagnetic Reference Field (IGRF-2005). Gridding of line and tie profiles using the minimum curvature algorithm (grid resolution: 500x500 m). The total magnetic intensity represents the measured magnetic data after removal of the variations due to changes in the magnetic field of the IGRF model. This yields the anomalous total magnetic intensity, which for practical purposes is the component of the anomalous magnetic field along the earth's field direction. With the IGRF removal, the statistical levelling represents the first step of the levelling method.

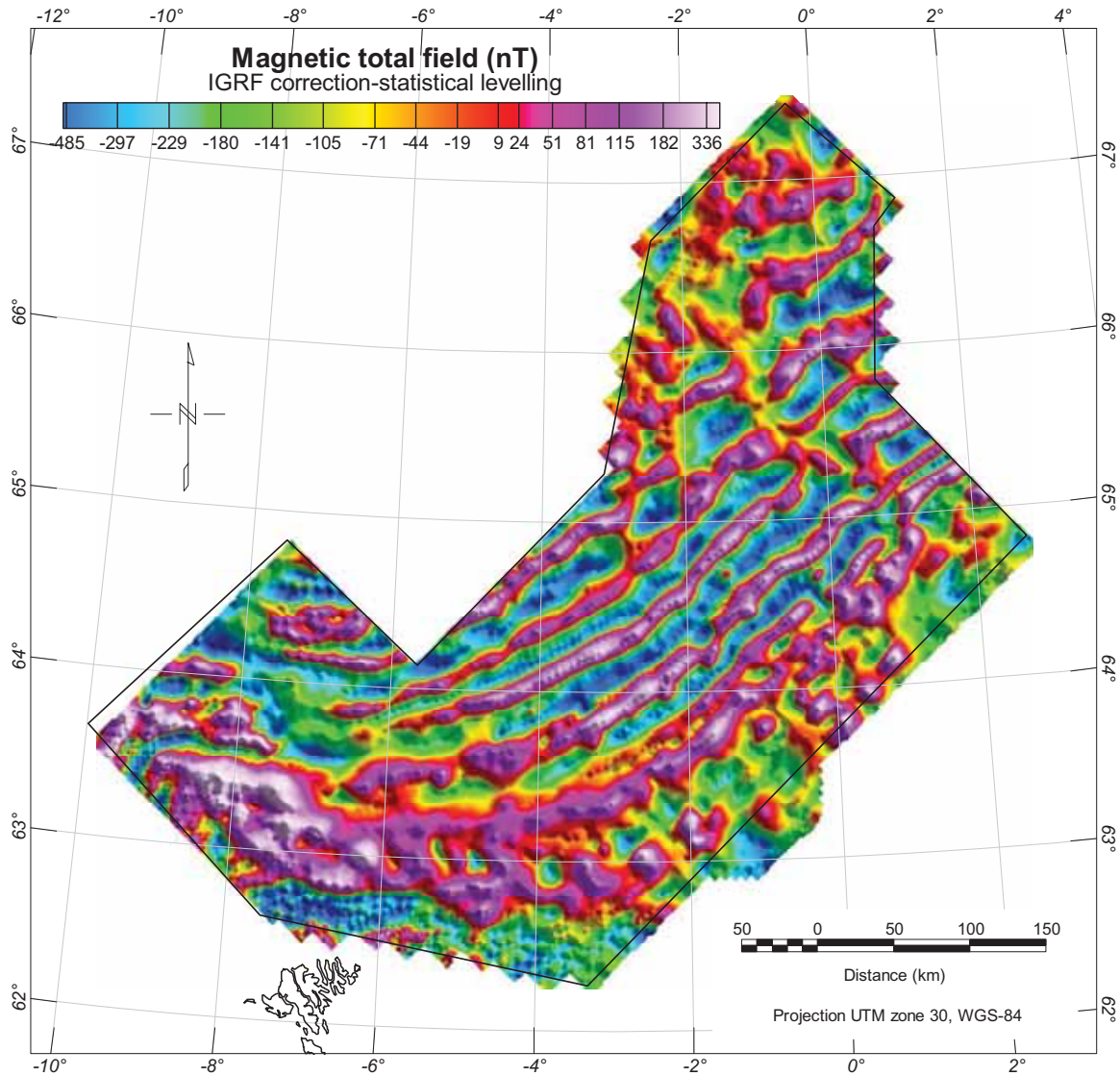


Figure 3.5 Full levelling magnetic grid of the magnetic profiles, lag corrected and referred to IGRF-2006. The levelling represents the second step of the levelling approach based on least-square technique. Gridding of the line profiles using the minimum curvature algorithm (grid resolution: 500x500 m).

### 3.2.3 Micro-levelling

To remove minor (“micro”) levelling errors still remaining along parts of some profiles after the statistical levelling, we performed micro-levelling techniques. We applied separately two micro-levelling techniques: 1) the Geosoft micro-levelling approach using a decorrugation technique (Geosoft 2005b) and 2) the moving median filtering method developed at NGU (Mauring et al. 2002, Mauring and Kihle 2006).

The moving median levelling method is described in detail in Mauring and Kihle (2006). A floating median filter was applied to each line. For a given line, the 1D median was determined at each station based on data values within a given distance of the station. We can in the same way find a 2-

D median value for a circular area around the station. The difference between the 2D and 1D median value was taken to be the micro-levelling error and was added to the magnetic value at that station after smoothing. This algorithm was particularly efficient to deal with small amplitude variation of the magnetic total field during the previous BAS-06 survey in the Barents Sea (Gernigon et al. 2007a). However, the result along the NB-07, where amplitudes are significantly higher, was somewhat disappointing as it created high-frequency noise at the end. After several tests, we decided not to use this moving median levelling method for this survey.

The Geosoft micro levelling has been realized using the PGW GX System of the available MAGMAP processing package (Geosoft 2005b). It proved to be more efficient for this specific case where the magnetic anomalies are more prominent. The PGW GX System applies a decorrugation process in the Fourier domain to isolate the levelling corrections before applying them to the original data (Figs. 3.6, 3.7). The NB-07 data have been decorrugated to reduce line-to-line levelling errors, which are visible as linear magnetic features parallel to the flight lines (Fig. 3.6). Decorrugation is simply a frequency domain procedure based on a directional cosine filter. This filter retains anomalies, from gridded data, in the flight line direction only. First, a Butterworth high-pass filter is set to four times the line spacing to pass wavelengths on the order of two to four line separations. Such a process results from a line-to-line levelling error. In a second step, a directional cosine filter is set to pass wavelengths only in the direction of the lines. We applied an amplitude limit of 20 nT with a zero amplitude mode in the noise channel allowing a shorter non-linear filter to be applied. Afterwards a line-based filter to separate the high frequency geological signal from the longer wavelength levelling errors was used. A low-pass non-linear filter was finally applied to clean the levelling error channel with a Naudy filter tolerance of 0.1 nT and an amplitude limit value of 40nT. The micro-levelling result was obtained by subtraction of the magnetic residual levelling grid (Fig. 3.6) from the original dataset (Figs. 3.5, 3.7).



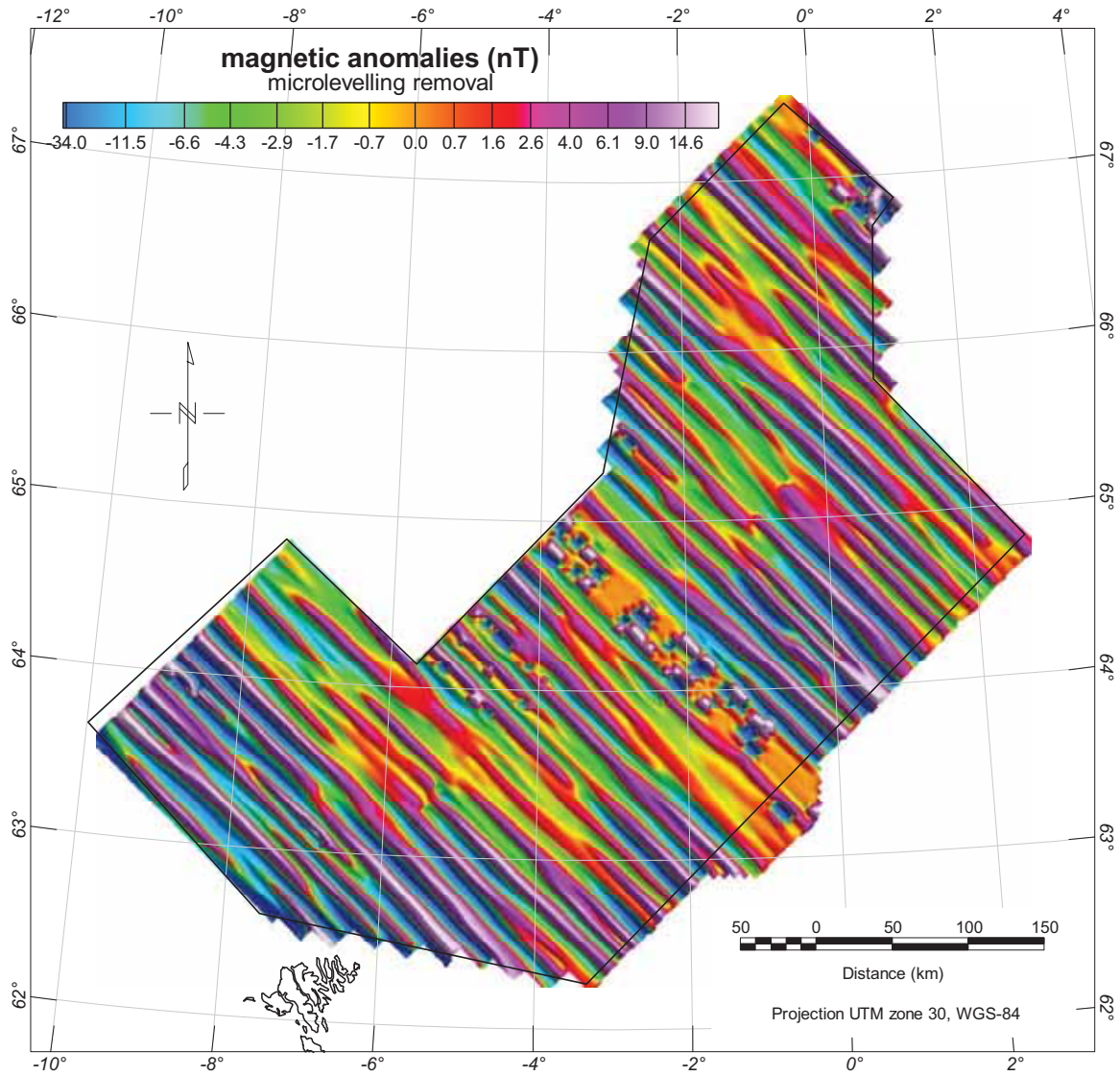


Figure 3.6 Magnetic residual after micro-levelling by decorrugation and subtraction of the total field obtained by statistical levelling (500x500m cell grid spacing). The NW-SE trends represent the micro levelling diurnal variations along the pre-existing lines.

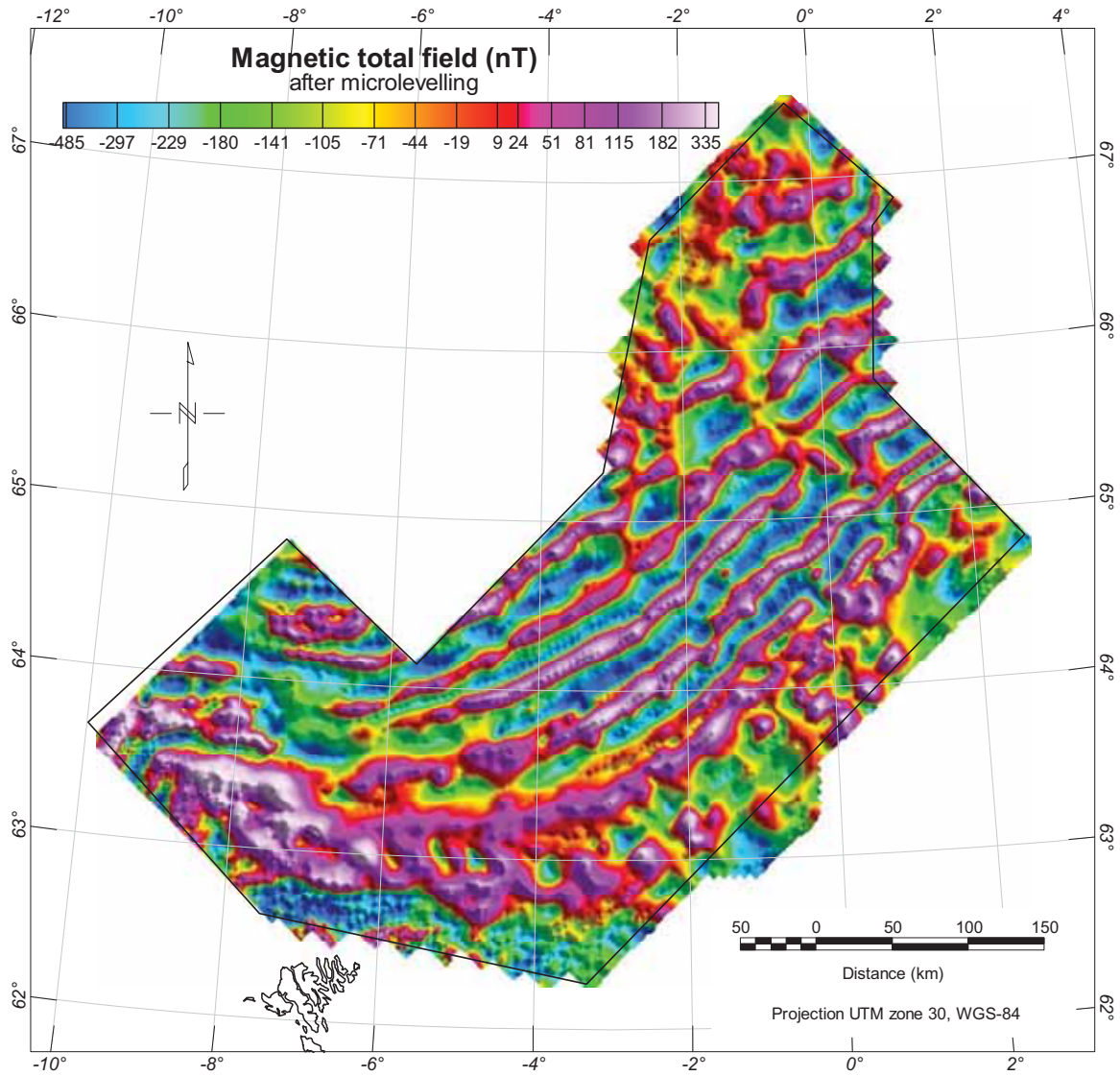


Figure 3.7 Total magnetic field after micro-levelling. Results from the FFT decorrugation technique of Geosoft. 500x500m cell grid spacing using the minimum curvature algorithm.

### 3.3 Gridding of the NB-07 dataset: important comments for interpreters

Most of the magnetic grids presented in this report refer to the minimum curvature gridding technique. The interpolated surface generated by minimum curvature is analogous to a thin, linearly elastic plate passing through each of the data values with a minimum amount of bending. Minimum curvature generates the smoothest possible surface while attempting to honour the data as closely as possible (Briggs 1974; Press et al. 2002). Minimum curvature produces a grid by repeatedly applying an equation over the grid in an attempt to smooth the grid. Each pass over the grid is counted as one iteration. The grid node values are recalculated until successive changes in the values are less than the maximum residuals value, or the maximum number of iterations is reached

(maximum iteration field). The minimum curvature gridding technique is efficient, fast and widely used in the Earth sciences.

However, the minimum curvature is not an exact interpolator and this means that the NB-07 data are not always honoured exactly after gridding (Fig. 3.8). A full sensitivity study with other gridding techniques was not realised in the present study but the processed profile values still allow interpreters and modellers to regrid the data using other gridding techniques and preferred software as they wish and according to their needs.

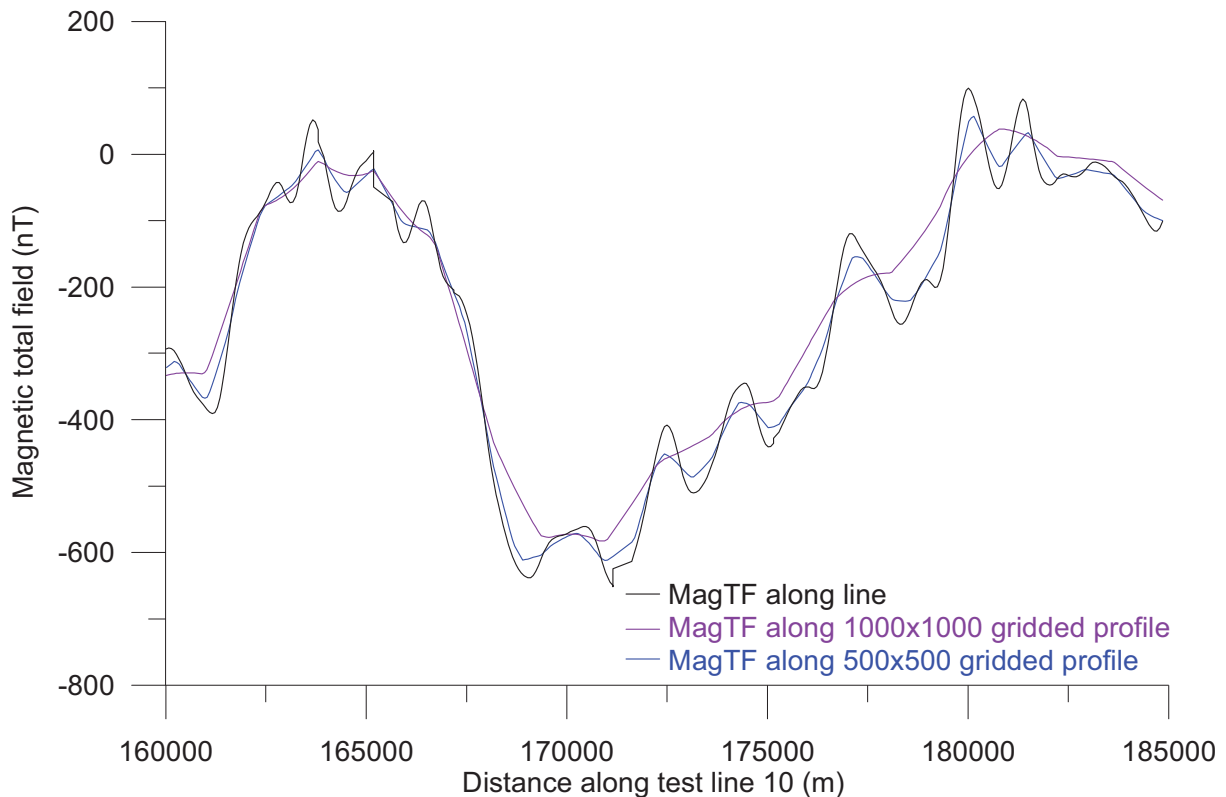


**Figure 3.8:** Different total magnetic field profiles extracted from grids and compared with the original signal measured along NB-07 line 10. The graphs illustrate the "smoothing" effects of the minimum curvature gridding technique according to different grid cell sizes. After extraction of the signal along the profiles and comparison with the non-gridded levelled signal, the result showed that a gridding at a 1000 m grid cell interval smooths the data, including the loss of some short-wavelength anomalies, north of the Faroes.

Gridding methods like the Kriging technique can be more relevant for specific parts of the survey area. The Kriging algorithm, for example, can be either an exact or a smoothing interpolator depending on the user-specified parameters. It can incorporate anisotropy and underlying trends in an efficient and natural manner and could be used locally to better refine linear magnetic features along the NB-07. The bi-directional gridding algorithm BIGRID was tested but induces artefact in the N-S direction. This may occur because BIGRID first interpolated values along the horizontal direction. One way to properly compare the two-gridding algorithms would be to rotate the lines from NE-SW to the E-W trend first.

Note also that the cell size is also critical when it comes to performing image enhancements in the Fourier domain or to define a proper resolution of the dataset. The grid cell size is mostly a function of the line spacing and depth of the magnetic sources (flight altitude+water depth) but is also a function of your needs and observation scale.

Some may consider that a small grid cell size ( $< 1/5$  line spacing) can create high-frequency noise and aliasing (the local "beading effects" along the linear anomalies) but it provides a better depiction of the spatial resolution. However, aliasing produced during the gridding at 500x500 and 1000x1000 (Fig. 3.9) induces annoying artefacts during 2D-FFT filtering (see next chapter). For example, downward continuation involves multiplying the Fourier spectrum of the image by an exponential function. This exponential function increases rapidly with frequency and if the cell size is very fine, the very highest frequencies will be substantially amplified. These high frequencies will generally be a mixture of noise (along the line direction) and interpolation effects (in the tie-line direction) and therefore, their amplification is undesirable. Similar initial noise also influences the derivatives and can produce unwanted artifacts. For 2D-FFT manipulation we rather choose a grid cell size of 1650x1650m.

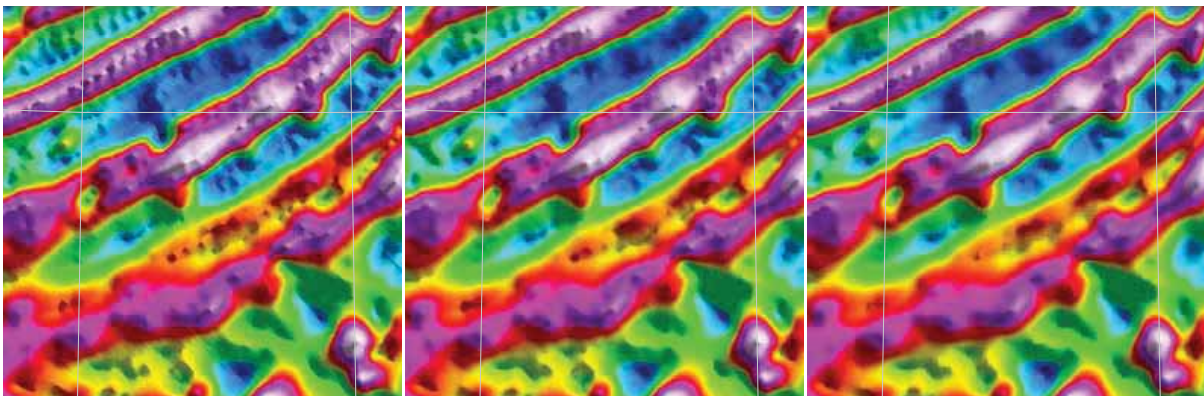


Figure 3.9 Zoom on different magnetic grids reduced to the pole, using different grid cell size. Note that an aliasing problem is observed for grid cell sizes of 500x500 (left picture) and 1000x1000 m (central picture). It decreases using a grid size of 1650x1650m ( $\sim 1/3$  line spacing)

For future interpretation and modelling in the survey area, we recommended the use of the two grids systematically combined with the original signal for a reliable interpretation. For any Fourier filtering that involves amplification of high frequencies we urge caution and recommend a cell size no finer than  $1/3$  to  $1/4$  of the line spacing.

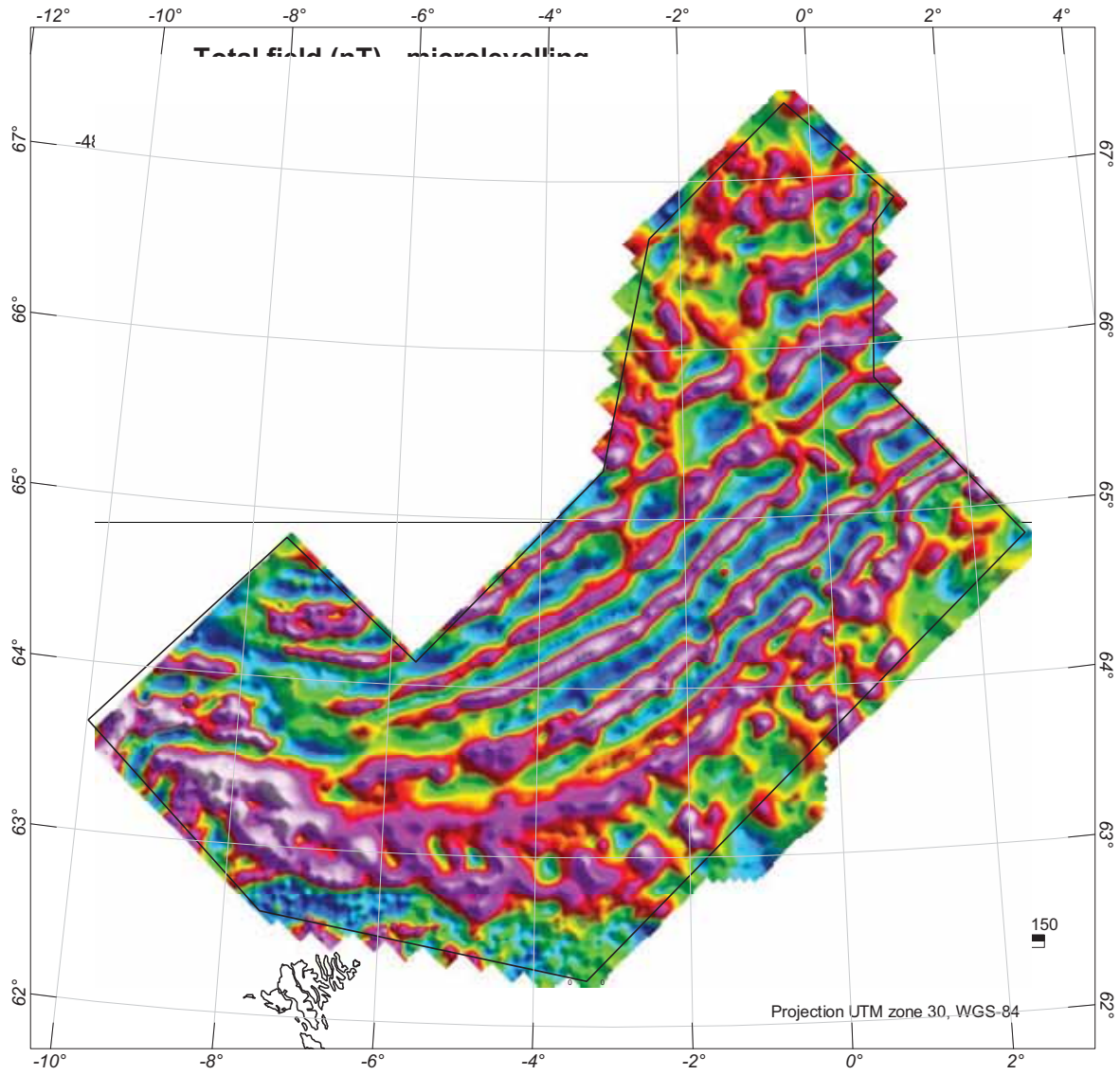


Figure 3.10 Total magnetic field after micro-levelling. Results using the FFT decorrugation technique of Geosoft with a 1650×1650m grid cell spacing. This grid has been used for most of the filtering involving 2D-FFT processing.

## 4 CONVENTIONNAL FILTERING TECHNIQUES

Laurent Gernigon

### 4.1 Potential field and integrated study

Affirmed development of the interpretation theory is usually connected with many case studies of successful application of seismic methods combined with filtered gravity and magnetic data in solving problems in exploration and structural geophysics. During the interpretation of the NB-07 survey, potential field techniques have been used intensively as irremediable and complementary tools for the interpretation of the survey area. It was also a good way to test the validity of other geophysical models and help majestically the seismic interpretation. Relevant filtering has been carried out in order to enhance the main structural changes and magmatic features observed along the NB-07.

The aim of this section is to briefly present and discuss the different processing techniques used to enhance and model the magnetic data across the NB-07 survey. Specific and preliminary interpretation based on these grids will be presented in the next part of this report (Chapter 9).

### 4.2 Wavelength filtering, frequency content and power spectrum

Magnetic (and gravity) anomalies whose wavelengths are long relative to the dimensions of the geologic objectives of a particular investigation are called regional anomalies. Because shallow geologic features can have large lateral dimensions, one has to be careful, but regional anomalies are usually thought to reflect the effects of relatively deep features. Anomalies whose wavelengths are similar to the dimensions of the geological objectives of a particular investigation are called local anomalies. In the processing of magnetic data, it is usually preferable to attempt to separate the regional and local anomalies prior to interpretation. Magnetic anomalies observed along the NB-07 survey characterise an amalgamation of sources reflecting the regional field, noise and lateral density and magnetic variations within the crust and upper mantle (e.g. Blakely 1995). Measured gravity anomalies, therefore, represent the combination of wavelengths associated with the spatially distributed sources.

During the NB-07 project, a number of transformation methods have been used after data levelling in order to enhance the main structural and magnetic features. These techniques used to separate regional from local gravity anomalies take many forms and can all be considered as filtering in a general sense (Blakely 1995). Many of these techniques are the same as those employed in enhancing traditional remote sensing imagery, seismic data or processing of digital elevation data (Milligan and Gunn 1997; Mari et al. 2001).

Filters have been applied to the NB-07 gridded anomalies which enable us to isolate, interpret or/and enhance the wavelengths of greatest interest, therefore facilitating geological interpretations

(e.g. Blakely 1995). The magnetic (and/or gravity) gridded datasets can be transformed from the space domain into the spectral domain and vice-versa using the Fast Fourier Transform (FFT). Transformation of the gridded data into the frequency domain is completed by application of a discrete 2D Fourier transform (DFT) (Bhattacharya 1966; Blakely et al. 1995).

For spectral analysis we use the Geosoft MAGMAP Discret Fourier Transform algorithm (Geosoft 2005a,b,c), which apply the method of Bhattacharyya (1966). The DFT algorithm works fast by exploiting symmetries that are present for images of certain dimensions. The algorithm implemented by Geosoft in Oasis montaj is explicitly the Winograd DFT (Geosoft 2005c, Winograd 1978). This FFT transformation requires that the image fills an entire rectangle, a condition not met by the NB-07. Therefore, any survey gaps or irregular edges will also need to be filled with synthetic data. The edge matching and the gap filling were achieved using the maximum entropy algorithm (Burg 1975).

Fourier transforms are usually displayed as 2-D power spectra with a logarithmic stretch applied to the data. The power spectrum of the NB-07 survey reflects the strength of the sine and cosine components at each frequency (Fig. 4.1). The reason for displaying with a logarithmic stretch is the huge variation in the amplitudes of the different spectral components. Most aeromagnetic datasets are dominated by the lower frequency Fourier components for the deep part of the basin (i.e. magnetic intensity is smooth at airborne altitude). The maximum and reliable frequencies present in the Fourier domain are function of the Nyquist number, which again is a function of the spatial grid size,  $NX_{\max}=1/2\Delta x$  and  $NY_{\max}=1/2\Delta y$ . Any higher frequencies present in the data will appear at lower frequencies and effectively contaminate the spectrum. This phenomenon produces the aliasing problem previously discussed and is an inevitable consequence of discrete sampling when the sampling rate is not sufficiently rapid.

The Fourier transform,  $F(\mathbf{u},\mathbf{v})$ , of the magnetic signal,  $T(\mathbf{x},\mathbf{y})$ , defined over a 2-D space is given by:

$$F(u, v) = \int_{-\infty}^{\infty} du \int_{-\infty}^{\infty} dv \cdot T(x, y) \cdot \exp[2\pi(ux + vy)]$$

If  $(\mathbf{x},\mathbf{y})$  are spatial co-ordinates in units of meters, then  $(\mathbf{u},\mathbf{v})$  are frequency co-ordinates in units of cycles per meter. In real world applications it is not possible to measure the signal of Interest continuously, nor is it possible to measure it indefinitely. To overcome these difficulties, the Geosoft FFT algorithm usually interpolates our data to a regular grid and then calculate the resulting Fourier transform. With a  $N \times M$  spatial grid with cell spacing of  $\Delta x$  and  $\Delta y$  in the x- and y-directions respectively, the FFT is calculated on an  $N \times M$  frequency grid with spacing of  $\Delta u = 1/N\Delta x$  and  $\Delta v = 1/M\Delta y$

$$F_{jk} = \Delta x \Delta y \sum_{n=1}^N \sum_{m=1}^M T_{mn} \exp \left[ 2\pi \cdot i \left( \frac{jn}{N} + \frac{km}{M} \right) \right]$$

where

$$F_{jk} = F\left(\frac{j}{N\Delta x}, \frac{k}{M\Delta y}\right) \text{ and } T_{mn} = T(n\Delta x, m\Delta y)$$

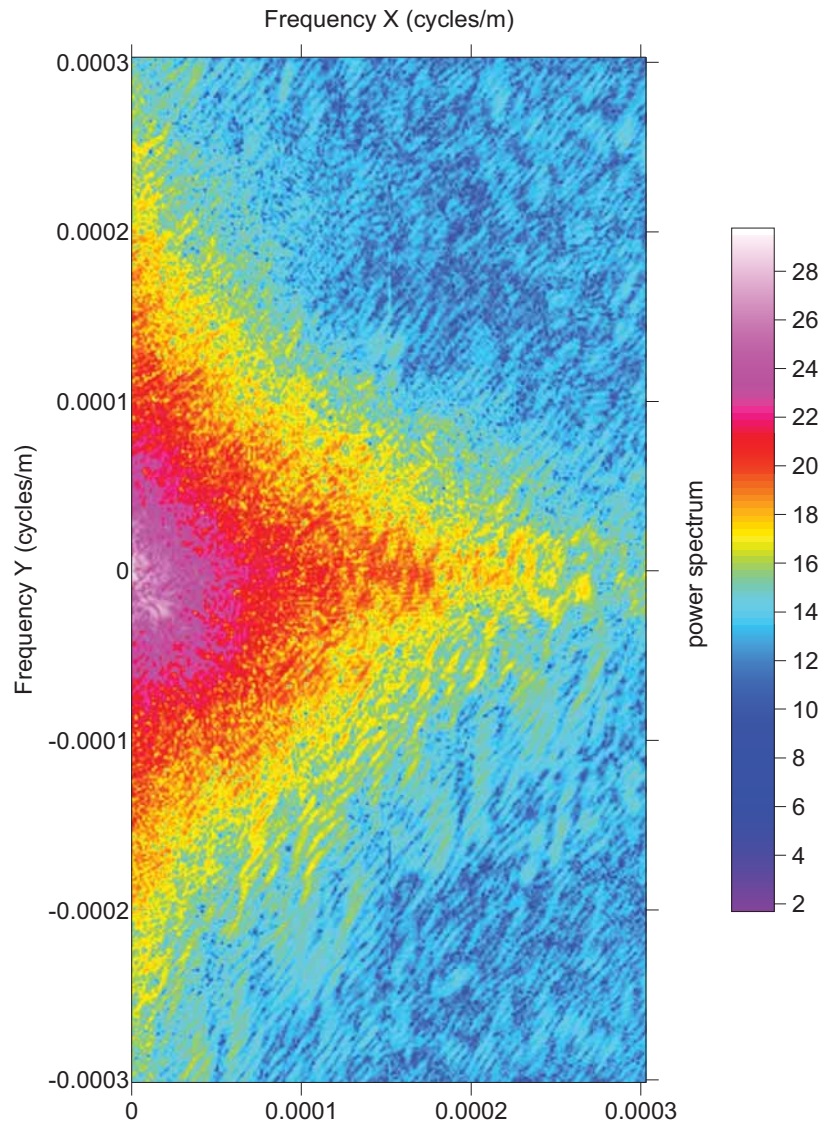


Figure 4.1 2D power spectrum and distribution of the frequency content of the NB-07 magnetic total field (RTP) gridded after micro-levelling. Red colours correspond to regions of high power, grading to yellow, green and then to blue, which represents the lowest power. The very centre of the frequency spectrum represents the average value in the image, while those frequencies immediately adjacent correspond to low frequency variation. Frequencies gradually increase as we move away from the centre of the frequency spectrum.

### 4.3 Magnetic sources

A relationship between the power energy spectrum and the depth distribution of magnetic sources can also be roughly investigated before any advanced interpretation. It was demonstrated for a simple magnetic prism by Battacharrya (1966) (Fig. 4.2). Battacharrya (1966) showed that the power energy spectrum of the magnetic total field produced by a synthetic prism ( $\Phi_{\text{prism}}$ ) can be



approximated as a function depending on depths to the top ( $z_{top}$ ) and base of the prism ( $z_{base}$ ) (Fig. 4.2). At medium to high wavenumbers (=long wavelengths):

$$\Phi_{prism}(k) \approx e^{-k \cdot z_{top}} - e^{-k \cdot z_{base}}$$

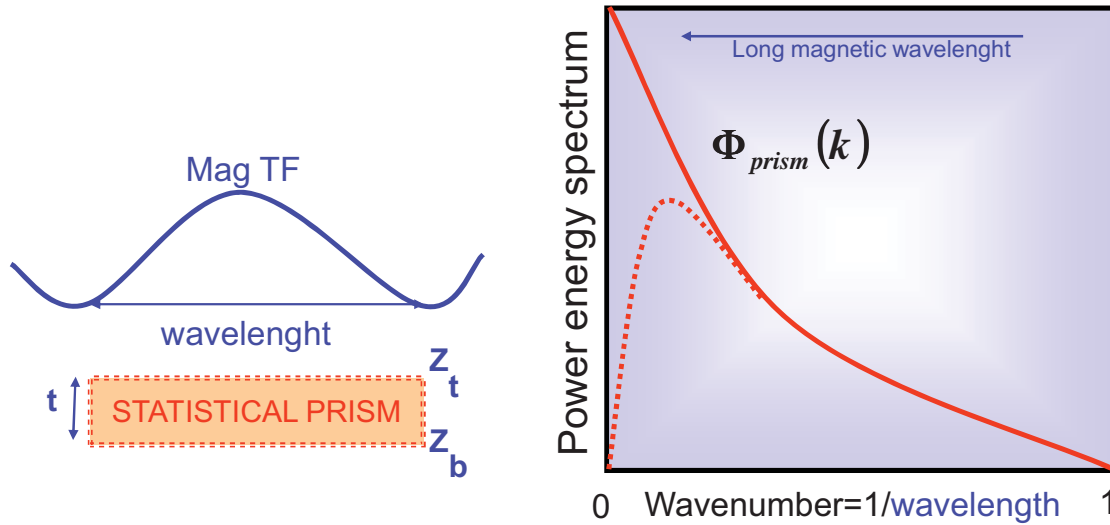


Figure 4.2 Magnetic total field produced by a simple prism (left) and power energy spectrum of this magnetic Total field as function of the wavenumbers ( $k$ ).

This fundamental approach also proposed by Spector and Grant (1970) provides information about the depth to a magnetic source sources. In their theory, the anomaly is assumed to be produced by a large number of blocks but the parameters describing any one block are assumed to obey probabilities common to an entire set of different sources. The slope of each linear segment provides information about the depth to a magnetic discontinuity and magnetic interfaces (Spector 1970).

If we examine the shape of a NB-07 power spectrum (Fig. 4.3), the “statistical” average depth to an ensemble of sources along the NB-07 survey can be easily evaluated using the value of the slope  $\alpha$  along the steepest straight segment observed along the radial spectrum divided by  $4\pi$ . We calculate automatic slopes using a gradient routine along few adjacent points (Fig. 4.3). Unfortunately, some artefacts at low wavenumbers persist and sometimes wrongly affect this estimation. It should be noted that it is easier and more reasonable to measure the slopes on a printout, as the spectrum is more stretched out. The graphical technique is time-consuming but it makes it easier to identify and validate straight-line segments. Due to graphical uncertainties we estimate an uncertainty of  $\pm 2\text{km}$ , in average for each depth calculation. This technique allows us a preliminary and quick look at the magnetic sources depth distribution of the NB-07 survey.

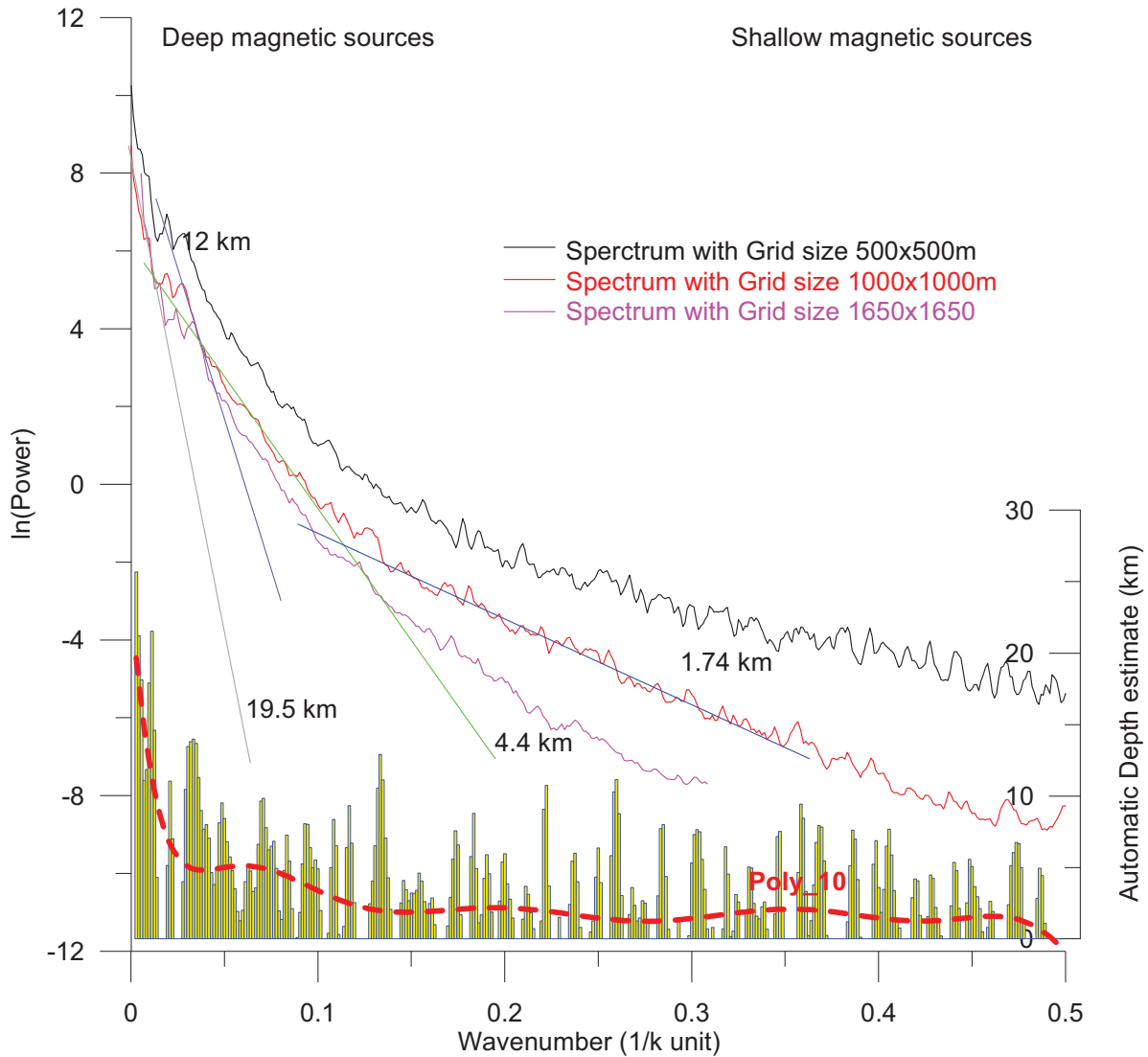


Figure 4.3 Frequency content and averaged power spectra computed for different grid size used during the minimum curvature gridding of the NB-07 magnetic total field then reduce to the pole using 2D-FFT. Note that the noise increases with smaller grid cell spacing. Steeper slopes increasing to the left of the plot, coincides with the deep-seated contribution. The depth estimate plot bar is an automatic 5 points slope and depth calculation, derived from the spectrum file (only for the 1000x1000 m grid). The poly-10 curve is an order 10 orthogonal polygonal calculated thought the depth estimation of the spectrum computed for the 1000x1000 grid size. It can be used to highlight the main segment and average statistical magnetic sources. The deepest set of sources along the survey is located at ~19.5 km and two other can be proposed at 4.4 km and 1.74 km in average.

#### 4.4 Reduction to the pole (RTP)

The magnetic data were reduced to the pole to properly register and locate the magnetic anomalies spatially above the magnetic bodies within the crust. Inclination and declination were derived from the IGRF-2006 model (formally 2005 since the IGRF is updated every 5 years only) (Fig. 4.4).

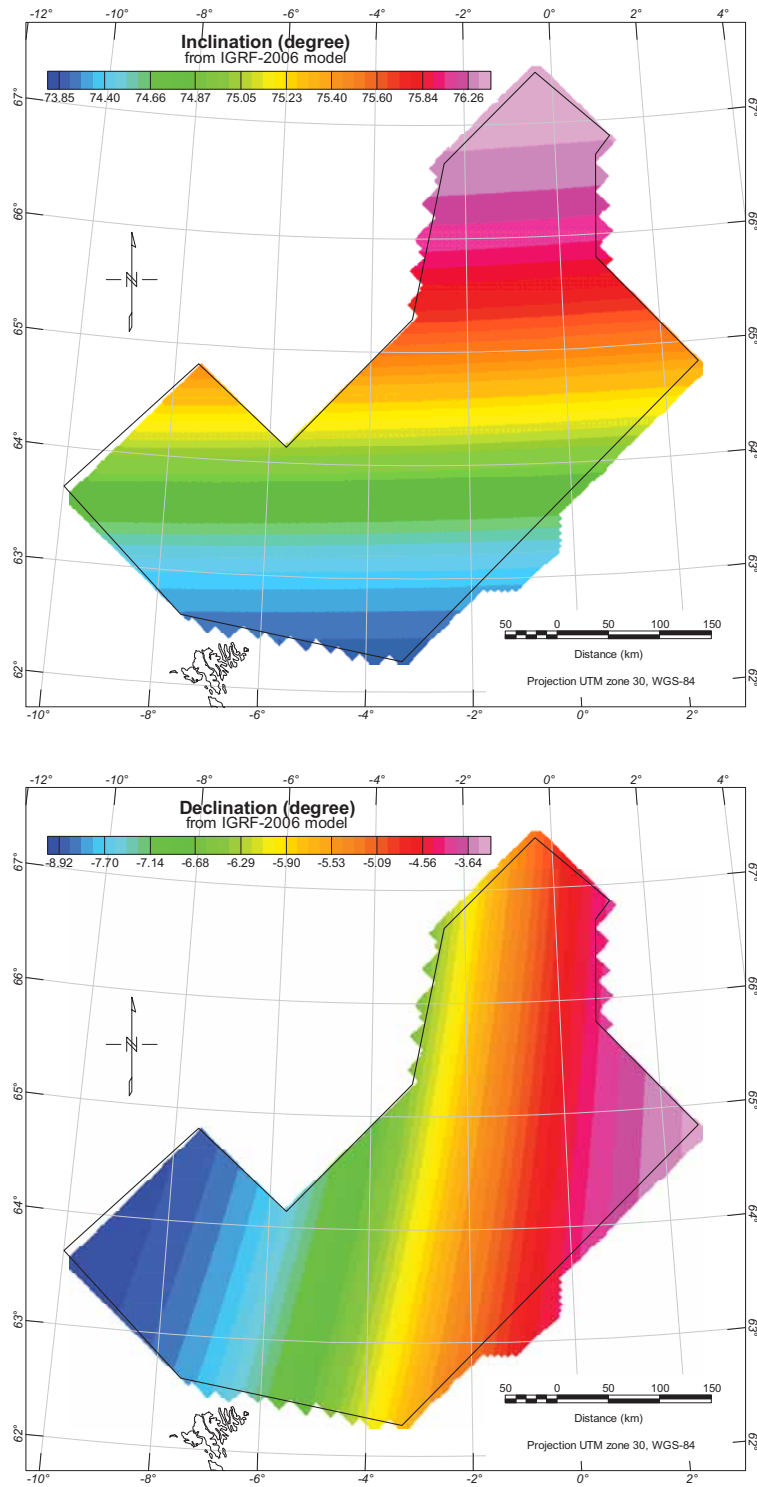


Figure 4.4 Values of inclination (top) and declination (bottom) of the geomagnetic field along the NB-07 survey area. IGRF-model available in 2006.

Even if only minor changes can be observed along the NB-07 at the Norway Basin latitude, the process is usually recommended for the application of magnetic data, and makes magnetic maps more reliable for geological mapping by removing some of the complexity involved in interpreting the anomalies (Blakely 1995).

The RTP is a process involving a phase transformation of the magnetic anomaly, within the Fourier domain. The measured total field anomaly is transformed into the vertical component of the field (Arkani Hamed 1988; Blakely 1995). At the latitude the NB-07 survey, we have found that the simplest and most effective technique is the one developed by GEOSOFT in the development of MAGMAP FFT processing (Geosoft 2005c). There are two ways to obtain the reduction to the pole. Running a 1D-FFT filter along each profile (Figs 4.5, 4.7) or running a 2D-FFT along the magnetic total field grid (Figs. 4.5, 4.8, 4.9). Assuming that all the observed magnetic field of a study area is due to induced magnetic effects, pole reduction was calculated in the frequency domain using Fourier convolution

$$\mathcal{H}(u, v) = \mathcal{F}(u, v) \cdot G(u, v)$$

$\mathcal{F}(u, v)$  is the Fourier transform of the magnetic field and  $u, v$  represent the frequencies co-ordinates in units of cycles per meter. The filter operator  $G(u, v)$  is simply multiplied by the transform of the grid on an element by element basis and the inverse transformation of  $\mathcal{H}(Mu, v)$  leading to the final RTP grid. The following operators (Grant and Dodds 1972) can be used (Figs. 4.5, 4.8; 4.9):

Using the 1D-FFT:

$$G(\theta) = \frac{1}{[\sin^2(I) + i \cdot \cos(I) \cdot \cos(D - \theta)]^2}$$

Using the 2D-FFT:

$$G(\theta) = \frac{[\sin^2(I) + i \cdot \cos(I) \cdot \cos(D - \theta)]^2}{[\sin^2(I') + i \cdot \cos(I') \cdot \cos(D - \theta)] \cdot [\sin^2(I) + i \cdot \cos^2 I \cdot \cos^2(D - \theta)]}$$

where:

$\theta = \tan^{-1}(u/v)$  is the wavenumber direction

$I$  is the magnetic inclination

$I'$  is the second magnetic inclination (=0 in this study)

$D$  is the magnetic declination

The assumption following this transformation is that the magnetic anomalies had been magnetised vertically at the pole and that the anomalies are observed from the pole. Key assumptions are that the magnetization of the source is entirely due to induced magnetization. Therefore the phase of the

anomaly is transformed into simpler symmetrical shapes that are assumed to lie directly over the magnetic sources (Blakely 1995). This assumption is essential for future mapping and analysis of the magnetic anomalies because it is assumed when applying edge enhancement, that the causative field is vertical. Consequently, some agree that the RTP filtering should be carefully considered. Moreover, it is assumed that both the magnetic field and the magnetization of the crust have constant directions within the study area (Arkani-Hamed 2007).

Statistics	Inclination along NB-07	Declination along NB-07
Minimum value	73.929451°	-9.62583637°
Maximum value	76.831749°	-2.95298958°
Mean value	75.1579384°	-6.05188218°
Standard deviation	0.668214115°	1.46640725°

Table 4.1 Minimum, maximum and mean values for both Inclination and declination directions observed in the NB-07 survey.

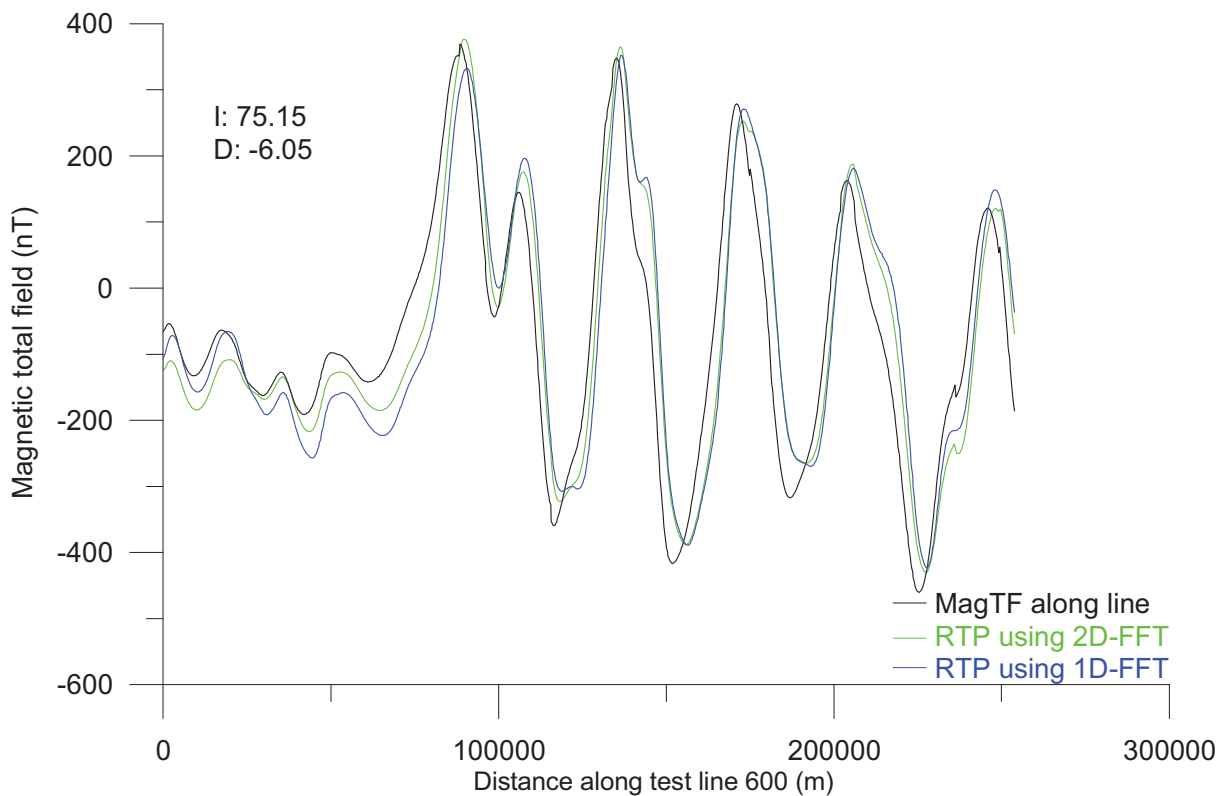


Figure 4.5 Differences between the 1-D and 2D FFT algorithms used to calculate the reduction to the pole along the NB-07 survey with the mean values of inclination and declination. The result is compared with the original magnetic total field.

The RTP filtering is also limited for large surveys because each RTP equation do not consider the synchronous variation of both inclination and declination. Each transformation only considers one value for inclinations and declinations. For the RTP transformation, we used the mean values of the inclination and declination directions (Table 4.1) and figure 4.6 shows that other values do not change the results of the RTP along the NB-07 significantly.

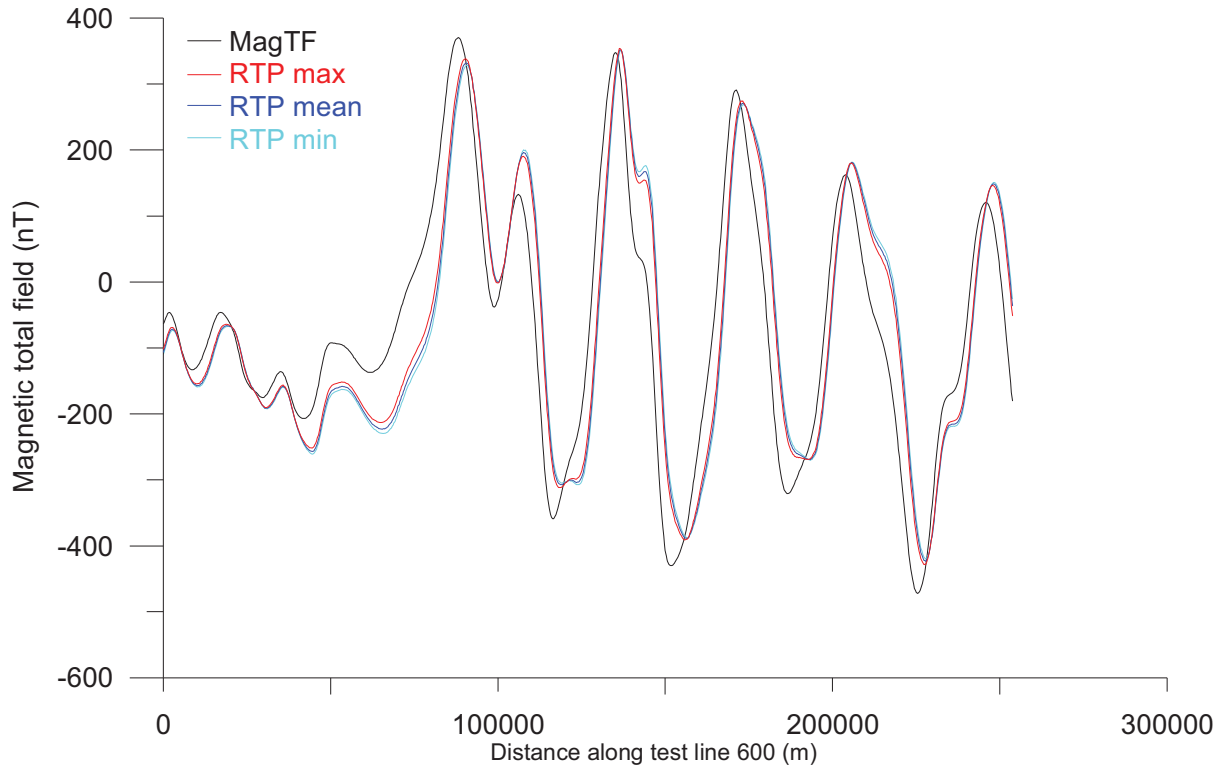


Figure 4.6 Differences between the 1-D FFT algorithms using different inclination and declination values. RTP transformation assumes only one value for both Inclination and declination. Since variations of these values along the survey area are small, only the mean value has been considered.

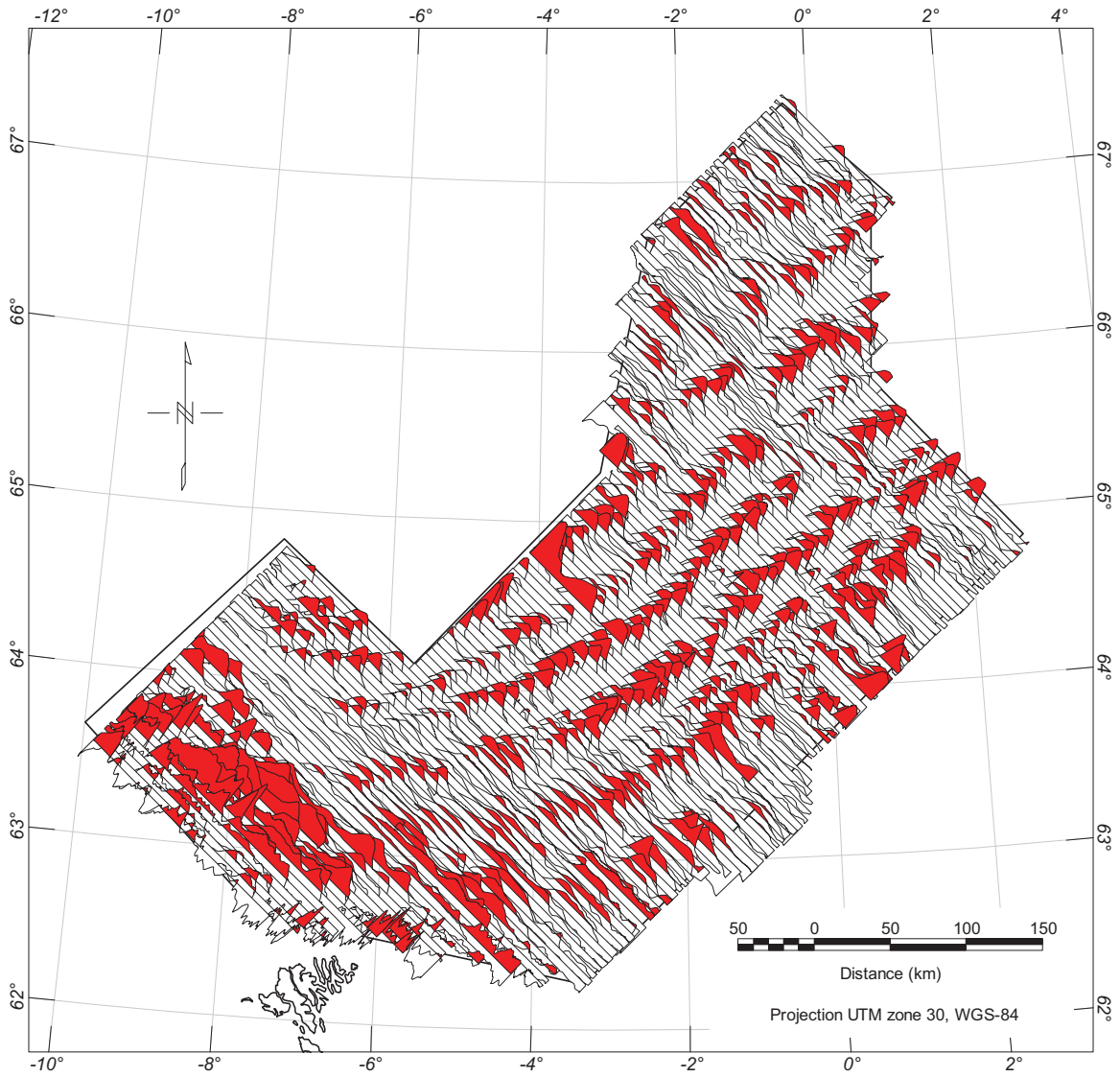


Figure 4.7 Profile map of the Total magnetic field reduced to the pole (I: 75.15; D: -6.05). The RTP was carried out using a 1D-FFT filtering applied to each line profile.

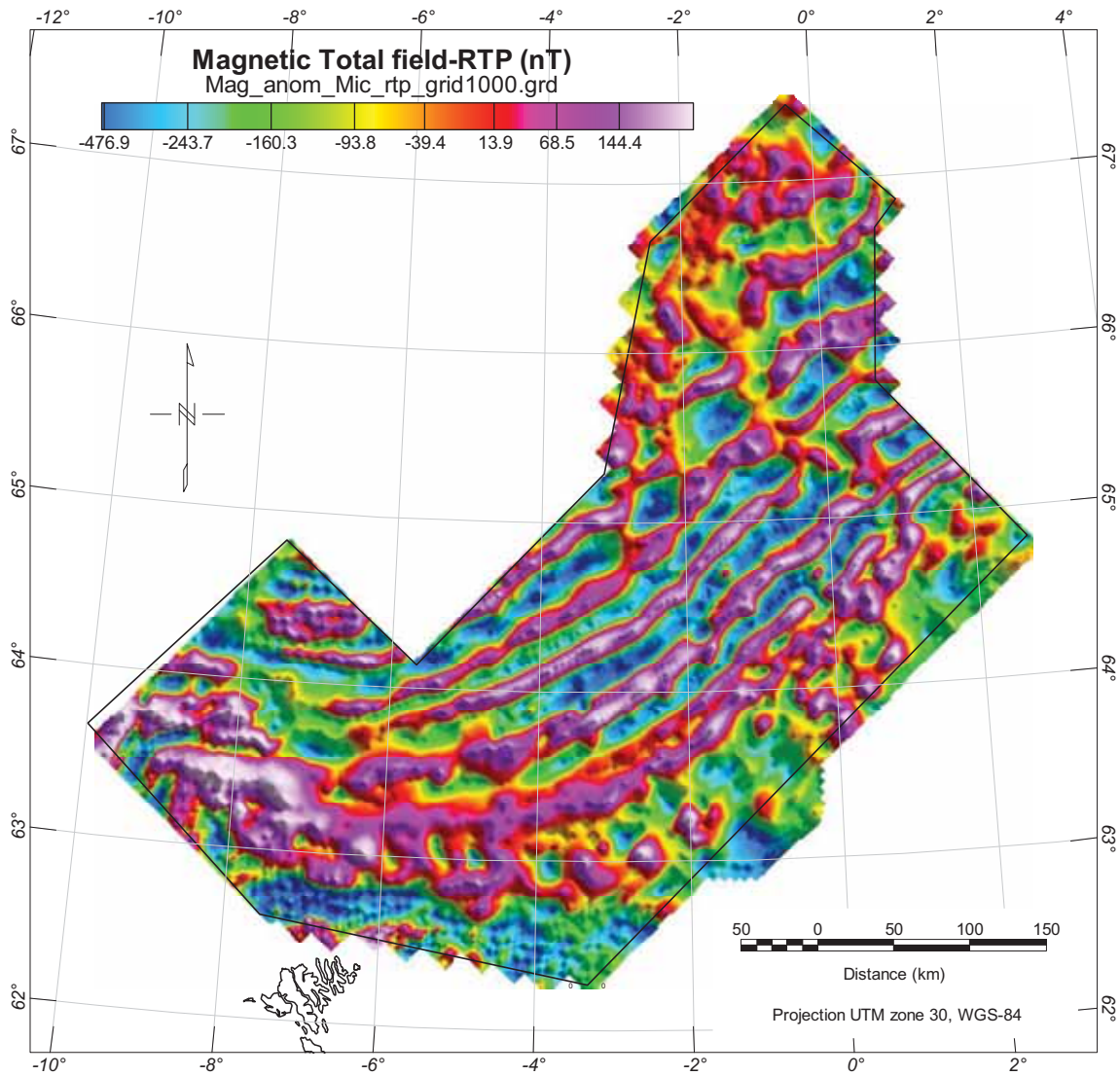


Figure 4.8 Gridded anomaly map of the total magnetic field reduced to the pole (Inc: 75.15; Dec: -6.05). The RTP was carried out using a 2D-FFT filtering along the microlevelled grid (1000x1000 m). The RTP transforms the anomaly into the one that would be observed with vertical magnetization and with a vertical Earth's field, i.e. the anomaly that would be observed if the sources were located at the Earth's magnetic north pole. As a result, reduction to the pole removes asymmetries caused by the non-vertical inducing field and places the anomalies more directly over their causative bodies, thus facilitating the interpretation of the magnetic dataset. Note that at the Norway Basin latitude, these changes are relatively small.



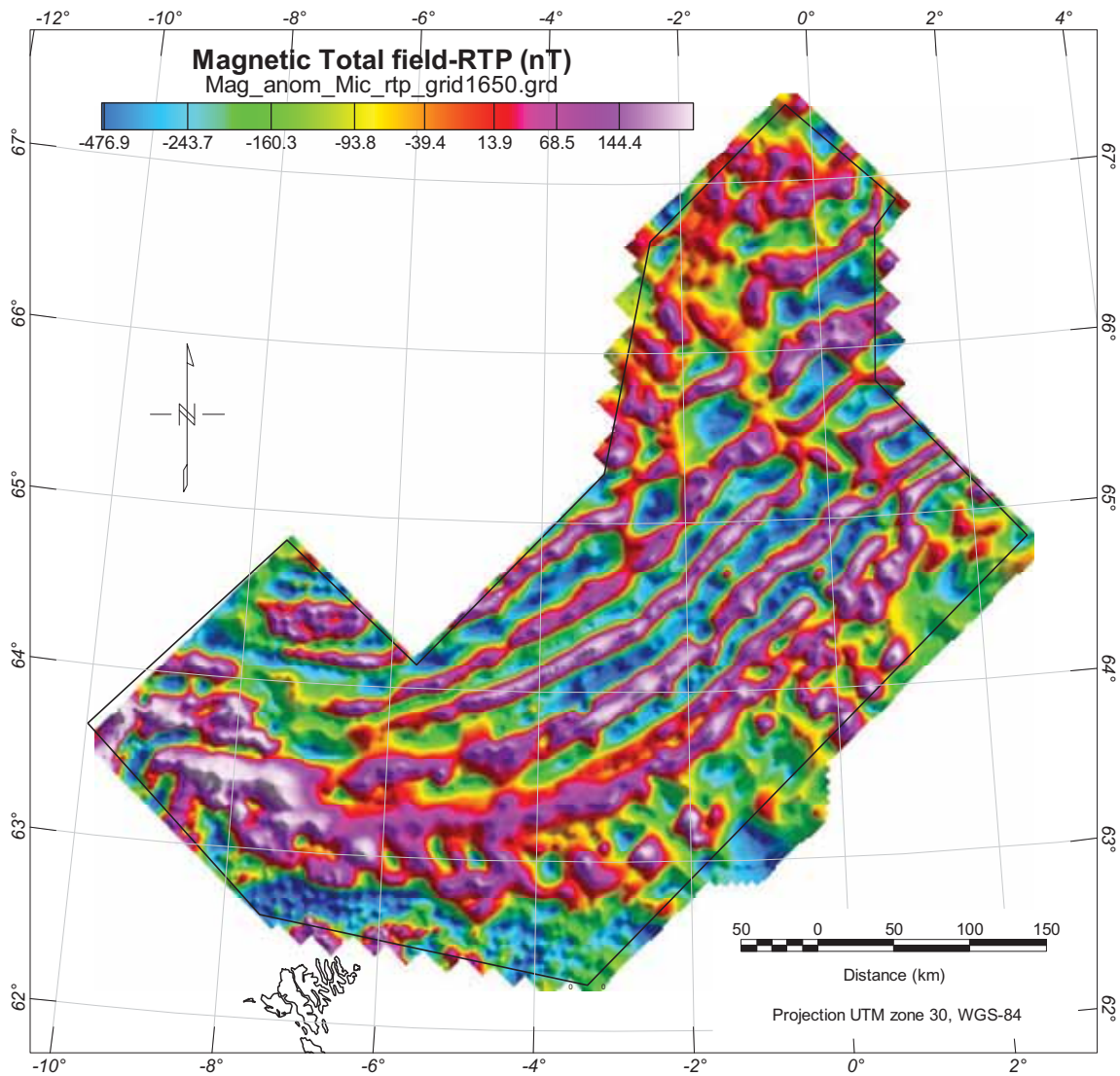


Figure 4.9 Gridded anomalies map of the total magnetic field reduced to the pole (I: 75.15; D: -6.05). For better display and to avoid instabilities during 2D-FFT filtering, we finally preferred this grid with a grid size of 1650x1650 m.

#### 4.5 Upward continuation

Upward continuation is a low-pass filtering process simulating the result of the survey if it was carried out at a higher elevation (Fig. 4.10). This process is based on the physical fact that the further the observation is from the body causing the anomaly, the broader the anomaly is. Upward continuations to 15 and 30 km have been used for the NB-07 survey to give indications about the main magnetic and tectonic units in the area (Fig. 4.10). Upward continuation underlines deep crustal blocks or deep sedimentary units of markedly different magnetic composition.

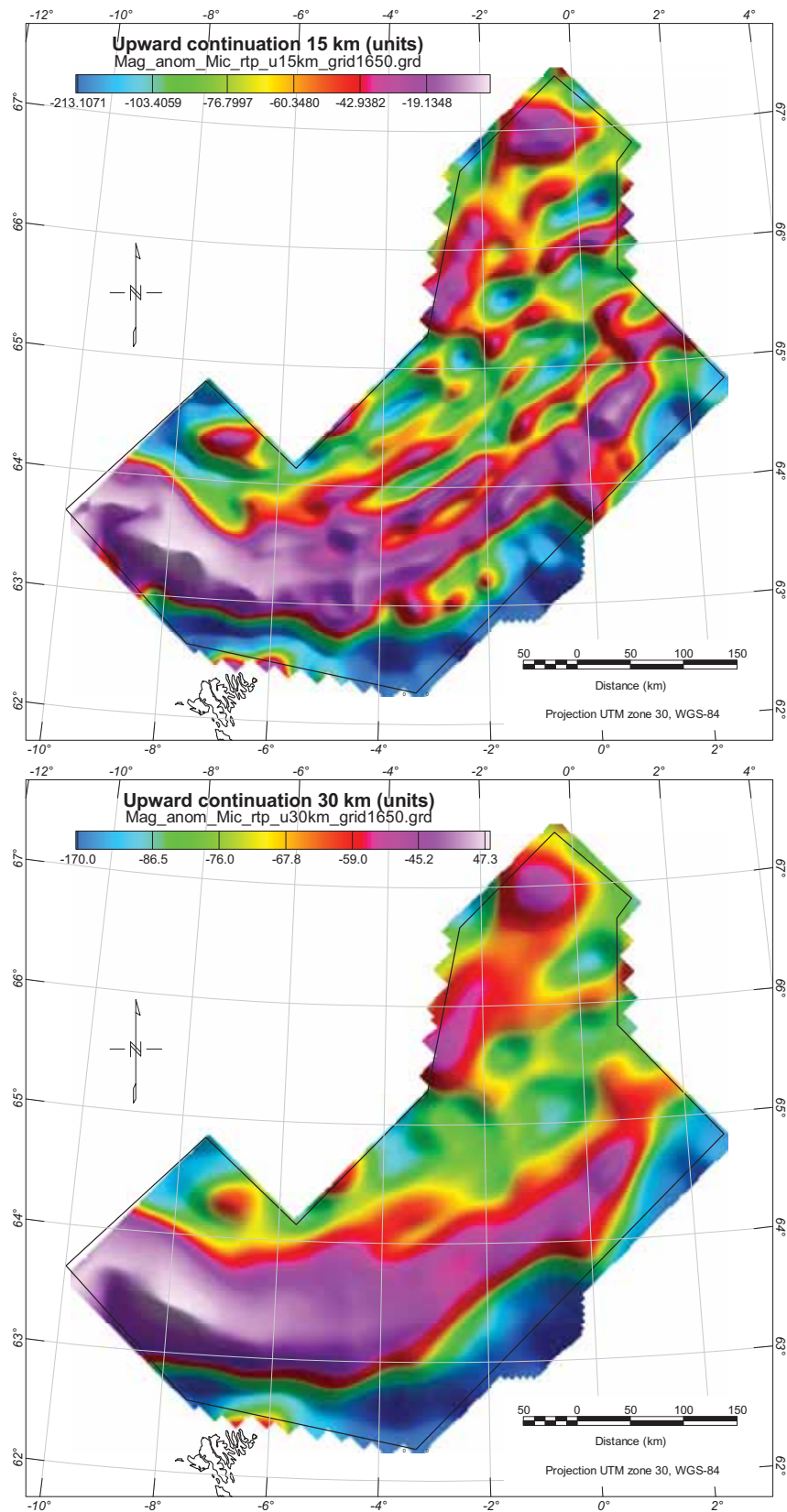


Figure 4.10 Upward continuation of the magnetic total field. Upward continuation uses wavelength filtering to simulate the appearance of potential-field maps if the data were recorded at a higher altitude. Large-scale regional anomalies and main crustal patterns are revealed.

#### **4.6 High-pass, low-pass and band-pass filtering**

To successfully delineate the shallow crustal feature, it is necessary to distinguish the short wavelength (noise) and long (regional) wavelengths due to deeper sources in order to isolate the wavelengths derived from upper crustal structures.

The regional anomalies can be estimated employing a variety of analytical techniques, including high-pass and low-pass filters (Figs. 4.11, 4.14, 4.15). The magnetic data were most useful to determine the presence, trends and depth of intrusions, faults and basement structures. High-pass filtering of the data at 50-30 km can be used to highlight sources typically at depths shallower than 10-15 km whereas 20-15 km high-pass filtering will be used for source depths shallower than 5 km (Figs. 4.11, 4.15).

Using band-pass filter, we can also investigate more precisely different ranges of wavelengths and estimated the depth distribution for different set of anomalies using the method of Spector and Grant (1970) to get the depth estimation of the sources assuming that the long wavelengths reflect the deeper sources (Figs. 4.12, 4.13, 4.14). Approaches to this problem are generally data- or model-based. Linear segments in the logarithmic power spectrum of the NB-07 (Fig. 4.3) correspond to different components of the field. The band-pass filtering has been designed to carry out the separation. This approach is used to separate expected basement effects from intrasedimentary sources and deep versus shallow crustal sources of the NB-07 magnetic data.

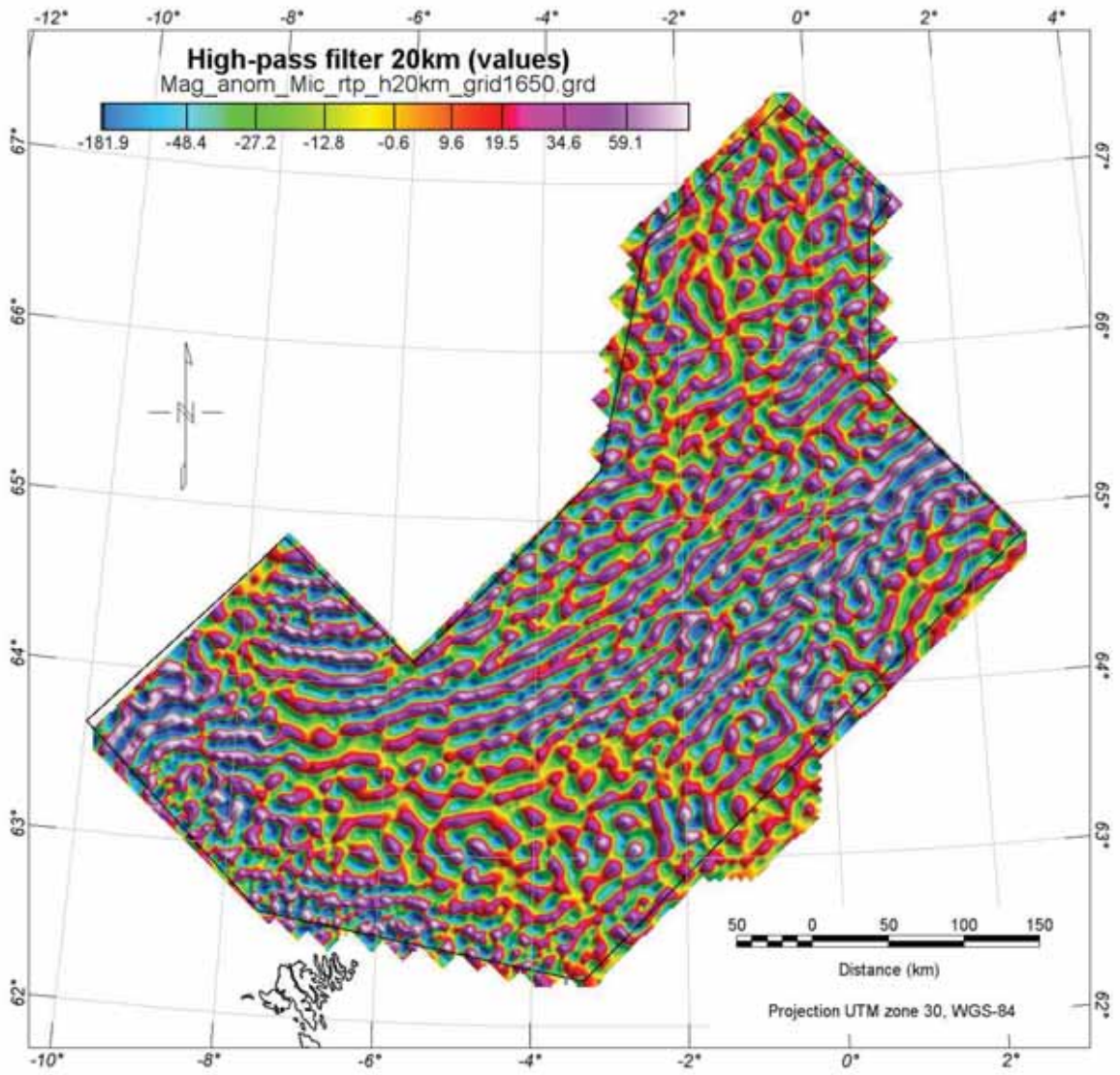


Figure 4.11 High-pass filtering (20km) of the magnetic total field, RTP. This filter underlines the distribution of the small wavelengths. Grid cell size at 1650x1650m.

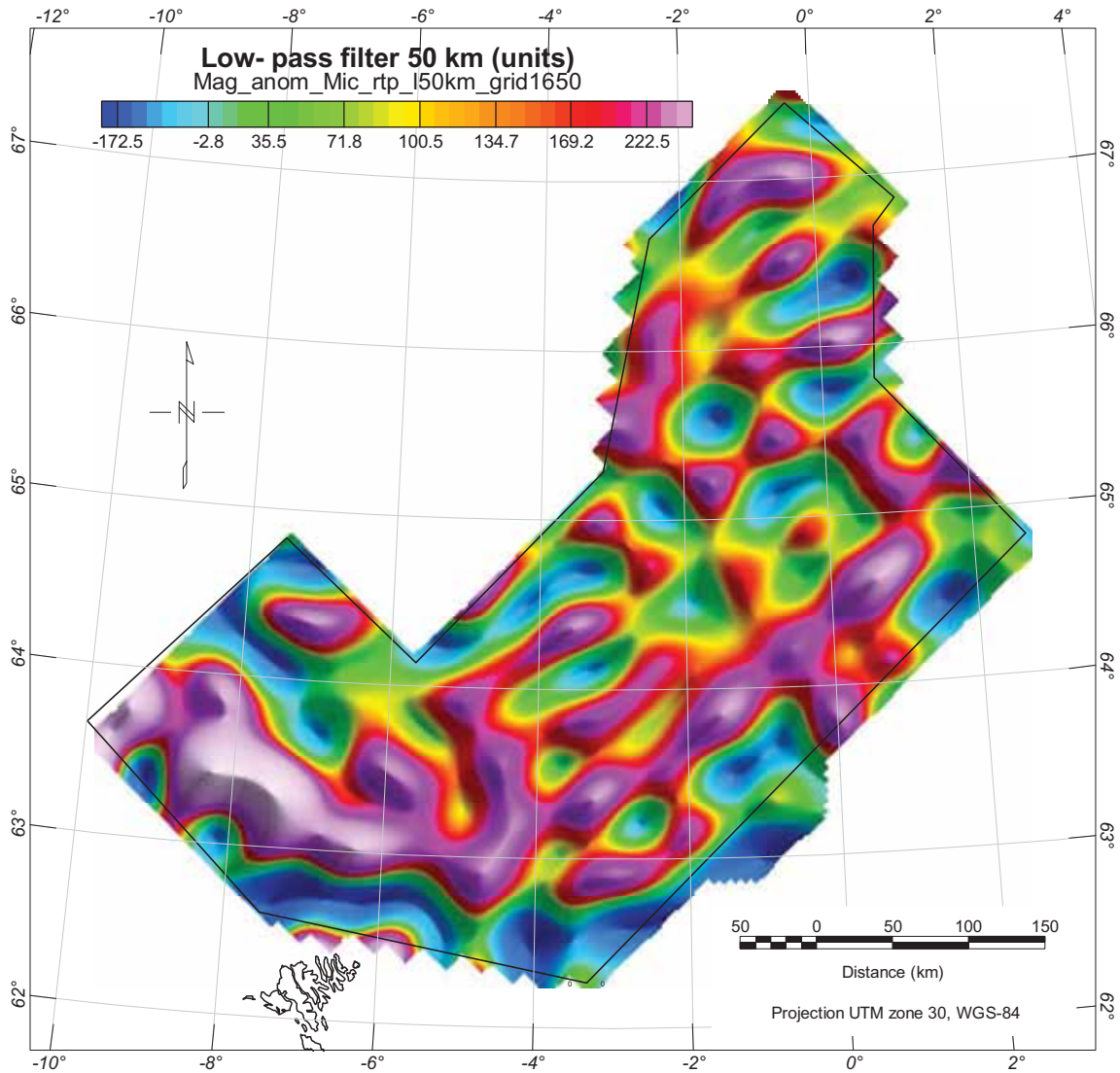


Figure 4.12 Low-pass filtering of the magnetic total field at 50km. This filter smooths the magnetic signal and underlines the distribution of the main magnetic units. These medium anomalies likely reflect mid-crustal sources and already illustrate the basin segmentation and complexity.

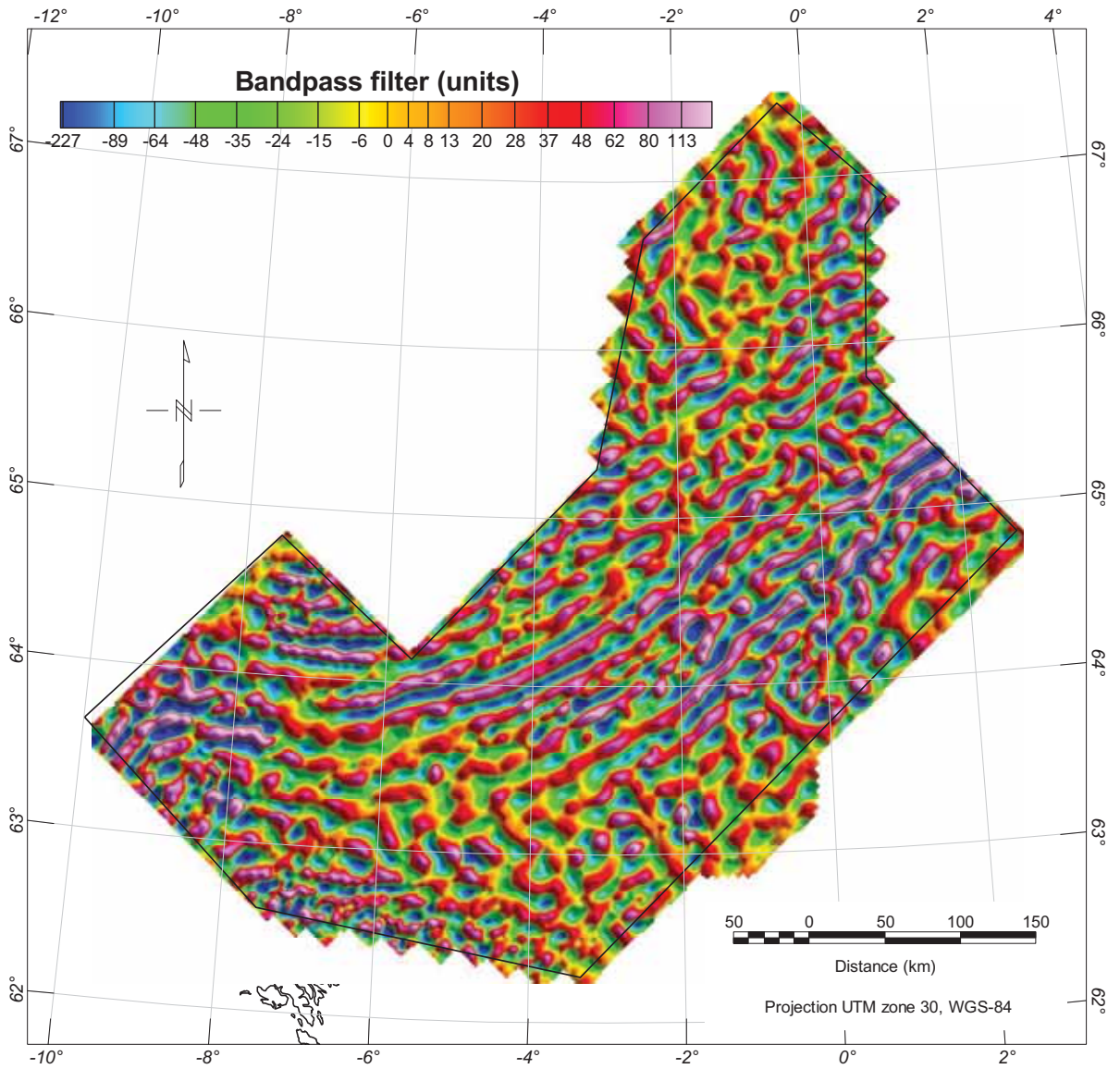


Figure 4.13 Band-pass sampling of the magnetic total field. This filter only considers the wavelengths specified in a certain range. This grid illustrate the anomalies sampled using a low wavenumber cutoff of 0.04 (in 1/k\_unit) and a high wavenumber cut-off of 0.6 in 1/k\_unit). According to the spectrum analysis, these anomalies should represent sources located in the 3-5 km depth interval.

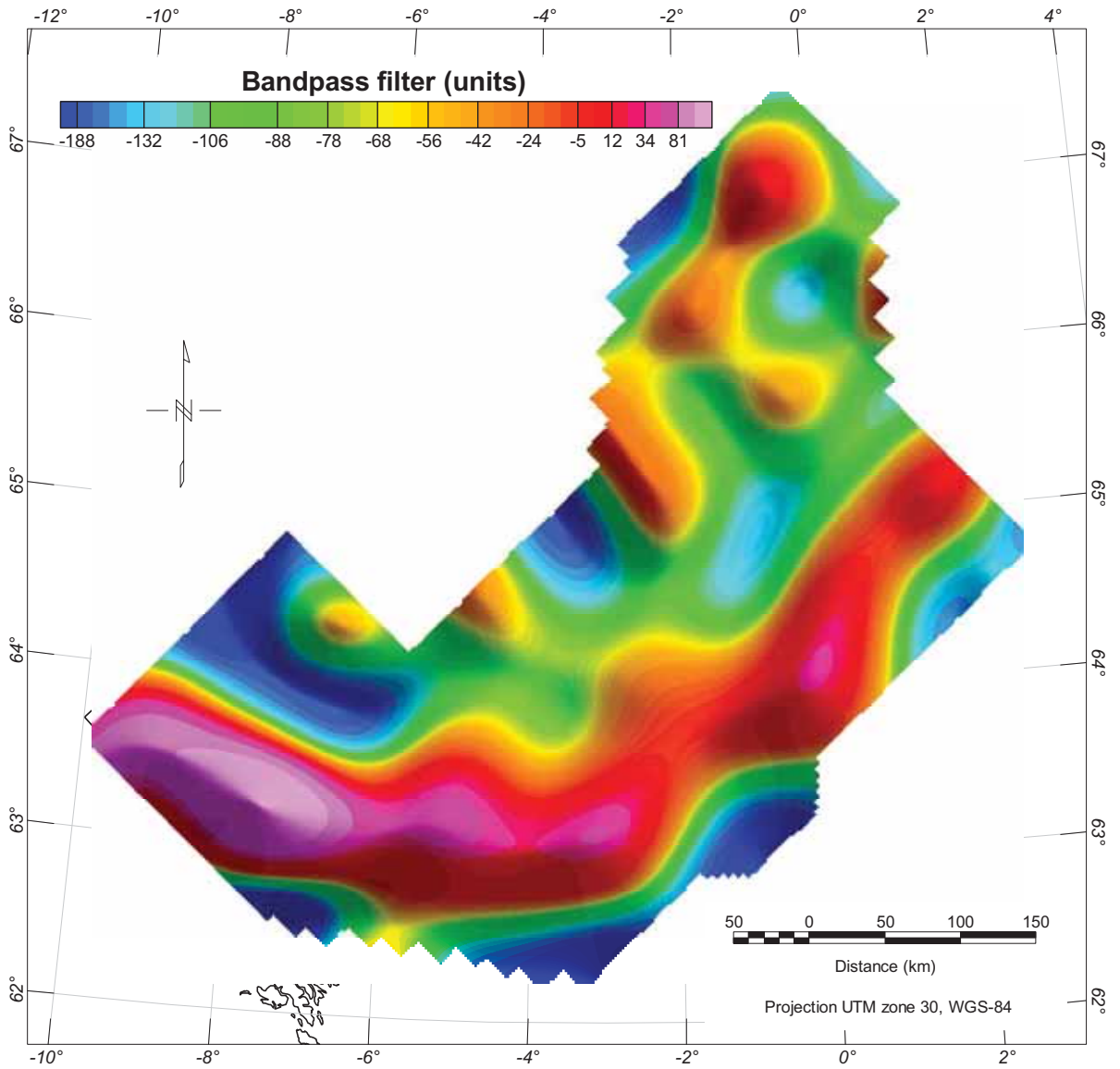


Figure 4.14 Band-pass filtering of the magnetic total field. This grid illustrates the anomalies sampled using a low wavenumber cutoff of 0 (in  $1/k_{unit}$ ) and a high wavenumber cut-off of 0.1 (in  $1/k_{unit}$ ). According to the spectrum analysis, these anomalies should highlight magnetic sources located at more than 15 km depth if we consider that all the long wavelengths are the results of deep sources.

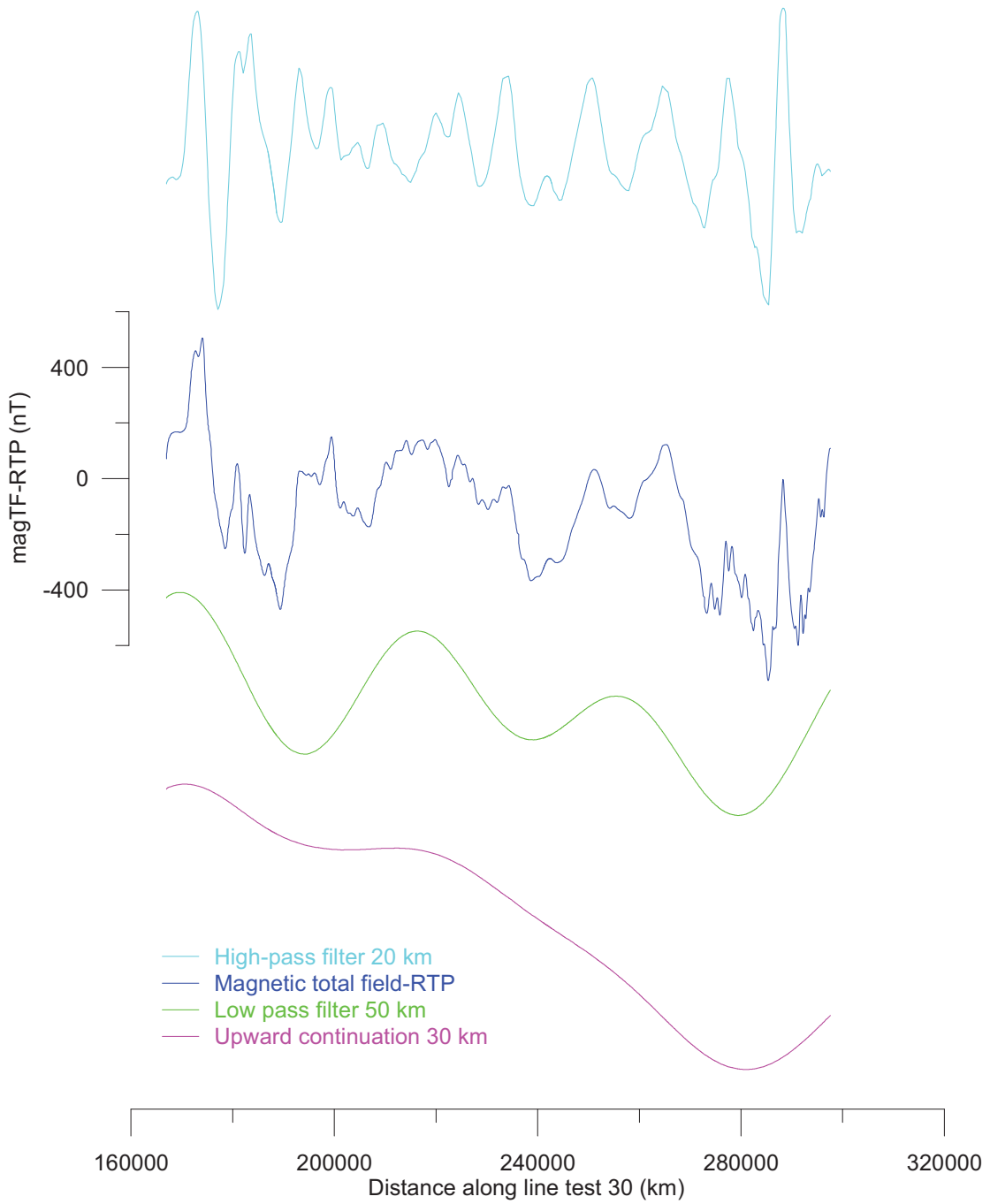


Figure 4.15 Example and comparison between high-pass, low-pass and upward continuation filters of the magnetic total field.



## 5 ENHANCEMENT OF TREND USING STRUCTURAL FILTERS

Laurent Gernigon

The purposes of this chapter are 1) to show the applicability of derivative and normalised filters in investigation of the structural setting along the Norway Basin and surrounding margins; 2) to evaluate the images produced by several enhancement techniques for lineaments mapping; 3) to prepare structural and depth to magnetic basement estimation maps (lineament) based on magnetic and gravity data interpretation. Some newly discovered lineaments and features might be subsequently used as a reference for future geological mapping, interpretation or re-interpretation.

### 5.1 Automatic gain control (AGC)

The automatic gain control filtering (AGC) was used to convert waveforms of variable amplitude to a grid that gives an equal emphasis to signals with both low and high amplitudes (Mudge 1991).

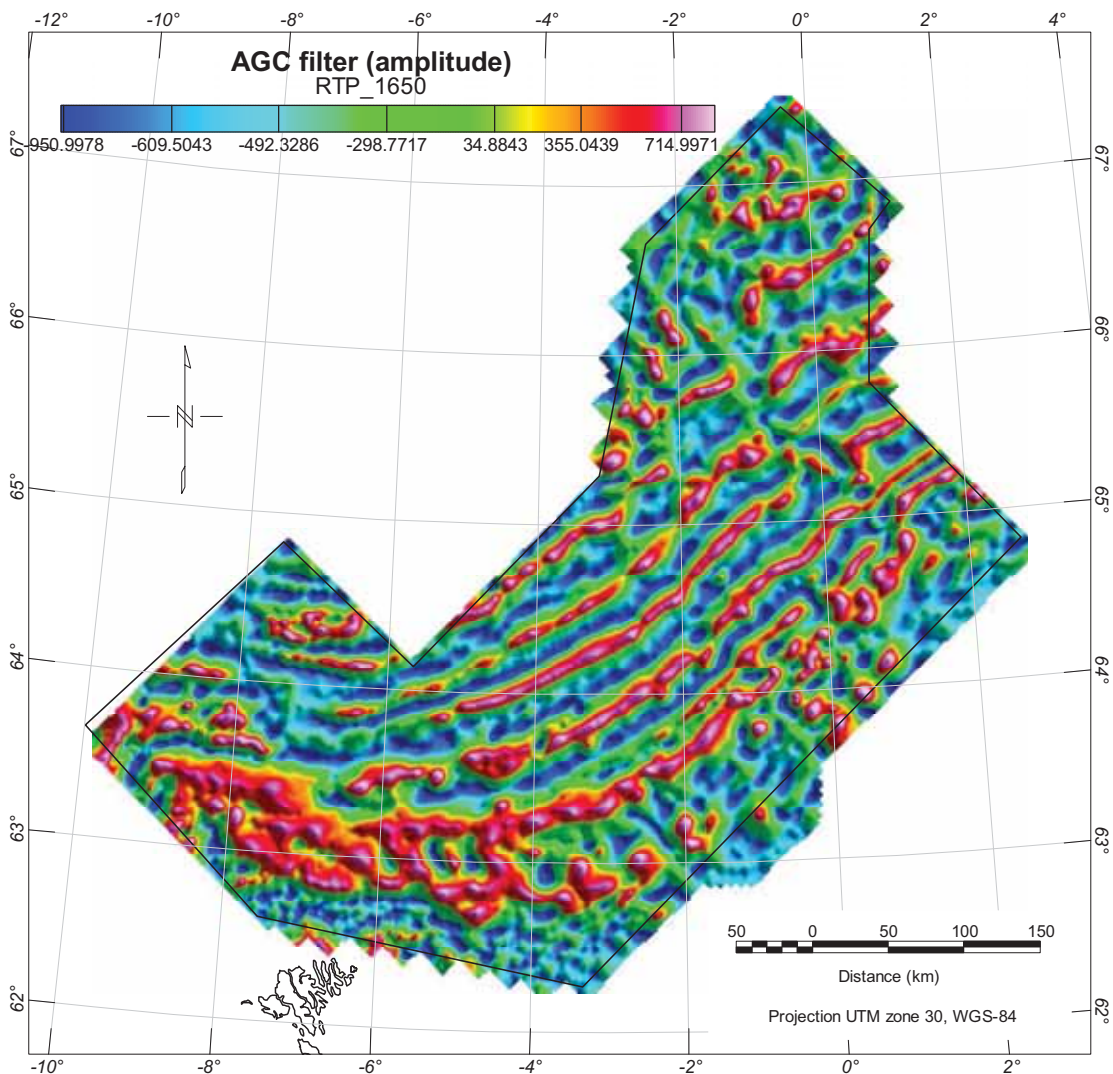


Figure 5.1 Automatic gain control filtering (AGC) of the NB-07 survey. To highlight the local anomaly details, automatic gain control (AGC) boosts amplitudes in areas with smooth anomalies, without sacrificing

**the long-wavelength information. Gain is estimated with a sliding square filter window, centred on each grid node.**

Like derivatives filters, the AGC filter is useful to underline structural features because it highlights trends with coherent alignments not always apparent in true amplitude data (Fig. 5.1).

## **5.2 Derivative filters**

Derivatives of the magnetic total field and its analytic signal have been computed within this study to enhance short wavelength features and main lineations. Computation of the three orthogonal derivatives, (x, y, z) within potential field modelling is considered as a universally applicable and basic processing step (Thurston and Brown 1994; Nabighian et al. 2005).

### 5.2.1 Vertical derivatives

Vertical derivatives (VDR) were used to enhance localised near-surface sources and trends, and to improve source resolution, assuming high-quality data (Fig. 5.2).

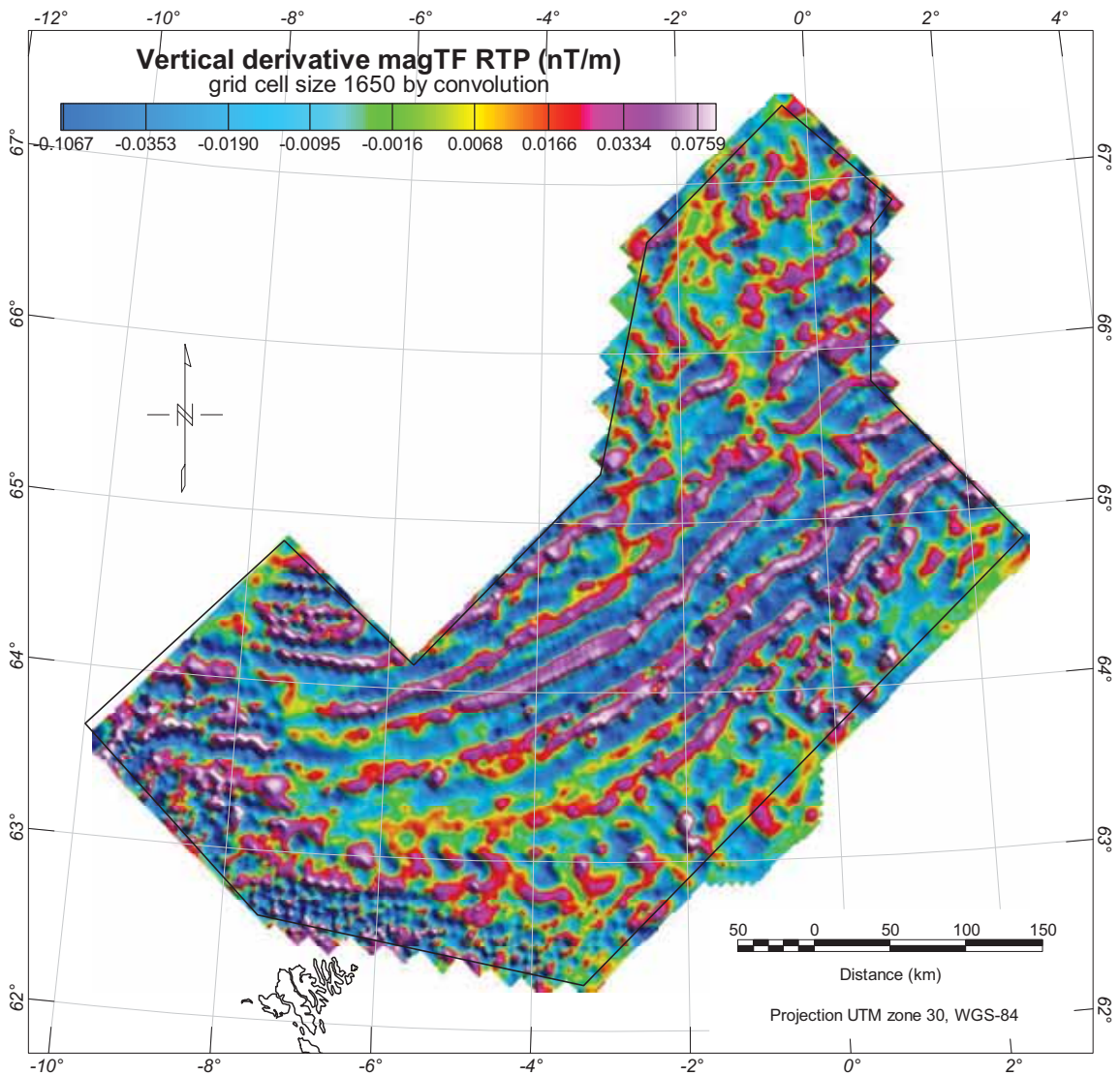


Figure 5.2 Vertical derivative obtained by convolution along the magnetic total field reduced to the pole and gridded with a cell size of 1650m using minimum curvature. The vertical derivative of an anomaly is related to the depth and geometry of the causative body. The gradient operator attenuates broad, more regional anomalies and enhances local, more subtle magnetic responses and as such is sensitive to shallow magnetic source bodies and contacts.

Transformation of potential field data into a derivative map enhances edges or contacts by placing anomaly maxima at the point of the maximum horizontal gradient identified within the x- and y-orientation of the grid. However, the key assumptions made when transforming gravity and magnetic field data into the three orthogonal derivatives are: (1) the potential field measured at the surface is the vertical component of the field; (2) that the lithological contacts giving rise to the anomalies are abrupt, near-vertical, and isolated from other sources. The first assumption is essentially true for gravity and for magnetic data reduced to the pole (Blakely 1995). In reality however, geological contacts are rarely vertical and density and magnetization can vary in all directions in a geological unit. Computation of the first vertical derivative has been referred to as a data pre-processing step, particularly before the interpretation of Euler and analytic signal (see Chapter 8).

Computation of the second vertical derivative as described by Blakely (1995) can be unstable (Fig. 5.3). The second vertical derivative, or rate of change of the fall-off rate of an anomaly, may be considered equivalent to a residualization of the data and is frequently used as an aid to delineating source bodies. However, because it is a derivative of a derivative (we remind you that the magnetic field is not an harmonic function), this filter emphasizes shallower sources and is also strongly affected by noise. Therefore, it must be used with some caution in interpreting basement structure.

### 5.2.2 The horizontal derivatives

The horizontal derivatives (HDR) can be used to predict the locations of major basement or sedimentary structures, igneous bodies and changes in basement grain (Grauch and Cordell 1987; Gunn 1997). Indirectly N-S and E-W directional filters have been found useful to locate suspicious N-W and E-W trending linear anomalies due to remaining levelling errors along the lines and tie-lines of the NB-07 survey (Figs: 5.4, 5.5, 5.6).

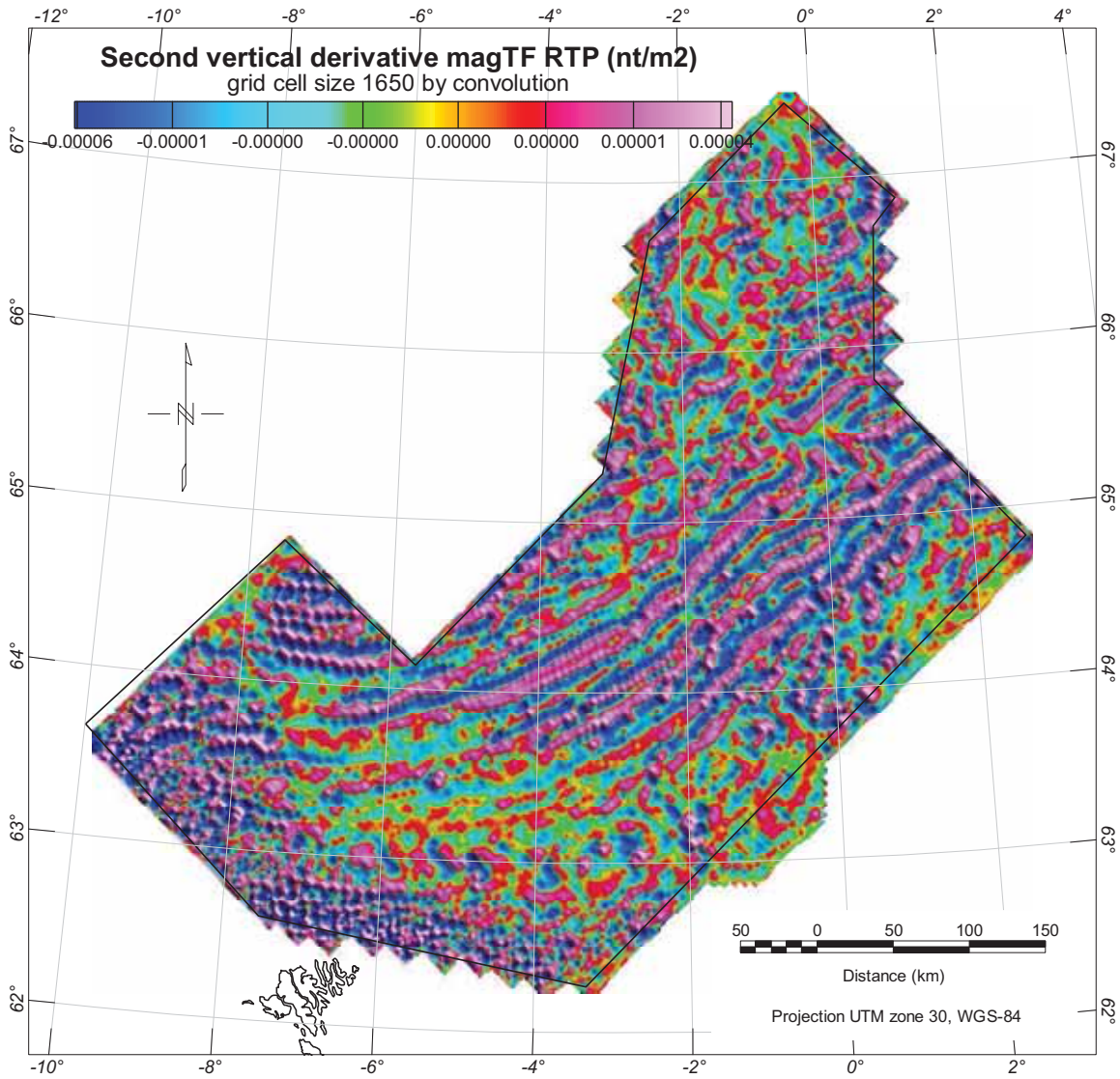


Figure 5.3 Second vertical derivative obtained by convolution along the magnetic total field reduced to the pole. The second vertical derivative can be seen as a regional-residual separation technique because it suppresses long wavelength anomalies related to regional influences. Due to filtering instability, this filter must be used with some caution in interpreting basement structure.

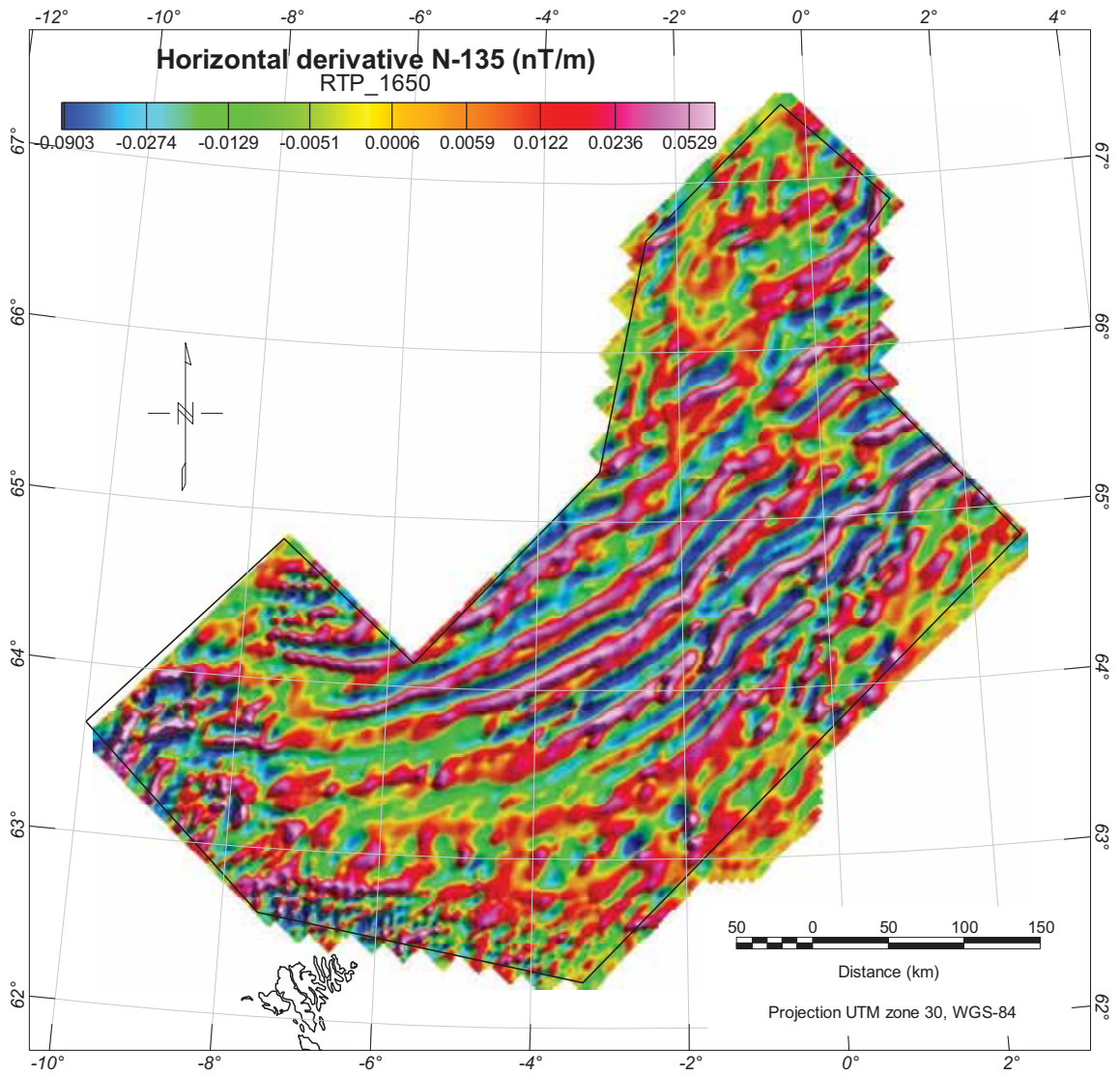


Figure 5.4 Directional horizontal derivatives in the NB-07 area. The filter enhances the high frequencies along the NW-SE trend.

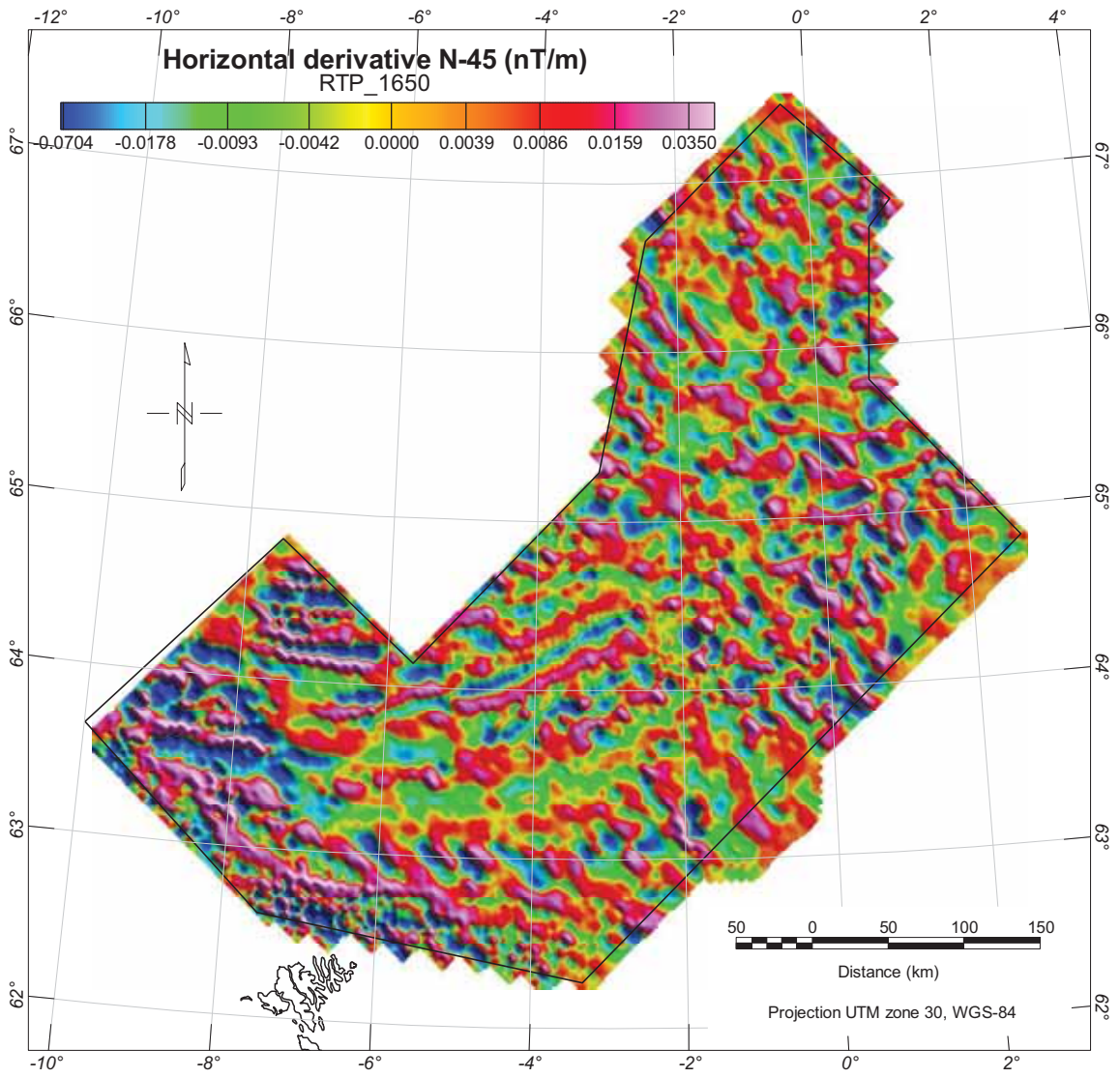


Figure 5.5 Directional horizontal derivatives in the NB-07 area. The filters enhance the high frequencies along the NE-SW trend.

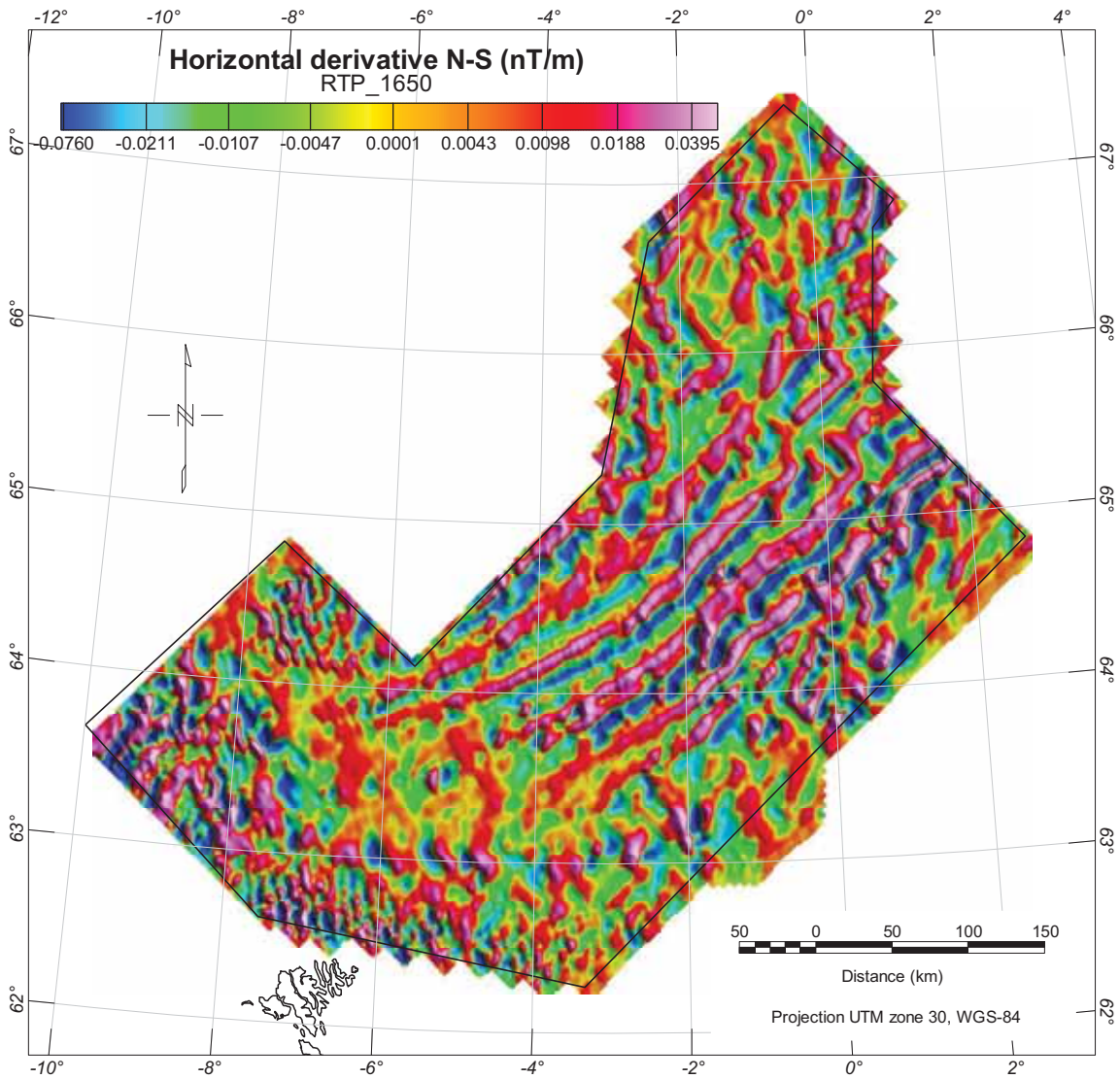


Figure 5.6 Directional horizontal derivatives in the NB-07 area. The filters enhance the high frequencies along the N-S trend.

### 5.2.3 The terrain slope filter or maximum horizontal derivative filter

Quite similar to the way the first directional derivative defines the slope at any point on the surface, the terrain slope filter has been applied to calculate the slope at any grid node of the NB-07 (Fig 5.7). Grid files of the terrain slope can produce contour maps that show isolines of constant steepest magnetic slope. The terrain slope filter or total horizontal derivative filter, calculates the slope at any grid node on the surface. For a particular point on the surface, it is based on the direction of steepest descent or ascent of the magnetic field at that point. This means that across the surface, the gradient direction can change. This operation is similar to the way the first directional derivative filter defines the slope at any point on the surface but is more powerful in that it automatically defines the gradient direction at each point on the map.



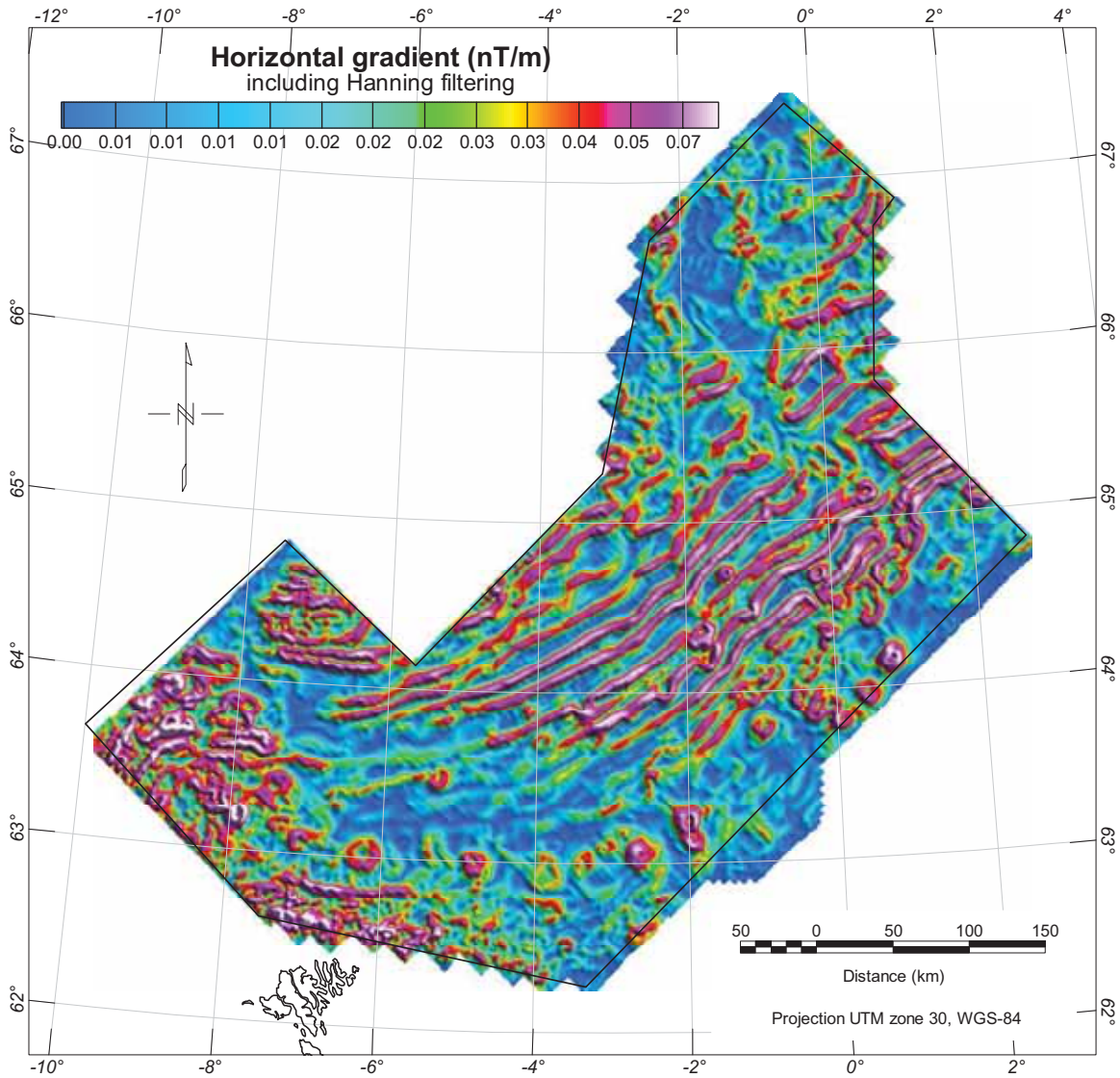


Figure 5.7 Maximum horizontal gradient of the NB-07 dataset, reduced to the pole. After the reduction-to-pole correction, a magnetic body is spatially more directly associated with the related magnetic response. The maximum horizontal gradient (more properly the maxima of the total horizontal gradient) of the anomaly slope is then located near or over the body edge. That is, the horizontal gradient operator in map form produces maximum ridges over edges of magnetic basement blocks and faults or other magnetic bodies. In addition, the horizontal gradient highlights linear and round-shaped features, related to magnetic contacts, in the data set.

### 5.3 Analytic signal - 3D total gradient

The concept of analytic signal applied to magnetic anomalies was developed in two dimensions by Nabighian (1972) based on a concept initially proposed by the French Ville in 1948. In two dimensions, the complex analytic signal of the magnetic signal  $M(x, y, z)$  can be expressed as (Thurston and Smith 1997):

$$A(x, y) = |A(x, y)| \cdot \exp(j\varphi)$$

with

$$|A(x, y)| = \sqrt{\left(\frac{\partial M}{\partial x}\right)^2 + \left(\frac{\partial M}{\partial y}\right)^2}$$

and

$$\varphi = \tan^{-1}\left(\frac{\partial M}{\partial z} \middle| \frac{\partial M}{\partial x}\right)$$

$|A|$  is the 2D analytic signal amplitude,  $\varphi$  the local phase. A common theme of the normalized derivatives is the concept of mapping angles (or functions of angles) derived from the gradients of the magnetic intensity.

Using 3D dimensional grid, the amplitude of the analytic signal  $A$  of  $M(x, y, z)$  is calculated by taking the square root of the sum of the squares of each of the directional first derivatives of the magnetic field.

$$|A(x, y)| = \sqrt{\left(\frac{\partial M}{\partial x}\right)^2 + \left(\frac{\partial M}{\partial y}\right)^2 + \left(\frac{\partial M}{\partial z}\right)^2}$$

The resulting shape of the analytic signal is expected to be centered above the magnetic body (Figs. 5.8, 5.9). This has the effect of transforming the shape of the magnetic anomaly from any magnetic inclination to one positive body-centered anomaly at least in 2D (Nabighian 1972). Analytic signal has been utilized widely for mapping of structures and for determining the depth of sources (Roest et al. 1992; Florio et al. 2006; Pilkington et al. 2000).

The main advantage of the total gradient over the maximum horizontal gradient is its lack of dependence on dip and magnetization direction, at least in 2D. When interpreting the analytic signal it is assumed that the causative sources are simple near-vertical or step-like geological structures (Roest et al. 1992; Roest and Pilkington 1993). Therefore, the 2D analytic signal has significant advantages over the simple derivatives and this application was utilized to map changes in basement structure, fabric and trends. Synthetic modelling has proved that the maxima of the analytic signal

are located over the edge of anomalous sources (Nabighian 1974, 1984, Roest et al. 1992). This simplification of the potential field, however, results in the compromise whereby during computation the sign of the original gravity and magnetic field is lost. Therefore, it cannot be determined whether the analytic signal anomaly represent positive or negative density or magnetic susceptibility contrast compared to its surroundings.

However, it should be reminded that the total gradient expressed in 3D is not so independent of the direction of magnetization (Xiong 2006), nor does it represent the envelope of both the vertical and horizontal derivatives over all possible directions of the Earth's field and source magnetization. Thus, despite its popularity, the 3D total gradient is not the correct amplitude of the real analytic signal in 3D. In a recent review, it appears that what is commonly called the analytic signal should be rather called "total gradient" in 3D (Nabighian et al. 2005).

In the 3D case, some factors produce offsets that are more difficult to predict than in the 2D case. Such factors primarily include the interference from neighbouring magnetic bodies, or from varying magnetization directions, terrain effects, 3D corners on body edges, or irregular boundary. Roest et al. (1992) have demonstrated that this is true for any 2D anomaly and suggested their generalization to 3D. However, the data should be interpreted with care in the 3D case. The properties of the analytic signal are strictly valid for isolated 2D bodies and one should use caution in extrapolating the conclusion of the 2D case to the 3D case. For 3D case, the shape and the absolute value of the analytic signal are also dependent of the directions of magnetization and of the Earth's field. The amount of offset is primarily determined by the depth to the top edge of the boundary below the observation level and by the dip of the boundary and by the directions of magnetization and of the Earth's field. In the most common 3D cases, the locations of the total gradient are always offset from edges of the causative bodies. The best results are obtained for vertical and relatively shallow thick dikes (Xiong 2006). For the 2D finite dipping step model, the locations of the maximas vary with both burial depth and dipping angle. All these factors become important as the size of study area becomes smaller because the small amounts of offset they cause become more significant. For local scale magnetic surveys, mutual interference from different bodies is the greatest limiting factor of the analytic signal method and this can render the method virtually useless. For large-scale magnetic surveys like the NB-07 or for shallower depths of causative bodies, the analytic signal method remains nevertheless a useful and fast way of delineating magnetic boundaries in the subsurface (Fig. 5.8).

The technique therefore requires interpretation in conjunction with other geophysical and geological information to maximize its potential. After calibration with known structures or other derived potential field products the analytic signal can be interpreted geologically with better confidence.

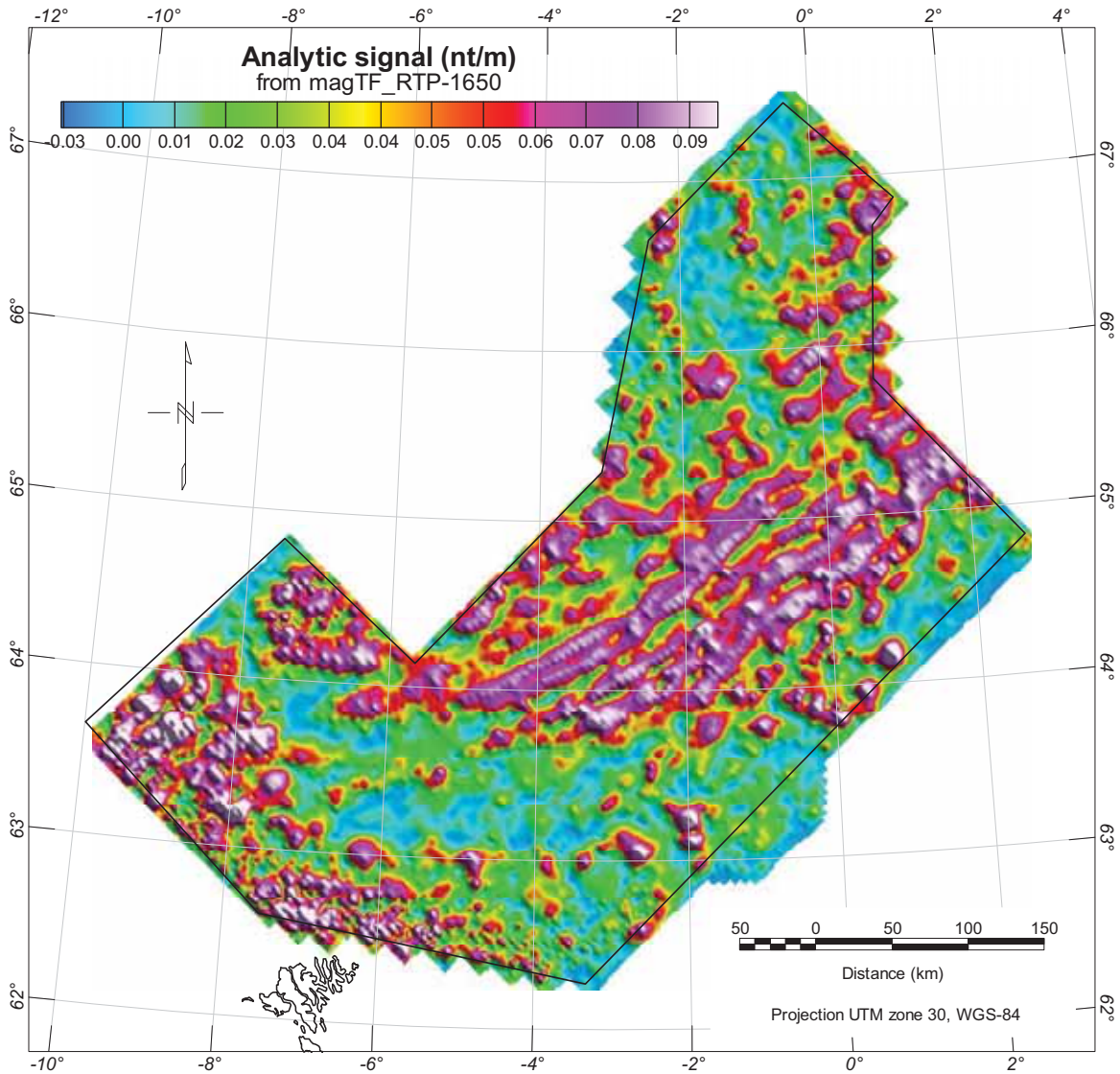


Figure 5.8 Analytic signal of the magnetic total field grid, reduced to the pole (1650x1650m cell size). The 3D analytic signal (“3D-Total gradient”) is the root-sum square of the vertical and horizontal gradients. Like the horizontal gradient, it is used to delineate the edges of bodies or contacts. It has the advantage over the horizontal gradient that it is independent of the dip of the contact, but the disadvantage that it is somewhat less continuous. It is therefore sometimes advantageous to use the two in parallel.

#### 5.4 Tilt derivative (TDR)

The tilt derivative filter (TDR) appears to be another powerful and normalised derivatives tool for shape and edge detection (Figs. 5.9, 5.10). It works notably pretty well to identify the magnetic chrons in the Norway Basin. The problems to be overcome in data enhancement using the TDR was to identify and map subtle anomalies attenuated in the dynamic range due to the presence of high amplitude magnetic anomalies, the continuity of individual bodies and the edges of structures.

The TDR is defined in terms of the ratio between the first vertical derivative of the potential field and his total horizontal gradient of the field (Miller and Singh 1994; Verduzco et al. 2004; Cooper and Cowan 2006).

$$TDR = \tan^{-1}(VDR|THDR)$$

where VDR and THDR are the first vertical and total horizontal derivatives of the magnetic total field  $M(x,y)$ , respectively

$$THDR = \sqrt{\left(\frac{\partial M}{\partial x}\right)^2 + \left(\frac{\partial M}{\partial y}\right)^2}$$

and

$$VDR = \frac{\partial M}{\partial z}$$

Its horizontal derivative is also defined by:

$$THDR = \sqrt{\left(\frac{\partial TDR}{\partial x}\right)^2 + \left(\frac{\partial TDR}{\partial y}\right)^2}$$

The TDR is restricted to values in the range  $+\pi/2 > \text{Tilt} > -\pi/2$ , and can be considered as an expression of the vertical derivative normalized by the total horizontal derivative. This measure has the property of being positive over a source and negative elsewhere (Fig. 5.9). The tilt filter technique tends to enhance mapping of the subtle magnetic anomalies and maximizes the geometrical contrast of the internal basin structure (partly constrained by seismics). The tilt angle was compared with other edge detection measures such as the horizontal gradient, the second vertical derivative and the analytic signal and found to have added some advantage of responding well to both shallow and deep sources along the NB-07 area (see later). Using synthetic models, Verduzco et al. (2004) showed that the TDR has its zero values close to the edges of the body for RTP fields. The enhanced amplitudes of the tilt derivative can be carried through to its total horizontal derivative (or local wavenumber) in which the edge anomalies are prominent and invariant to geomagnetic inclination, thus making this derivative effective for mapping geologic edges.

Combined with its total horizontal derivative, results were particularly useful for the structural interpretation along the NB-07. The tilt angle results were combined and systematically compared with other filtered datasets (using transparency in Oasis Montaj) to provide a set of interpretative maps presented and discussed later.

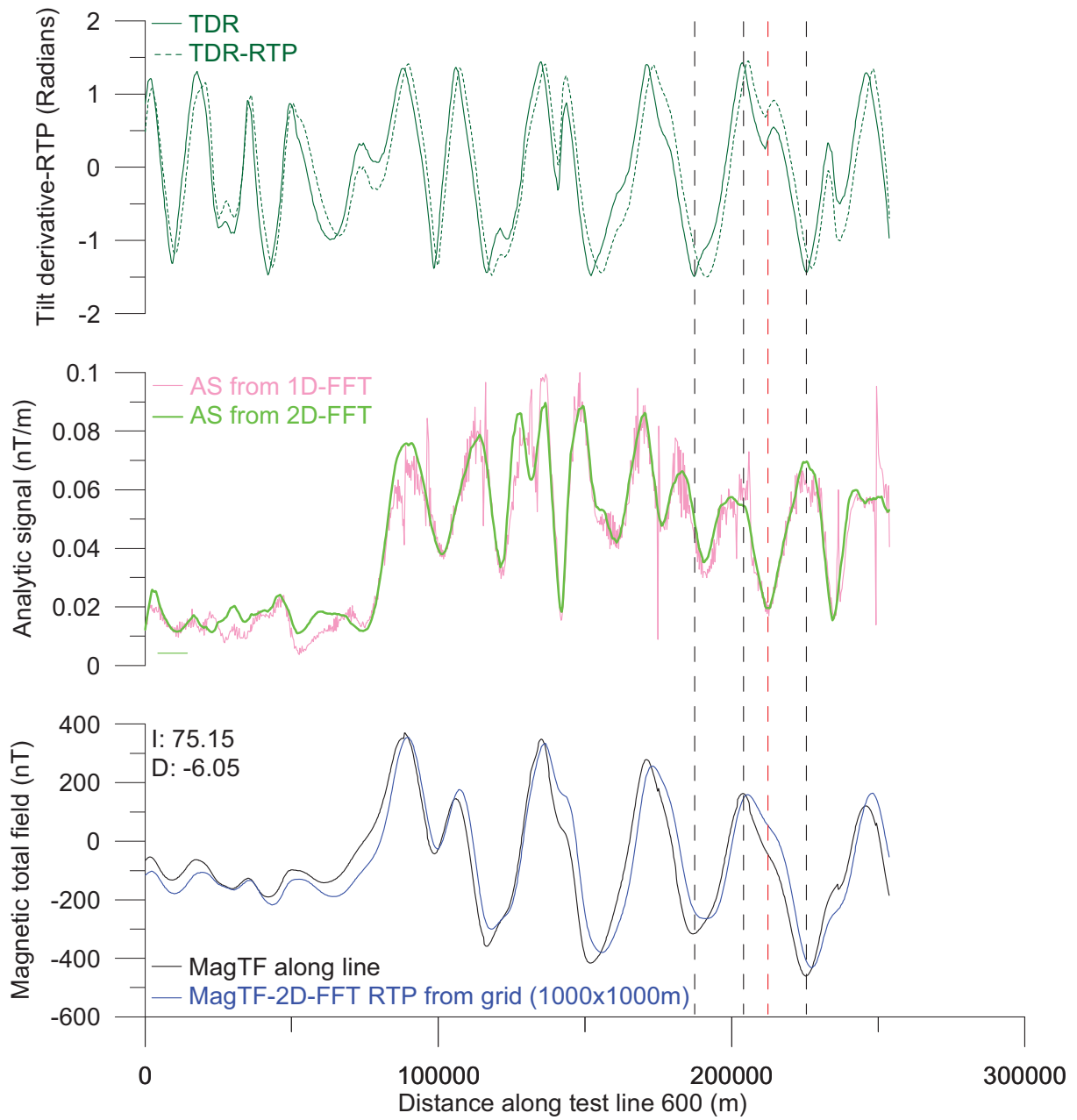


Figure 5.9 TDR and analytical signal filtering along line 600. The TDR filter is particularly effective in identifying subtle anomalies and their edges.

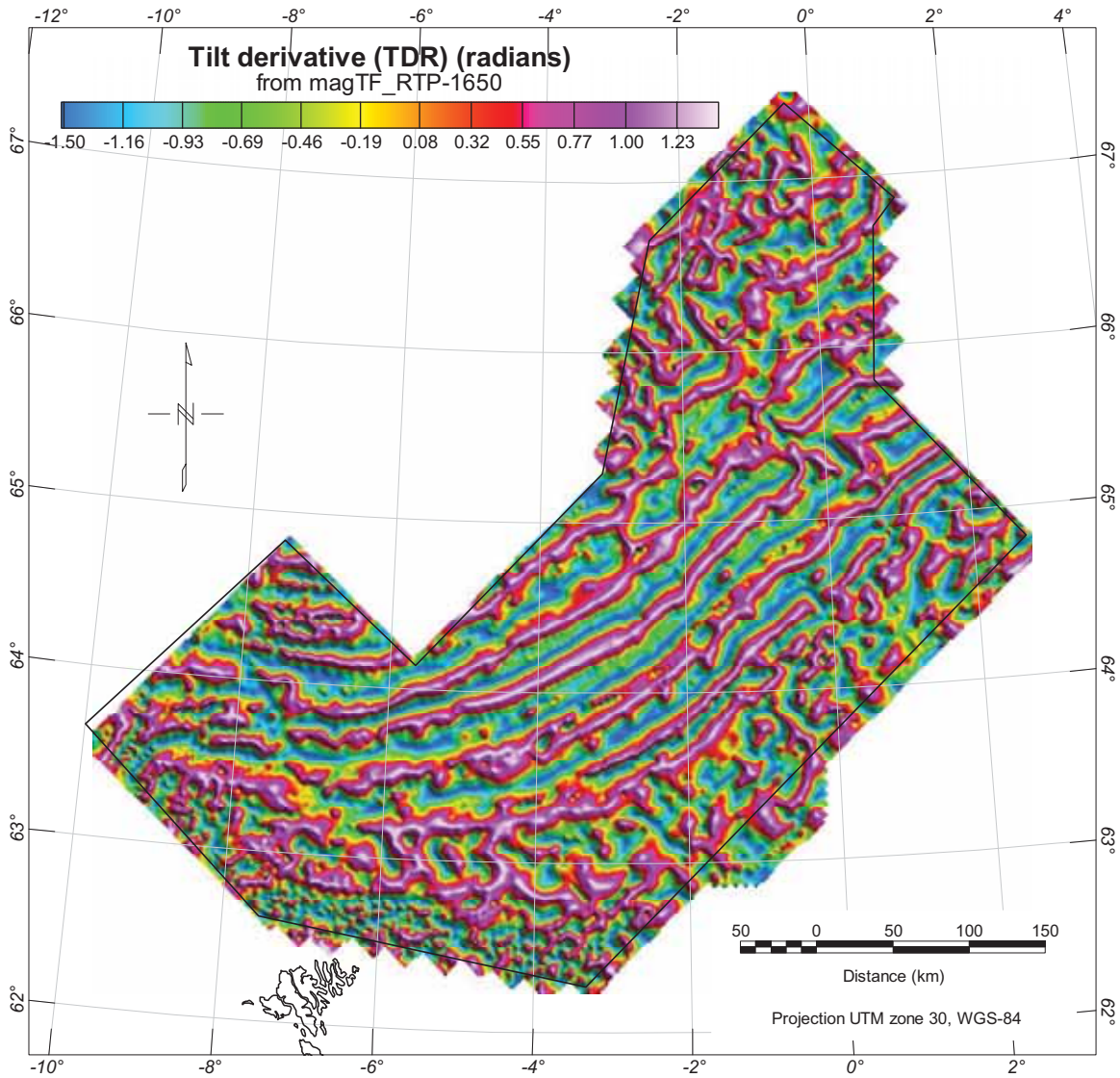


Figure 5.10 Tilt derivative of the magnetic total field RTP. The tilt derivative (TDR) is an alternative method to derive the maximum gradient anomalies associated with magnetic contacts. The result is strongly peaked along the maxima of the horizontal gradient. This display gives a much sharper definition of the magnetic contacts than the horizontal gradient map. For the NB-07 interpretation, this filter proves to be interesting to map and identify the magnetic chrons.

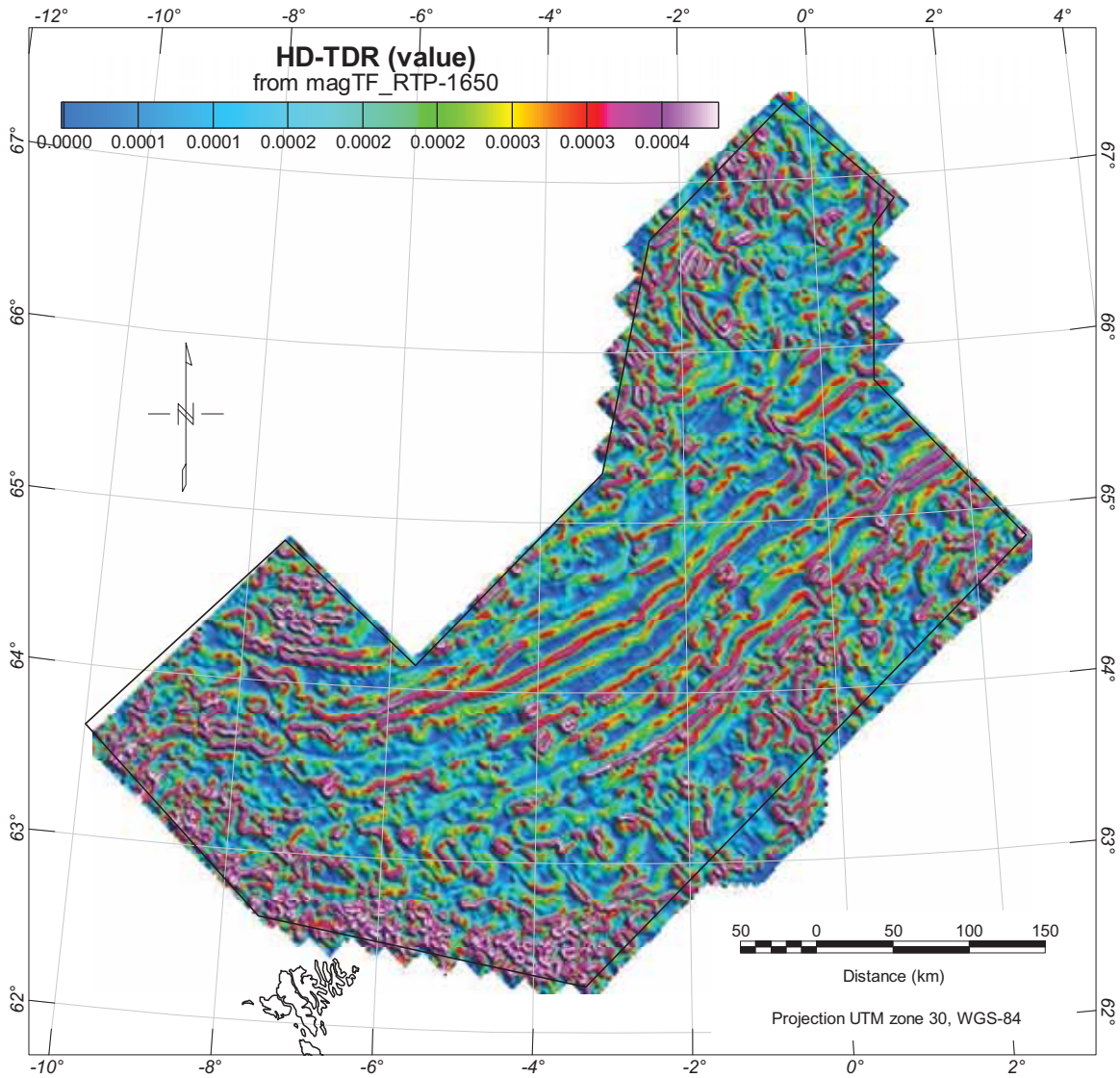


Figure 5.11 Horizontal derivative of the tilt derivative (HD-TDR) of the magnetic total field grid (1650x1650), reduced to the pole. The different patterns underline major magnetic units and major lineaments.

### 5.5 TDX filtering

Cooper and Cowan (2006) and Fairhead and Williams (2006) have modified the tilt derivative so that the total horizontal derivative is now normalized by the vertical derivative (Fig. 5.12). They named it TDX but neither of their papers mentions the origin of the name TDX. Note that the two definitions of TDX are slightly different in the two papers. Fairhead and Williams (2006) use the first vertical derivative in the denominator, whereas Cooper and Cowan (2006) use its absolute value:



$$TDX = \tan^{-1} \left[ \frac{THDR}{VDR} \right]$$

where VDR and THDR are the first vertical and total horizontal derivatives, respectively

$$THDR = \sqrt{\left(\frac{\partial M}{\partial x}\right)^2 + \left(\frac{\partial M}{\partial y}\right)^2}$$

$$VDR = \frac{\partial T}{\partial z}$$

The angle defined by the TDX expression is effectively  $\text{sign}(\text{Tilt}) \times (\pi/2 - |\text{Tilt}|)$ , and like the Tilt is also constrained between  $+\pi/2 > \text{TDX} > -\pi/2$ , but has a much sharper gradient over the contact (Cooper and Cowan 2006; Fairhead and Williams 2006).

We also propose a nice combination of the TDX with a Laplacian filter [0,-1,0,-1,4,-1,0,-1,0] applied to the original TDX grid: It can be used to better highlight the inflection points on both edges of the anomalies (Figs. 5.13, 5.14). This filter was used to delineate properly the magnetic chrons in the Norway Basin.

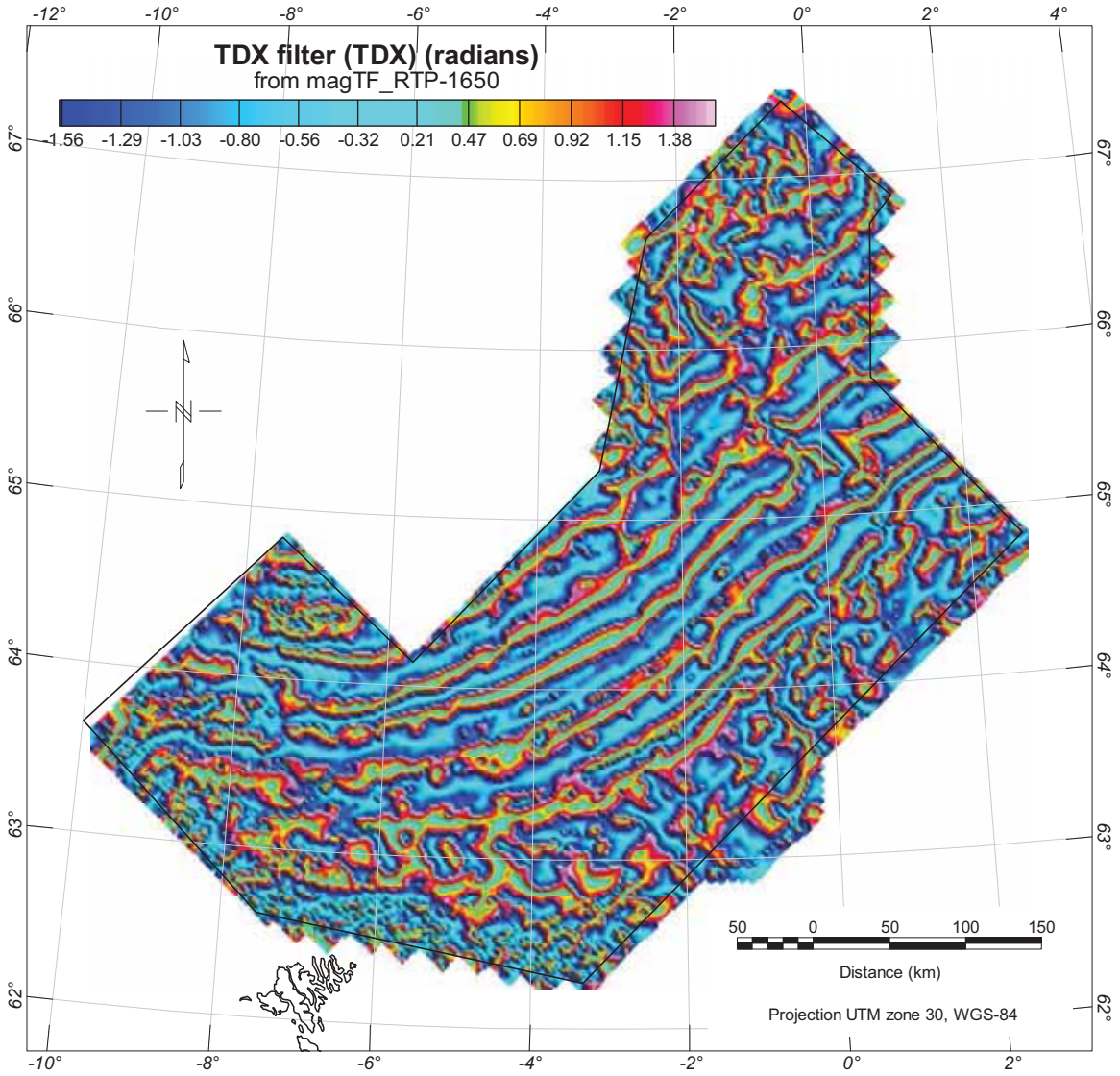


Figure 5.12 TDX filter of the magnetic total field grid (1650x1650m) reduced to the pole. The different TDX patterns underline major magnetic units and major lineaments.

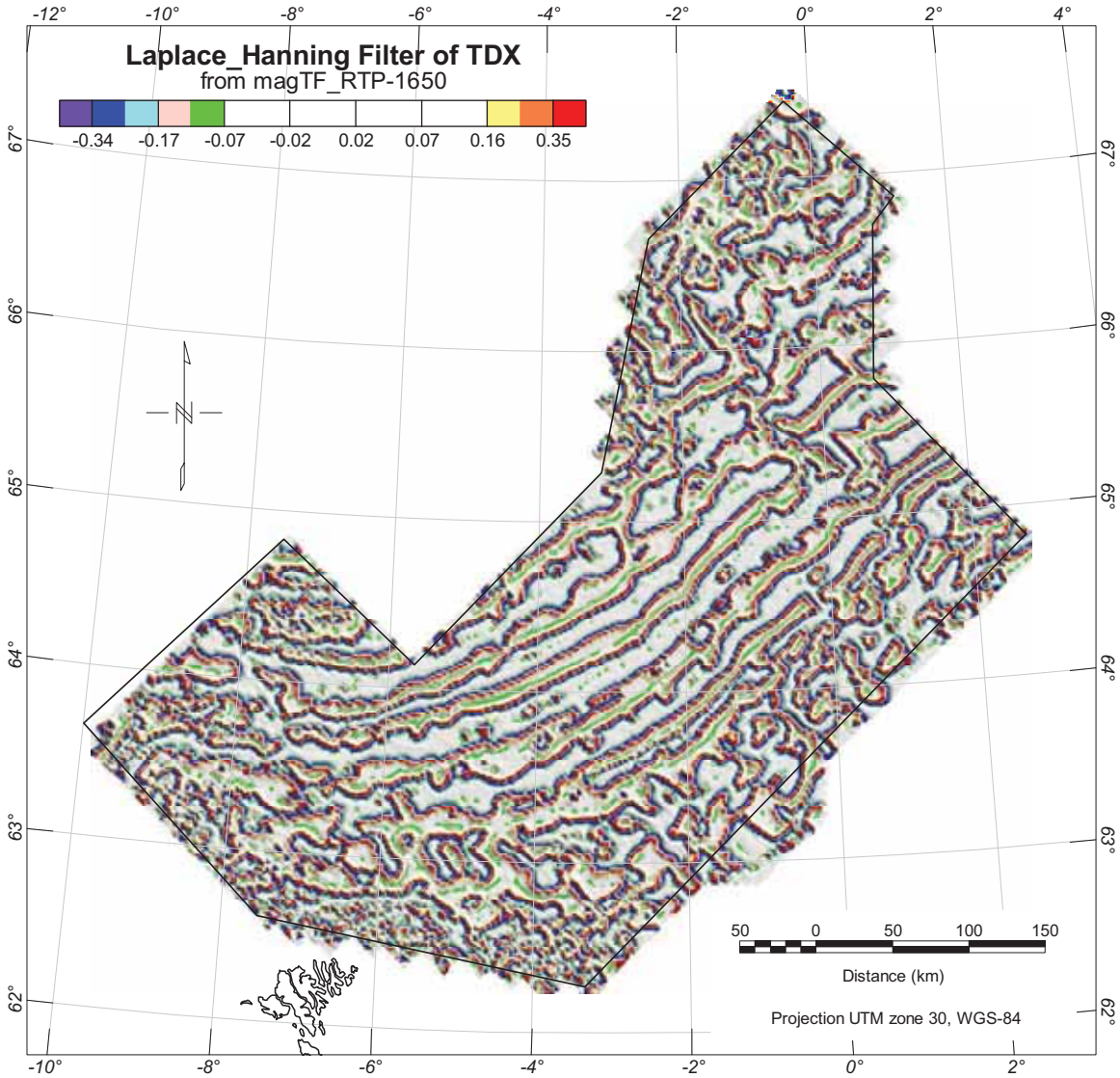


Figure 5.13 2D Laplacian filter  $[0,-1,0,-1,4,-1,0,-1,0]$  applied to the TDX of the magnetic total field grid (1650x1650m) reduced to the pole. A Hanning filter  $[0.06, 0.1, 0.06, 0.1, 0.36, 0.1, 0.06, 0.1, 0.06]$  has subsequently been applied to smooth the edges. This filtering highlights the main inflection points of the TDX grid.

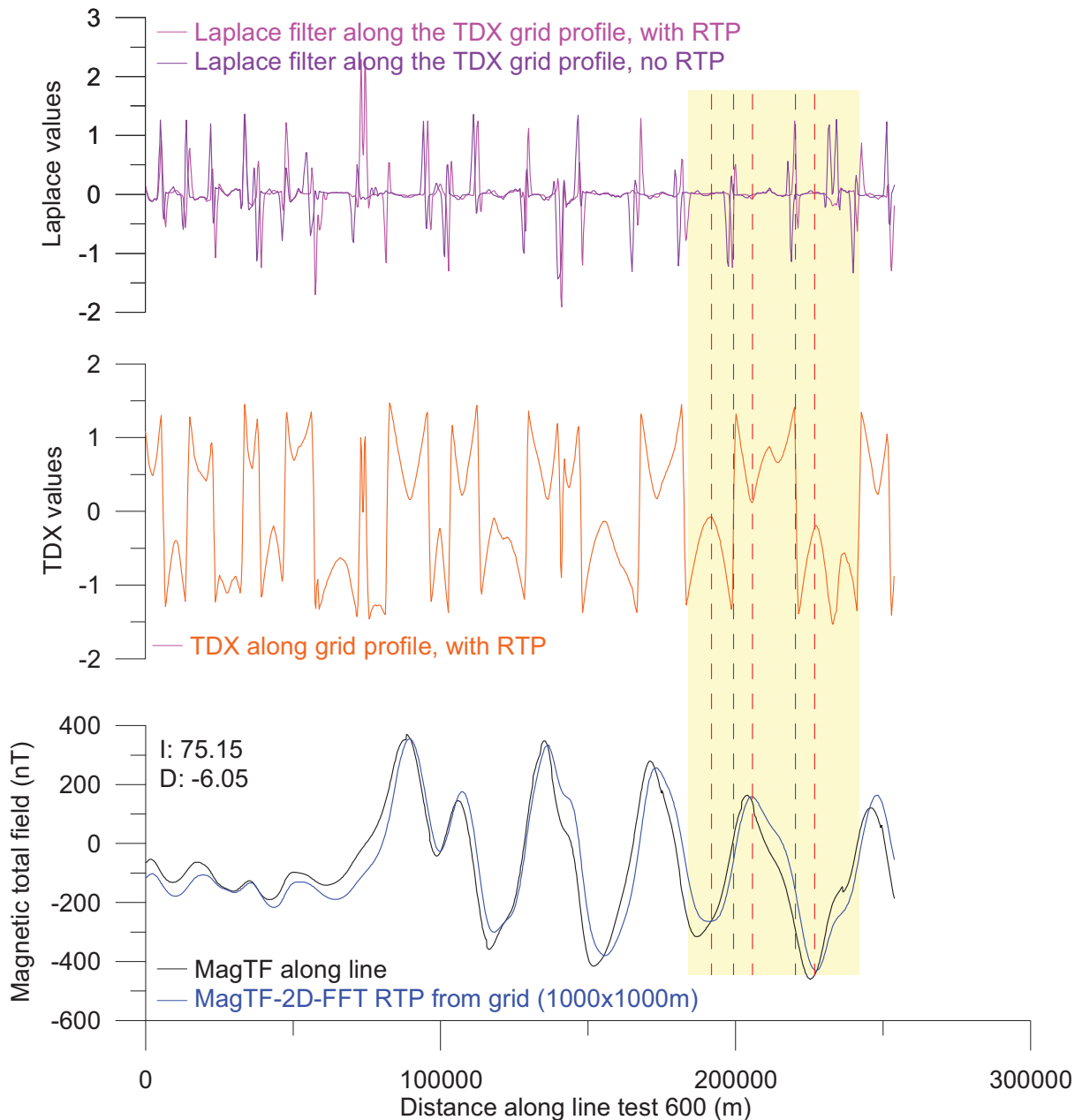


Figure 5.14 Example of different edge detection filters applied to line 600. The TDX filtering highlights the main inflection points of the TDX grid including maximum and minimum for each anomaly. A 3x3 Laplace filter applied to a TDX grid is mostly useful to underline the points of tangency.

## 5.6 Pseudogravity

Pseudogravity is the gravity anomaly that would be observed if density contrasts were proportional to magnetization contrasts (Baranov 1957). It is calculated from magnetic observations and is used to compare gravity and magnetic observations to distinguish between the effects of different rock types. Aeromagnetic data are then transformed into pseudogravity data assuming Poisson's relation between gravity and the NB-07 magnetic total field (Fig. 5.15). Under the assumption that the

basement is magnetised uniformly by induction, the pseudogravity field can be attributed to the density (susceptibility) variations along the NB-07. Under ideal conditions, the pseudogravity field could provide an approximate representation of the basement domains when the sediments are nonmagnetic, whereas the original gravity field may also include variation of density within the sedimentary section and the crust. A pseudogravity transformation might be a useful strategy in interpreting magnetic anomalies because a comparison with real gravity data could help to build an interpretation of the shape and size of the sources. The Geosoft software was used for performing this transformation using Fourier convolution with a filter operator defined by:

$$G(\theta) = \frac{g \cdot \rho / J}{[\sin(Ia) + i \cos(I) \cdot \cos(D - \theta)]^2 \times r}$$

With

$\rho$ : density contrast in g/cm<sup>3</sup>

$g$ : gravitational constant=6.670E-8

$I$ : Geomagnetic inclination

$Ia$ : Inclination for amplitude correction. Default is 20°. If  $|Ia| < |I|$ ,  $|Ia|=|I|$

$D$ : Geomagnetic declination

$J$ : magnetization in Gauss

$\theta = \tan^{-1}(u/v)$  is the wavenumber direction

$r$  is the wavenumber in ground\_unit=2 $\pi$ k where k is cycles/ground\_units

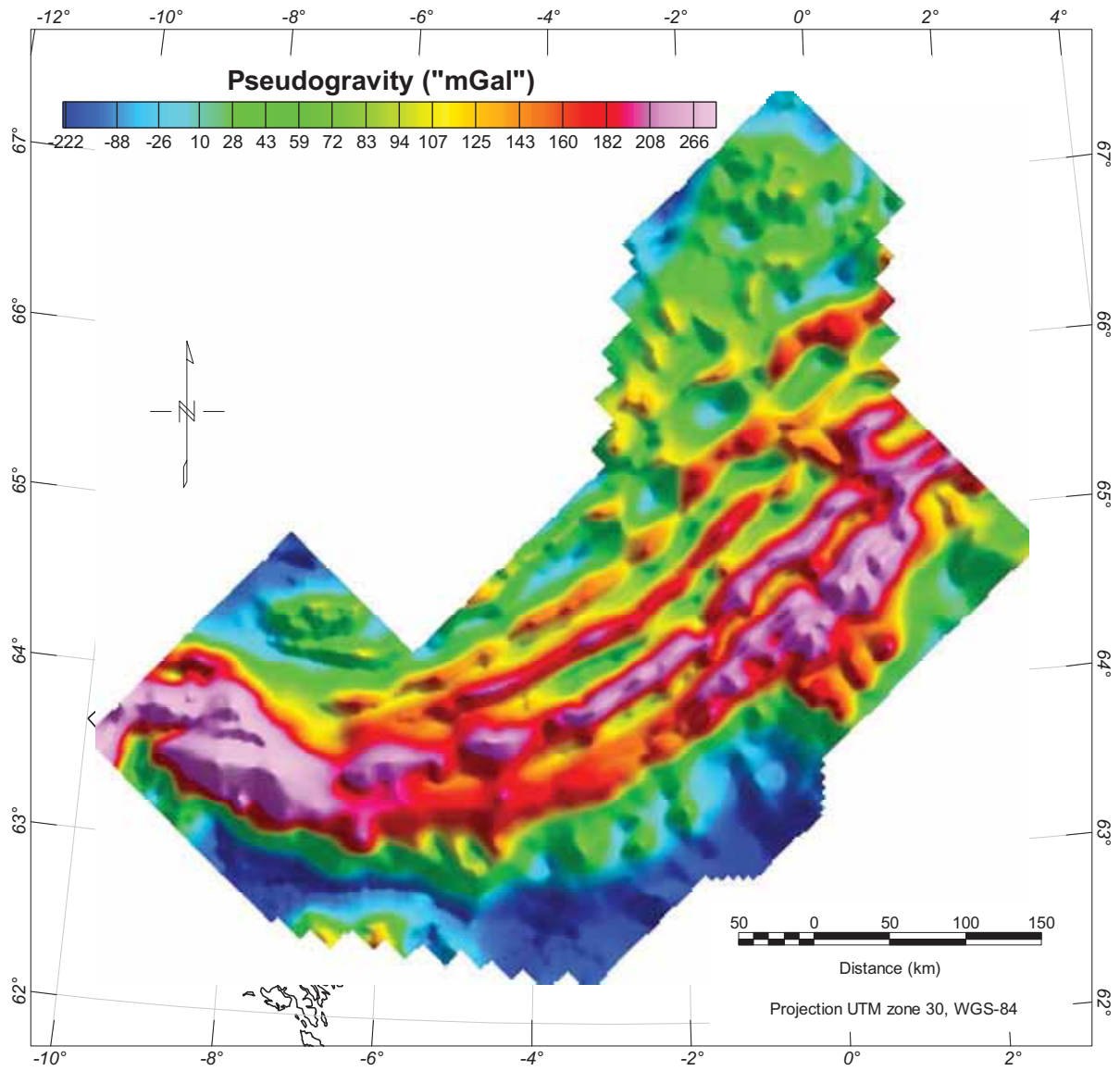


Figure 5.15 Pseudogravity of the NB-07 survey. The pseudogravity was computed using a density contrast of  $1.5 \text{ g.cm}^{-3}$  and a magnetization of  $3 \text{ A/m}$ . Inclination:  $75^\circ$  and declination:  $-6.5^\circ$ .

## 6 FINAL MERGE AND COMPARISON WITH PREVIOUS COMPILATION

Laurent Gernigon and Odleiv Olesen

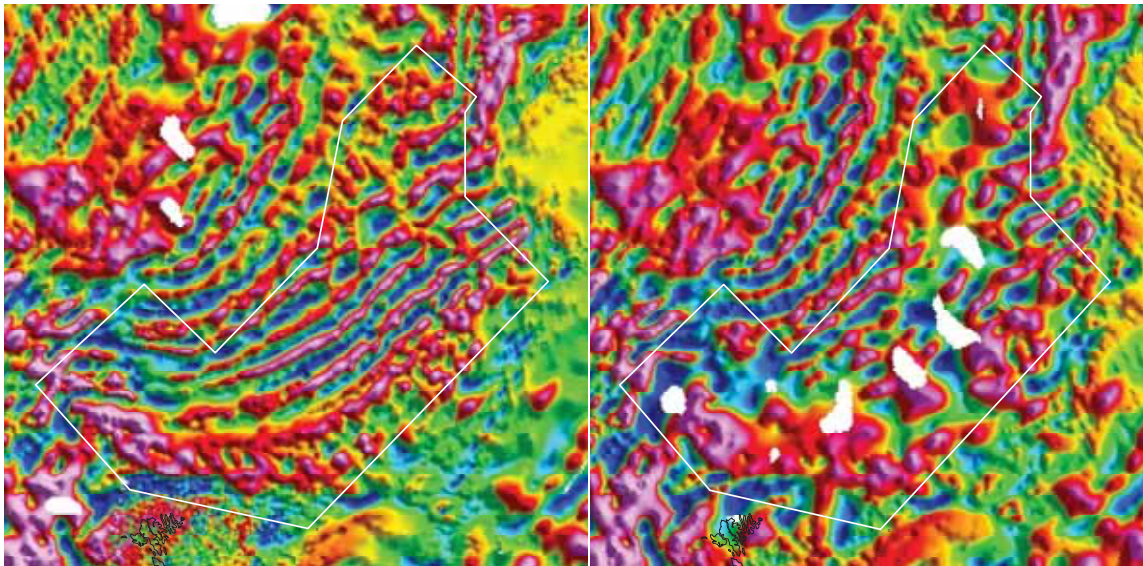
### 6.1 Merge of the NB-07 grid with the former regional grid

The NB-07 grid has been merged with the pre-existing NGU magnetic compilation of the Norwegian Greenland Sea (Olesen et al. 2006; Olesen et al. 2007). The Oasis montaj GridKnit module was used to merge the two geophysical grids with different cell size, projection or grid type (Geosoft 2005d). The blending method merged the grids via standard smoothing functions. Trend removal operations were performed with respect to the regional grid. The maximum trend order has been specified or adjusted automatically based on a fitting tolerance. However, this technique locally “forces” the magnetic trend envelope of the NB-07 to be adjusted with the surrounding dataset. Since the surrounding magnetic dataset are partly old (NGU-1971 survey), has low resolution and is less reliable the merge process could wrongly influence the initial quality of the NB-07. For local interpretation and modelling, we consequently recommend to use the original NB-07 grid. The final grid can only be provided to partners, which also purchased the regional NGU magnetic dataset.

### 6.2 Comparison with other compilations

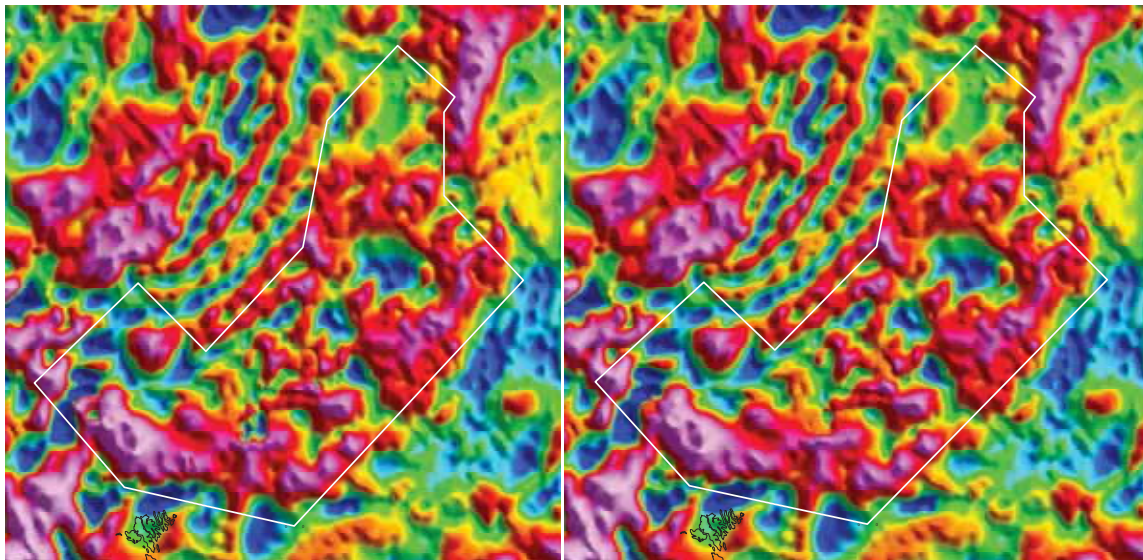
The Figure 6.1 illustrates the NB-07 results and the major differences from the previous public domain compilations. Figure 6.1b is the vintage compilation of Verhoef et al. (1997) and Figures 6.1c and 6.1d represent the recent release from the world magnetic anomaly map (Hemant et al. 2007; Maus et al. 2007). This compilation derived from release aeromagnetic surveys (Including previous NGU works) over land areas, research vessel magnetometer traverses at sea, and observations from earth-orbiting satellites (CHAMP), supplemented by anomaly values “artificially” derived from oceanic crustal ages. The anomaly field is shown at an altitude of 5 km above the WGS84 ellipsoid and gridded at 3 minutes of arc spacing (~5.5 km). The A version (Fig. 6.1c) differs in its handling of areas without near-surface data, which are filled with the 5 km downward-continued CHAMP magnetic model. In contrast, the B version (Fig. 6d) contains both model data derived from CHAMP, and marine data, with a priority given to the marine. Both versions, when upward-continued to satellite altitude, reproduce the magnetic anomaly field derived from the CHAMP satellite.

These models are particularly suited for inferring large-scale structure and composition of the lithosphere. However, a rapid comparison shows that the NB-07 survey provides, without surprise, a better resolution both for high and low frequency content (Fig. 6.1). Even anomalies with kilometric wavelengths disappear on the vintage compilation (Fig. 6.3, 6.4) the contrast is even more obvious if we compare transects extracted along the same profile (Fig. 6.3).



a) New compilation including the NB-07

b) Old compilation (Verhoef et al. 97)

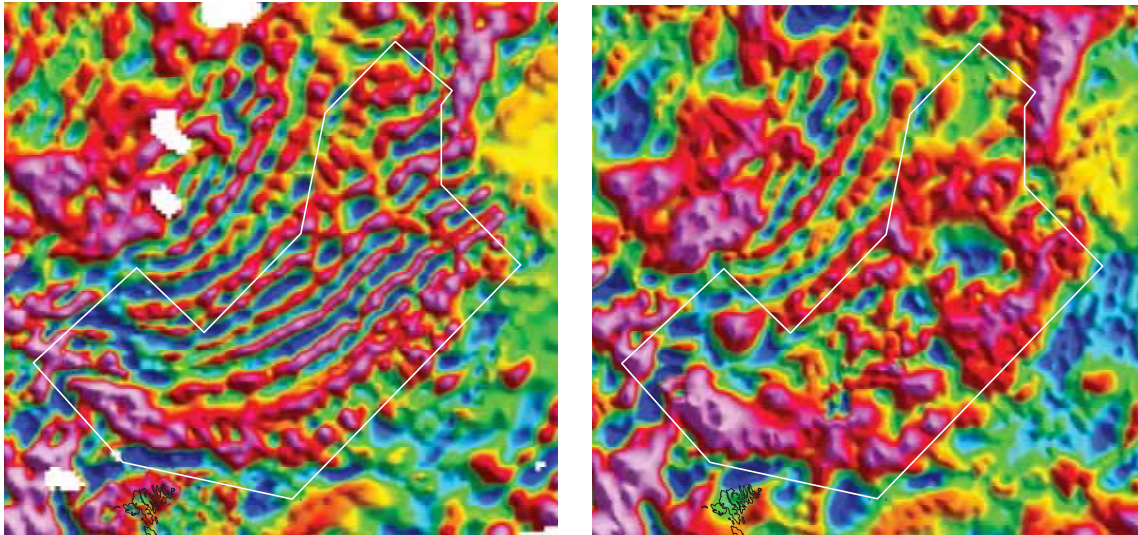


c) World magnetic map version A

d) World magnetic map version B

Figure 6.1 NGU final compilation compared with previous public domain compilations. a) Final compilation after the merge of the NB-07 with the pre-existing NGU compilation (500x500m). b) Vintage marine compilation from Verhoef et al. (1997) gridded at 1650 m. c) World magnetic map including satellites CHAMP data version A (3 min of arc spacing)(Hemant et al. 2007). d) World magnetic map version B (3 min of arc spacing) (Hemant et al. 2007). The new compilation provides much more details and reliability.





a) Final NGU compilation (5000x5000m)

b) WMA version B (Hemant et al., 2007)

c) 40-Low pass filter of (a)

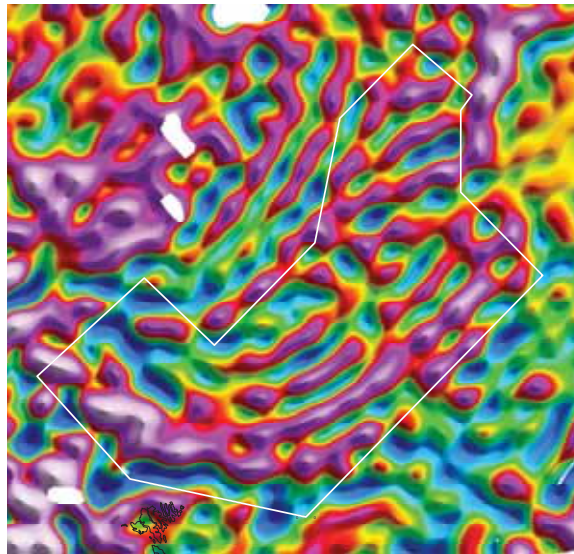


Figure 6.2 Medium to long wavelengths anomalies of the NGU final compilation compared with previous public domain compilations. a) Final compilation after merging the NB-07 with the pre-existing NGU compilation (gridded at 5000x5000m for a better comparison). b) World magnetic map version B (3 min of arc spacing). c) 40 km low-pass filtering of the NGU final compilation. You can notice that even the medium to long wavelengths can change locally.

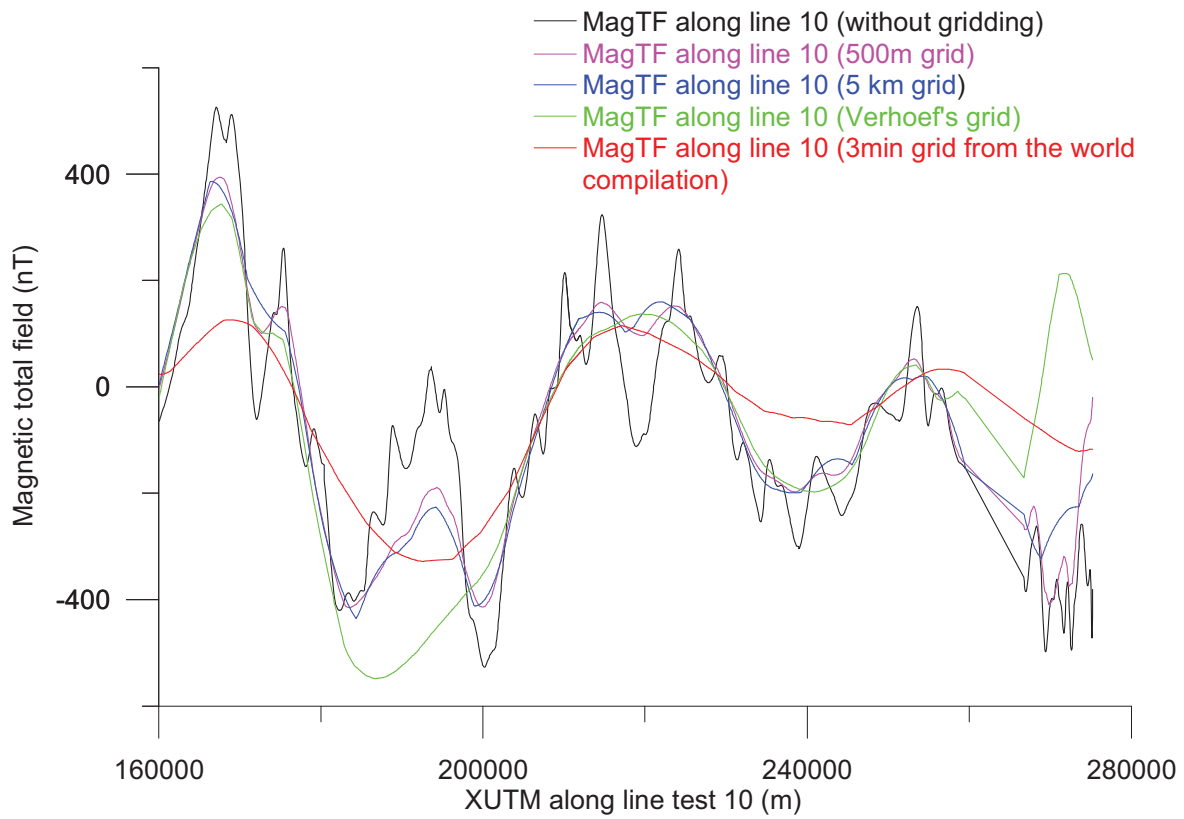
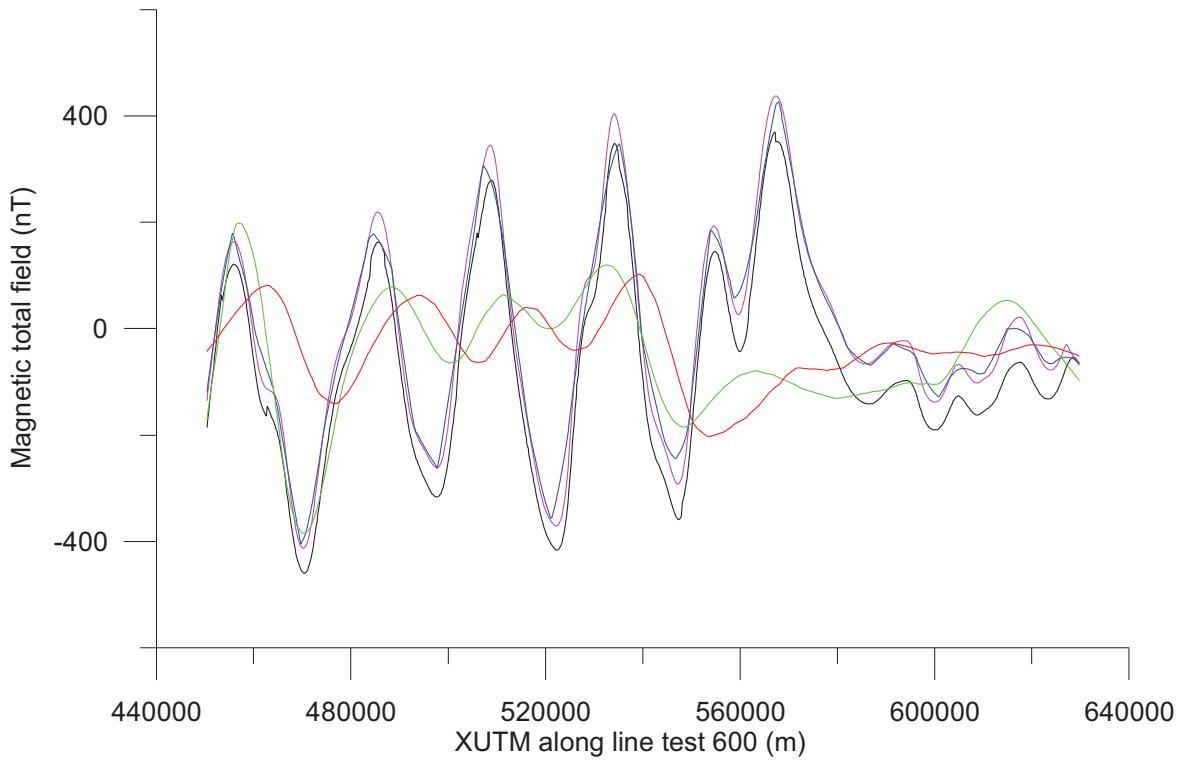


Figure 6.3 Different magnetic total fields extracted for different grid spacing and compared with other compilations. Using profiles, the differences are even more obvious. The NB-07 clearly provides a significant improvement for short as well as long wavelengths.

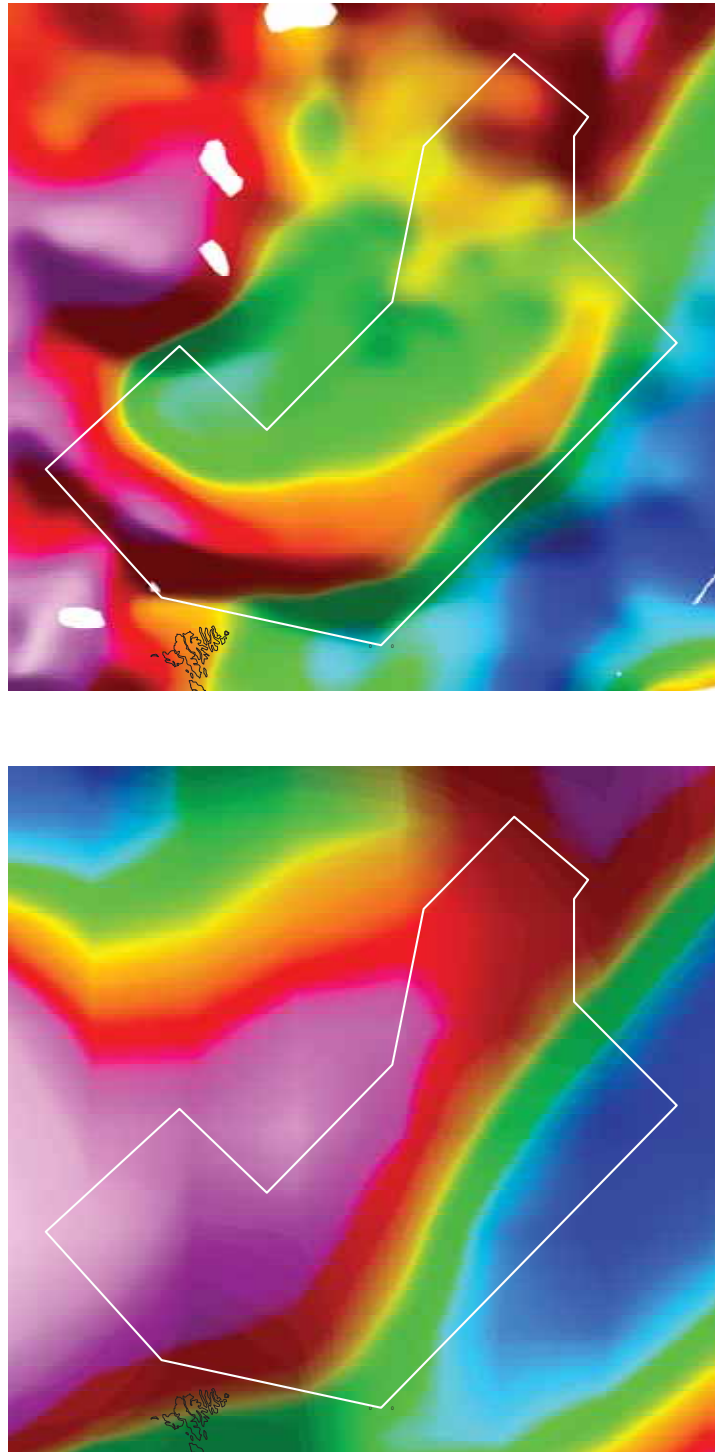


Figure 6.4 Long wavelengths along the NB-07. On top, upward continuation of the NGU compilation at 50 km. The figure below is the magnetic satellite Champ MF5 model (vertical component at zero geoid altitude).

## 7 OTHER DATASETS

### Laurent Gernigon

#### 7.1 Bathymetry

Bathymetric data used for the deep-water part of the map originate from satellite altimetry data released by (Smith and Sandwell 1997). We also merged the satellite gridded data with recent multibeam echosounding bathymetric data acquired between 1999 and 2001 by Gardline Survey for the Norwegian Petroleum Directorate. The grid presented in this report (Fig. 1.2) is 1 km x 1 km.

<b>Multibeam echosounding (MBES) data</b>			
Acquisition:	1999	2000	2001
Vessel	MV Sea Surveyor	MV Sea Surveyor	MV Ocean Endeavour
MB Echosounder (hullmounted)	Simrad EM12	Simrad EM12	Simrad EM120
Periods	25.06 – 26.09 11.10 – 23.10	05.06 – 14.08	01.07 – 08.08
Processing software	Neptune (Simrad)	Neptune (Simrad)	Neptune (Simrad)
Grid/map software	CFloor (Roxar)	CFloor (Roxar)	CFloor (Roxar)
Original Grid cell size	200*200m	200*200m	200*200m

**Table 7.1 Description of the NPD Law of the Sea multibeam echosounding data acquired in the Norwegian Sea between 1999 and 2001.**

#### 7.2 Gravity

The regional NGU compilation of Skilbrei et al. (2002) is used in the present study. This compilation is offshore based on measurements of c. 59 000 km of various shipboard gravity measurement provided by the Norwegian Petroleum Directorate, oil companies, and the Norwegian Mapping Authority (Fig. 7.1). This dataset was merged with previous Geosat and ERS-1 satellite compilations available in the deep-water areas of the Norwegian-Greenland Sea (Laxon and McAdoo 1994; Laxon and McAdoo 1994; Andersen and Knudsen 1998). The surveys have been levelled using the International Standardization Net 1971 (IGSN 71) and the Gravity Formula 1980 for normal gravity. The combined dataset has been interpolated to square cells of two km size using the minimum curvature method. Both Bouguer and isostatic grids have been computed using this compilation and the high-resolution bathymetric data.

### 7.3 Seismic reflection

Seismic reflection profiles provided by the Norwegian Petroleum Directorate were combined with gravity and magnetic data for interpretation and modelling. Some of the old multichannel seismic data available along the study area have been already introduced by Skogseid and Eldholm (1987). We also get access to recent Law of Sea seismic transects acquired by the Norwegian Petroleum Directorate between 1996 and 2000. It should be noted that the seismic data were only available in two-way traveltimes. EasyDepth™ from Beicip Franlab was used for the depth conversion of the lines and allows us to produce a segy file converted to depth. We interpreted and simply converted the seismic sections using a linear velocity versus depth function from sea bottom to top oceanic basement. This model of instantaneous velocity ( $V_p=1.9+0.4 \cdot \text{time}$ ) refers to the more recent velocity regional velocity database ( Myhre and Eldholm 1980; Breivik et al. 2006; Engen et al. 2006). These depth models were used for potential field modelling and directly imported into the GM-SYS package.

<b>Multichannel seismic data</b>		
	1999	2000
Company	Gardline Surveys	Fugro Geoteam
Vessel	MV Sea Surveyor	RV Geolog Dimitry Nalivkin
Time of surveying	30.06 - 26.07	
Source	4 * 40 cuinch	1600 cuinch array
Source depth	3 - 4m	4m
Shot interval	25m	25m
Streamer	1200m (Fjord)	3000m (Teledyne)
Streamer depth	3 – 8m	4 – 8 m
No of groups	96	240
<b>Processing:</b>		
Company	READ Well Services A/S	Fugro Geoteam
Processing software	DISCO/FOCUS	Promax
Samplerate	Resample 2 ms	Resample 2 ms
Velocity picks	Every 2 km	Every 2 km
Stack	24 fold	60 fold
TVF	Low-cut 3 -15Hz, Highcut 25 – 150 Hz	Low-cut 3Hz, high cut 35 – 250Hz
Migration	Phase-shift	T-X migration
Scaling	AGC 1000ms window	AGC 200ms window, 80% addback

**Table 7.2 Description of NPD Law of the Se seismic data sets acquired in the Norwegian Sea between 1999-2000.**

The interpretation of 3 transects and depth-conversion has been realised during this work. We used key horizons presented in the previously published papers and used well information provided by NPD to constrain the geologic model. We note, however, that the final

interpretation suffers from the lack of high quality lines and a sparse seismic dataset, which could not allow us to fully constrain the meaning of all anomalies

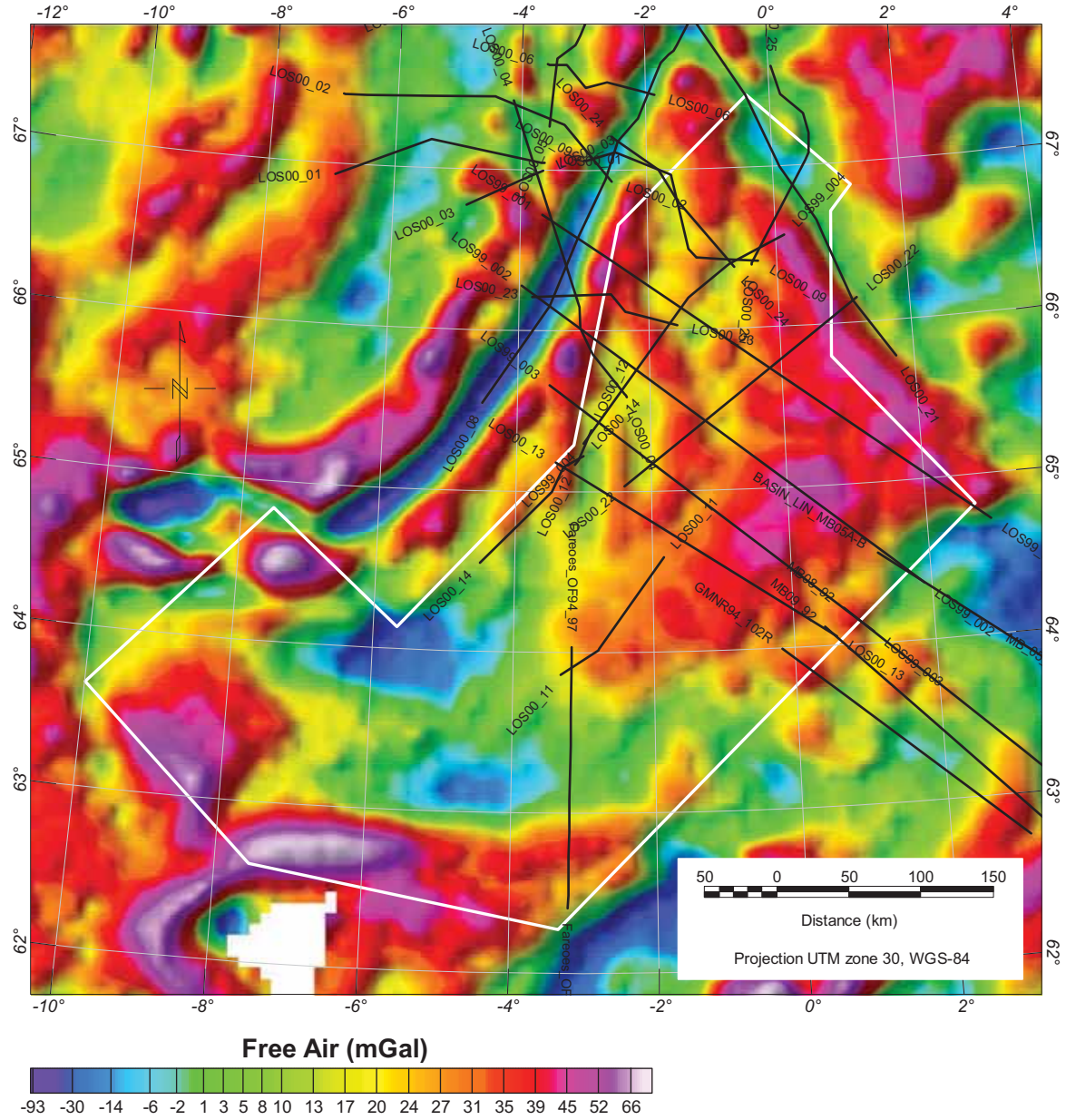


Figure 7.1 Free air gravity and location of the seismic data available around the NB-07 survey.

## 8 ESTIMATION OF MAGNETIC DEPTHS

Laurent Gernigon

### 8.1 Implications

Magnetic depth estimation plays an important role in magnetic interpretation. A complete and quantitative interpretation of potential field data aims at estimating information about depth, dimension and contrast in the relevant geological units. Magnetic depth estimates are often a reasonable approximation to the magnetic basement (i.e., metamorphic, igneous, oceanic). Basement depth (or equivalently, sedimentary thickness) is a primary exploration risk parameter. Estimates of basement depths are directly applicable to thermo-kinematical modelling and thermal maturity applications (e.g. heat flow estimation, source-rock burial-depth, distribution and volume).

However, keep in mind that such an interpretation suffers from inherent ambiguity. As a matter of fact, it is impossible to obtain all three types of information simultaneously without other a priori information (e.g. geological context and seismic data). These methods usually work for simplified source geometries (dimensions) and are most of the time independent of the susceptibility contrast. The depths estimated by some methods can be used as the final, quantitative solution in some ideal situations (i.e., the anomaly is well isolated and the noise is insignificant or well removed).

In this chapter, we present the results obtained using different techniques including: 1) the 3D Located Euler deconvolution of the magnetic total field, 2) the deconvolution of the tilt-angle derivative and 3) the Source Parameter Imaging function (SPI).

### 8.2 Euler deconvolution

The Euler method uses Euler's homogeneity equation to construct a system of linear equations, and then determines through a least-squares inversion one time for one window the (vertical and horizontal) position of a single source for a given source geometry (Thompson 1982; Reid et al. 1990). Euler deconvolution was first presented by Thompson (1982) for profile data and by Reid et al. (1990) for gridded data. Thompson (1982) showed that Euler's equation can usefully be written in the form:

$$(x - x_0) \frac{\partial M}{\partial x} + (y - y_0) \frac{\partial M}{\partial y} + (z - z_0) \frac{\partial M}{\partial z} = N(B - M)$$

With

$(x_0, y_0, z_0)$  the location of the magnetic source whose total field  $M$  is detected at  $(x, y, z)$ ;

B the magnetic regional field and N the structural index

It requires the use of the horizontal and vertical derivatives of the magnetic field if they are not observed. Thompson (1982) called the fall-off rate (i.e., the negative of the degree of homogeneity) the structural index (N). Synthetic tests (Blakely 1995; Barbosa et al. 1999; Bainbridge et al. 2002; Ravat et al. 2002; Silva and Barbosa 2003; Keating and Pilkington 2004; FitzGerald et al. 2004; Stavrev and Reid 2007) indicate (1) that the Euler method can locate with accuracy the outline and depth of a variety of simple geometrical shapes; 2) that the structural indices will cluster and determine the best structural interpretation. Although detailed as vertical contact, faults with a large throw may be best displayed with a structural index of zero (Table 8.1).

Euler's homogeneity equation is valid for bodies of arbitrary shape, characterised by these indices. In practice, the Euler method assumes idealized structures such as contact, thin sheet (dike), vertical or horizontal cylinder and 3D sphere. Application of the technique throughout this study was completed using the Geosoft executable E3DECON.GX. The Geosoft E3DECON.GX algorithm is based on the method described by Reid et al. (1990). This section therefore briefly describes the theory advantages and limitations behind the technique and presents its applications on the NB-07 survey area.

Euler 3-D deconvolution is a semi-automated technique enabling rapid qualitative interpretation and depth estimation of source depths from large gridded gravity and magnetic datasets (Reid et al. 1990b; Barbosa et al. 2000; Pilkington et al. 2000; Hsu 2002; Mushayandebvu et al. 2004; Florio et al. 2006). The technique has considerable advantages. 1) It can operate on large datasets extremely quickly; 2) provide a qualitative interpretation of geological structures; 3) provide depth estimates on the source of the anomalies 4) magnetic data do not need to be reduced to the pole (Reid et al. 1990) and 5) it is also insensitive to magnetic inclination, declination and remanence since these become part of the constant in the anomaly function of a given model.

### **8.3 Interpretation of the structural indices**

Careful consideration of the distribution and clustering of Euler solutions is, however, required to discriminate which solution best represents the causative source at depth within the crust. We note that different structural index maps often produce similar clustering of solutions with NB-07 that should not theoretically correspond to the particular structural index. This phenomenon may be explained by the gradients analysed by the chosen structural index, and the gradients associated with the anomaly being mapped.

Although in theory interpretation of the Euler solutions requires no pre-geological knowledge, Reid et al. (1990) acknowledge that this can be significantly beneficial. Reid (1990) claims that



the choice of structural index remains a limitation of the traditional Euler technique. These limitations arise as a product of some of the simplifying assumptions of the technique, which assume that the source is; (1) equivalent to a simplified geometrical feature (2) spatially homogeneous (3) independent of neighbouring magnetic sources (4) has a heterogeneous magnetization or density.

Along the NB-07, geological structures are probably arbitrarily shaped sources, and therefore are not simply modelled or defined by the structural index. The fact that the sources may not be internally or spatially homogeneous (i.e. the density and shape of the source change with depth or along strike), or the source-to-observation distance increases (thus the anomaly shape changes with depth) or other sources impinge each other's spatial positions are inherent sources of scatter (Reid et al. 1990b; Keating and Pilkington 2004). Consequently, it is necessary to examine a number of structural indices to compare results and clustering of solutions for several individual features. Alternatively, in such situations geological constraints from external data sources would be beneficial to the interpretation of the NB-07 dataset in the future.

Complexities also arise with respect to the depth of burial of the source. Ravat (1996) noted that there was a strong inter-dependency between the choice of the structural index and the distance of the source-to-observation, and that with increased distance the results were biased towards the higher structural indices, explained by the exponential decay of a source anomaly with depth. It can be predicted that with increasing depth the attenuation rate of the anomaly is less, therefore deeper sources may only be represented by higher values (Ravat 1996). The relationships between the source type and the observation level are considerably altered following upward continuation of the observation level, increasing the possibility of mis-identification of the true structural index (Ravat 1996).

Nevertheless, we found some correlation with the main trends underlined by the NB-07. Comparison with the gravity anomalies also suggests some shallow sources around gravity highs and deeper sources along the main gravity low. This relationship confirms evidence for shallow and deep basement, respectively.

Structural Index	Magnetic field	Gravity field
0	contact	Sill/dike/step
0.5	thick step	Ribbon
1	Sill/dike	pipe
2	pipe	sphere
3	sphere	

Table 8.1 Summary of the structural indices for simple geometric models from a magnetic anomaly or

gravity anomaly (Reid et al. 1990; Marson and Klingele 1993; Blakely 1995; Bainbridge et al. 2002; FitzGerald et al. 2004).

#### 8.4 Located 3D Euler method

The Euler technique assumes that the magnetic grid accurately represents the anomalous field. The absolute level of the anomalous field is however, rarely known. Thompson (1982) and Reid et al. (1990) assumed the anomalous field to represent the regional value. The Geosoft algorithm, however, computes the anomalous field and the coordinate of the same source body ( $x_0, y_0, z_0$ ), and their uncertainties (standard deviations) within a data window, solving them through a least squares inversion method. The vertical and horizontal derivatives or the total horizontal gradient (AS) of the total field anomaly, to be inverted for  $x, y, z$  and anomalous field are advantageous because they automatically de-emphasise the regional field (Blakely 1995).

Euler deconvolution usually assumes a "moving window" technique (Reid et al. 1990). This standard technique produces a mathematical solution for every position of the window estimating the unknowns after each sequential movement. The minimum and maximum depths that can be resolved are related to the grid cell size and the window size selected highlighting the importance that the quality of dataset and the nature of the investigations which may be achieved when using regional datasets.

For this report, we preferred the "located 3D Euler method", which is a modified version of the standard Euler deconvolution (Bainbridge et al. 2002). The located 3D Euler method refines the standard method by first running a peak-finding routine (Blakely and Simpson 1986), which locate peaks and estimate an appropriate windows size before the deconvolution. This method produces far fewer solutions because only a small subset of the grid will be at the centre of peaks in the dataset (Fig. 8.1). Combined with discrimination techniques, we can obtain more reliable Euler solutions. Only upper crustal sources (<10 km) have been selected in the following examples.

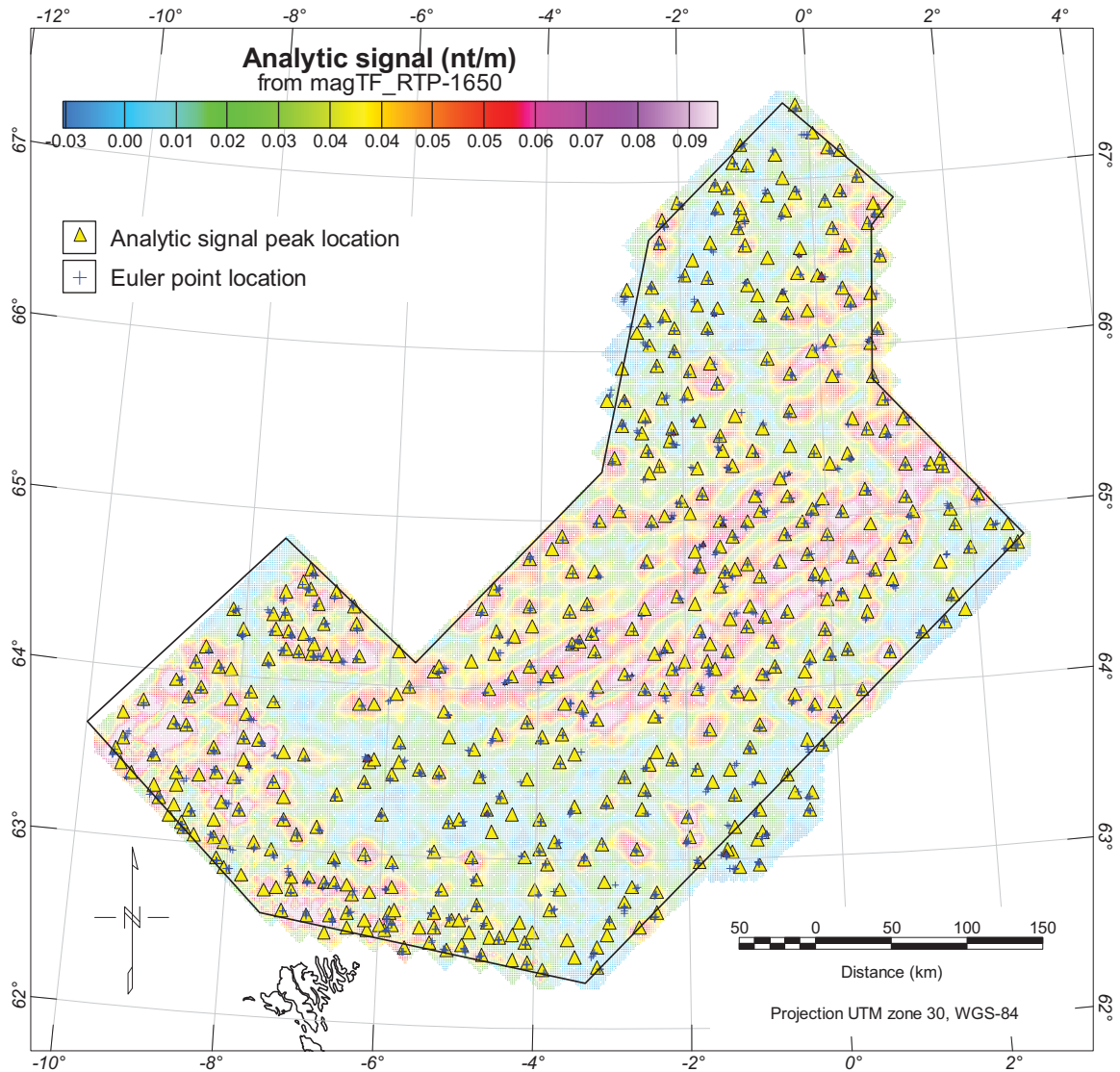


**Figure 8.1** Peak of the Total horizontal gradient (e.g. analytic signal) and location of the discriminated Euler points.

A pre-processing of the dataset used the analytic signal as the primary grid for Euler deconvolution. However, such procedures may increase the ratio of noise to signal within the grid, therefore, such pre-processing is limited by initial quality of the dataset, because noise will contribute to the scattering of solutions. In the present project, we used an upward continuation of 250 m to remove some remaining noise along the NB-07 already gridded with a grid cell of 1650x1650 to reduce aliasing. Nevertheless, this could have significant consequences upon the determination of source-to-window ratio and would complicate the depth interpretation of the deconvolution (Ravat et al. 2002). Peak detection was automatically obtained using the Blakely grid peak-picking algorithm of Blakely and Simpson (1986).

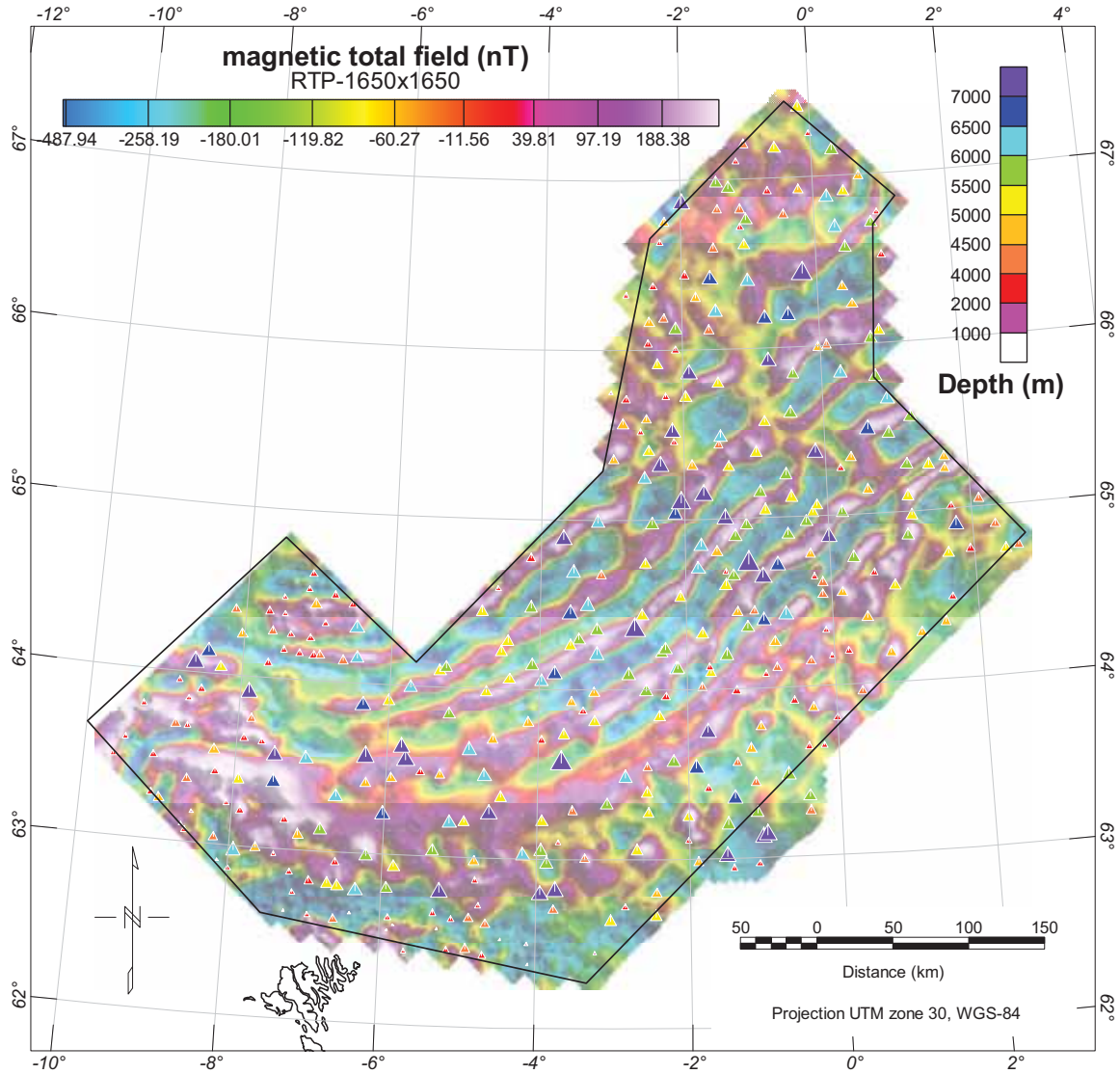


Figure 8.2 Result from located Euler deconvolution over the NB-07. Result using a structural index of 1.

During the Nb-07 modelling, a suite of maps, encompassing all the different structural indices, was required to accurately assess the different geological structures present within a study area particularly within complex regions. Best results for NB-07 have been obtained using Located Euler solution using indices of 1, 2 and 3. Using indice 0, the located Euler method did not provide enough solutions. The more relevant Euler solutions for indices 1,2 and 3 are displayed on Figs. 8.2, 8.3, 8.4

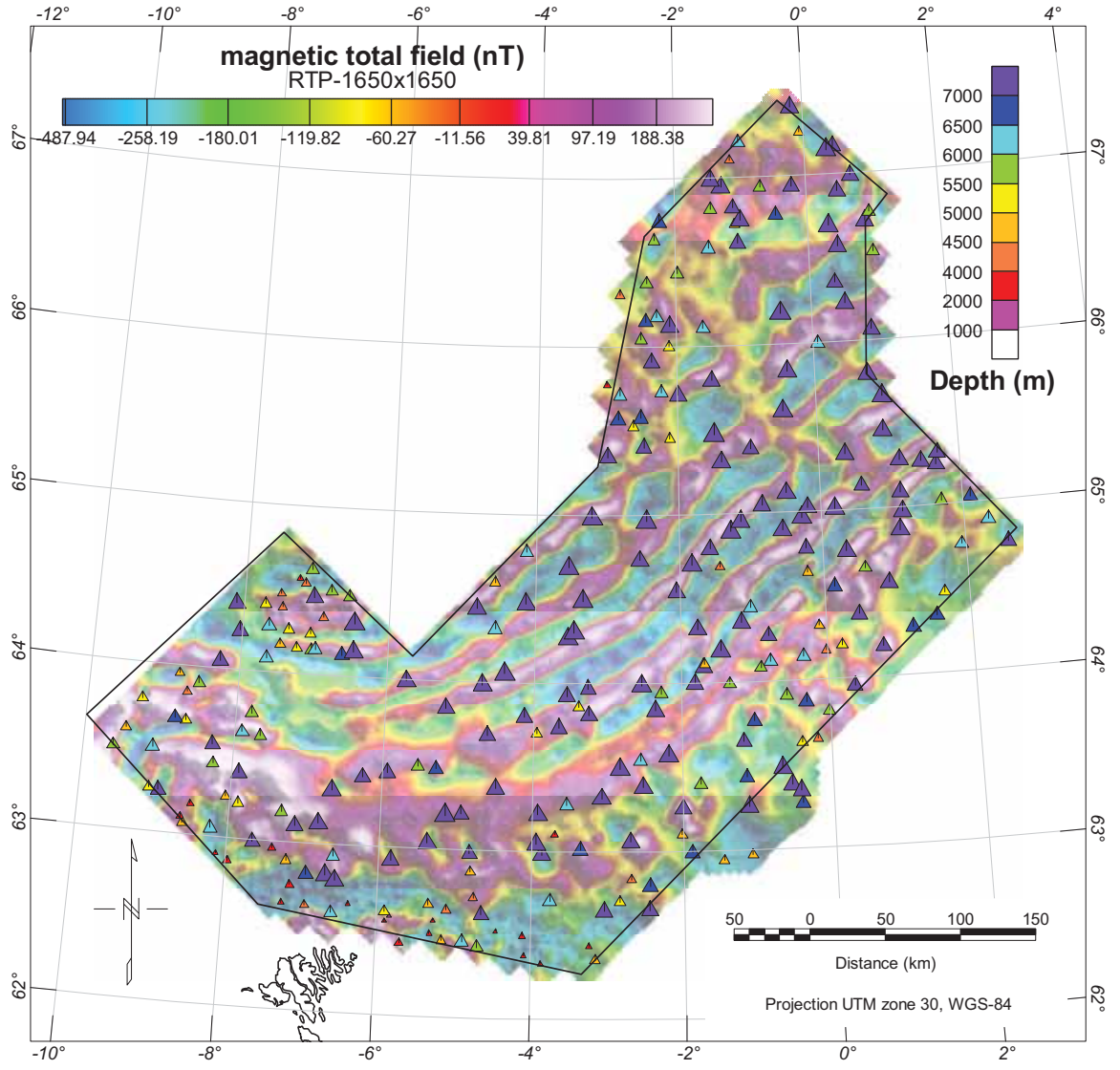


Figure 8.3 Result from Located Euler deconvolution over the NB-07. Result using a structural index of 2.

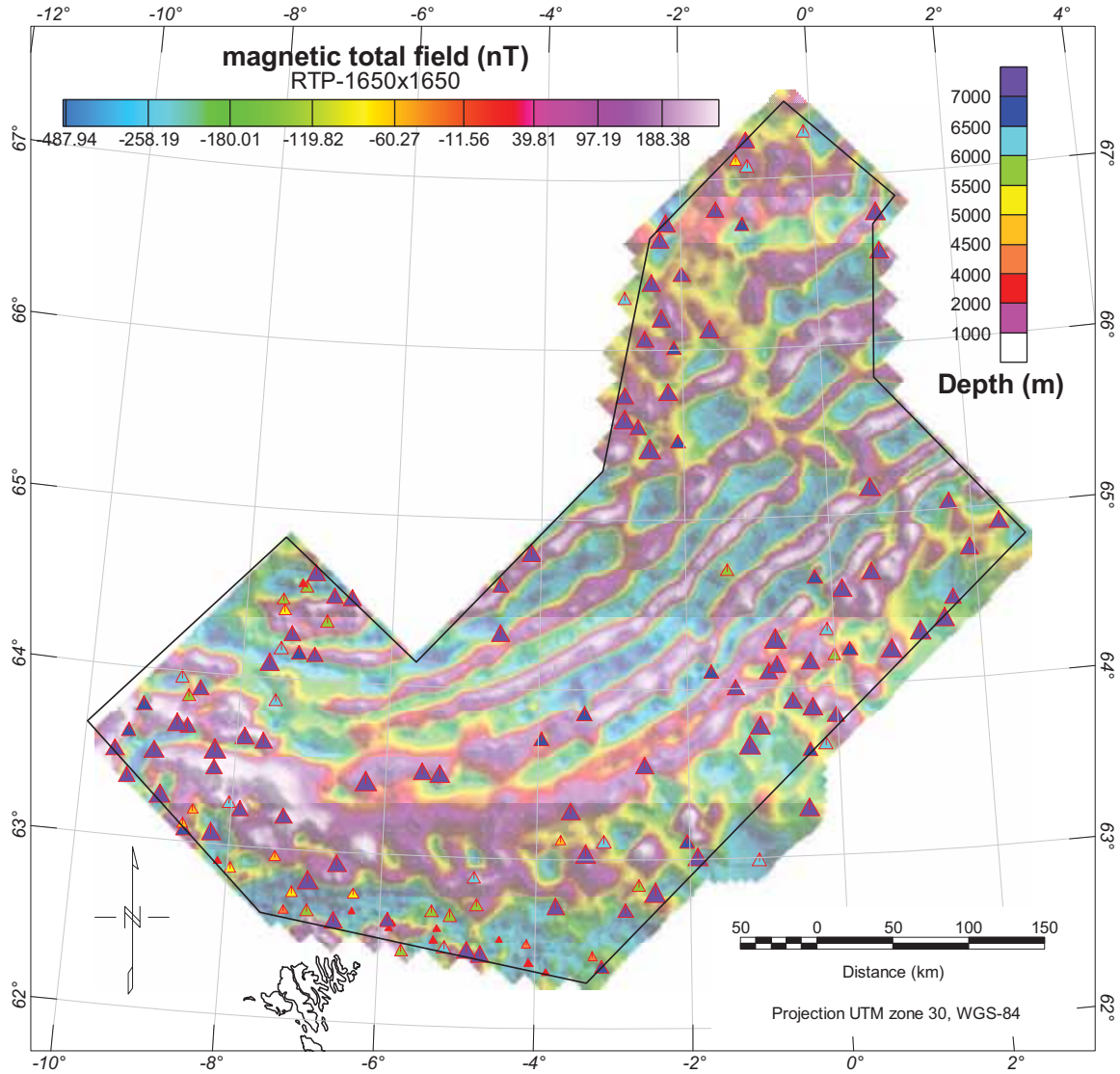


Figure 8.4 Result from located Euler deconvolution over the NB-07, using a structural index of 3.

### 8.5 Euler deconvolution of the tilt-angle derivative

During this project we have also tested a new method for interpretation of gridded magnetic data which, based on derivatives of the tilt angle, provides a simple linear equation, similar to the 3D Euler equation. This new approach (Salem et al. 2008) estimates both the horizontal location and the depth of magnetic bodies, but without specifying prior information of the structural index. Using source-position estimates, the nature of the source can then be inferred.

In the strategy of Salem et al. (2008), we first calculate the total gradient (“3D analytical signal”) of the tilt derivative. The total gradient of the tilt angle is sharper than the total

derivatives of the field and generates better defined maxima centered over the 2D body edges. The peak locations of the grid were found using a method for detecting the peaks of a grid similar to that of Blakely and Simpson (1986). This method uses the same Euler deconvolution's technique, previously described for the magnetic total field. The Euler deconvolution method spans only the data points falling within a specified distance of the peak locations to estimate the source location parameters ( $x_0, y_0, z_0$ ). Once the source location has been obtained, a value for the structural index is precised. The choice of data window size is a function of the data quality and the degree of interference of anomalies from nearby sources. For isolated anomalies, a larger data window can be used to overcome the effect of noise. For multiple neighbouring sources, a smaller-size data window is appropriate to reduce interference effects. The solution is accepted based on the following criteria:

1. a correct range based on the structural index (e.g., 0 to 2 for 2D source)
2. an accepted range for the source depths that the interpreter may accept as possible solutions. Only source depths <10 km have been considered
3. The horizontal source coordinates that should be close to the location of the detected peak
4. an acceptable threshold for the estimates of the standard deviation from the least-squares solutions (Thompson 1982)

The relevant Euler solutions derived from the tilt derivative and for indices 1, 2 and 3 are displayed on Figures. 8.5, 8.6 and 8.7.

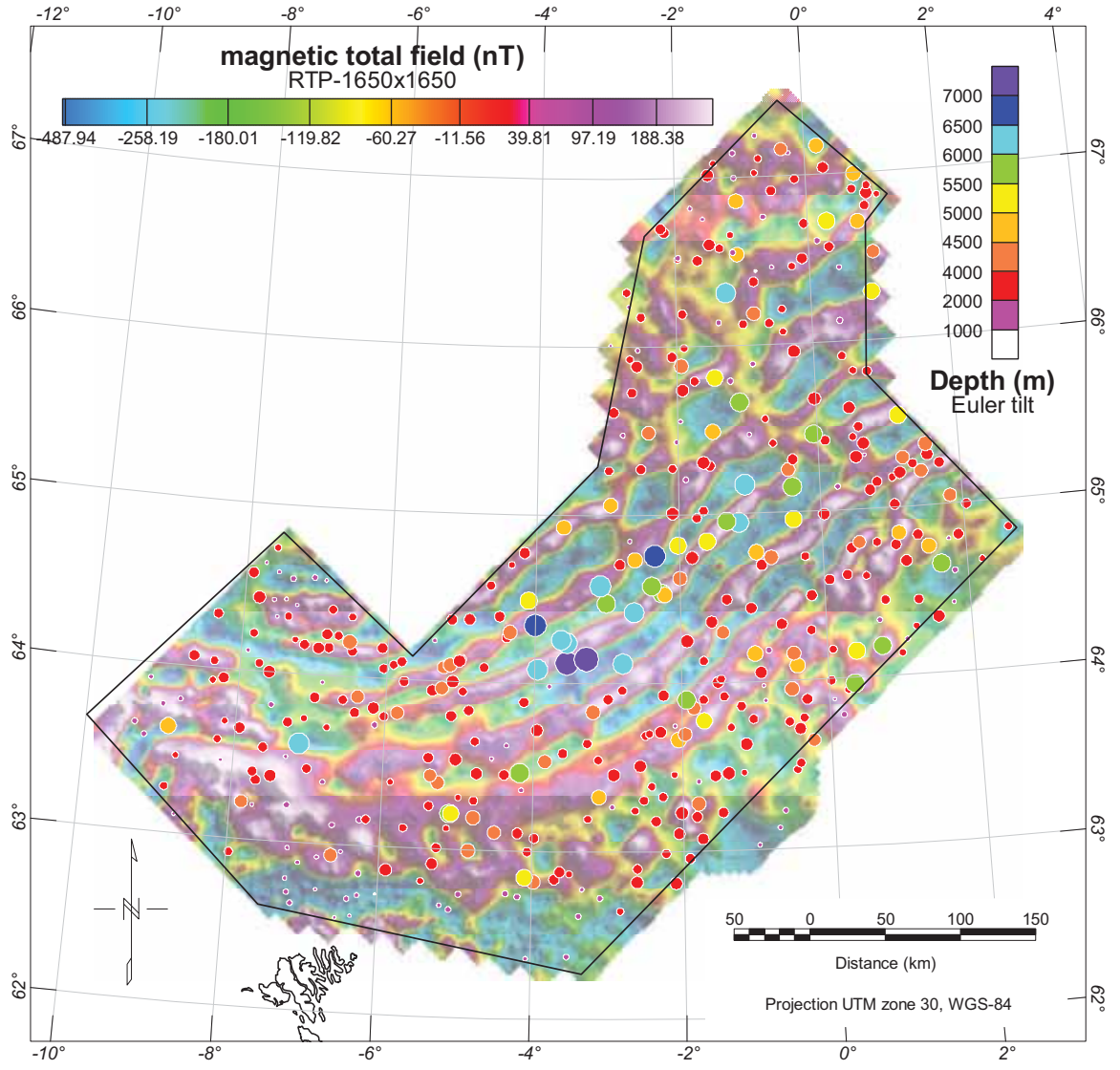


Figure 8.5 Result from located Euler deconvolution over the NB-07, using its tilt derivative. Depth solutions using a structural index of 1.



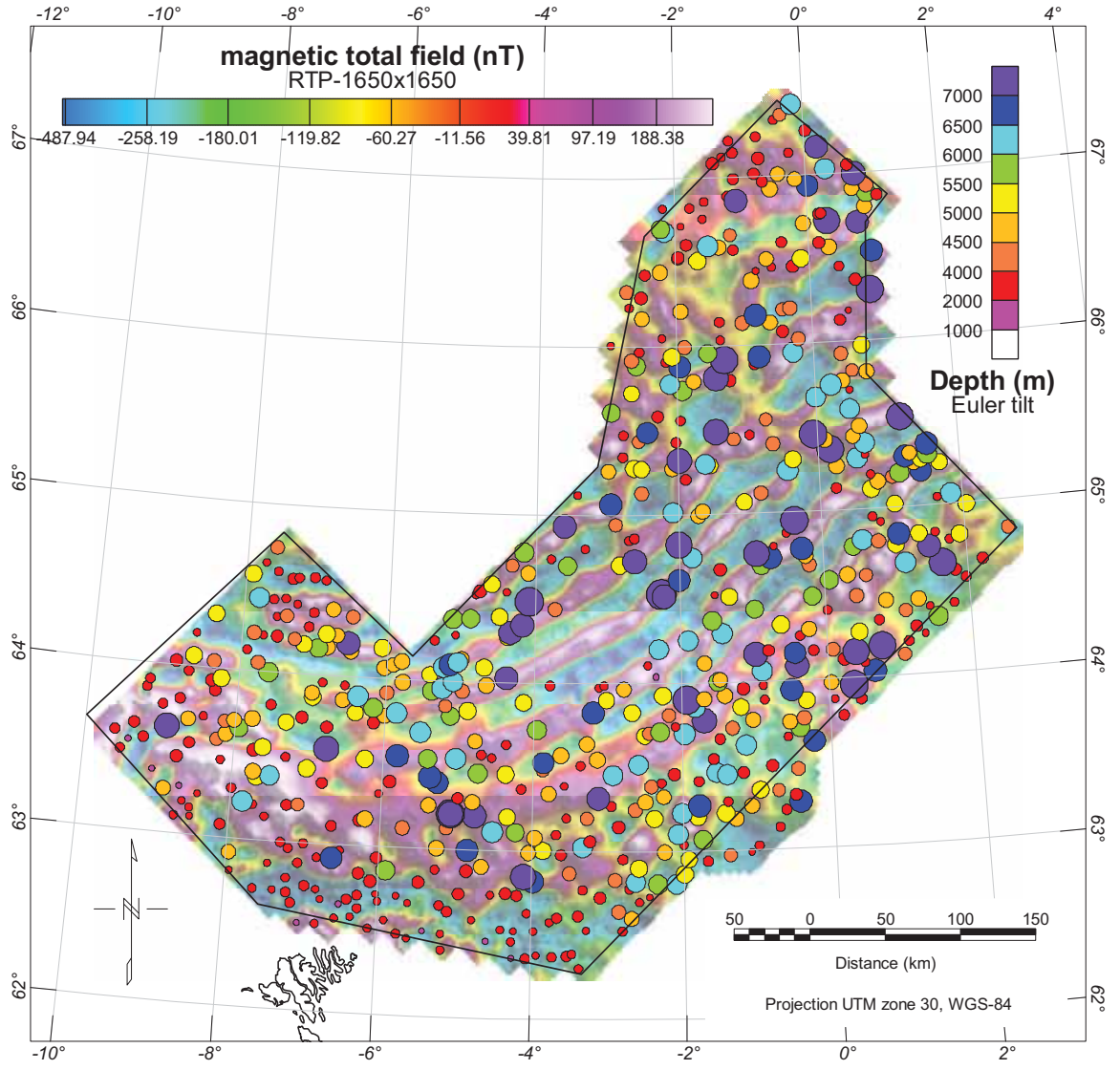


Figure 8.6 Result from located Euler deconvolution over the NB-07, using its tilt derivative filter. Depth solutions using a structural index of 2.

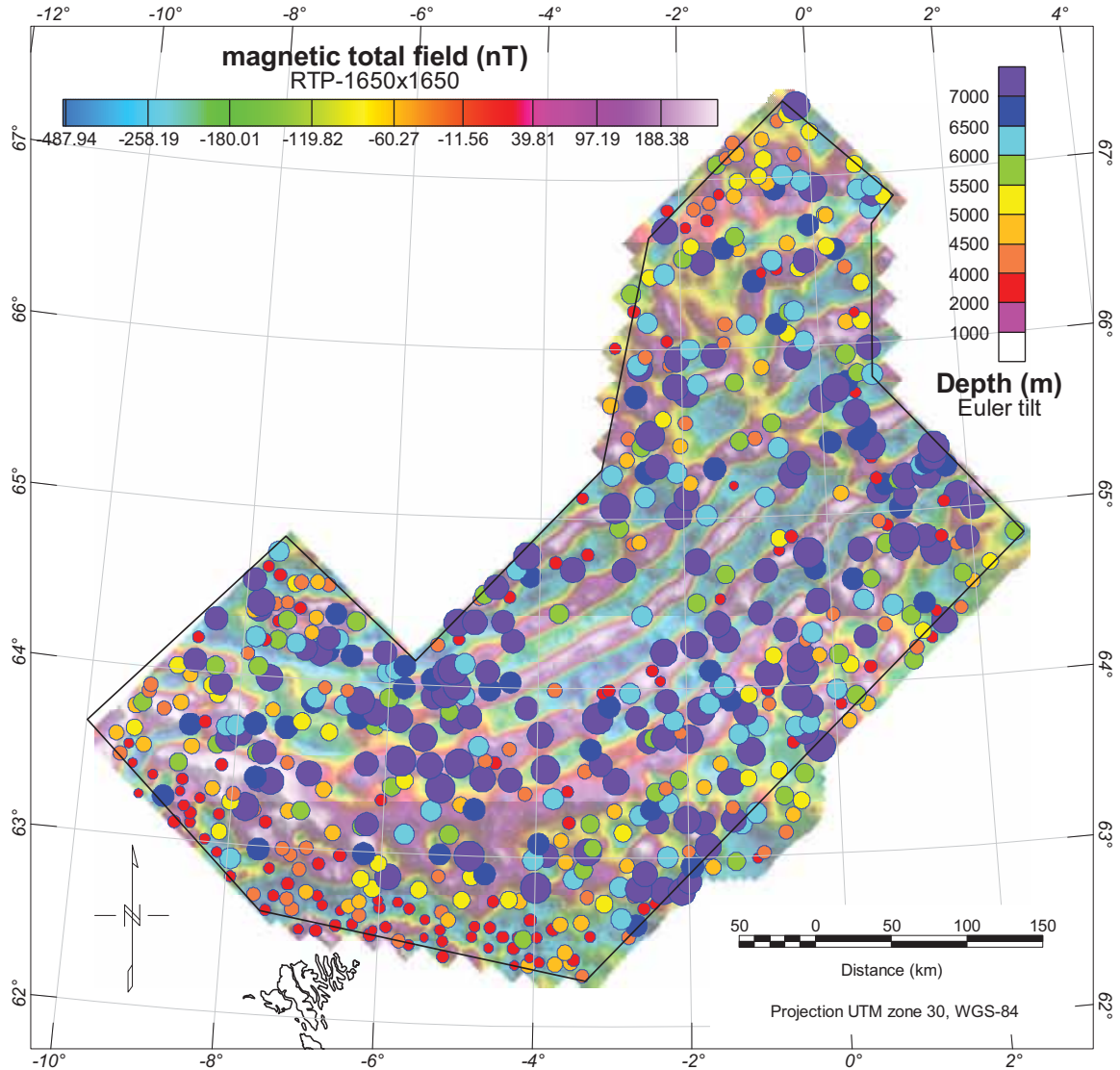


Figure 8.7 Result from Located Euler deconvolution over the NB-07, using its tilt derivative filter. Depth solution using a structural index of 3.

## 8.6 Source parameter imaging (SPI)

The source parameter imaging (SPI) technique is another quick method for calculating the depth to magnetic sources (Thurston and Smith 1997). The SPI methods used the local frequency  $f$  of the magnetic signal, which is defined as the rate of change of the local phase  $\theta$  with respect to  $x$ .

$$f = \frac{1}{2\pi} \frac{\delta}{\delta x} \theta$$

Where the local phase  $\theta$  is defined by:

$$\theta = \tan^{-1} \left( \frac{\partial M / \partial z}{\partial M / \partial x} \right)$$

Using the local wavenumber  $k = 2\pi f$  and using the differentiation rule

$$\frac{\partial(\tan^{-1} \phi)}{\partial x} = \frac{1}{(1 + \phi^2)}$$

Thurston and Smith (1997) show that the wavenumber  $k$  could be linked with the total horizontal gradient  $|A|$ , formerly called analytic signal and complex derivative filters of the magnetic field.

$$k = \frac{1}{|A|^2} \left( \frac{\partial^2 M}{\partial x \partial z} \cdot \frac{\partial M}{\partial x} - \frac{\partial^2 M}{\partial x^2} \cdot \frac{\partial M}{\partial z} \right) \text{ with } |A| = \sqrt{\left( \frac{\partial M}{\partial x} \right)^2 + \left( \frac{\partial M}{\partial z} \right)^2}$$

For a sloping contact, Thurston and Smith (1997) demonstrate that the “local susceptibility”  $K$  at the maxima of the local wavenumber can be a function of the total gradient ( $A$ ), the local wavenumber ( $k$ ), the local depth ( $h$ ) and the dip ( $d$ ) of the contact using the following equation:

$$d = \frac{1}{k} \text{ and } K = \frac{|A|}{2kFc \sin d}$$

Using the wavenumber, the phase and the total horizontal gradient at each wavenumber maxima, the local dip, and “susceptibility contrast can be derived. The SPI produces a more complete set of coherent solution points, do not require any windows assumptions and is easier to use (Fig. 8.8). The SPI’s accuracy has been shown to be +/- 20% in tests on real data sets with drillhole control and this accuracy is similar to that of the Euler deconvolution (Thurston and Smith 1997). However, this technique remains relatively simple and assumes that the sources are simply sloping contacts, with infinite depth extend. It also assumes no interferences from adjacent anomalies. Then and not at least this model considers no remanence magnetization.

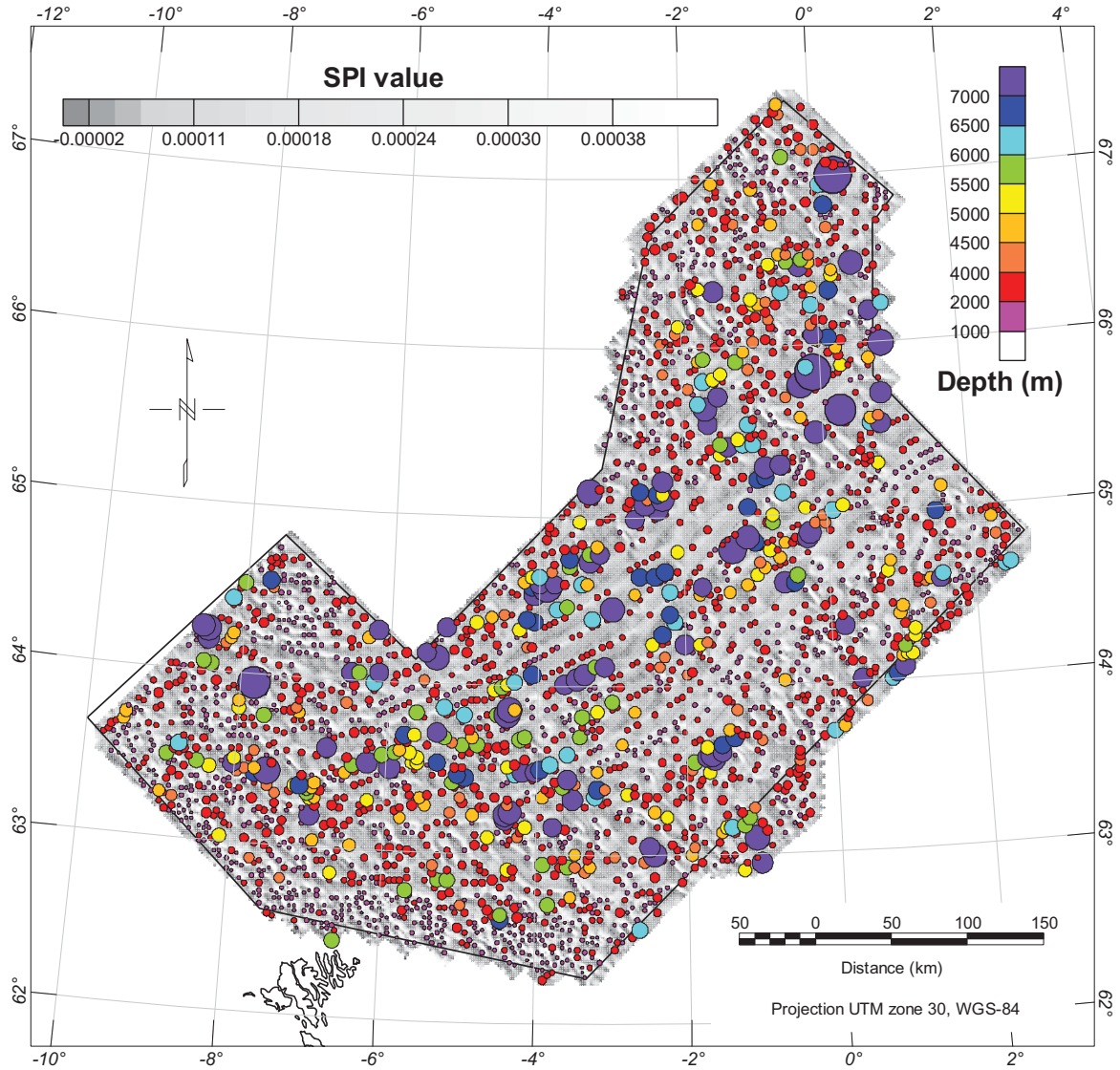


Figure 8.8 Results from Source parameter imaging (SPI) depths plotted on the SPI edge detection grid based on the local wavenumber technique of Thurston and Smith (1997). Each depth solution focuses along each maxima of the local wavenumbers.

## 8.7 Werner deconvolution

The Werner deconvolution method (Werner 1953; Gunn 1997) was applied to the new magnetic dataset and has been used to estimate and/or underline the potential depth of magnetic source along specific transect (see Chapter 10). The basic assumption of the Werner deconvolution is that all magnetic anomalies are the result of either a sequence of dykes or edge interfaces. The strike length and depth of the source bodies are also assumed to be infinite while

the width of each body is assumed to be either: (1) finite, representing a dyke; or (2) approaching zero such that it represents an interface between two bodies of differing magnetic susceptibility. The robustness of the technique is such that no reduction to the pole is required and it works effectively with both induced and remnant magnetizations. The results were compared with the Euler solutions computed in the previous part of the chapter. Despite limitations, Glebovsky et al. (2003) shows that this technique can be particularly successful to map the oceanic top basement. Cochran and Karner (2007) also got some results along the Red Sea margin. In general, the sediments within a basin have relatively weak magnetic susceptibilities compared with those of crystalline–volcanic basement at the base of the sediment column.

However, Werner (1953) recognised that analysing magnetic anomalies could be complicated because of the interference from adjacent anomalies and the effect of noise (e.g. diurnal variations, non-two-dimensionality and induced versus remnant magnetism). For this reason, the Werner deconvolution algorithm uses simple models for the sources and a quadratic form for the source/noise interference to determine the magnetization properties of the causative bodies. To reduce the noise we applied first an upward continuation filter to smooth the NB-07 magnetic grid. If the deconvolution is successful in defining a ‘real’ source, then depth estimates should define either the edges of the causative body or the depth range of an interface or the upper boundary of an intrusion. Inverse methods like Euler and Werner deconvolution did, however, not lead to satisfying results, as the main contrast is located at the side of the sources and not at the top or base. This makes the results of the Werner and Euler-deconvolutions difficult to interpret for marine magnetic anomalies.

## 9 INTERPRETATION

Laurent Gernigon

### 9.1 Introduction

The Norwegian–Greenland Sea comprises of a complex system of active and aborted spreading ridges and oceanic basins, initiated in earliest Eocene times after the continental breakup between Eurasia and Greenland (Fig. 9.1). In the central part of the Norwegian–Greenland Sea, the Jan Mayen Fracture Zone (JMFZ) forms broad and dominant scars on the seafloor and represents a major crustal boundary of Northeast Atlantic (Johnson and Heezen, 1967; Talwani et al., 1977). The JMFZ divides the Mohs Ridge from the Kolbeinsey and the Aegir ridges to the south (Fig. 9. 1). The Aegir Ridge represents the aborted spreading spreading center of the Norway Basin located between the Jan Mayen microcontinent and the Møre volcanic margin. The NB-07 survey covers the specific spreading system located between the Møre Marginal High and the Aegir Ridge.

This region has been the subject of many key geophysical surveys and early plate kinematics investigations (Vogt et al. 1970; Talwani and Eldholm 1977; Nunns 1983; Sirastava and Tapscott 1986). Compared to the Norwegian continental shelf, where intense petroleum exploration contributed substantially to general knowledge on volcanic margin formation and pre-breakup rift system, the tectono-magmatic evolution of the Norwegian Sea oceanic domain remained far from being well understood but remains an important domain to understand the dynamic of the mid. Norwegian margin (Eldholm and Grue 1994; Ren et al. 1998; Skogseid et al. 2000; Berndt et al. 2001a; Brekke et al. 2001; Gernigon et al. 2003a; Lien 2005; Mjelde et al. 2007).

Detailed geophysical description of the rift to drift transition along the Norwegian–Greenland Sea is essential to better understand and evaluate rift dynamics, fundamental geodynamic processes and changes in paleogeography. Few modern aeromagnetic surveys covering neighbouring area, showed that a large part of the old data could be mis-interpreted due to geophysical artefacts, caused by inappropriate levelling, poor navigation records and/or inadequate and sparse spacing of old pre-existing magnetic profiles (Verhoef et al. 1997; Olesen et al. 2006; Gernigon et al. 2008). The Norway Basin area was covered by vintage surveys that were included in the magnetic compilation of Verhoef et al. (1997) (Figs. 1.3 and 9.3) The most recent magnetic acquisition (NRL-90) only covered the Aegir Ridge itself but does not extend further west (Jung and Vogt 1997). The NB-07 survey filled the gaps and covers most of the breakup and early spreading system initiated between the Faroes Plateau and the East Jan Mayen Fault Zone (EJMFZ) in Early Tertiary time. The survey covers a large part of the Møre volcanic margin and extends almost close to the Aegir Ridge.

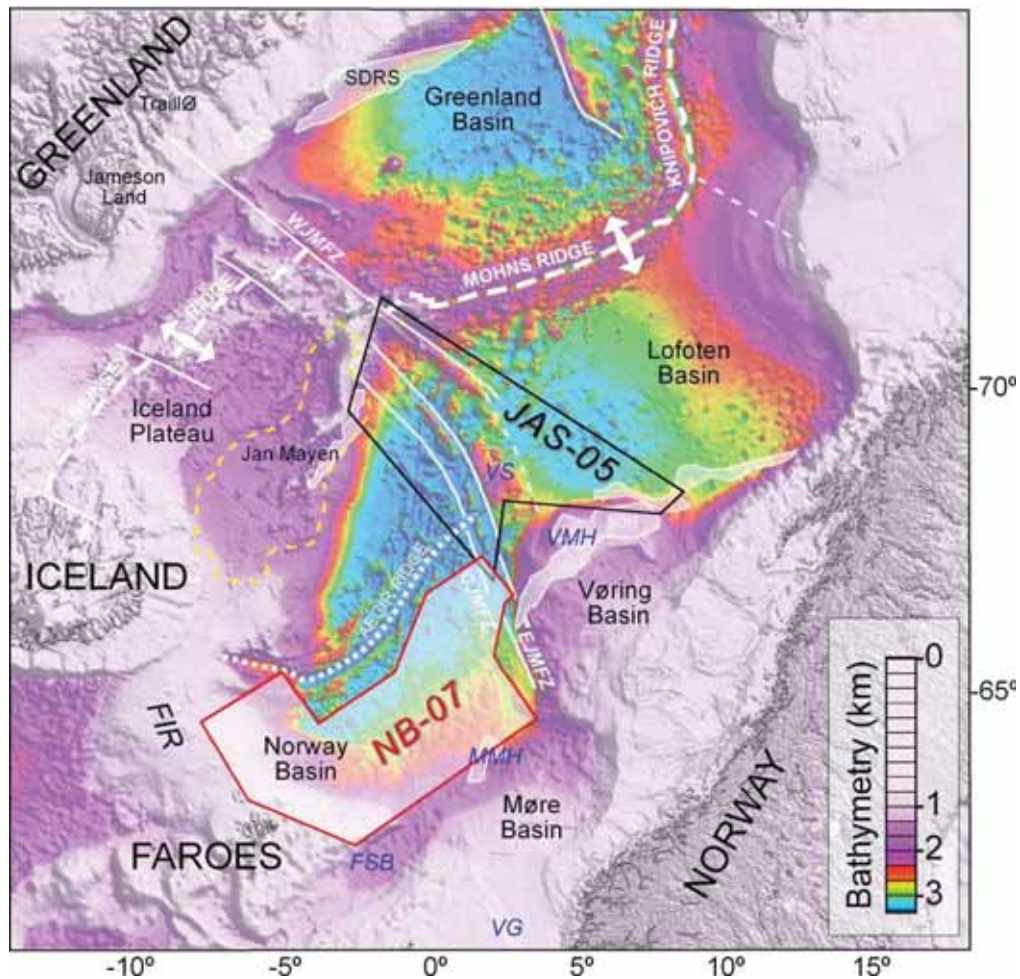


Figure 9.1 Bathymetric map and main physiographic features of the Norwegian-Greenland Sea. Sea-floor spreading led to the formation of Reykjanes, Aegir and Mohns Ridges. Spreading along the Aegir Ridge decreased until ceasing in the Oligocene. A progressive ridge jump along the Kolbeinsey Ridge happened during the same period, connecting the Mohns and Kolbeinsey Ridges and leading to the formation of the Jan Mayen microcontinent. The Jan Mayen Fault Zone (JMFZ) consists of three distinct segments named the western (WJMFZ), eastern (EJMfZ) and central Jan Mayen Fractures zones (CJMFZ), respectively. The polygons represent the outline of the recent JAS-05 and NB-07 aeromagnetic surveys and main study area on the Norway basin. Seaward-dipping reflector sequences (SDRs) represent thick volcanic lava flows extruded during the breakup along the Vøring Marginal High (white outlines). FSB: Faroes-Shetland Basin, FIR: Faroes-Iceland Ridge, MMH: Møre Marginal High, VG: Vicking Graben, VMH: Vøring Marginal High, VS: Vøring Spur.

On the basis of these ambiguous data, the spreading evolution of the Norwegian Greenland Sea and JMFZ have been nonetheless the subject of many regional and geodynamic studies (Talwani and Eldholm 1977; Lundin and Doré 1997; Torsvik et al. 2001; Mosar et al. 2002; Lundin and Doré 2002; Lundin and Doré 2005; Tsikalas et al. 2005; Scott et al. 2005; Olesen et al. 2007; Scheck-Wenderoth et al. 2007). Some contributions particularly rise challenging questions about the timing, variability and origin of atypical magmatic events affecting the

Norwegian-Greenland Sea and surrounding volcanic margins (Breivik et al. 2006; Greenhalgh and Kusznir 2007; Meyer et al. 2007; Olesen et al. 2007; Breivik et al. 2008). These contributions agree that a clear understanding of the tectonic and magmatic history of the Norwegian oceanic domain is essential when dealing with breakup, spreading rate evolution, intraplate magmatism and the influence of deep but controversial sub-lithospheric mechanisms involving a potential Icelandic mantle plume. However, a proper understanding of dynamics of break-up, evolution of basins situated on conjugate margins and the formation of the oceanic crust requires higher quality data. In term of isostasy, flexure and temperature evolution of deep offshore basins Gernigon et al. (2006), Lucazeau et al. (2003) and Kusznir and Karner (2007) show notably that the rift to drift evolution of any rifted margins should be better considered for reliable basin modelling. Fundamentally, a better investigation of the spreading history and associated magmatic events should help us to better assess the parameters and mechanisms involved during and after the onset of the breakup on the mid-Norwegian margin. Furthermore, accurate plate reconstruction requires good constrains on the spreading system to define a better fit and improved rotation poles. Studies also suggest that mantle pulses and/or spreading reorganisation in the oceanic domain could trigger compressive stress and sand influx in the proximal part of the contiguous margins (White and Lovell, 1997). Consequently a better spreading tectonic calendar of the Norway Basin should help to refine and/or constrain the tectonostratigraphic setting of the adjacent rifted margin and sedimentary basins.

The objective of this chapter is to update and re-examine the geophysical and tectonic setting of the Norway Basin and surrounding continental passive margins affected by significant breakup and post-breakup magmatism. We summarize the geological background of the study area and we present and discuss a preliminary interpretation of the aeromagnetic NB-07 survey. The new aeromagnetic survey integrated with gravity and recent seismic data already aims to document and model some important aspects of the early spreading history of the Norwegian-Greenland Sea. Our contribution attends to provide a new magnetic chron interpretation, a potential field modelling along specific transects and some elements of discussion dealing about 1) volcanic margin formation, 2) the meaning of the COT, 3) the initiation of a spreading centre, 4) the mechanics of spreading centre emplacement and 5) the subsequent spreading evolution of the oceanic basin.

## **9.2 Geodynamic and geological background of the Norway Basin: Review of previous works**

### **9.2.1 Breakup and magmatism**

The geodynamic evolution of the Norway Basin initiated with the onset of oceanic spreading by the splitting apart of Eurasia and Greenland in the Early Tertiary. This major tectonic event was accompanied by significant volcanic activities associated with the formation of the North



Atlantic Igneous Province (NAIP). The onset of the 'breakup event' is generally regarded as having been virtually synchronous throughout the NAIP but we maintain that this is still based on very few accurate data points and mostly rely on onshore basaltic exposures (Meyer et al., 2007).

Along the Møre volcanic margin, volcanic sequences (SDRs) have been recognized on seismic data but these features have not yet been drilled (Fig. 9.1). Consequently, age of volcanism along the study area is still mostly based on regional considerations and interpretations. Ocean Drilling Program (ODP) efforts on the mid-Norway margin at the Vøring Marginal High (Fig. 9.1) drilled similar seismic features (Leg104) and recovered volcanic rock successions that record the magmatic activity from the early continental break-up phase. The volcanic sequences also include the SDRs interpreted as tilted subaerial and transitional-type tholeiitic MORB lava flows, with interbedded volcanoclastic units (Eldholm et al. 1989; Planke and Eldholm 1994; Berndt et al. 2001a). The lower volcanic sequences comprise a series of intermediate extrusive flows and volcanoclastics, erupted prior to the onset of MORB-type magmatism and derived, at least partially, from continental source material. The Early magmas of the Vøring Marginal High have been inconsistently dated by Rb-Sr isochrones to  $57.8 \pm 1.0$  Ma (LeHurray and Johnson 1989) and  $63 \pm 19$  Ma (Taylor and Morton 1989). Recent Ar-Ar geochronology investigations indicate that the lower basaltic series are much younger, 56–55 Ma (C25n-C24r) (Sinton and Duncan 1998).

South of the Møre Marginal High, the Faroe Islands (Fig. 9.1) rest on top of the subsided, continental Faroes–Rockall plateau and are separated from the British Isles by the Faroes–Shetland Basin and the Rockall Trough. The Faroe islands expose up to 3 km of flood basalts – the Faroes Plateau Lava Group – which is divided into three main basaltic formations (Waagstein 1988; Ellis et al. 2002; Waagstein et al. 2002). All basaltic lavas have been erupted subaerially and are tholeiitic. The three volcanic formations are all exposed onshore on the Faroe Islands. The lowermost formation differs from the olivine tholeiites in the upper and middle formations in being silica-oversaturated and being more crust-contaminated. The lower formation is capped by a Paleocene coal-bearing sequence, which is evidence for a break or decrease in volcanic activity. So far, no hiatus has been documented between the middle and upper formation but a mantle source change occurs at this transition (Meyer et al. 2007).

From other age compilations sills and lavas within the NAIP have yielded a wider range of ages from the end of the Cretaceous (65 Ma) to Eocene (48 Ma). Taking all of the NAIP into consideration, Saunders et al. (1997) concluded that the NAIP magmatic activity occurred in two main phases. Phase 1 began about 62 Ma ago (C27r), and lasted for 2–4 Ma and most of the associated magmas were erupted through and onto the continental crust. Phase 2 began at about 56 Ma (C25n/C24r) and accompanied plate breakup, separation and seafloor spreading, and continues to the present day on Iceland. Saunders et al. (1997) note that continental contamination of extrusives was prevalent during Phase 1 but also during Phase 2. Some of the magmas associated with Phase I were rich in MgO (so called picrite), indicating that the source

region of the liquids could be abnormally hot and that the widespread and simultaneous activity of Phase 1 indicates an abnormally high mantle flux rate. They suggest that this phase may have been associated with the arrival of a start-up plume, or alternatively it could represent the arrival of a pulse of hot mantle, following a period of weak plume activity during the Cretaceous.

Jolley and Bell (2002a, 2002b, 2002c) incorporate more recent published age-dates from within the NAIP and discriminate three phases of igneous activity. Their Phase 1 covers the dates prior to ~60.5 Ma (before C26r) that are postulated to record the initial impact of the proto-Icelandic “Plume” beneath the Paleocene North Atlantic lithosphere. Phase 1 activity appears to be concentrated on West Greenland at the western margin of the NAIP and in the Hebridean area at the southeastern margin of the NAIP. Jolley and Bell (2002) also note that the focus of Phase 1 magmatic activity appears to be limited to the western and southeastern margins of the NAIP but may reflect the lack of detailed knowledge in some areas, like the Faroes and contiguous margin areas.

Phase 1 may be followed by a more extensive Phase 2 including volcanic sequences emplaced between 60.7- 57.5 Ma (C26r-C25r). The first evidences of lavas of this age have been observed around the Erland Volcano (Jolley and Bell 2002b) and in thick volcanoclastic sequences in the Faroes islands (Ellis et al. 2002). During Phase 2, volcanic activity basalt sequences erupted in West Greenland, the Irmiger Basin, the Faroes Plateau, the Vøring Marginal High and the Faroes-Shetland Basin.

The last volcanic Phase 3 of Jolley & Bell (2002a) corresponds to the extrusion of enormous lava volumes concentrated along the volcanic margins of the proto-North Atlantic and Norwegian Sea. As part of the Phase 3, the Middle Lava Formation of the Faroes has been matched with the Milne Land Formation in East Greenland (Larsen et al. 1999) and the uppermost lavas probably correlate with part of the seaward dipping reflector sequences (SDRs) seen north of the Faroes. Radiometric dates for these lavas cluster around 56-53 Ma (C25n-C24b) and their emplacement accompanied the onset of seafloor spreading in the North Atlantic (Storey et al. 2007). New radiometric data also suggest that excessive volcanic activity continued after 53 Ma in the region of the East Greenland lithosphere between 66 and 69°N (Jolley and Bell 2002a; Storey et al. 2007). An additional initial phase, during Late Cretaceous times, has also been suggested by Morrissey (2003) and Archer et al. (2005) and seems to be centred within the Rockall Trough.

It has been widely postulated in the literature that the early magmatic activity (62-58 Ma) in the North Atlantic could coincide with the arrival of the proto-Iceland “Plume” beneath the NAIP and that thereafter there was more or less continuous but spatially separated activity culminating in the massive regional outpouring of flood basalts at the time of continental breakup (55-53 Ma); or alternatively that after the initial Phase 1 activity there was a 3-4 Ma incubation period before a renewed and intense activity concomitant with the breakup stage

(Jolley and Bell 2002a; Saunders et al. 1997; Storey et al. 2007). Meyer et al. (2007), in their recent review of the NAIP, indicate an onset of igneous activity at ~60 Ma. They point out that a large part of the NAIP is undersampled and note that there is only a single data point on the mid-Norwegian margin and that there is a continuing debate about the reliability of the dataset. From the spread of published radiometric age data and in consideration of ages derived from detailed stratigraphic correlations between igneous events and their tectonostratigraphic effects, magmatism could develop from the Cretaceous/Tertiary boundary to the early Eocene. Evidence for early intrusive activity in the NAIP is provided by the widespread emplacement of inboard sill complexes in the Cretaceous sedimentary basins of the NW European pre-breakup margin and the early age of some of the emplacement of central complexes (e.g. Archer et al. 2005). Evidence of “overcrusting” on the Vøring Spur, west of the Vøring Marginal High (Fig. 9.1), also suggests that high magmatic activity still continued locally after the breakup, probably during mid-Late Eocene (Gernigon et al. 2008).

Differing views and discussion in the plume versus non-plume debate can be illustrated by the recent reviews of Smallwood and White (2002), Lundin and Doré (2005) and Meyer et al., (2007). Smallwood & White (2002) accept the traditional model that development of the rifted continental margins and subsequent seafloor spreading in the North Atlantic was dominated by interaction between an Iceland Plume and the continental and oceanic rifts and believe that there is evidence that at the time of breakup a thin sheet of hot asthenospheric mantle propagated beneath the lithosphere across a 2500 km diameter region corresponding to the NAIP. They believe that this event corresponds to the arrival of the Iceland plume head and caused a transient uplift, massive volcanism, and a rapid transition from continental stretching to seafloor spreading.

In contrast, Lundin & Doré (2005) critically re-examined the Iceland mantle plume model in the light of recent advances in understanding and concluded that the classical model is untenable for Iceland and the NAIP. They relate Early Paleocene magmatism (62-58 Ma) to a short-lived attempt at seeking a new rift path, intermediate in time and space between the Labrador Sea-Baffin Bay and NE Atlantic-Eurasia Basin rifts. They suggest that the final breakup in the Early Eocene (56-53 Ma), was accompanied by voluminous extrusive magmatism and was achieved by exploiting inherited structures.

Even if the mantle plume hypothesis is often mentioned to explain the formation of this anomalous magmatism, some authors also argue that voluminous breakup magmatism may simply reflect compositional heterogeneities and/or plate-driven dynamic processes in the upper mantle and not necessarily excess mantle temperature associated with a deep thermal boundary (Anderson and Natland 2005; Foulger et al. 2005). Meyer et al. (2007) summarize these ideas and review alternative models for the development of the NAIP, including lithospheric delamination, meteorite impact, fertile mantle, chemical anomalies, small-scale- and edge-driven convection and mantle plume models as possible alternatives. They conclude that although the mantle plume concept most successfully explains most of the observations, it does

have unexplained aspects that remain to be addressed. They note that some of the alternative models explain some aspects of rifted margin well but that in many cases existing datasets and geodynamic concepts are incomplete.

### 9.2.2 Spreading and geodynamic setting of the Norway Basin

Soon after breakup, normal sea-floor spreading occurred simultaneously along the Mohns and Aegir Ridges offset by the JMFZ, acting as a complex and active oceanic transform zone between the two spreading systems (Fig. 9.1). Vogt et al. (1970) interpreted the first symmetric magnetic anomalies in the Norway Basin and confirmed the idea that the Aegir ridge is a now extinct spreading axis as first speculated by Johnson and Heezen (1967) few years before. Later, Talwani and Eldholm (1977) and Nunns, (1983) identified magnetic anomalies from C23 (51.7-50.7) to possibly C7 (25.6-24.7) and suggest a fan-shaped distribution of the magnetic anomalies. Talwani and Eldholm (1977) suggested that a variable spreading rate occurs along the axis and according to Munns (1983), a complementary fan-shaped spreading should have occurred between C18 (40.13-38.4 ma) and C7 (25.6-24.7 Ma), west of the Jan Mayen. The idea of conjugate fan-shaped spreading system was later developed by Lundin and Doré (2002) which suggest similar fan-features south of Jan Mayen and the Blosseville Coast. Nevertheless, Scott et al. (2005) challenged this V-shaped model and claim that the quality of the vintage magnetic coverage was not at sufficient high quality to validate this idea. Instead Scott et al. (2005) involved a complex system of spreading anomalies displaced by numerous oceanic transforms and shear zones that affected and displaced the Jan Mayen microcontinent.

Around C7-C5A (25.6-11.9), a major geodynamic event in the Norwegian-Greenland Sea is usually proposed, when, a NNW-SSE to NW-SE, clockwise rotation of the opening direction took place leading to the initiation of the WJMFZ (Lundin and Doré 2002; Mosar et al. 2002). During that period, spreading along the Aegir Ridge decreased until it became extinct and the spreading axis migrated westwards to initiate the Kolbeinsey Ridge, which is still active today (Jung and Vogt 1997; Lundin and Doré 2002; Mosar et al. 2002). The opening at the new spreading axis along the Kolbeinsey Ridge resulted in the separation of the Jan Mayen microcontinent (Scott et al., 2005) (Fig. 9.1). Vogt et al. (1980) showed that the first Kolbeinsey Ridge anomalies are readily identifiable out to 6B, thus refuting an intermediate spreading axis between C7-C5, still proposed few years later in the PhD work of Unternehr (1982). Referring to the geomagnetic time scale of Cande and Kent (1995), the end of spreading along the Aegir Ridge occurred after magnetic chron C13n (33.5-33.0 Ma) (Jung and Vogt 1997; Unternehr 1982; Breivik et al. 2006). The Deep Sea Drilling Project (DSDP) site 337, located in the southeastern flank of the Aegir Ridge (Fig. 9.4) recovered tholeitic basalt basement from 17.5 to 25.5 overlaid by mid-Oligocene to Late Eocene (Talwani et al. 1976). Assuming an age of 29 Ma of the youngest fossils and a spreading rate of 5-8 mm/years, Talwani et al. (1976) concluded that the spreading in the Norway Basin ended 25-27 Ma ago,

which agrees with chrons C7-C8. Nevertheless, the C7 anomaly has so far never been clearly identified.

Jung and Vogt (1997) also observed a systematic asymmetry of both topography and bathymetry across the extinct Aegir Ridge but also Kolbeinsy, Mohns and Knipovich Ridges. Vogt (1986) initially proposed that the asymmetry may be the result of a relative faster motion of the North American plate (20mm/year) over the mantle compared with a nearly stationary Eurasian plate. However, Jung and Vogt (1997) show that the regional asymmetry does not prevail throughout the entire Aegir Ridge and that the asymmetry could be examined following flow lines direction since earlier interpretations only considered sea floor spreading direction. Jung and Vogt (1997) re-examined the structure of the Aegir Ridge by use of a more recent survey and show that the Aegir Ridge valley deepens southwards and that the previous apparent asymmetry described by Vogt (1986) does not exist. By means of the NRL-90 survey; they also identified magnetic chrons between C21(47.9-46.2 Ma) and C13 (33.5-33.0 Ma) and concluded that chrons between C12 (30.9-30.4 Ma) and C7 (24.78-24.73) cannot be resolved due to ultra – slow spreading.

### **9.3 Refined magnetic chron interpretation, structure and spreading history of the Norway Basin**

#### **9.3.1 Potential field data**

Despite the non-uniqueness of gravity and magnetic data interpretation, the seismic and potential field data are complementary and should be integrated. Despite limitations, potential field data provide a relatively inexpensive method to quickly assess large regions, especially in areas where conventional seismic data are sparse. In the oceanic domain, magnetic data allow a 4D mapping of the spreading system since each anomaly (magnetic chron) can refer to the chronostratigraphic time scale of Cande and Kent (1995) (Fig. 9.2). To get specific information about the lateral and depth extent of specific bodies, manipulation of gravity and magnetic grids was necessary using filtering techniques as described in the previous chapters. By applying and/or combining simple or more advanced filters, shallow features with shorter wavelengths can be separated from deeper, longer wavelengths geology. Furthermore, wavelengths for shallow and deeper geological features overlap, which leads to the non-uniqueness of the interpretations. Assuming reasonable geological geometries in the forward modelling, we can better understand the structure and nature of the Norway Basin and surrounding volcanic margins.

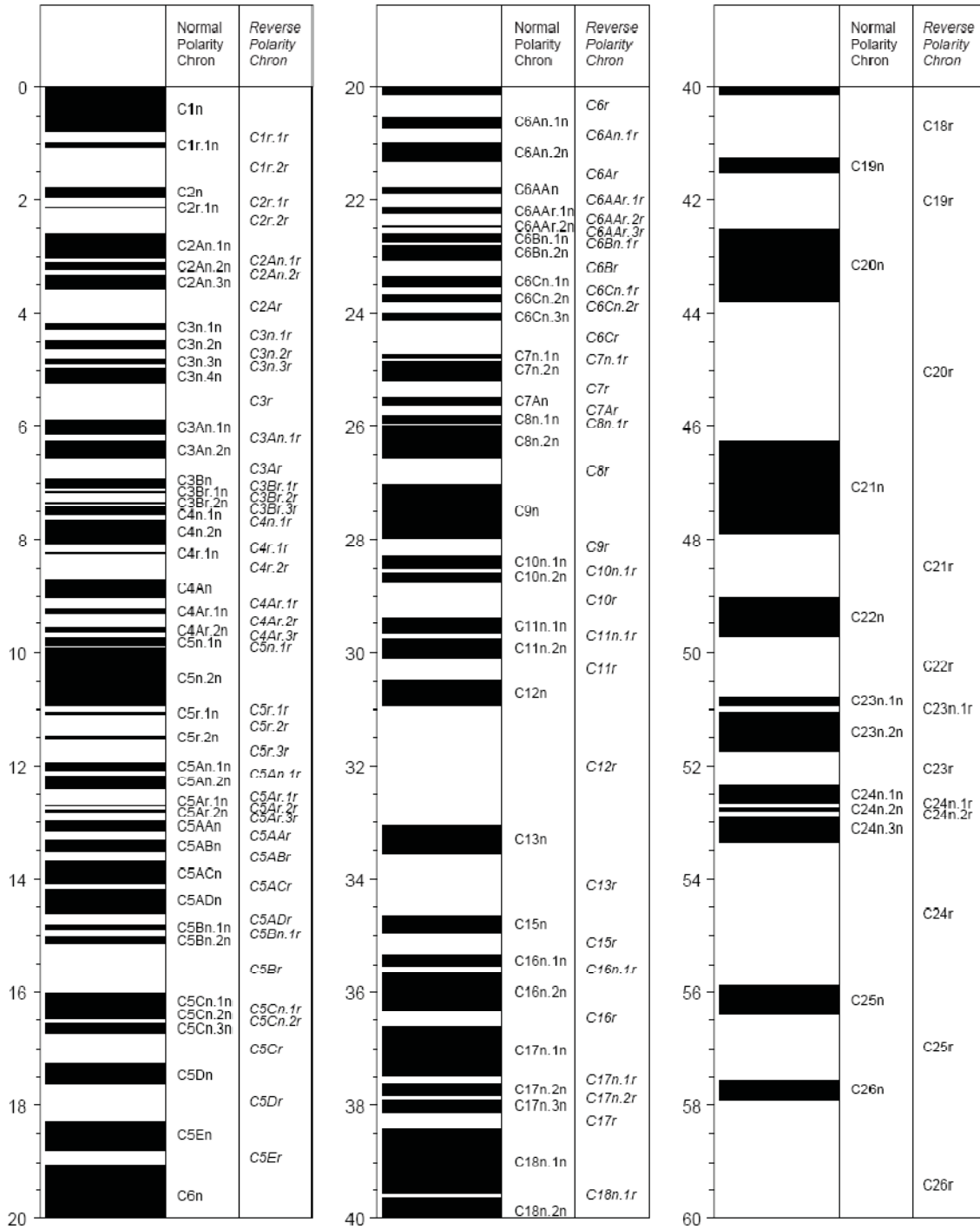


Figure 9.2 Revised calibration of the geomagnetic polarity time scale for the Late Cretaceous and Cenozoic after Cande and Kent (1995). This chart provides the correlation between the magnetic chronos locally identified in the Norway Basin and their absolute ages in Ma.

### 9.3.2 Methodology

The magnetic data along the NB-07 were studied to infer the nature and age of the crust and the seafloor spreading evolution. We have used the new aeromagnetic survey to re-interpret the position, age of magnetic chrons and seafloor spreading history, west of the Møre Marginal High and north of the Faroes Plateau (Figs. 9.3 to 9.14).

The new total field magnetic grid contains signals with a wide range of amplitudes, reflecting the varying depth, geometry and susceptibility contrasts of sources. The TDX normalised filtering technique (Cooper and Cowan 2006) was particularly used in this study to identify magnetic reversal sequences (Fig. 9.4). The problem to be overcome in data enhancement using the TDX filter was to identify and map subtle anomalies attenuated in the dynamic range due to the presence of high amplitude magnetic anomalies, the continuity of individual bodies and the edge of structures (e.g chapter 5). Combined and blended with the original grid and/or the plot profiles, the filtered grid has been used to better highlight and pick the inflection points on both edges of the anomalies (Figs. 9.4, 9.8). For the mapping, we do not consider any reduction to the pole (RTP) for simplicity and for a better correlation with surrounding regional surveys and previous interpretations (Fig. 9.3). We also extracted automatically strike and dip of each anomaly to help our interpretation (Fig. 9.4). The interpretation of the Aegir Ridge NRL-90 magnetic survey by Jung and Vogt, (1997) and our previous re-interpretation of the JAS-05 (Olesen et al. 2006; Gernigon et al. 2008) have been considered as the most recent and reliable guides to reassess the chrons interpretation on the Norway Basin.

The interpretation of the magnetic chrons has been correlated with synthetic profiles calculated using a forward modelling Matlab routine (Mendel et al. 2005) assuming a constant spreading direction (Fig. 9.5). The Matlab routine offers the user the possibility to model a more realistic and progressive transition zone between two inversely magnetized blocks. This method initially developed by Tisseau and Patriat (1981) consists in performing the forward modelling with a fictitious spreading rate, initially estimated from the TDX anomalies. Different spreading parameters and a geomagnetic reversal time scale of Cande and Kent (1995) were used to calculate the position and width of magnetised parallelepipeds corresponding to each successive epoch of normal and reversed polarity of the Earth's magnetic field. The synthetic models assume that the magnetized bodies are placed at a constant depth of 4 km without correction for sediment thickness. The thickness of the magnetic layer was set to 2 km and the magnetization of the magnetic source is predominantly of remanent origin with a constant magnetization of  $\pm 2$  A/m. Contamination is also simulated by narrowing the blocks before the computation of the magnetic anomaly profiles. This method is often used to model magnetic anomaly profiles across slow-spreading ridges and provides a first way to calibrate and test the validity of the magnetic chrons interpretation.







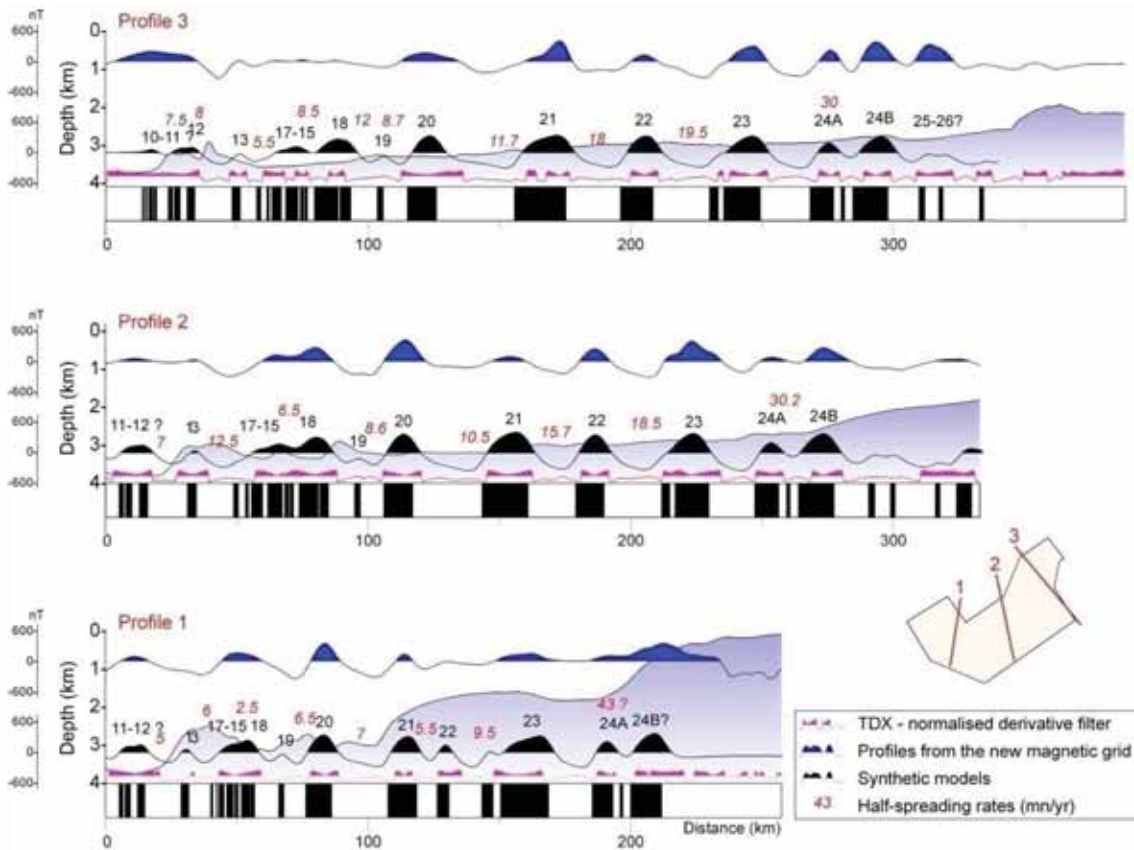


Figure 9.5 Interpretation of the magnetic chrons deduced and correlated with synthetic profiles.

### 9.3.3 Description of the magnetic pattern of the NB-07 survey and chron interpretation

The magnetic anomalies currently observed along the NB-07 reflect the different structure, composition and geodynamic history of the oceanic crust of the Norway Basin and surrounding margins. Several magnetic domains with different magnetic pattern can be observed along the new NB-07 survey. The intermediate wavelength anomalies (10-50 km) result mostly from seafloor spreading modulated by the effects of basement topography, local seamounts, fracture zones and other oceanic spreading discontinuities. This sub-section will be discussed later in the context of plate tectonic evolution. The following set of interpretation maps (Figs. 9.6 to 9.14) illustrates our interpretation of the new survey combining different filtering techniques of both magnetic and gravity data.



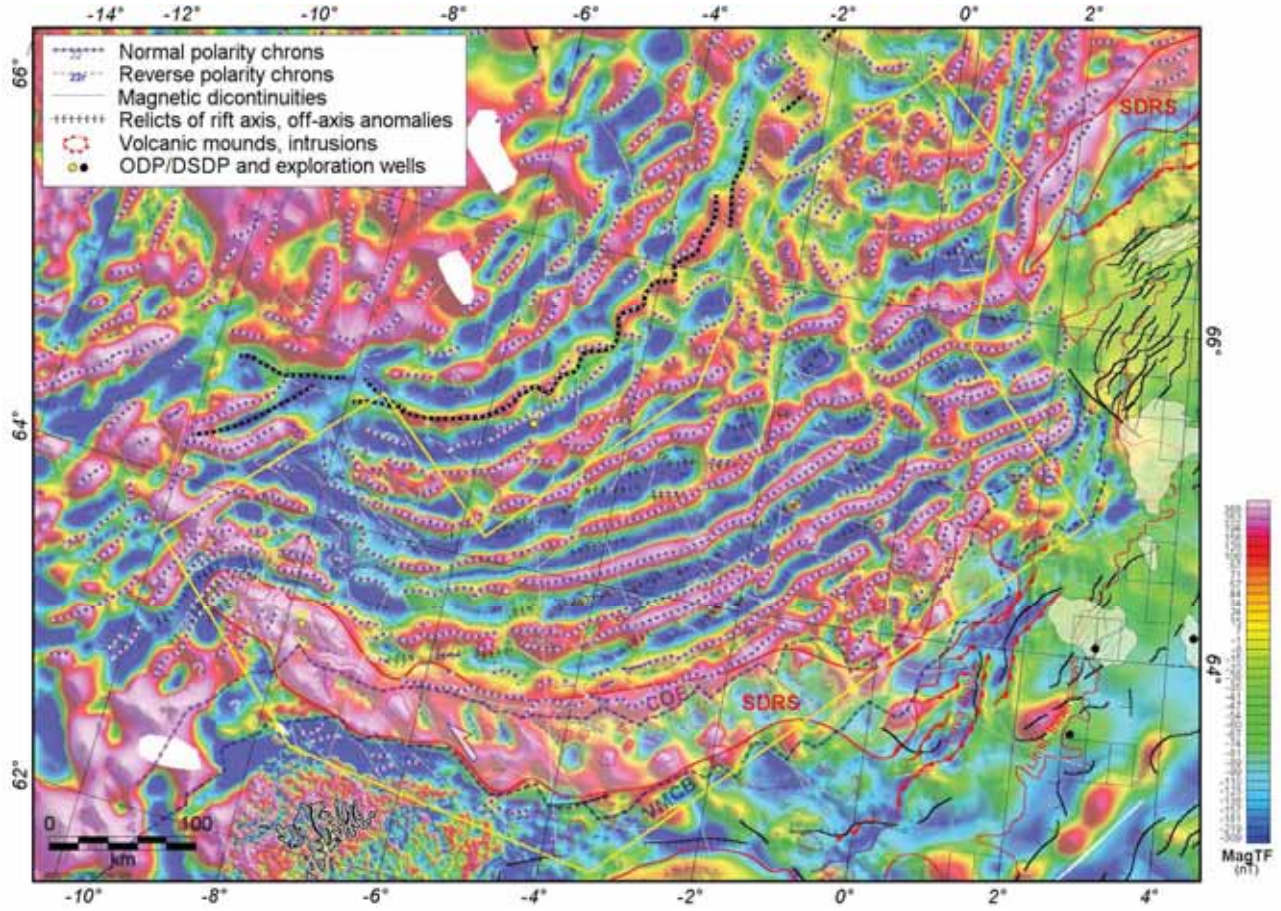


Figure 9.7 Magnetic total field overlain by the identified and interpreted magnetic chrons (C24 to C13), the magnetic discontinuities and a tentative COB (Continent-Ocean Boundary) and VMCB (Volcanic Margin-Continent Boundary) interpretation.



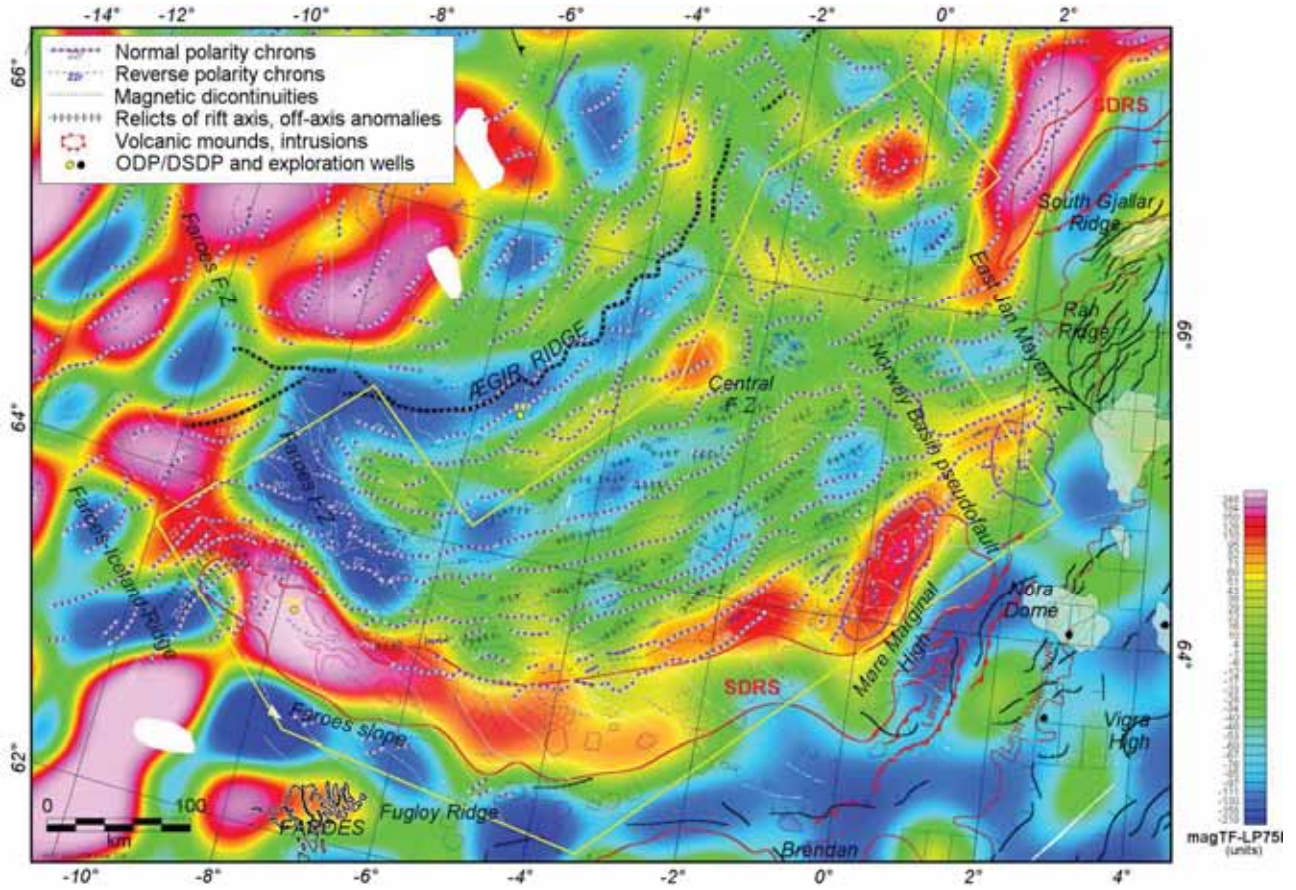


Figure 9.9 Low-pass filter of the magnetic total field grid (75 km) overlain by the identified and interpreted magnetic chrons and magnetic discontinuities. This map illustrates the regional segmentation of the magnetic field pattern which coincides with different oceanic domains.

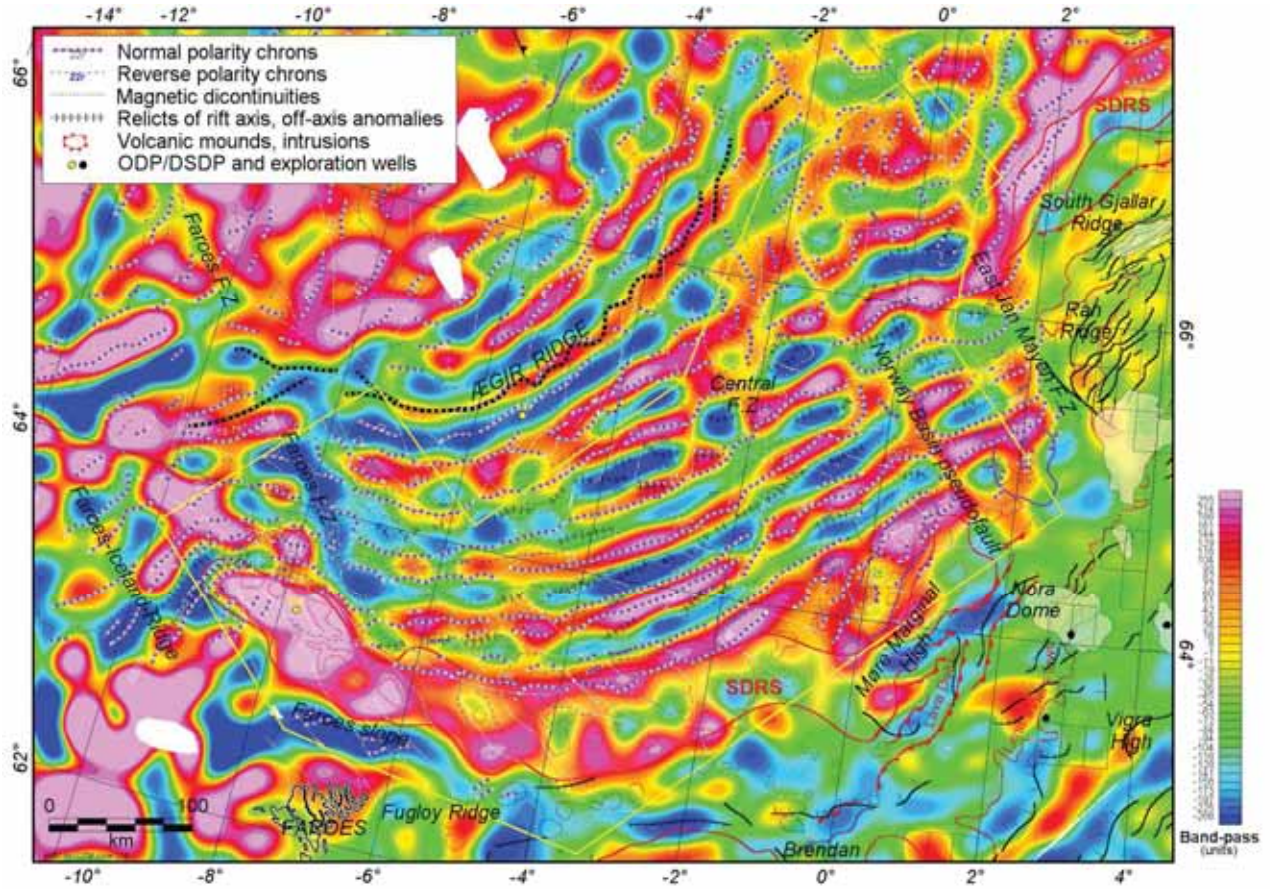


Figure 9.10 Band-pass filtering of the magnetic total field grid (long wavenumbers cutoff of 0 to 0.03 1/k-unit) overlain by the identified and interpreted magnetic chrons and magnetic discontinuities. This map illustrates the main oceanic anomalies and highlights the trends of the first and second order regional discontinuities observed in the Norway Basin.





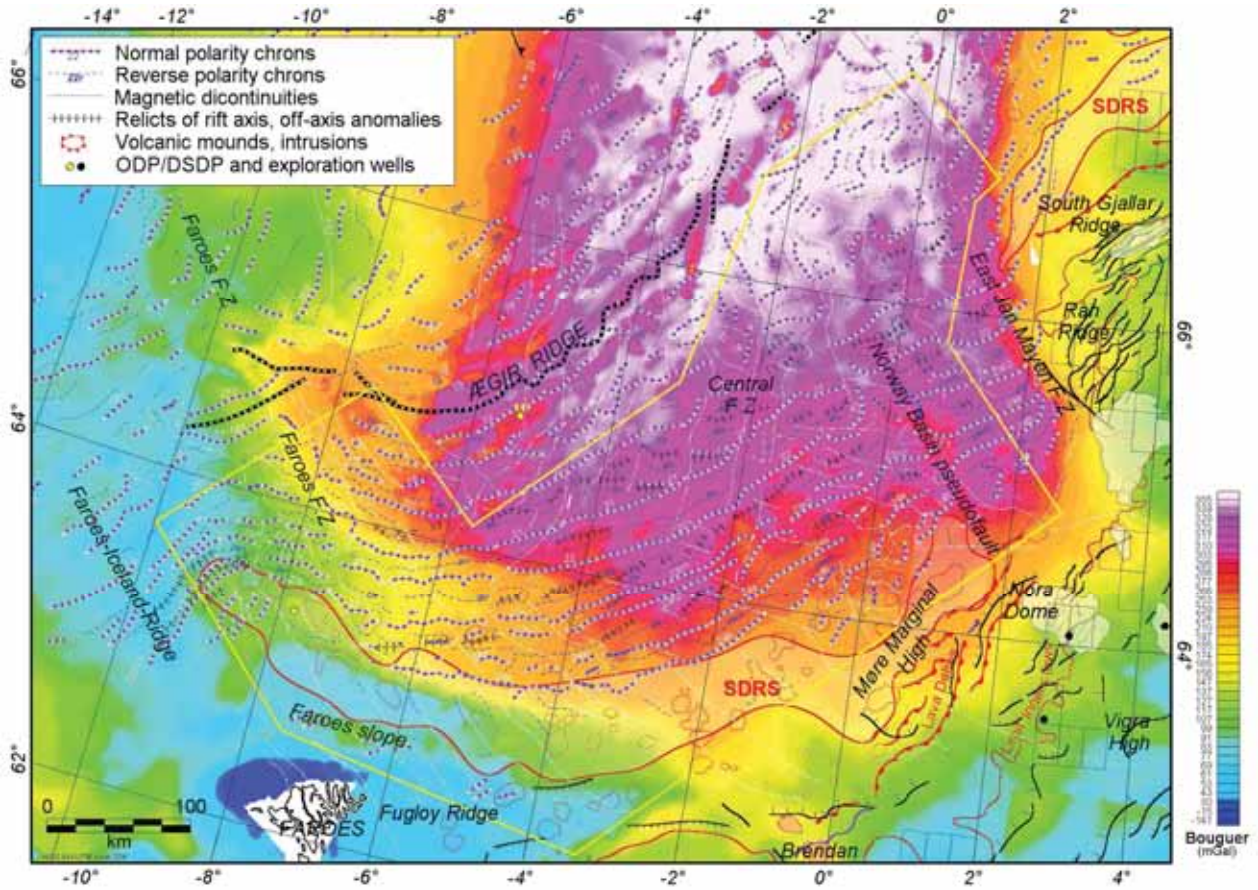


Figure 9.12 Map of gridded Bouguer gravity anomalies (reduction 2200 kg.m<sup>-3</sup>) overlain with the identified and interpreted magnetic chrons and magnetic discontinuities.

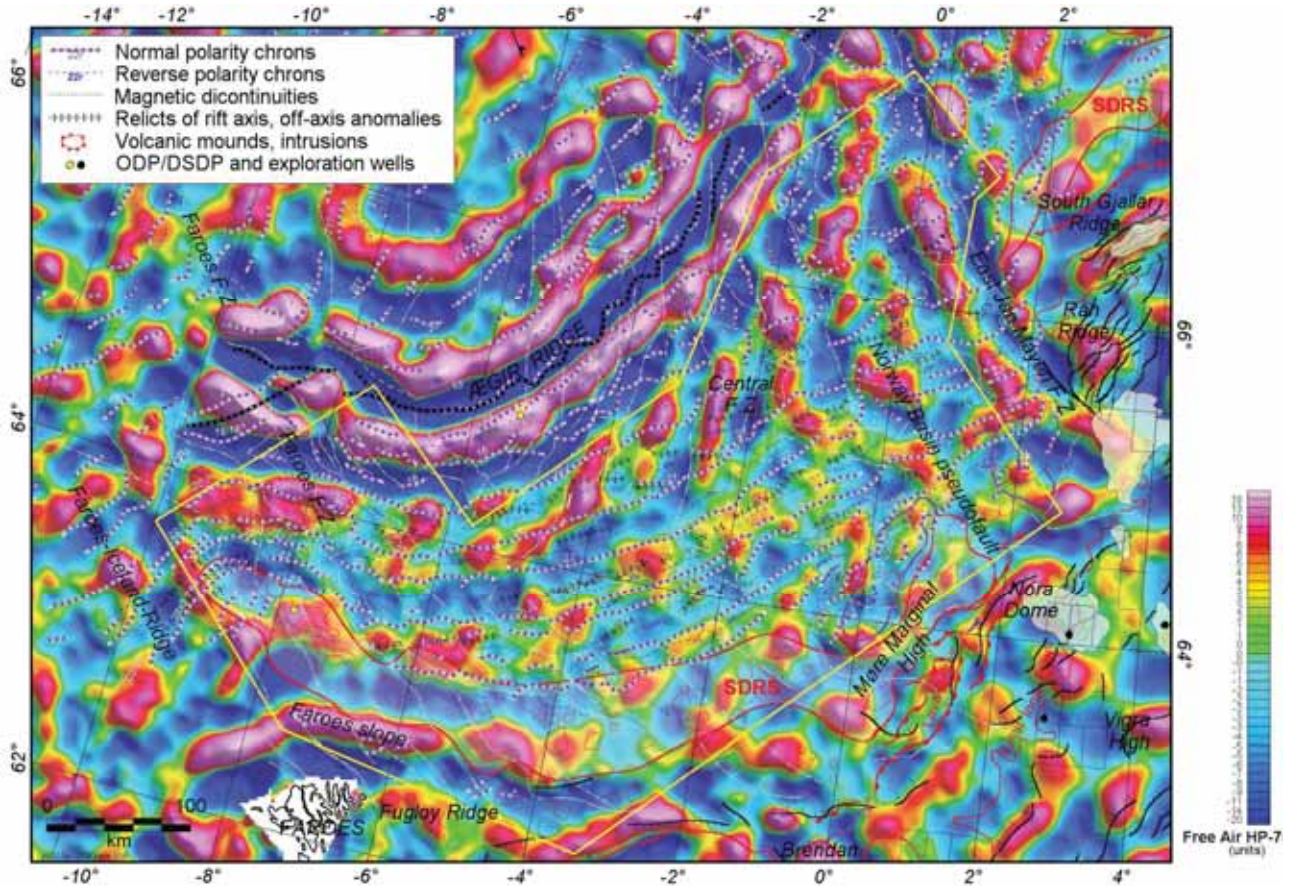


Figure 9.13 High-pass filtering of the Free-Air anomalies (75 km) overlain by the identified and interpreted magnetic chrons and magnetic discontinuities.

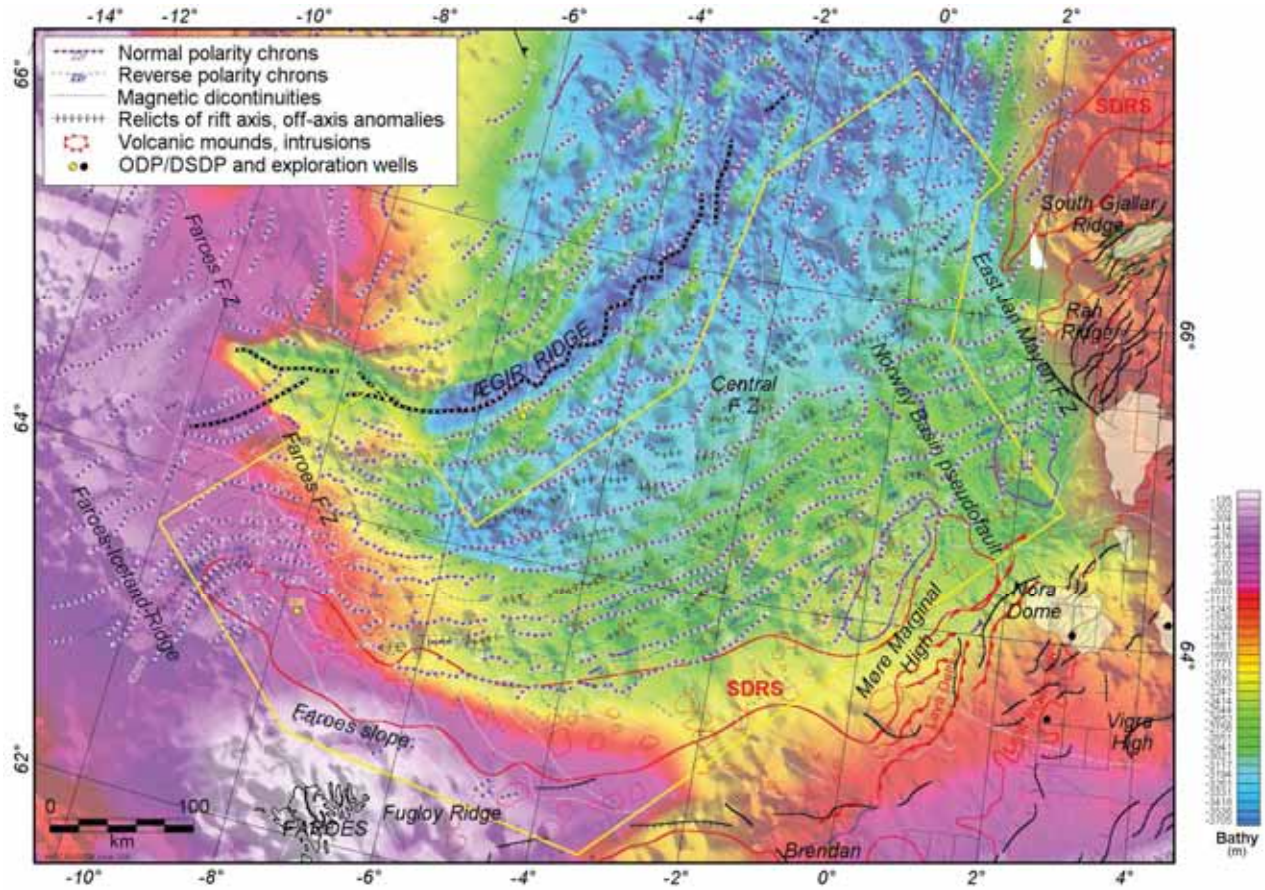


Figure 9.14 Map of the regional Bathymetry overlain by the identified and interpreted magnetic chrons and magnetic discontinuities.

### Domain 1: The Continental-Ocean Transition (COT) of the Møre volcanic margin.

This domain represents the Continent-Ocean Transition (COT) of the Møre volcanic margin between the Møre Marginal High and the magnetic anomalies C24 (Fig. 9.7).

By definition our terminology of COT characterizes a region on the Møre margin that lies between the outboard edge of highly attenuated, unequivocal continental crust and the inboard edge of unequivocal oceanic crust. The COT could include both sedimentary, volcano-clastics and magmatic components in proportions that vary both along and across the margin. It may include areas of failed spreading cells. The Continent–Ocean Boundary (COB) is defined as the inboard edge of unequivocal oceanic crust and corresponds to the change from ‘transitional continental crust’ to ‘transitional igneous crust’ in the scheme of Direen et al. (2008). Mapping a proper COB in detail along the Møre volcanic margin is complex. This arises because it can be difficult to distinguish the transition from heavily intruded continental crust to fully oceanic crust on such a margin. It is, nevertheless, useful to define a line that approximates to this boundary and this has been done using the geophysical features defined by the new survey and other geophysical datasets. Direen et al. (2008) also introduce the terminology of Volcanic Margin-Continental Boundary (VMCB) to specify the outboard edge of unequivocal continental crust (Fig. 9.7). These abbreviations (COT, COB, VMCB) will be used in the following part of the report.

Along Domain 1, the magnetic pattern of the COT is relatively chaotic with magnetic clusters arranged in alternating positive and negative patterns (Figs. 9.7, 9.8). East of the COT, linear and curved anomalies coincide with different basaltic and magmatic boundaries, including buried strato-volcanoes, dike swarms and prograding lava deltas (Fig. 9.15). Some of the magnetic cluster coincide with the Outer High features described by Berndt et al. (2001) and interpreted as mounds of volcanoclastics and hyaloclastic material emplaced near sea level (Planke et al., 2001). Small round-shaped anomalies 10-20 km wide can be observed and may represent local intrusions, volcanic plugs or volcanic mounds (Figs. 9.16, 9.17, 9.18). High-amplitude, high-frequency anomalies are usually characteristic of shallow igneous intrusions and correlation with circular gravity high likely reflect mid to upper crustal magmatic intrusions. North of 63°N, seismic data show that the chaotic magnetic domain locally coincides with seamounts probably emplaced in a shallow marine or sub-aerial setting as suggested by the lava deltas observed (Fig. 9.15). Along the COT, volcanic, basic, gabbroic intrusions encountered in flood basalt provinces have been interpreted and commonly exhibit a strong gravity and magnetic signal due to their high density and magnetic minerals content.

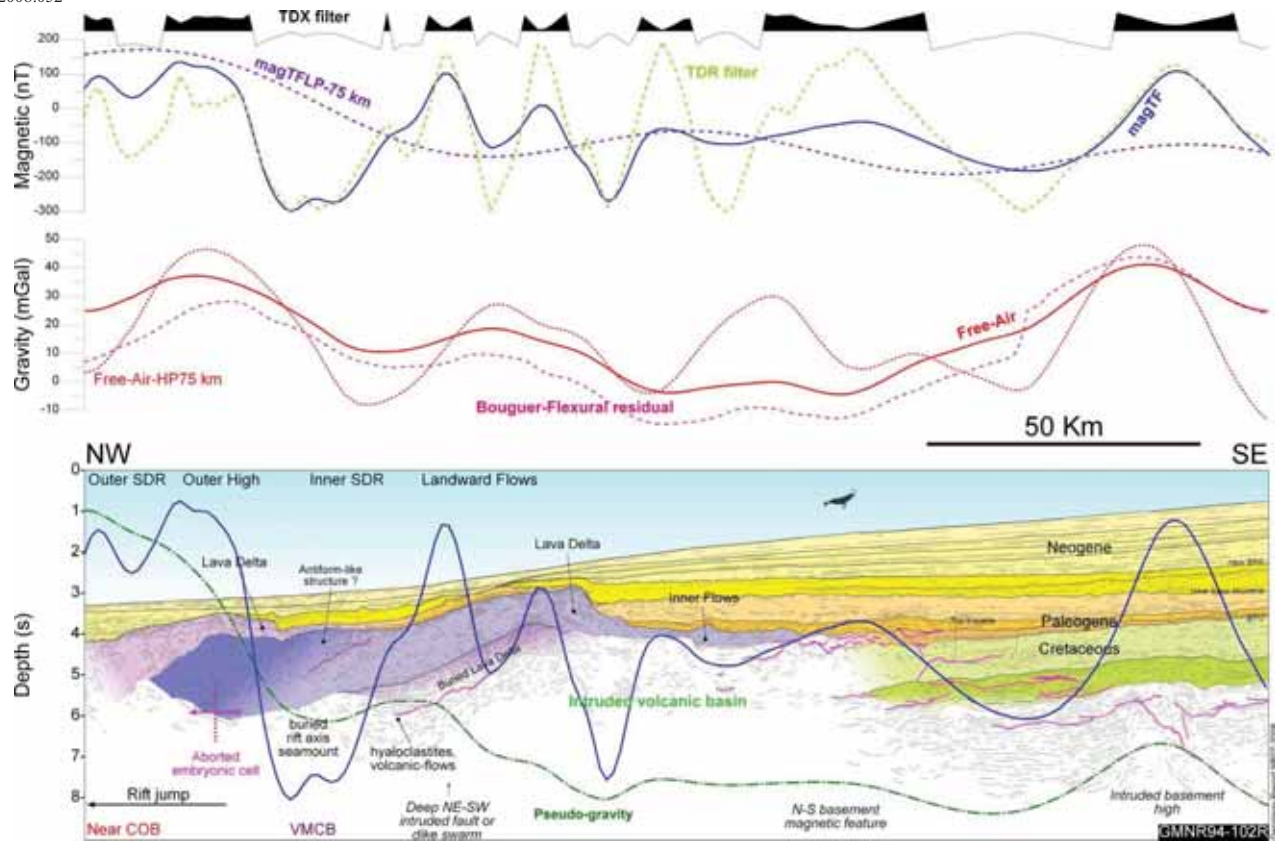


Figure 9.15 Interpretation of the main volcanic facies observed along the GMNR94-102R. The section also shows the gravity and magnetic signature observed along the volcanic margin. Volcano-stratigraphic monenclature after Planke et al. ( 2001).

In the western part of Domain 1, linear and more significant anomalies develop and represent anomalies C24b and C24a (Hagevang et al. 1983; Skogseid and Eldholm 1987) (Fig. 9.5, 9.6, 9.7, 9.8). Sub-chrons C24a and C24b almost coincide with C24n.1n (52.6-52.3 Ma) and C24n.3n (53.3-52.9 Ma) in the geomagnetic polarity time scale of Cande and Kent (1995). A nominal and “ultimate” COB has, therefore, been drawn at the level of C24r and marks the inboard edge of unequivocal oceanic crust, when the magnetic signature seem to be fully driven by oceanic spreading processes (Fig. 9.7). The COB is mostly located near the outer part of the SDRs package, which often correlates with a marginal positive magnetic anomaly. C24b and C24r represent the first evidence of continuous to semi-continuous positive anomalies observed along the survey. Clearly the resolution is limited and the complexity of the geophysical anomaly pattern (e.g. across the Faroes–Iceland Ridge) and limitations in data coverage to the south make such an interpretation difficult.

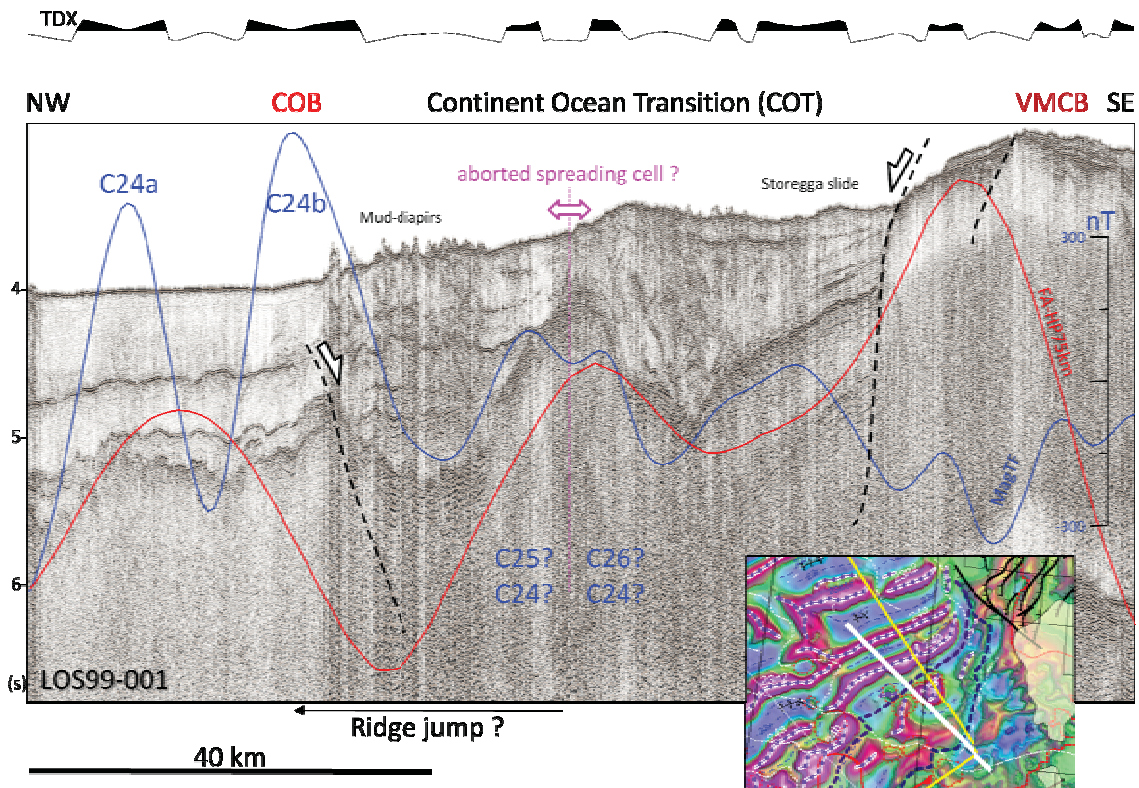


Figure 9.16 Seismic observation along the COT near the Jan Mayen transform margin. The red curve represents the Free-air gravity anomalies after high-pass filtering at 75 km.

South of the JMFZ and east of the C24b, double anomalies observed along the COT on the VBEAM -00 Survey of TGS-Nopec have been previously interpreted as possible C25-C26 early spreading anomalies by Gernigon (2002) due to a typical magnetic pattern. However, the new survey shows that these anomalies do not extend far the south and do not constitute apparent evidences for a continuous spreading system prior to C24r. However, it could correspond to an isolated and embryonic spreading cell initiated at C25-26 or an aborted ridge

initiated at C24 (Fig. 9.16). On seismics, these two anomalies represent a mound south of Jan Mayen Transform Margin in the central part of a graben feature that developed along the COT.

East of C24r, no clear linear anomalies have been observed but dominant positive anomalies can be observed and can be interpreted as intrusions, volcanic plugs or aborted spreading cells, initiated from C26n to C24n. A band-pass filtering of the magnetic total field suggests that positive cluster alignments developed parallel to the C24 anomalies in the outboard part of the COT (Fig. 9.10). The eastern flank of these ambiguous but not-so disorganized anomalies has been considered as the potential VMCB. A 50 km wide segmentation of the long wavelengths segments from North to south can also be observed and different magnetic clusters seems to be separated by discrete E-W to NW-SE lineaments, which could indicate a lateral segmentation of the Inner SDRs and Outer High features (Figs. 9.9, 9.10).

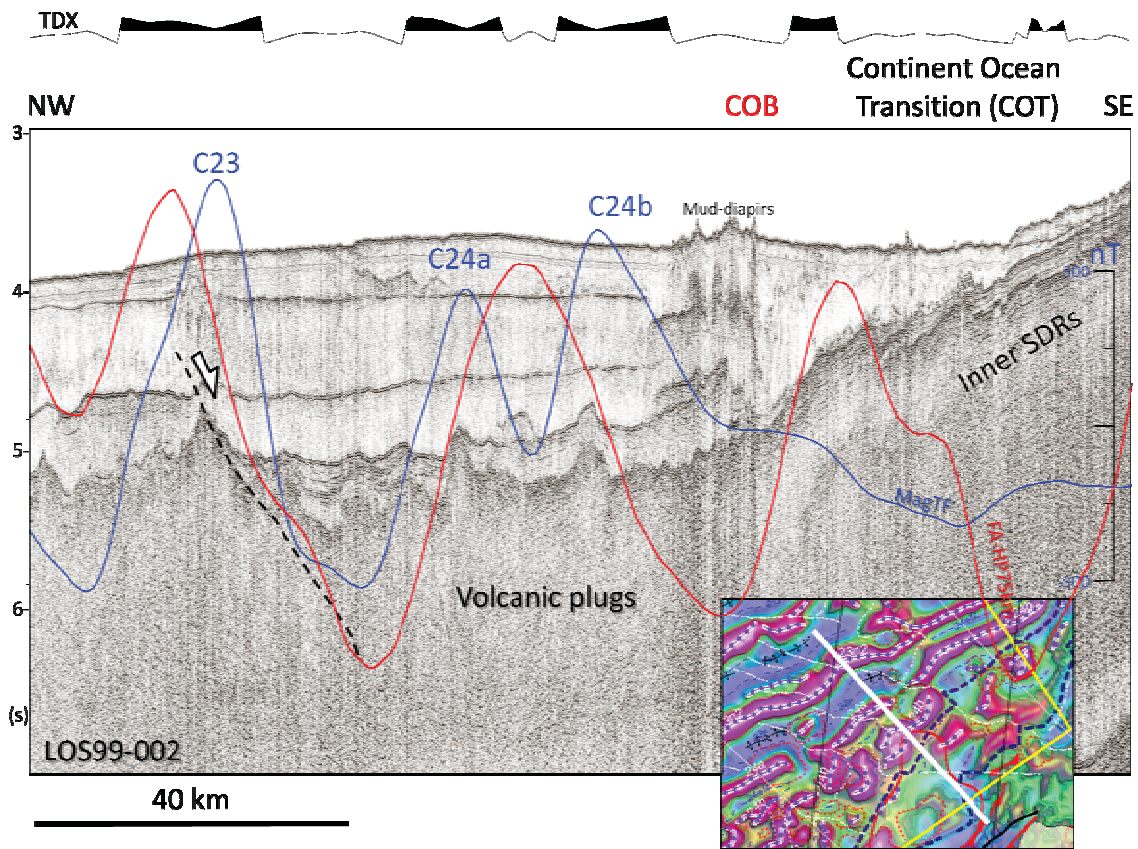


Figure 9.17 Seismic observation along the COT south of the Norway Basin pseudofault. Note that the COB often coincides with fluid escape and mud diapirs. The COB is interpreted east of the C24b anomaly, on the outer edge of the Inner SDRs.

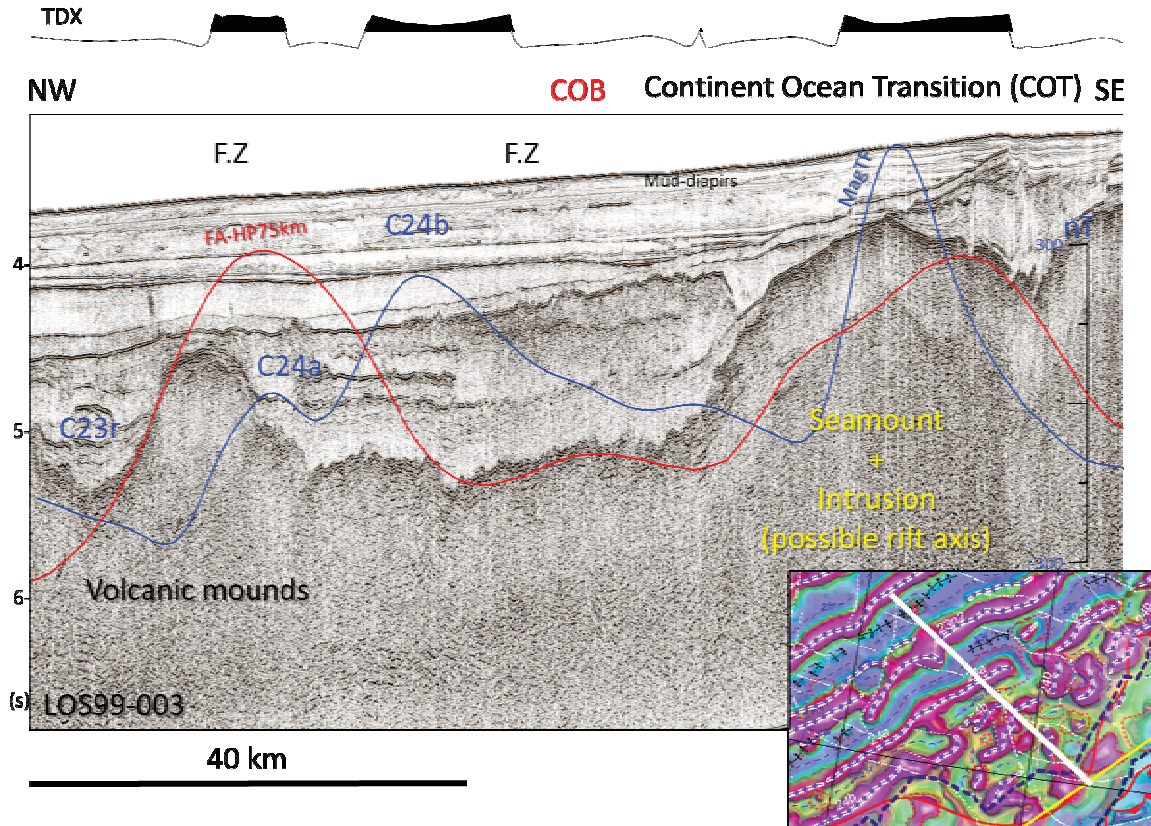


Figure 9.18 Seismic example of large volcanic mounts along COB, west of the Møre Marginal High. Some of the largest seamounts fit with gravity highs and could represent aborted spreading cells emplaced along the proto-breakup axis.

Domain 2: the Møre-Faroes volcanic shear margin

Southwest of the Domain 1, Domain 2 represents the transition between the Møre volcanic margin (Fig. 9.4). This transition is interpreted as a complex volcanic shear margin that developed north of the Faroes Plateau. The transition between Domain 1 and 2 coincides with a progressive shift (~50 km) of the Inner SDRs to the west, south of line GMNR94-102R line and shows a different magnetic pattern (e.g. Berndt et al. 2001a). Magnetic circular patterns similar to those described in Domain 1 can be observed in Domain 2 but locally the prominent magnetic anomalies become more linear to the southwest (Fig. 9.19). They probably represent intrusions emplaced along shear zones.

The interpretation shown in Figure 9.19 indicates minor local offsets in the COB. Between 4°E and 5°E, a NW-SE fault zone coincides with a major 50 km clockwise displacement of the magnetic units. Similar NW-SE faults can be observed and could explain the lozangic and sigmoidal magnetic pattern of the dominantly magnetic anomalies observed directly north of



the magnetic low area. The lozangic magnetic pattern could represent a transtensional fault pattern including strike-slip faults injected by mafic intrusions arranged along the slope.

North of the Faroes islands, the slope of the continental margin mostly coincides with a low NE-SW magnetic ribbon area and contrasts significantly with the adjacent lozangic pattern dominated by positive higher amplitudes. Inside the magnetic low, high-frequency anomalies interpreted as dike swarms and/or lava contacts can be observed. The VMCB is defined at this level (Fig. 9.19).

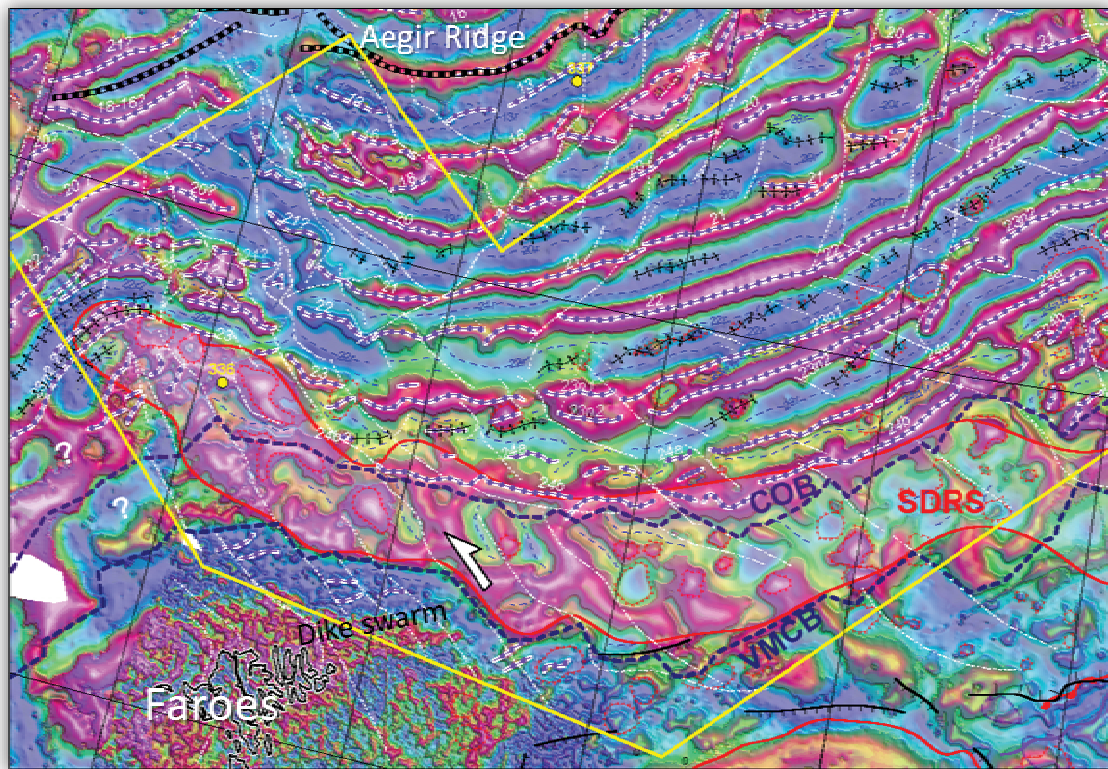


Figure 9.19 Zoom along the domain 2, which characterise the Faroe volcanic shear margin and the complex and unclear transition between the Norway Basin and the the Faroes-Iceland Ridge

A 484.5-m sedimentary section was discontinuously cored to basement at DSDP Site 336 (water depth, 811.0 m) on the northern flank of the Faroes-Iceland Ridge (Fig. 9.19). DSDP Site 336 is located in the northern part of Domain 2 and tied in basaltic rocks dated to Late-Mid-Eocene by Talwani et al. (1978). Radiometric ages vary between 40.4 and 43.4 Ma and the oldest sediments overlying the basement are at least as old as Late Eocene (Talwani et al. 1978). Goll (1989) re-evaluated the ages of the lower sedimentary sequences and propose an age of 43-47 Ma for the oldest sediment above the basalts. However, these ages are slightly younger than magnetic chrons C21r (49.0-47.9 Ma) but do not really fit with our magnetic chron interpretation because the C21 is located 50-70 to the north. These ages are problematic

in light of the new survey. We believe that the basaltic layer drilled by the DSDP well 336 could eventually represent late basaltic flows and not necessarily the original oceanic basement.

### Domain 3: Early oceanic spreading from C24 to C22

West of C24, oceanic anomalies have a regular and general pattern, formed by alternating positive and negative bands, whose width is in the order of tens of kilometers and whose length can reach 1 000 km (Figs. 9.6, 9.7, 9.8). The spread in amplitudes is due to a number of factors, but mostly involving the spreading rates between strips of alternative polarity and the depths level of the top oceanic basement. The amplitude of the anomalies, in the order of -400-500 nT, and their high gradients, indicate that the source bodies are close to the surface. The two main effects are illustrated by the synthetic models calculated in figure 9.5. Such simple assumption can generally account for much of the amplitude and strip geometries in the Norway Basin. Long wavelength component may also suggest relative (but still unclear) contributions of the mid and lower oceanic crust and possibly the upper mantle.

The magnetic anomalies between C24a/C24b (53.3-52.9 Ma) and C20 (43.7-42.5) are particularly well developed and contrast with the COT. The linear pattern highlighted by the NB-07 suggests a different and more homogeneous dynamic. The magnetic pattern development is a result of a relatively fast spreading rate coupled with infrequent reversals. Anomalies C23n2n (51.7-51.0 Ma), C23n1n (50.9-50.7 Ma), C22n (49.7-49.0 Ma), C21n (47.9-46.2), C20n (43.7-42.5 Ma) and their reversals have been easily identified in most of the survey area (Figs. 9.2, 9.20).

In the southwestern part of the NB-07 survey, the connection with the magnetic trends observed along the Faroes-Iceland Ridge is however more uncertain (Figs. 9.6, 9.7, 9.8, 9.20). Although there are broad lineations that are NE-SE oriented, perhaps correlative with average magnetization polarity, proper identification of the magnetic chrons is still unclear probably because of late volcanic and intrusive activities distributed over a broad swath (as on Iceland) rather than being confined to a narrow accretion axis. Faulting on the northern flank of the Faroes-Iceland Ridge and possible discrete ridge jumps (Smallwood and White 2002) do not allow a one to one correlation with the chrons interpreted in the Norway Basin. Furthermore, the poor quality of the vintage magnetic data outside the new survey (South Jan Mayen, southern part of the Faroes-Iceland Ridge) do not always allowed us to favour a reliable interpretation of this domain.

Anomalies C24A and C24B are usually well developed in the central part of the Norway Basin and form a clear pair, south of the Jan Mayen transform margin. To the south, C24A and C24B seem to merge and cannot be dissociated. Spreading rates from C24a to C24b vary between  $39.5 \pm 2$  to  $16.2 \pm 2$  mn/yr and decrease from the central part of the survey both towards northeast and southwest (Fig. 9.20).

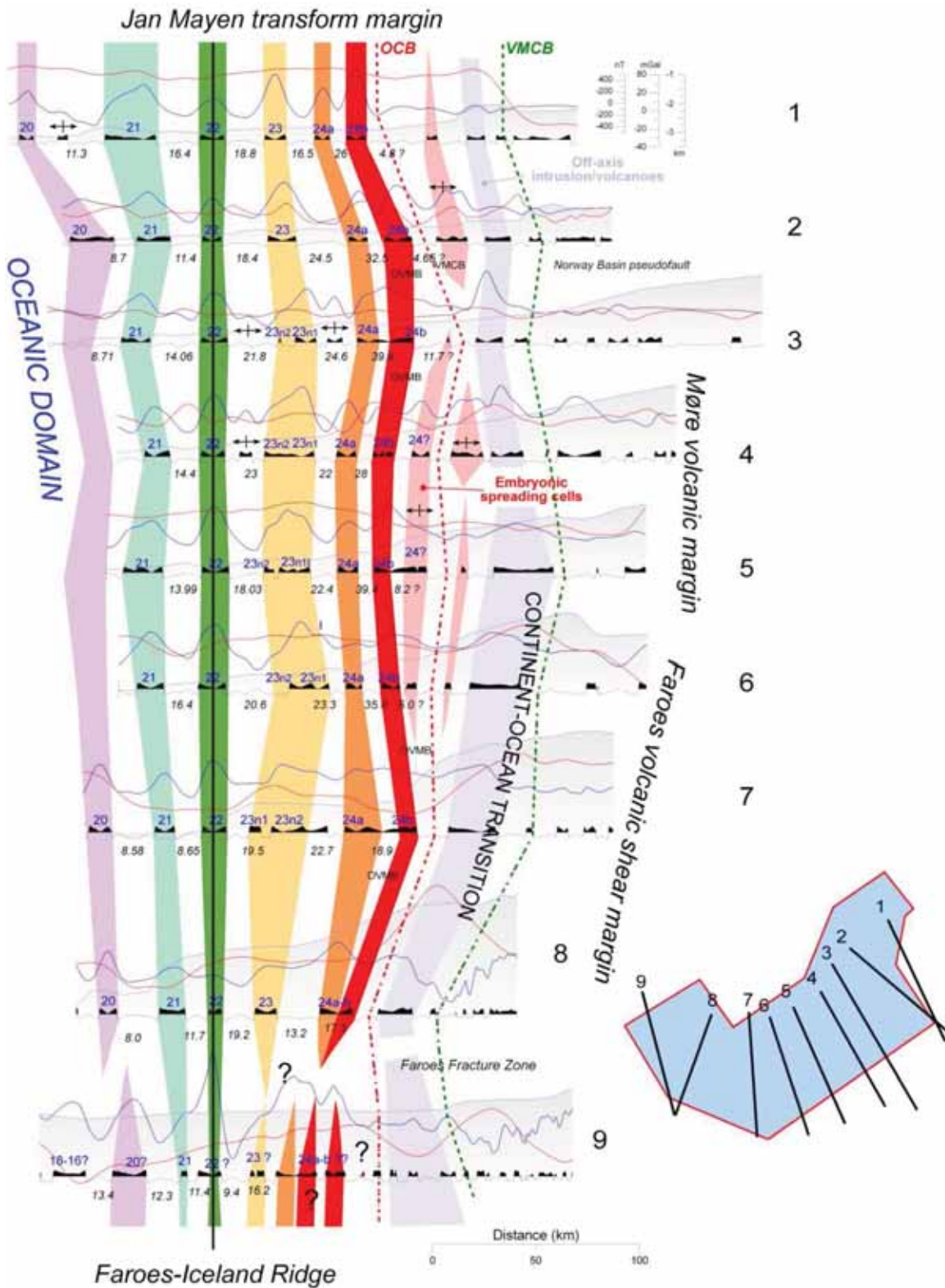


Figure 9.20 Bathymetric, gravity and magnetic transects across the COT and the early spreading system of the Norway Basin. Blues labels indicate the magnetic chrons and black labels the spreading rates in mm/year.

Anomaly C23 locally splits into two sub-chron Anomalies C23n2n and C23n1n which are well identified on the NB-07. The anomalies are more or less continuous and form continuous and lateral 50 to 150 km long segments in the central part of the basin. Near the Jan Mayen transform margin and north of the Faroes-Island Ridge the segments are smaller and 10 to 50 km long. Between C24a and C23, the half-spreading rates decrease from  $24.6 \pm 2$  to  $9.4 \pm 2$  mm/year but still decrease from the central part of the survey toward the northeast and southwest.

Anomalies C23 overlap sometimes and/or are displaced by minor discontinuities involving small non-rigid transform faults. Such offsets do not exceed 50 km and are less than 5-10 km in average. Both normal and reverse strips around C23 are also affected by circular anomalies of opposite polarities in the central part of the NB-07 survey (Figs. 9.6, 9.7, 9.8, 9.20, 9.21). From C23 to C22, the spreading rates are quite similar with values between  $23 \pm 2$  to  $11.4 \pm 2$  mm/year and also decrease from the central part towards the northeast and southwest (Fig. 9.20).

Some positive and circular anomalies have been observed and concentrate along the negative strip C23r between C24a and C23n2n and along C22r between and C23n1n and C22n (Figs. 9.20, 9.21). Negative round anomalies also affect the positive chrons C23n1n and C23n2. These round-shaped and atypical anomalies can be observed from C23r to C22r (~52.3 to 47.9 Ma) and can locally be interpreted as off-axis seamounts, emplaced along the trend of minor fractures zones. Between C23n1 and C22, subtle anomalies in the central part of the C22r and C23r could eventually represent some isolated and aborted spreading cells or some ridge tips initially being part of overlapping spreading centres (Figs. 9.6, 9.7, 9.8, 9.21).

The last process was described in detail by Macdonald et al. (1987) when true faults between slightly displaced oceanic ridge segments fail to develop because the lithosphere is too thin (hot) and weak. They show that the propagation of two spreading centres along strike can often overlap and curve towards each other, encircling a zone of shear and rotational deformation leading to the formation of overlapping spreading centres. Progressive shear and rotational deformation could continue until one overlapping spreading centres links with the other. As continuous spreading is established, the “decapitated” ridge tip is abandoned and the overlap zone rafts away.

C22n and C20n are also clear anomalies, characterised by a broad magnetic low at C21r (49.03-47.9 Ma) and C20r (46.2-43.7 Ma). C22n, C21 and C20 have been easily mapped from the EJMfZ to the Faroes-Iceland Ridge (Figs. 9.6, 9.7, 9.8). C22 appears to be more continuous and less segmented compared to the older C23 and C24 chrons. C22 is wider in the central part of the Norway Basin and thins towards the south and along the Jan Mayen transform margin. Inversely, C21n and C20n are wider close to the East JMFZ and thin to the south.

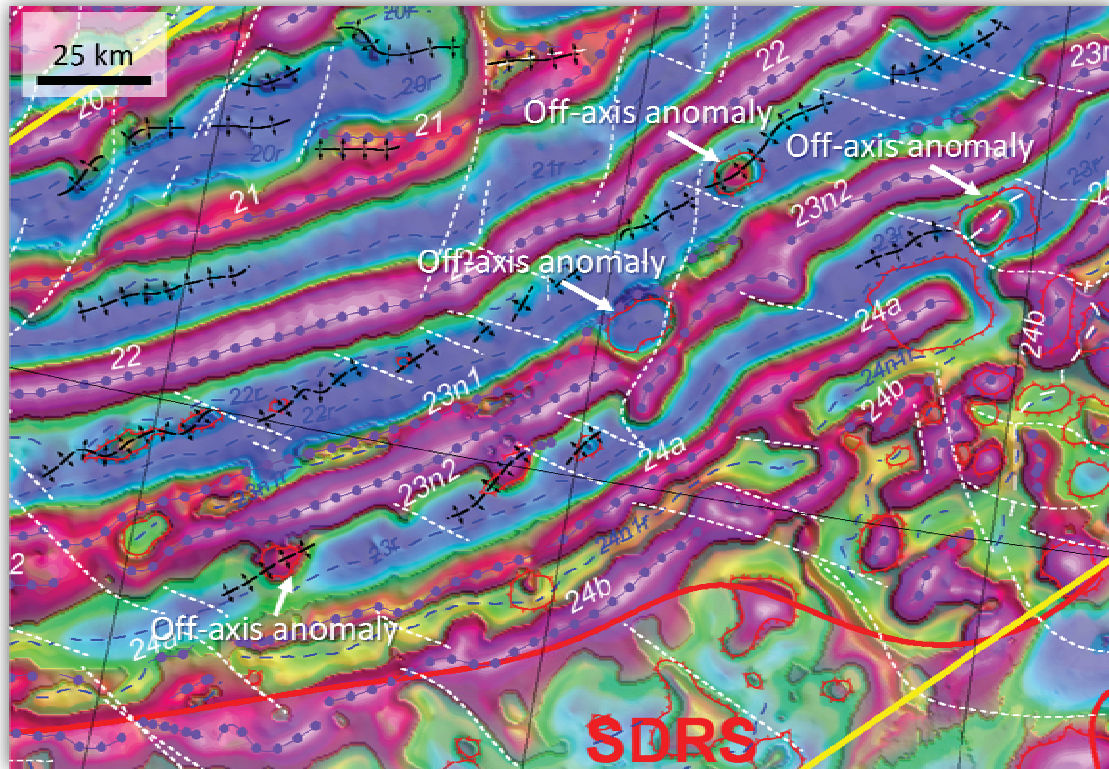


Figure 9.21 Examples of round features with opposite polarities compared to their surroundings. They are interpreted as off-axis volcanic mounds or aborted rift features. Dashed lines represent discrete third order (non-rigid) discontinuities.

#### Domain 4: Fan-shape and plate reorganisation from C22 to C10

After C22n, an important geodynamic adjustment occurred at the spreading centre. The transition from C22n to C20n reflects a progressive change in the Norway Basin (Figs. 9.6, 9.7, 9.8, 9.21). The spreading direction changes from NW-SE between C24 to C22 to NNW-SSE/N-S after C22n (Fig. 9.22). Oblique spreading and re-orientation of the main spreading directions initiated after C22n are evidenced by a 10-20° obliquity of the chrons C20 to C21n which are locally divided by crack propagation of the growing C20r (Fig. 9.22). The change of spreading directions envisages the creation of a new spreading center and its subsequent growth at the expense of the old ridge. The old rift is progressively replaced by a propagating spreading center orthogonal to the new spreading direction.

From C22 to C21, spreading rates vary from  $16.4 \pm 2$  to  $8.6 \pm 2$  mm/year but in contradiction to the older anomalies the spreading rate seems to increase from north to south in most of the Norway Basin except near Faroes-Iceland Ridge where the spreading rate slightly decrease from south to north (Fig. 9.20).

West of C20, the new survey allows us to identify anomalies C18n, C17 and C13 near the Faroes-Iceland Ridge (Figs. 9.6, 9.7, 9.8, 9.21). To the north, the magnetic pattern is not so obvious to interpret and mostly witnesses a significant shearing and dislocation of the oceanic crust. Some anomalies have been tentatively interpreted as C18n, 17n and C13n in the westernmost part of the survey.

From C22 to C13 (and possibly C11-10 in the northern part of the Norway Basin), a crudely northward-widening fan-shaped magnetic anomaly pattern was generated along the Aegir Ridge. Compared to the model of Nunns (1983) and Vogt (1986), the new dataset clearly show that the onset of the fan-shaped evolution starts at C21 instead of C18 as previously proposed. Comparison with the conjugate system is locally unclear due to poor coverage, especially in the southern part of the Jan Mayen Ridge. Nevertheless, the fan-shaped pattern clearly observed on the eastern side of the Aegir Ridge requires the existence of simultaneous spreading from more additional axes and propagating features between Jan Mayen Iceland and Greenland (Talwani and Eldholm 1977; Nunns 1983; Skogseid and Eldholm 1987; Kuvaas and Kodaira 1997; Lundin and Doré 2002; Scott et al. 2005; Lundin and Doré 2005b). Otherwise, it can also require a complex intraplate rift deformation and anticlockwise rotation of the south Jan Mayen area (Gaina et al. in preparation). The last hypothesis could explain the space problem when dealing with the plate reconstruction of this microplate between Norway and Greenland.

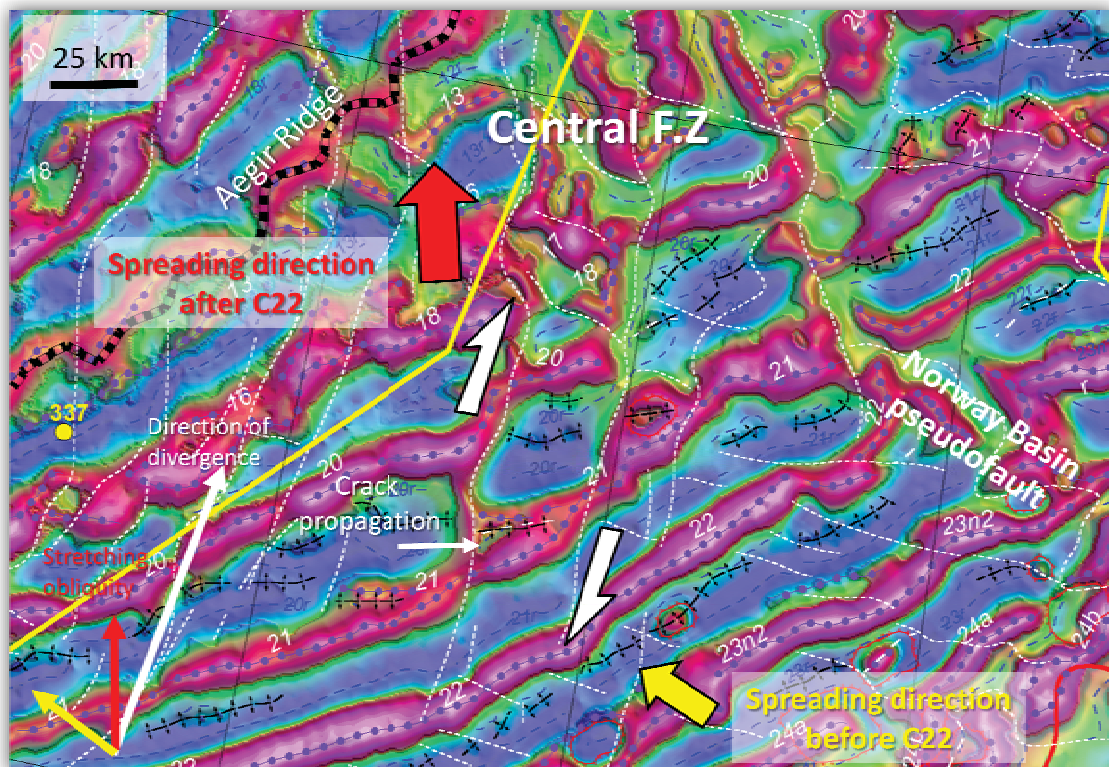


Figure 9.22 Significant Early-mid Eocene cinematic reorganisation of the Norway Basin between C22n and C21 (49.7-46.2 Ma). The spreading direction changes from NW-SE from C24 to C22 to NNW-SSE/N-S after C22n. Chrons C21n are locally divided by crack propagation of the growing C20r.

### 9.3.4 Segmentation the Norway Basin

The pattern of magnetic anomalies, in addition to being highly regular in most of the NB-07 survey, is locally dislocated by first, second and third order discontinuities of the ocean floor (applying the offset order terminology of Macdonald et al. 1991).

#### First order discontinuities

The East Jan Mayen Fault Zone (EJMFZ) and the Faroes-Iceland Ridge represent regional and major first order discontinuities at the scale of the North Atlantic and fix the borders of the survey area (Fig. 9.1).

The JMFZ, to the north, represents a broad zone and consists of three distinct segments respectively named the western, eastern and central Jan Mayen fractures zones (WJMFZ, EJMFZ, CJMFZ) (Blystad et al. 1995). These segments have been recently reinterpreted using the previous aeromagnetic survey JAS-05 (Olesen et al. 2006; Gernigon et al. 2008). The EMFZ and CJMFZ run sub-parallel to each other across the northern part of the Norway Basin and the magnetic trends suggest a change from N130° at its western end to about N°150 at its eastern end. The signature of the EJMFZ is the most distinguishable on the JAS-05 grid and the traces of the CJMFZ and WJMFZ correspond to net offsets and local displacement of the magnetic chrons. After breakup, the JMFZ behaved as an oceanic transform (*sensu stricto*) and acted as a first-order discontinuity of the Norwegian-Greenland Sea, accommodating the seafloor spreading at the Aegir and Mohns Ridges. The EJMFZ has recently been reinterpreted as a leaky transform branch of a regional triple junction between the Vøring Marginal High and the Greenland margin (Gernigon et al. 2008).

The main offset observed along the volcanic shear margin north of the Faroes Plateau (Domain 2) coincides with a broad, negative and disturbed transition zone where shifts and displacements of most of the magnetic chrons from C24 to C13 can be observed in the southwestern part of the NB-07 survey (Figs. 9.6, 9.7, 9.8). It coincides with the location of the so-called “Faroes Fracture Zone” sometimes proposed in the literature but never clearly documented (Doré et al. 1997; Kimbell et al. 2005). However, compared to the EJMFZ, the trace of this “Fracture Zone” is not perfectly linear but exhibits a wavy magnetic low pattern which partly reflect a bathymetric effects between the shallow Faroes-Iceland Ridge complex and the deep oceanic basin to the northeast. Even if it is unclear at an early interpretation stage, it is also possible that this “Faroes Fracture Zone” represents a complex overlapping and competing spreading system involving an unstable oceanic domain evolving along the trend of the Faroes-Iceland Ridge, influenced in depth by the Iceland “anomaly”.

#### Second-third order discontinuities

No prominent discontinuities are observed in the Norway Basin itself. However, second and third order discontinuities have been highlighted by the new survey. A large number of small offsets ridge-axis discontinuities can be seen on the new survey but differ from classic transform faults. South of the EJMFZ, a large band of disturbed anomalies coincides with the location of the Norway Basin Fracture Zone proposed by (Skogseid and Eldholm 1987). The new NB-07 survey suggests that it does not show the characteristics of a real oceanic fracture zone but instead an accommodation zone between two spreading systems with different heterogeneous spreading rates (Fig. 9.23). This process generally involves the lengthening of one spreading segment at the expense of its neighbour as the offset between them migrates along the strike of the ridge.

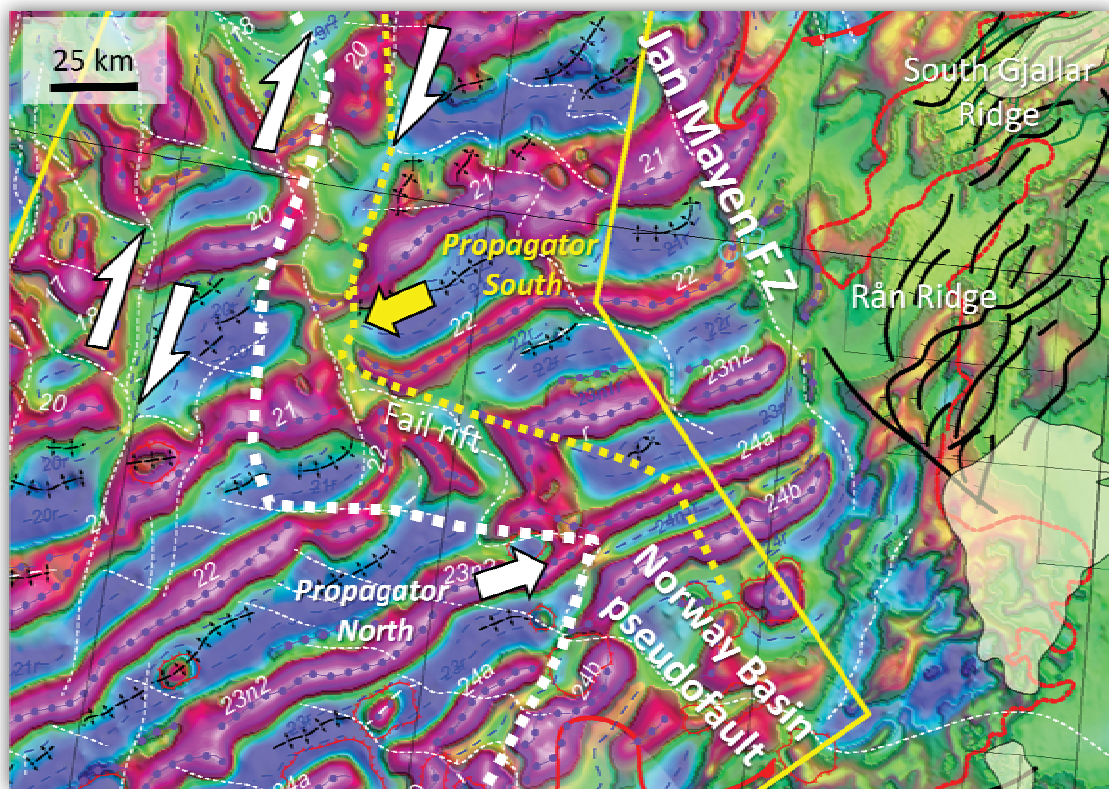


Figure 9.23 Detail of the Norway Basin “pseudofault”, located south of the Jan Mayen transform margin. The Norway Basin defines characteristic wavy magnetic pattern pointing in the direction of two propagator features. Between the propagating and the failing rift, the lithosphere is progressively transferred from one plate to another, giving rise to a shear zone with a quite distinctive magnetic fabric. Northern and southern segments are divided by the pseudofault and interacted together.

This ridges migration creates a wake of “pseudofaults” and failed rifts that are oblique to the ridge axis and point in the direction of offset migration. Hey et al. (1980, 1988) have described the complex processes that take place at the tip of such propagating features (Fig. 9.24).



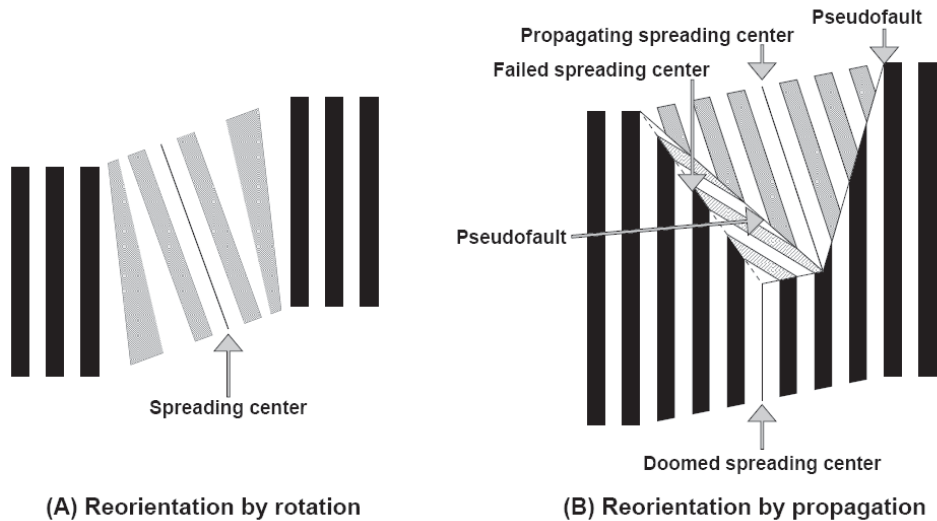


Figure 9.24 Models of spreading centre reorientation by (A) gradual rotation and (B) propagation. Modified from Hey et al. (1980, 1988).

Pseudofaults define a characteristic wavy or V-shape feature pointing in the direction of propagation. Between the propagating and failing rifts, the lithosphere is progressively transferred from one plate to another, giving rise to a shear zone with a quite distinctive magnetic fabric. Accordingly, the northern and central segments are separated by this pseudo fault. From the magnetic pattern which emphasizes the “Norway Basin pseudofault”, we propose that between C24 and C21, the central segment propagated between the northern segment C24a and C24b (Fig. 9.23). Then, between C24a and C22, a dynamic change happened and the northern segment propagated inside the southern part. Finally, from C21 to C13(C10 ?) the central segment propagated again towards the north.

In the central part of the survey several N°100-130-oriented lineations have been interpreted and represent minor offset of the anomalies C24 to C22. As previously described, small overlaps have been also observed along C23 and C22 but no major fracture zones can be observed. However, after C22, the oceanic Domain 3 is affected by much larger offsets of anomalies C21 to C13. These offsets represent major NNW-SSE to N-S trending oceanic fracture zones (Figs. 9.6, 9.7, 9.8, 9.22). Shifts of 10 to 50 km of C21n and C20n are particularly well documented in the NB-07. The fault offsets increase from south to north similar to the spreading rates (Fig. 9.20). The survey highlights several intra-oceanic fracture zones that form a large regional shear zone (the Central Fracture Zone) which seems to extend even on the conjugate part of the spreading system. In the northern part of the survey area, the central shear zone interacts with the Norway Basin pseudo-fault observed south of the EJMFZ and produces a complex and chaotic magnetic pattern which reflects significant dislocations of the oceanic basement. The Central Fracture Zone also coincides with similar trends and elongated anomalies observed on gravity (Figs. 9.11, 9.12, 9.13).

### Segmentation: from continental rift to spreading stage

These first order discontinuities are usually interpreted as a consequence of plate tectonics involving the spreading between Eurasia and Greenland since Early Tertiary time (Talwani and Eldholm 1977a). However, the origin and causes of segmentation of mid-oceanic ridges by long-lived transform boundaries such as the EJMfZ and Faroes F.Z are poorly understood. The segmentation at the mature oceanic spreading stage may be directly linked to the latest continental rift configuration link or not with the inherited structural pattern of the margin. The JMfZ seems to correlate with the mid- to upper crustal segmentation of the southern Vøring Basin and its transition zone between South Gjallar Ridge and Rån Ridge (Gernigon et al. 2003; Raum et al. 2006). Doré et al. (1997) and Fichler et al. (1999) already noted that the NW-SE lineaments, in the trend of the JMfZ, are sub-parallel to older, NW-SE Caledonian and/or Paleoproterozoic, deep-seated shear zones. They conclude that the Jan Mayen Lineament and the nascent JMfZ might have been influenced by much older inherited structures. Along the mid-Norwegian margin, some of the NW-SE lineament merges landwards into post-Caledonian detachments observed on the mainland and on the Trøndelag Platform (Olesen et al. 2002; Osmundsen et al. 2002; Ebbing et al. 2006). Complex onshore-offshore correlation could exist on the Møre volcanic margin but requires more investigations to reveal. Some links with the western part of the margin, as proposed by (Ebbing et al. 2006) remains speculative and is still a matter of discussion.

In the Faroes area, some lineament mark distinct magnetic and gravity anomalies shift in the vicinity of the East Faroese High and Fugloy Ridge. Kimbell et al. (2005) propose that the “Faroes Fracture Zone” could be the prolongation of the NW-trending Clair Lineament (Rumph et al. 1993). According to Kimbell et al., (2005), the Clair Lineament offsets the magnetic anomaly associated with the Corona Ridge in the Faroes-Shetland Basin and truncates or offsets further magnetic anomalies believed to be due to basement sources beneath the Faroe–Shetland Basin (Rumph et al. 1993). It could also define a marked boundary in terms of sediment thickness variation within the main Faroes–Shetland Basin and the Flett Sub-basin.

Some offsets, could also be linked with the NW-trending Magnus Lineament described by Rumph et al. (1993). This lineament marks a zone of disruption towards the northeastern end of the Faroes–Shetland Basin, the northern margins of the Erlend and West Shetland platforms and the southern margin of the Magnus Basin. Its position is well resolved by gravity and magnetic data but the geological meaning of such a linear lineament is still unclear.

In fact, the development of the Faroes shear margin, likely occurred along the complex trend of a larger oblique accommodation zone that initially formed between the Viking Graben, the Møre Basin and the Faroes–Shetland Basin. Other studies have also demonstrated that the pre-breakup segmentation and inheritance has likely contributed to the location of similar, long-lived, oceanic transforms (Behn and Lin 2000; Bonatti 1996).

Some of the second or third order discontinuities like the Norway Basin pseudofault and the transition zone between Domain 1 and Domain 2 also represent discontinuities observed on the gravity map and may represent pre-breakup crustal heterogeneities. The transition between Domain 1 and Domain 2 coincides with a different gravity and magnetic configuration between the northern and southern parts of the Møre Basin. An advanced interpretation of the outer Møre Basin is, however, beyond the scope of the present report. It appears that the second order segmentation of the oceanic domain could coincide with the crustal and basin segmentation of the ridge complexes observed near and underneath the inner lava flows of the outer Møre Basin as observed in the outer Vøring Basin (Gernigon et al. 2003).

## 10 GRAVITY AND MAGNETIC MODELLING

Laurent Gernigon

### 10.1 Modelling methods and assumptions

#### 10.1.1 Forward modelling approach

Most of the seismic lines available in the present study are located in the Norwegian sector of the survey area and were provided by NPD. Only one seismic profile, provided by Jardfeingi constrains the Faroes margin. The interpretation process described here was designed to quantitatively validate the interpretation of the NPD LOS00-13, LOS99-02 and the OF94-97 seismic lines and roughly constrain the crustal geometry of the Norway Basin (Fig. 10.1). As the geometry is generally well constrained by the reflection seismic data down to at least basement depths, the main unknowns in modelling are the densities and magnetic properties of the bodies, and the geometries of bodies in the deep crust. Forward modelling allowed us to refine and adjust the initial geometry as much as possible.

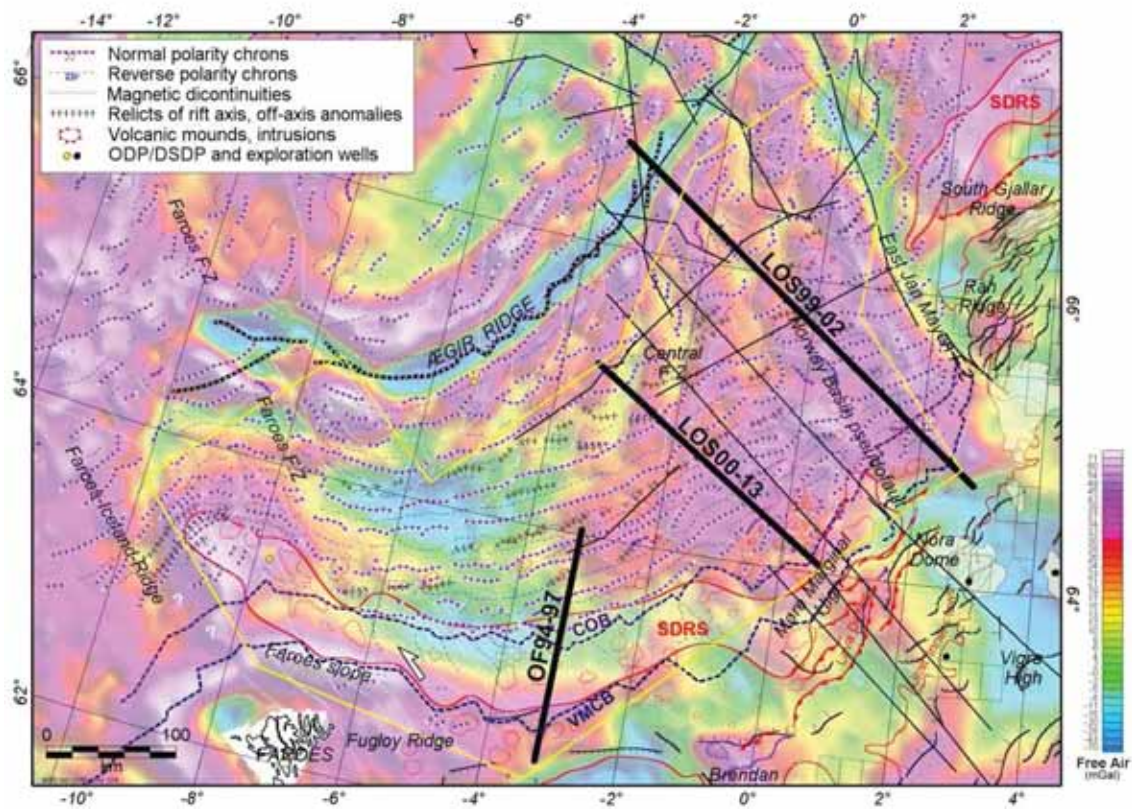


Figure 10.1 Location of the three seismic lines used for potential modelling.

The 2<sup>3</sup>/<sub>4</sub>D forward modelling has been carried out using the commercial software GM-SYS (Northwest Geophysical Associates Incorporation 2006). GM-SYS is an interactive gravity and magnetic modelling program applying a method of summing the effects of irregular polygons modified after Talwani (1973). The method also uses the divergence theorem (Blakely 1995) for the magnetic modelling. With the 2<sup>3</sup>/<sub>4</sub>D approach, the structures (bodies) of varying and limited extent, both laterally and perpendicularly to the line, in front of and behind the plane of the profile may be defined, and their effect included in the calculated anomaly.

Seismic transects have first been depth-converted using the software Easydepth<sup>TM</sup> from Beicip-Franlab (Beicip-Franlab 2002) and the depth-converted SEG-Y files have been imported as background and guide in GM-SYS. Wherever possible, features interpreted on the seismic data have been used to constrain the geometries of the basin and various bodies used for the modelling. The modelled bodies in the top 4-6 km of section below the water-bottom were comparatively well-constrained by the seismic interpretation and changes in reflection character. Sometimes, some of the horizons could not be picked consistently all along the transects due to abundant mud diapirism and fluid escape observed in the northwestern part of the Norway Basin. However, the few lines still allowed some good constrain of the top oceanic basement typically expressed as strong amplitude reflections. Below this, the seismic data quality is locally relatively poor owing to noise and multiples, and no seismic interpretation was attempted. In these regions, which include the middle crust to the Moho, bodies have only been modelled in order to fit the overall gross shapes of the potential fields and to be consistent with the limited velocity information. For depth conversion, we used regional and simple velocity laws derived for previous compilation and OBS results (Myhre and Eldholm 1980; Breivik et al. 2006).

The gravity and magnetic fields of the petrophysically-attributed geometric models were then concurrently forward modelled and refined by inversion techniques when necessary. This was achieved by calculating and integrating the gravity and magnetic anomalies sourced by bodies in the section. This approach was considered reasonable, given the generally 2D strike of the geological features imaged at the scale of the seismic section.

The model was built in different steps including: 1) the definition of the 2D crustal geometry, 2) the lateral and perpendicular extension of the main seismic horizons to infinity in order to reduce the edge effects when necessary; 3) the definition of the appropriate density values and 4) the forward modelling interaction.

We associate to every sedimentary interval of velocities a density using appropriate velocity-density functions (Fig. 10.2) based on appropriate estimation of the geological setting and their uncertainties (Nafe and Drake 1957; Gardner et al. 1984; Carlson and Herrick 1990; Larsen et al. 1994; Christensen and Mooney 1995; Birch 1996; Godfrey et al. 1997). The average density

for each polygon can then be calculated from the interval velocities. Top basement and Moho usually coincide with the main density contrasts in the lithosphere.

The body responses are modelled in their correct x, y and z locations not projected into a plane. The calculations do not take account of the sphericity and curvature effect of the Earth over the distance of the baseline. Induced errors due to this assumption, based on comparison of similar modelling and spherical 3D models by (Wienecke et al. 2007) are of the order of 10%. Given the noise envelope of approximately 1-3 mGal, the uncertainties of our geological model itself and the dynamic range of the data (c. 100 mGal), this is not considered significant.

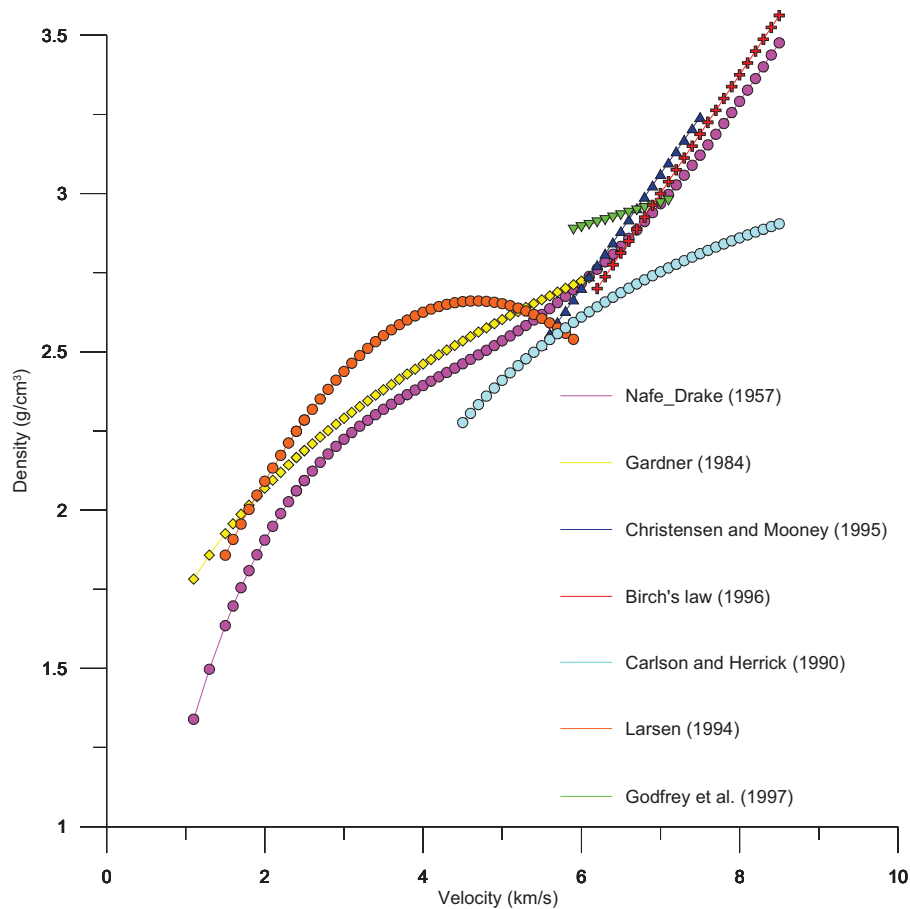


Figure 10.2 Velocity-density functions for different geologic settings including oceanic sediments and crust. Compilation by courtesy of Laura Marello, NGU.

### 10.1.2 Magnetic modelling

Interpretation and modelling of magnetic data is usually more complex and tricky compared to gravity data. The magnetic susceptibility between different rock types can differ by orders of magnitude in contrast with gravity data, where crustal densities differ up to 30%. Our model assumes reasonable geological assumptions but the readers should be aware that the magnetic modelling considers some simplifications and uncertainties due to the lack of direct measurements and method limitations.

For modelling, magnetic induction ( $J_I$ ) is assumed to be the principal method of generating magnetic anomalies in continental crust; in these bodies the dimensionless apparent Königsberger ratio ( $k$ ), the ratio of the remanent field to the inducing field, is set to zero. In oceanic crust and some of the inferred igneous bodies within the COT,  $k$  is non-zero, implying a large contribution from magnetic remanence ( $J_R$ ).

Magnetic data are normalized to the current magnetic field, but was frequently reversed in the Earth's geologic past, resulting in strong negative magnetizations on the data set. The true values of  $k$  might be significantly different to those modelled if there is a high angle between real remanent vectors and the current inducing field vector. In the absence of detailed magnetic measurements on drill cores from the Norway Basin oceanic basement, the paleo-magnetic properties of the crust along the NB-07 survey remain the least-constrained part of the validation process.

The difficulty in relating the magnetic anomalies to their source bodies can be alleviated by applying a reduction-to-the pole (RTP) operator that reduces an anomaly to what it would like if the body was located at the north pole and was magnetized by the geomagnetic field there (Baranov, 1957, chapter 4.4 of this report). The RTP transformation of total field magnetic anomalies is intended to remove the skewness of the anomalies. The transformation should make the anomalies overlie the sources, make it possible to correlate the magnetic anomalies with other types of geophysical anomalies (e.g., gravity) and geological information, and aids their interpretation. We considered this approach but in reality, the equivalent source method could be subject to instabilities due to a variety of reasons (e.g., spacing of sources, altitude difference between observations and the sources). As also illustrated in a previous chapter, the different approaches of RTP (1D-FFT or 2D-FFT for example) can also significantly increase or decrease the initial total field amplitudes of the anomalies. Therefore, it could influence our estimation of the magnetization. Nevertheless, it appears to be a first and reasonable approach at this preliminary stage of the Norway Basin interpretation.

For susceptibility parameters, we used previous compilations that define the ranges and average values for various continental and oceanic rock types (Dobrin and Savit 1988; Clark 1997). The detailed geology of the Faroes Plateau drilled by two scientific boreholes (Loppra and Vestmanna) and the ODP Leg 104 on the outer Vøring Plateau provided limited information on

magnetic physical properties. Paleomagnetic data from a 907-m thick volcanic sequence from Hole 642E on the Vøring Plateau, Norwegian Sea, has been presented in details by Schönharting and Abrahamsem (1989). NRM, susceptibility, k(Q)-ratio, stable inclination, and polarity values were determined for 520 samples obtained from 118 flows, 7 dikes, and 12 volcanoclastic units and are summarised on figure 10.13.

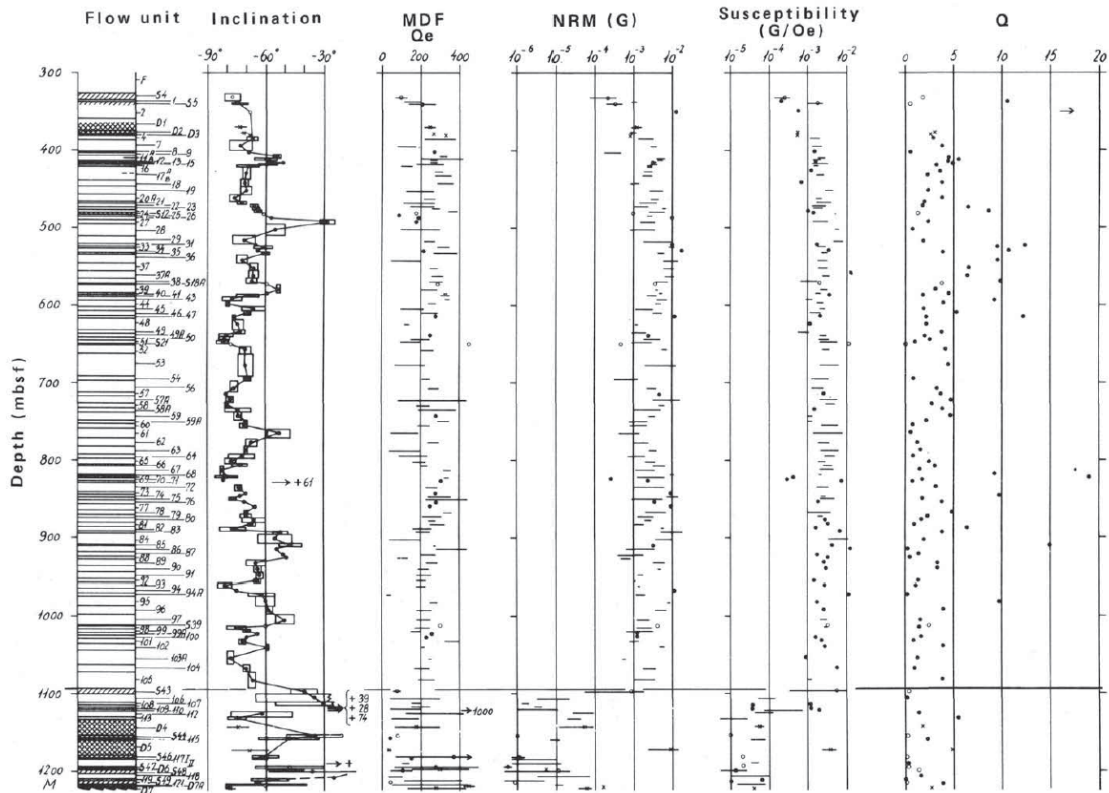


Figure 10.3 Compilation of magnetic data from the volcanic sequence of ODP Hole 642E (from Schönharting and Abrahamsen 1989). Flow unit numbers from 1 to 121 represent lava flows. DI1 to D7 represent dikes and S4 to S49 numbers represent volcanoclastics). The graph illustrates the stable inclination in degrees, the median destructive field (MDF), the natural remanent magnetization (NRM) and the Q-ratio. Note that the values used the old nomenclature in Gauss (=  $47\pi$  SI). The boundary between the upper and the lower series is at 1087 mbsf and illustrates a clear polarity change. The reverse upper series is correlated with chron 24r of the magnetic polarity time scale, with an age of ca. 54 Ma. The normal polarity of the lower series is correlated with chron 25, indicating a hiatus between the two series.

Other Susceptibility measurements and magnetic logs from the Lopra-1/1A and Vestmanna-1 well have been presented in details by Abrahamsen et al. (1984), Abrahamsen (2006) and Abrahamsen et al. (2006) and provided relevant informations about the breakup related volcanics magnetic properties (Table. 10.1, Fig. 10.4). The basalts drilled by the Lopra well fall into high- and low-susceptibility groups with no overlap. The high-susceptibility basalts (seven



cores) have susceptibilities between  $4-88 \times 10^{-3}$  SI. Basalts from the Lopra-1/1A well have a mean susceptibility of  $22.1 \pm 3.5 \times 10^{-3}$  SI while samples of volcanoclastics (lapilli-tuff and tuff) have a mean value of  $0.85 \times 10^{-3}$  SI. The mean values of rock magnetic parameters for 303 basalt plugs from the Vestmanna-1 well are:  $k = 13.3 \pm 0.6$ ,  $J_1 = 11.8 \pm 0.6 \times 10^{-3}$  SI and  $J_R = 4.64 \pm 0.25$  A/m. The reversely polarised, lowermost (hidden) part of the c. 4½ km thick lower basalt formation correlates with Chron C26r. The upper (exposed) part of the lower basalt formation correlates with Chrons C26n, C25r and C25n and the more than 2.3 km thick middle and upper basalt formations correlate with Chron C24n.3r.

Sample No.	Depth m	Rock type	Weight g	Density g/cm <sup>3</sup>	NRM mA/m	Suscept-bridge 10 <sup>-3</sup> SI	High > 2 × 10 <sup>-3</sup> 10 <sup>-3</sup> SI	Low < 2 × 10 <sup>-3</sup> 10 <sup>-3</sup> SI	Q-ratio NRM/(F × Sus)
59	2219.00	basalt	18.966	2.361	4406	1.43		1.43	77.4
57	2275.00	basalt	22.222	2.857	2180	87.96	87.96		0.623
46	2441.00	basalt	23.857	2.865	9027	46.65	46.65		4.864
44	2456.00	basalt, ves.	33.653	2.488					
43	2475.00	basalt, ves.	18.421	1.981	0.7	0.55		0.55	0.032
40	2558.00	basalt, ves.	17.973	2.708	1.3	0.71		0.71	0.046
39	2559.80	basalt, ves.	22.920	2.711	1.5	0.64		0.64	0.060
38	2560.20	tuff, lapilli	21.428	2.336	0.4	0.61		0.61	0.015
37	2562.00	tuff	29.838	2.345					
36	2570.00	basalt	9.353	2.379	38.5	0.69		0.69	1.406
34	2610.00	basalt, alt.	18.741	3.167	3412	69.17	69.17		1.240
33	2630.00	tuff, lapilli	13.720	2.404	587	1.60		1.60	9.224
31	2690.00	tuf, lapilli	8.082	2.276	365	1.83		1.83	5.022
30	2780.00	basalt	21.170	2.929	7171	76.89	76.89		2.344
26	2970.00	tuf, lapilli	18.744	2.553	304	3.77	3.77		2.030
25	3030.00	basalt	18.515	2.808	1146	26.67	26.67		1.080
19	3233.50	tuff	9.915	2.572		0.72		0.72	
16	3328.00	basalt	18.471	2.875	106	1.13		1.13	2.346
15	3382.00	basalt	14.066	2.919		63.36	63.36		
13	3438.00	tuf, lapilli	19.505	2.549	1.8	0.62		0.62	0.074
12	3464.50	tuf, lapilli	17.287	2.605	12.0	0.64		0.64	0.470
9	3500.50	basalt	16.494	3.001	0.8	0.83		0.83	0.024
6	3512.50	tuff	23.953	2.648	38.2	0.39		0.39	2.433
5	3514.50	tuf, lapilli	13.372	2.511		0.58		0.58	
5	3514.50	tuf, lapilli	15.648	2.607		0.58		0.58	
4	3531.00	basalt	27.341	2.940		0.88		0.88	
b:		Mean		2.63	1516	16.20	34.47	0.85	1.85
		Standard deviation		0.27	2585	28.80	21.00	0.39	2.34
		Mean error		0.05	593	5.88	3.90	0.10	0.55
		N		26	19	24	29	17	18 <sup>*)</sup>
a & b:		Mean		2.68	1895	22.1	34.5		2.16
		Standard deviation		0.27	3276	23.6	21.4		2.45
		Mean error		0.05	525	3.5	4.0		0.40
		N		32	39	46	29		38 <sup>*)</sup>

\*) Excluding sample No. 59

Table 10-1 Magnetic susceptibility, remanence (NRM), k-ratio and density properties of the Lopra 1/1A from (Abrahamsen 2006)

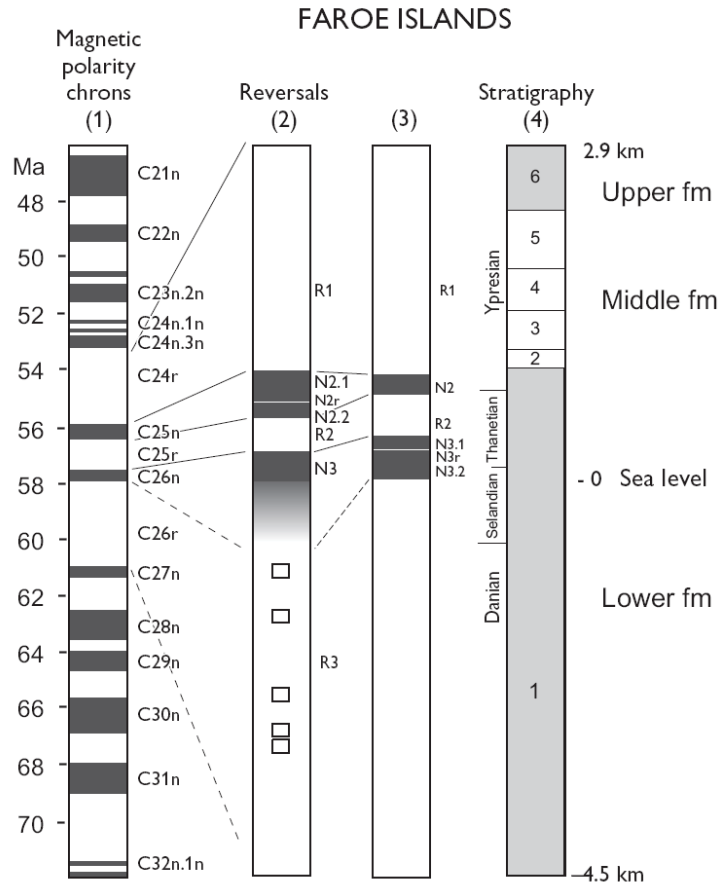


Figure 10.4 Compilation of magnetic reversals within the c. 6½ km thick basalt pile of the Faroe Islands, showing stratigraphy and the correlation with the Geomagnetic Polarity Time Scale. After Abrahamsen (2006).

After breakup, the continuity of the expansion and the succession of the reversals likely give rise to the sequence of sea-floor bands alternate normal and reverse polarities in most of the Norway Basin. We consider the present day knowledge about the oceanic crust to set and test the magnetic model of the oceanic crust in the Norway Basin.

The model for “typical” oceanic crust structure was derived from ophiolite observation and seismic velocity analysis. Often referred to as the “Penrose model,” following the name of the international conference on ophiolites where it was established, this layered oceanic crust is as follows: 500 m of basalts, 1500 m of dikes, and 5000 m of gabbros, which together give an average thickness of 7 km of oceanic crust upon unaltered mantle (Juteau and Maury 1997). Since the establishment of this basic model, drilling and dredging show that the model can be more complex due to spatial and temporal variations of the magmatic and tectonic processes which can to be realistically adopted to fast to slow spreading system such as the Norway

Basin. Ultramafic rocks such as serpentinized peridotites, also called serpentinites, are notably reported in the new crustal models (Cannat et al. 1995; Cannat 1996).

Magnetic properties of extrusive basalts of the oceanic crust were the subject of numerous studies as a result of the important amount of dredged and drilled samples made available to the scientific community. The magnetic minerals in oceanic basalts are predominantly titanomagnetites associated with various amounts of titanomaghemites, an alteration product of titanomagnetites. The primary natural remanent magnetization (NRM) of basalts is acquired during the extrusion process and is a thermal remanent magnetization. Magnetic properties can show significant variations between flows depending, in particular, on iron and titanium content but also at the within-flow scale depending on local crystallization conditions and alteration progression. On average, NRM of young basalts is in the range of 10–20 A/m, but can reach higher values on the order of >80 A/m for young flows with high iron content. The Königsberger ratio ( $k$ ) is almost always greater than one in basalts and can often reach 100 confirming that magnetization of the basalt layer is dominantly of remanent origin. This property favours the magnetic recording of past inversions of the polarity of Earth's magnetic field leading to the pattern of lineated magnetic anomalies observed along the NB-07 survey.

Extensive magnetic measurements by the Deep Sea Drilling Project (DSDP) program, in the late 1970s and early 1980s also showed that magnetization of the basaltic extrusive layers was not homogeneous. This is mostly a consequence of rocks alteration caused by circulation of seawater in the rocks pores and cracks whereas NRM decreases typically down to values on the order of a few A/m (Bleil and Petersen 1983).

Oceanic intrusive rocks have also been the subject of fewer studies than basalts due to increasing difficulties in sample accessibility. Rocks from escarpments, tectonized areas, and ophiolites are thus overrepresented and might not represent the norm. From what we know, the sheeted dike layer (layer 2B) shows contrasting magnetizations. Typical remanent magnetization in dikes is typically 0.1–0.01 A/m, but stronger magnetizations in the order of 1 A/m are found in the freshest samples. Königsberger ratios are lower than in basalts but usually above one (ophiolites dikes have lower  $k$ -ratio) showing that magnetization of submarine dikes is for its most part of remanent origin. This remanent magnetization is mainly acquired during alteration and its relationship with the geomagnetic field at the time of emplacement is not yet clear.

Gabbros found below oceanic basalts are coarse-grained igneous rocks (seismic layer 3) and the dominant magnetic mineral is magnetite. Curie temperatures in gabbros are consequently dominantly found in the range 550°C–590°C. The intensity of magnetization is quite variable spanning several orders of magnitude and depends on the concentration of magnetic minerals, which is often rather low, giving on average NRM in the range 0.1 A/m. In a few sites, some gabbros were reported and give rather high NRM values due to their high concentration of magnetite of primary origin or resulting from serpentinisation (Pariso and Johnson 1993;

Dyment et al. 1997; Allerton and Tivey 2001). Gabbros can preserve a record of the magnetic field acquired during the cooling of the units shortly after intrusion at the spreading axis. Gabbros could also contribute to the magnetic anomalies but their low NRM and depth usually make them marginal contributors.

Recent studies also show that the occurrence of serpentinitized peridotites (also called serpentinites) within the oceanic crust was more and more observed and could be considered to explain some long-wavelength anomalies. Magnetization of peridotites is acquired during the serpentinitisation process, which is the reaction of the silicate minerals of peridotites (mostly olivine) with water producing serpentine and pure magnetite. Remanent magnetization is variable in the range of 0.1 –10 A/m, peak values of 25A/m have been reported, which suggest that these serpentinite samples could be as magnetized as young basalts (Dyment et al., 1997).

## 10.2 Flexural models

One of the problem in our modelling was to get a good estimate of the Moho underneath the Norway Basin. Only the wide-angle transect of Breivik et al. (2006) provides a local estimation of the mantle-crust transition. One way to extrapolate this Moho was to calculate and test approximate flexural mohos according different realistic rigidities of the lithosphere. The 3D modelling of the flexural Moho was achieved using the ASEP algorithm of Wienecke et al. (2007).

If the lithosphere has finite strength, sediments and water deposited on its surface will form a load that is partially supported through such strength. The way in which the lithosphere responds under these circumstances can be approximated using equations that describe the deformation of a thin elastic plate (Watts, 2001 and references therein). Using this approximation, and various inputs, alternative Moho geometries can be evaluated along the Norway Basin assuming different values for the flexural rigidity (apparent elastic thickness) of the lithosphere during sediment loading. The flexure of the plate only considers the topographic and internal loads and the plate's rigidity. If the crustal plate has a high flexural rigidity, then almost no "root" is produced and the deflection is small. For a low flexural rigidity we expect larger deflection.

However, the strength of the lithosphere is likely to vary spatially across the region, but it is possible to use the set of models based on different uniform elastic thickness values to analyse this variation by identifying which model works was for the Norway Basin.

The 3D flexural modelling was used to predict the position of the Moho surface ("flexural Moho") assuming a value for the effective elastic thickness ( $T_e$ ) of the lithosphere (Fig. 10.5). We used a density of  $2850 \text{ kg}\cdot\text{m}^{-3}$  for the average density of the reference plate density and  $3250 \text{ kg}\cdot\text{m}^{-3}$  for the mantle. Different flexural Mohos were generated in 3D for  $T_e=1 \text{ km}$  to  $20$

km using the ASEP algorithm (Wienecke et al. 2007). In order to validate the models; we compare the different result with the only seismic Moho available along the NB07 survey. We also precise that the modelling assumes a regional flexuration of a relatively homogeneous plate. Consequently, the flexural Moho mostly fits the oceanic crust. Uncertainties likely exist near the COT and readjustments have therefore been considered using forward modelling. This observation clearly illustrates the need for good geological constrains on both side of the COT in order to model properly this complex transition zone.

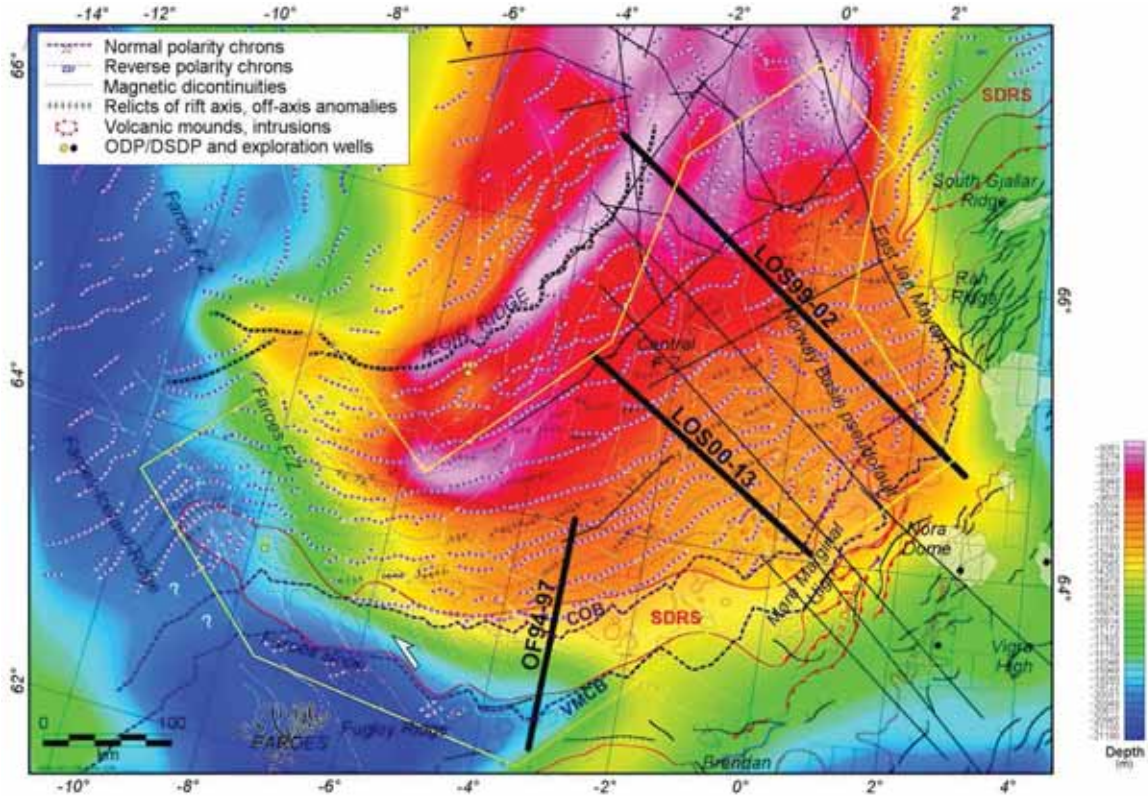


Figure 10.5 Example of flexural Moho computed for an elastic thickness value of 2 km in the Norway Basin area.

The approach described is relatively simplistic, as it does not account for the complexities of the rifting and subsidence history of the Norway Basin and surrounding basins. It could be refined later by subdividing the sedimentary sequences and allowing, in a more realistic fashion, for the variation of lithospheric strength with time.

### 10.3 Description of the modelling along Section 1, LOS99-002 profile

#### 10.3.1 Model setup

The LOS99-002 profile runs east-west in the central part of the Norway Basin from the More Marginal High to the Aegir Ridge (Fig. 10.1). The transect covers the Møre volcanic margin, the COT and the early spreading system up to the aborted Aegir Ridge (Fig. 10.6). The initial geometry of the upper part of the model is based on our interpretation and depth conversion of seismic reflection line LOS-99-002 provided by NPD. Information on the velocities for the upper part of the section vary from 1.75 to 2.6 km/s and has been derived from the velocity model proposed by Breivik et al. (2006) in agreement with the regional Vp-waves compilation of Myhre and Eldholm (1980). Information about the deeper parts of the profile is also constrained by the OBS transect of Breivik et al. (2006). The OBS transect was combined with the depth converted multichannel transect and used as a starting model to calibrate the density and susceptibility values and to fit the flexural Moho depths deduced from the 3D flexural modelling. West of the LOS99-002 profile, the OBS profile 8a-96 from Raum (2000) was used to constrain the eastward termination of the extrusive magmatic layers, including the continental part of the transect described on Figure 10.6.

Where layers had significant P-wave velocity variations, they were subdivided and attributed densities corresponding to their average P-wave velocities at the COT, the Moho depth was not properly constrained by the OBS model of Breivik et al. (2006) and has been deduced by forward modelling.

We stick as much as possible to the initial crustal geometry and adjust when necessary the density values to fit the observed gravity. The density adjustment has been carried out assuming reasonable minimum and maximum boundaries around a medium values. Variation does not exceed  $100 \text{ kg}\cdot\text{m}^{-3}$  of the initial densities setup, which is reasonable taking into consideration the uncertainties of the velocity models ( $\pm 0.2 \text{ km/s}$ ) and density-velocity relationships (Fig. 10.2). Average densities used for each body are summarised in Table 10.2 and the results from the forward modelling are presented in Fig. 10.6.

The upper part of the seismic section represents a 2 to 2.5 km thick sedimentary basin. The sediments reach a maximum thickness in the central part of the profiles and thin progressively towards the Aegir Ridge and pinch out above the SDRs observed in the eastern part of the profile. The seismic facies that characterise the Cenozoic depocentre is mostly transparent, locally chaotic and show evidences of fluid escape and mud diapirism which locally does not allow a reliable picking of the main horizons.

Refracted arrivals from the sedimentary section show that Vp-wave velocities are typically 2.1–2.2 km/s up to 2.8 km/s in the deepest part of the oceanic basin. This coincides with average density values of 2050 to 2250  $\text{kg}\cdot\text{m}^{-3}$ .

The top basement often shows as a high-amplitude reflection, sometimes obscured by strong reflections within the lower sedimentary section. The oceanic basement topography is very

rough but smooth along the COT where SDRs have been observed. The main faults observed on seismics usually match with some of the discontinuities observed on the magnetic grid. Fault displacements and the basement rugosity, increase progressively from east to west, with significant faults observed close to the Aegir Ridge and along the main N-S to NNE-SSW shear zones observed after C22n.

According to the OBS model, the refracted arrivals from the upper oceanic basement are best modelled by a pronounced velocity gradient, giving velocities typical of the basaltic oceanic layer 2A (5.0–5.7 km/s).  $V_p$  increases from 6.1 to 6.6 in the middle layer and most likely represent isotropic gabbros facies (Layer 2B). We choose average density values of  $2500 \pm 100 \text{ kg}\cdot\text{m}^{-3}$  for the upper Layer 2A and densities of 2700 to  $2850 \text{ kg}\cdot\text{m}^{-3}$  for the Layer 2B).

Body	Velocity (km/s)	Average density – flexibility ( $\text{kg}\cdot\text{m}^{-3}$ )	Susceptibility (SI) Range (average)	Remanence (A/m)	Polarity	Comments
Sea water	1400	1030	0	0	-	
Sediment Unit A	1.75-2.0	$2050 \pm 100$	$10^{-5}$ - $10^{-3}$ ( $5 \cdot 10^{-4}$ )	0	-	mostly carbonate, shales, mudstone
Sediment Unit B	2.0-2.2	$2100 \pm 100$	$10^{-5}$ - $10^{-3}$ ( $5 \cdot 10^{-4}$ )	0	-	mostly carbonate, shales, mudstone
Sediment Unit C	2.0-2.8	$2250 \pm 100$	$10^{-5}$ - $10^{-3}$ ( $10^{-3}$ )	0	-	possibly some detrital magnetite
Upper oceanic crust (layer 2A)	4. 5-6.0	$2500 \pm 100$	$5 \cdot 10^{-4}$ - $10^{-1}$ ( $2 \cdot 10^{-2}$ )	1-10 ( $5 \text{ A}\cdot\text{m}^{-1}$ in average)	R/N	oceanic basalt-sheeted dikes
Middle oceanic crust (layer 2B)	6.0-6.8	2700-2850	$5 \cdot 10^{-4}$ - $2 \cdot 10^{-3}$ ( $10^{-3}$ )	0.5-1 ( $0.75 \text{ A}\cdot\text{m}^{-1}$ in average)	R-N (negligible if $J_{\text{TRM}} < 1 \text{ A}\cdot\text{m}^{-1}$ )	Isotropic gabbros
Lower oceanic crust	7.0-7.2	2900-3100	$5 \cdot 10^{-4}$ - $2 \cdot 10^{-3}$ ( $10^{-3}$ )	$10^{-3}$	R/N (negligible)	cumulate gabbros
SDRs sequences	4. 5-6.0	2450-2550	$5 \cdot 10^{-4}$ - $10^{-1}$ ( $2 \cdot 10^{-2}$ )	4-5	R/N	altered basalt-fresh basalt-sheeted dikes
Upper Mantle	>8	3250-3330	0.01-0.1 (serpentinized)	negligible	R/N (negligible)	Peridotite, local serpentinisation ?
Cenozoic	1.75-2.35	$2050 \pm 100$	$10^{-5}$ - $10^{-3}$ ( $5 \cdot 10^{-4}$ )	negligible	negligible	
Cretaceous	2.5-4.5	$2400 \pm 100$	$10^{-5}$ - $10^{-3}$ ( $5 \cdot 10^{-4}$ )	negligible	negligible	
Pre-Cretaceous sediments (continental)	5.0-5.5	$2600 \pm 100$	$2 \cdot 10^{-4}$ - $10^{-1}$ ( $4 \cdot 10^{-4}$ )	negligible	negligible	
Upper continental crust	6.1-6.6	$2800 \pm 050$	$10^{-4}$ - $10^{-1}$ ( $5 \cdot 10^{-3}$ )	$10^{-2}$	negligible	
Continental Lower crustal body	7.1-7.3	2.9-3.1	$5 \cdot 10^{-4}$ - $2 \cdot 10^{-3}$ ( $10^{-3}$ )	$10^{-3}$	negligible	

Table 10-2 Average density, susceptibility and remanence used for each sedimentary and crustal units.

Most of the lower crustal velocity displayed high values (7.0–7.2 km/s) increasing from west to east and likely represent gabbroic cumulates (oceanic Layer 3). Densities from 2900 up to 3100  $\text{kg}\cdot\text{m}^{-3}$  have been used to model the gravity effect of this layer.

The top mantle velocity is close to  $8.0 \pm 0.15$  km/s, possibly slightly lower beneath the Aegir Ridge. Density variations from 3250 to 3300  $\text{kg}\cdot\text{m}^{-3}$  have been selected to adjust the longest wavelengths.

Near the COT, the crustal thickness increases to 12–13 km close to C24 and up to 18–20 km near the Møre Marginal High. Here, the transition crust, located before C24b corresponds to the SDRs. SDRs have lower velocities (4.8–4.9 km/s) and we used average densities of 2450 to 2500  $\text{kg}\cdot\text{m}^{-3}$  to model the lava piles observed along the COT. Beneath the SDRs, basal velocities are 6.0–6.8 km/s and densities vary from 2700 to 2850  $\text{kg}\cdot\text{m}^{-3}$ . A velocity and density increase is seen also in the middle oceanic crust. Velocities are 6.65–6.8 km/s in the top, and 6.8–7.0 km/s in the bottom as described by Breivik et al. (2006). This was modelled using densities of 2700 up to 2900  $\text{kg}\cdot\text{m}^{-3}$ . Higher densities (3000–3100  $\text{kg}\cdot\text{m}^{-3}$ ) were used to represent the high velocity lower crust particularly observed before anomalies C23.

### 10.3.2 Gravity signature along the LOS99-002

The free air gravity anomaly map is derived from satellite altimetry measurements and an average uncertainty of  $\pm 5$  mGal can be expected along the transect.

Along the LOS99-0002, the free air gravity anomalies vary from -23 to 54 mGal. The continental side the profile starts on the southwestern flank of the large negative free-air gravity anomaly over the Møre Marginal High. To the west, a significant long-wavelength anomaly is observed and the gravity increases to a 54 mGal high around magnetic chron C23. The long wavelength anomalies coincide with a broad gravity high domain which forms a triangular shape in the northern part of the NB-07 survey area (Figs. 10.6, 10.1). This region seems to delimit the East Jan Mayen Fault Zone to the north, the Central Fracture Zone to the west and the COB to the east. From C23 to C13, the gravity field decreases towards the Aegir Ridge, and the ridge valley itself has a prominent negative gravity anomaly at -23 mGal.

Using reasonable density values in the crustal section, derived from the model of Breivik et al. (2008), a first density modelling did not reproduce the observed gravity, but shows a regional trend rising over the oceanic basin. To explain the regional and global decrease of the gravity field from east to west and assuming that the OBS model of Breivik et al. (2006) is correct, a progressive density decreases in the mantle was necessary. As pointed out by an earlier contribution of Breivik et al. (1999), this could be the result of a lateral temperature change in the mantle. Assuming a simple cooling history of the oceanic basin, a basic temperature model was first adapted along the transect, using ages deduced from the magnetic chrons and the plate



cooling model of Parsons and Sclater (1977). Assuming thermal expansion, a reasonable density distribution within the lithosphere mantle was roughly estimated.

After the regional trend readjustment, the long wavelengths are mostly influenced by the densities distributions observed in the middle and lower oceanic crust. However, local and minor density re-adjustment down to a density value of  $3220 \text{ kg}\cdot\text{m}^{-3}$  in the upper mantle were still necessary to fit the regional wavelengths (100-200 km). Possible sources for mantle density variations between the continental and oceanic side could be compositional, if there were variations in the degree of mantle depletion for example. As the oceanic mantle melts and magma is extracted to form oceanic crust, iron is preferentially drawn into the melt and leaves a less dense residue mantle behind (Korenaga et al. 2001).

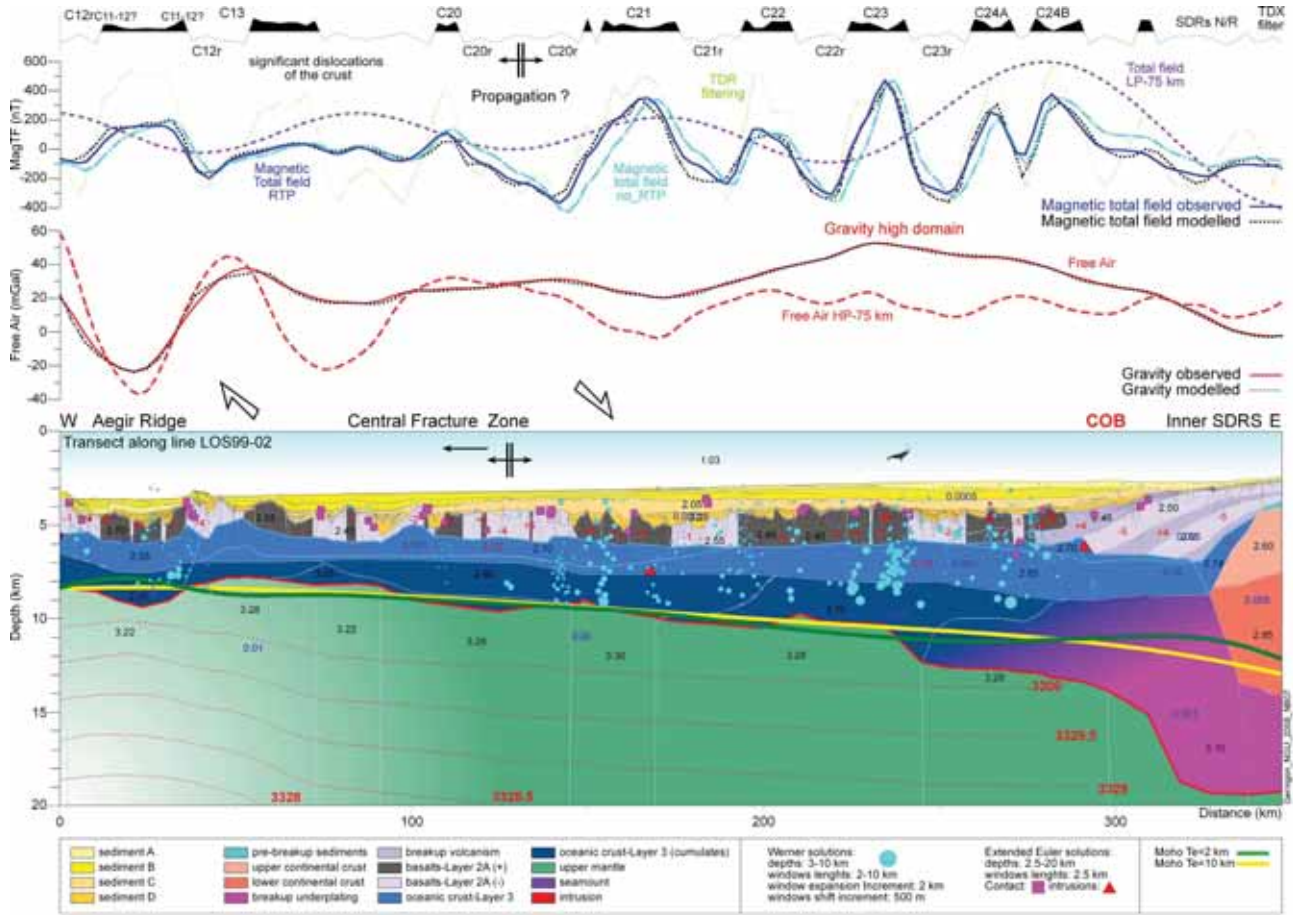


Figure 10.6 Potential field modelling along the depth-converted LOS99-02 seismic profile. The detail geometries of the bodies are controlled by reflection and refraction seismic data and compared with the flexural Mohos deduced assuming different flexural elastic thicknesses of the plate. The top panel represents the TDX, tilt derivative, low-pass filtering and observed and calculated residual IGRF and RTP corrected magnetic anomaly (nT). The middle panel represents the observed and calculated free air gravity anomaly and the 75 km high-pass filtered free air gravity (mGal). Densities (black labels) are in  $1000 \times \text{kg m}^{-3}$ . Red densities (in  $1000 \times \text{kg m}^{-3}$ ) represent the mantle densities assuming thermal expansion.

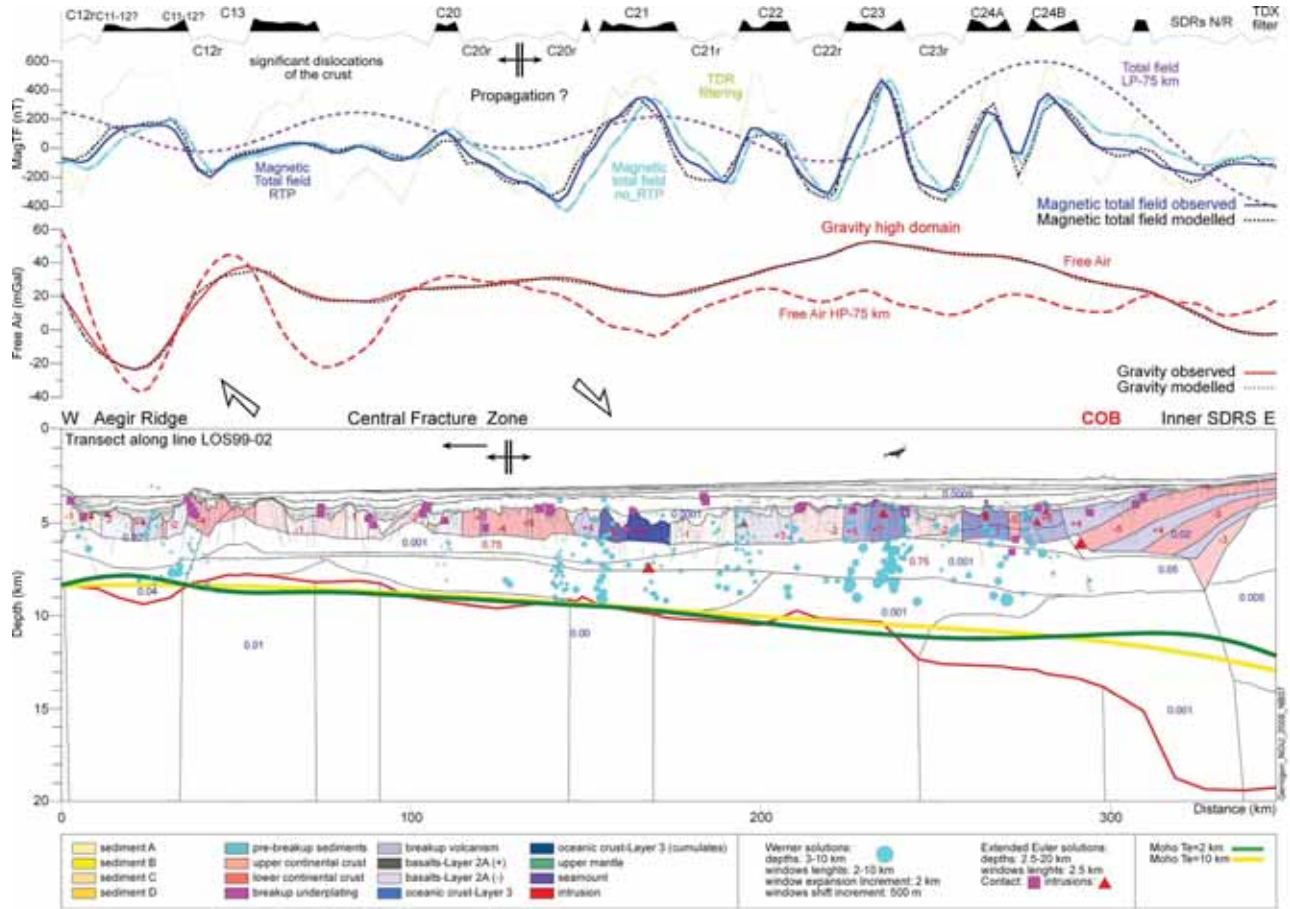


Figure 10.7 Magnetic modelling along the depth converted LOS99-02 seismic profile. The detailed geometries of the bodies are constrained by reflection and refraction seismic data and compared with the flexural Mohos deduced assuming different flexural elastic thicknesses of the plate. The top panel represents the TDX, tilt derivative, low-pass filtering and the observed and calculated residual IGRF and RTP corrected magnetic anomaly (nT). The middle panel represents the observed and calculated free air gravity anomaly and the 75 km high-pass filtering of the free air gravity (mGal). Along the transect, susceptibilities (blue labels) are in SI units and remanence values (red labels) are in A/m.

Sea water alteration and mantle serpentinisation can also decrease the mantle density especially if large faults affect the whole crust as observed in the central shear zone domain and on the flank (Macdonald and Fyfe 1985). This could induce density changes in the upper mantle of the same magnitude as the thermal signal. Near the Aegir Ridge, faulting is most important and lower densities in the upper mantle are required to fit the observed gravity signal. The relative gravity low observed from the Aegir Ridge flank up to km-170 is interpreted as the result of lower densities values both in the lower oceanic crust and in the upper mantle. It could be the result of the upper mantle serpentinisation or it can also be explained by deep and frozen gabbroic intrusions in the upper mantle as suggested by Jung and Vogt (1997) or a combination of both.

East of the transect, SDRs have been observed (Fig. 10.6). Such flood basalt constructions usually show large intra-lava variations in physical properties which is confirmed by volcanostratigraphic and petrophysical studies. Petrophysical data shows that the  $V_p$ -wave velocities and densities range of SDRs volcanic sequences produced by the same melt may be as large as 1.5-7.5 km/s and that basalt density in average can easily vary from 2000 to 3000  $\text{kg}\cdot\text{m}^{-3}$ . Planke (1994b) shows that poorly consolidated tuffs are in the low-velocity/density range, while melts emplaced at the base of the crust are in the high-velocity/density range. Volcaniclastics, hydroclastites, basalt flows and intrusions have intermediate velocities and density. Analyses of core and log data in subaerial flood basalts show variation in  $V_p$ -wave velocities and rock densities can also be influenced by fracturation and alteration processes. For the purpose of our study, we modelled the lava piles using average densities from 2450 to 2500  $\text{kg}\cdot\text{m}^{-3}$  assuming higher rocks alteration and lower densities in the shallow piles. Similar densities have been used for the upper part of the oceanic crust (Layer 2A). Modelling suggests that the density of Layer 2 could locally vary between 2450 to 2550  $\text{kg}\cdot\text{m}^{-3}$  to locally fit the medium and short wavelengths.

The forward density modelling agree with thick and high density lower crust and a deep Moho (close to 20 km) beneath the SDRs. Between C23 and C24 Moho is modelled around 12 km. Between C23 and the Møre Marginal High, the flexural Moho does not fit the forward modelled Moho and a discrepancy a 5 km was observed. Between C23 and the Møre Marginal High, the average density and the elastic thickness are probably different from the western part of the transect. Between C23 and the Aegir Ridge, the oceanic crust varies between 9 to 10 km and we obtained a good fit with the flexural Moho. This observation shows the limitation and the complexity of regional flexural modelling approach near the volcanic margin. The combination of flexural and forward modelling can solve such issues.

### 10.3.1 Magnetic signature along the LOS99-002

Along the LOS99-02, the amplitude of the magnetic anomalies varies between from -400 to 500 nT (Fig. 10.7). The most prominent anomalies are observed on the eastern part of the transect

and seems to decrease in amplitude to the west. We can already note a correlation between the “rugosity” of the oceanic basement and the magnetic signature. Highest anomalies characterized by ~30-40 km wavelengths anomalies are observed when the basement is smooth and low anomalies (<300 nT) represent highly faulted basement after C21.

West of the C24b, the anomalies are mostly a combined effect of the sea-floor expansion and the polarity reversal of the Earth’s magnetic field and agree with the classic model of Vine and Matthews (1963). The magnetic model proposed for LO99-002 considers that the remanence of the upper basaltic crust is the main cause of the anomalies and requires that  $J_R \gg J_I$ , (i.e. that the contribution of the induced magnetization by the present field is negligible). The best magnetic fit in the oceanic domain (between C24b and C12r) was obtained using lateral  $J_R$  variation between +9 and -5 A/m. The lowermost remanence coincides with local shear zones and may be the result of basalt alteration. A possible propagation feature and possible ridge jump is also interpreted between C21 and C20. The distribution of high amplitude anomalies also coincides with the depth distribution of higher density lower crust but their high gradients indicate that the source bodies are mostly close to the top basement. A relationship between spreading rates, melt production and the remanence of the basaltic layers can be proposed as suggested by Dymant et al. (1997)

Along the COT, the SDRs has been successfully modelled as the superposition of upper normally polarized series of basalt and reversely polarized series as suggested by Schreckenberger (1997) for the Vøring Plateau. Remanence values of 3 to 5 A/m were used to model the main volcanic units as they agree with the values recorded in the ODP and Lopra drillholes. Stacking the different polarized series allowed us to decrease and inhibit the amplitude of the calculated magnetic anomalies without decreasing the remanence. To some extent, the respective distribution in depth of the normally and reversely polarized series remains speculative but rely on the fact that the volcanism occurred between C26 and C24.

#### **10.4 Description of the modelling along of the Section 1, LOS00-13 profile**

The LOS00-13 transect lies in the central part of the survey area between the COT and the eastern flank of the central shear zone observed after C22 (Figs. 10.1, 10.8).

The second profile LOS00-13 is relatively similar to the first one and we use almost similar assumption for the forward modelling. However, we do not have so much information about the deep nature of the crust. The Moho is extrapolated from the 3D flexural modelling and locally readjusted using forward modelling. Along the LOS00-13 transect, the modelling predicts a Moho between 9 and 20 km underneath the COT. The model includes the upper sedimentary section constrained by seismic reflection data and with density values between 2000 to 2200  $\text{kg}\cdot\text{m}^{-3}$ , the upper basaltic crust with densities of 2400 to 2550  $\text{kg}\cdot\text{m}^{-3}$ , and a middle and lower crust with higher densities between 2850 and 3100  $\text{kg}\cdot\text{m}^{-3}$ .

East of C22, the oceanic basement is relatively smooth and faulting and block dislocations increase near the central shear zone. Along the COT, SDRs can be also observed but the dominant feature is a 75 km wide seamount observed east of C24b. Evidence of lava deltas suggest that the seamount was emplaced near sea level.

#### 10.4.1 Gravity signature along the LOS00-13

Along the LOS00-13, the free air gravity anomalies vary from 0 to 40 mGal (Figs. 10.1, 10.8). West of C21, the gravity field decreases towards the Central Fracture Zone which coincides with NS to NNE-SSW-oriented, elongated gravity anomalies enhanced by the 75 km high-pass filtering of the free-air gravity (Figs. 9.12, 10.8). The main long-wavelength and regional anomaly ( $\lambda=150-200$  km) can be explained by the lateral distribution of the high-density lower crust at depth and by a lateral decrease of the mantle density, lower underneath the oceanic shear zones. The gravity low coincides with a basement low and a region of important faulting. To the east, the seamount coincides with clear positive anomaly enhanced by the 75 km high-pass filtering. The anomaly around the seamount has been modelled assuming a narrow mid-crustal gabbroic intrusion at  $3100 \text{ kg}\cdot\text{m}^{-3}$  emplaced beneath the seamount.

#### 10.4.1 Magnetic interpretation along the LOS00-13

Along the LOS00-13, the magnetic anomalies are clearly defined between C24b and C20 and show high amplitudes in the order of 400-600 nT (Fig. 10.9). Their high gradients and our modelling indicate that the source bodies are most likely close to the top basement surface. The most prominent anomalies are observed in the eastern part of the transect at C24a and decrease in amplitude to the west and to the east. Along the COT, some anomalies have been observed but the amplitudes do not exceed 300 nT.

The best magnetic fit in the oceanic domain (between C24b and C12r) was obtained using lateral  $J_R$  variations of +8 to -5 A/m (Fig. 10.9). Between C23 and C22, a round positive anomaly has been observed inside the reversely polarized sequence and has been interpreted as an off-axis seamount emplaced during a normal period.

The SDRs, at the COT, have also been modelled as the superposition of upper normally polarized series of basalt and reversely polarized series as recommended for the first transect (Fig. 10.9). The remanence values of -3 to 5 A/m were used for the main volcanic units and the effect of stacking different polarized series inhibits the amplitude of the calculated magnetic anomalies. The model is complicated because the polarities of the seamount appear to be negative in the upper part of the crust.

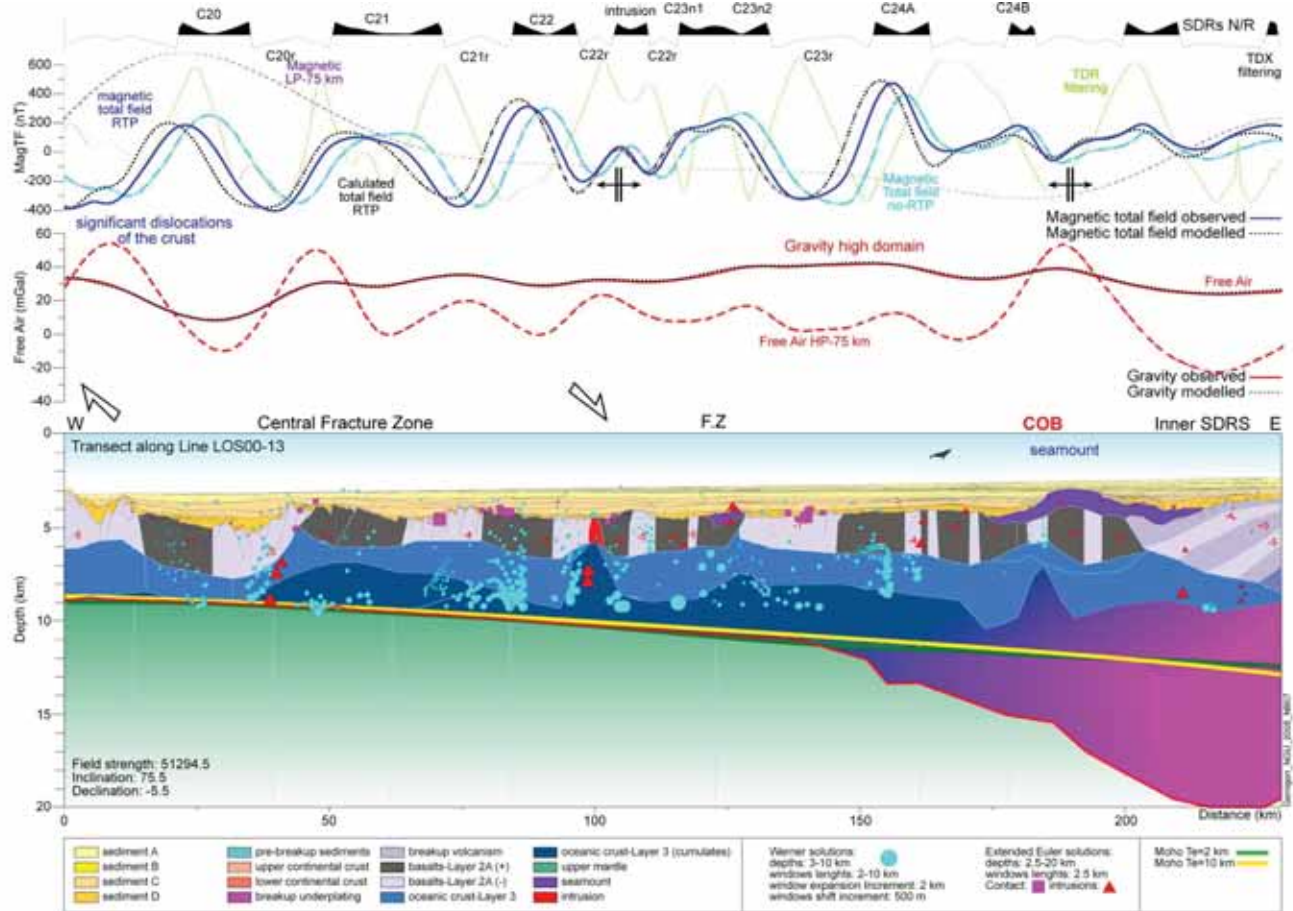


Figure 10.8 Potential field modelling along the depth converted LOS00-13 seismic profile. The detail geometries of the bodies are controlled by reflection and refraction seismic data and compared with the flexural Mohos deduced assuming different flexural elastic thickness of the plate. The top panel represents the TDX, tilt derivative, low-pass filtering and the observed and calculated residual IGRF and RTP corrected magnetic anomalies (nT). The middle panel represents the observed and calculated free air gravity anomaly and the 75 km high-pass filtering of the free air gravity (mGal). Densities (black labels) are in  $1000 \times \text{kg} \cdot \text{m}^{-3}$ .

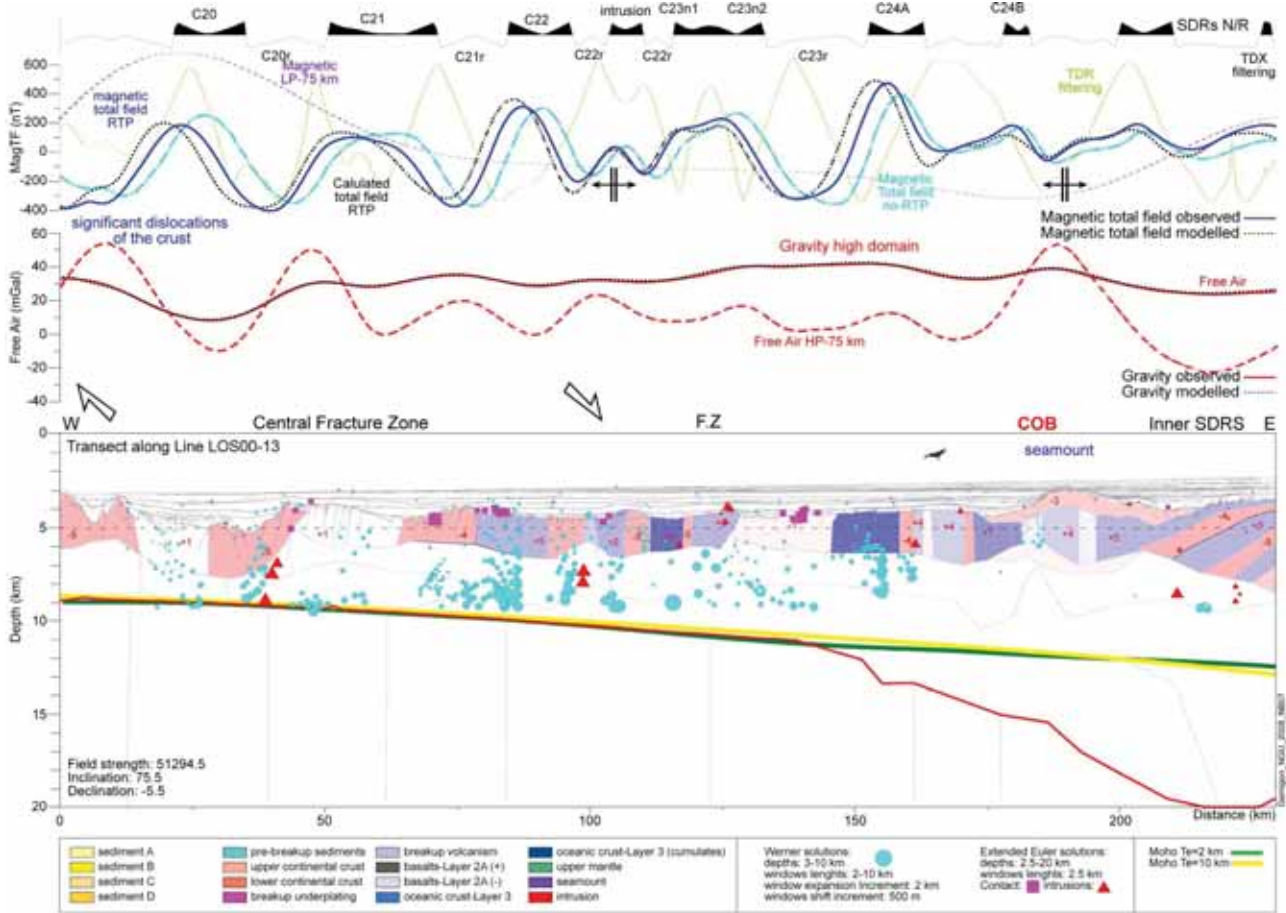


Figure 10.9 Magnetic modelling along the depth converted LOS00-13 seismic profile. The details geometries of the bodies are controlled by reflection and refraction seismic data and compared with the flexural Mohos deduced assuming different flexural elastic thickness of the plate. The top panel represents the TDX, Tilt derivative, low-pass filtering and observed and the observed and calculated residual IGRF and RTP corrected magnetic anomalies (nT). The middle panel represents the observed and calculated free air gravity anomaly and the 75 km high-pass filtering of the free air gravity (mGal). Susceptibilities (blue labels) are in SI units and remanence (red labels) in A/m in the lower panel.



## 10.5 Description of the modelling along Section 1, Faroes transect OF94-97

The Faroes transect along the seismic line OF94-97 is located in the central part of the survey area between the northeastern part of the Faroes Plateau (Fulgøy High) and the central part of the survey near magnetic chron C23 (Figs. 10.1, 10.10). The transect is trending N-S, 45° oblique to the main magnetic trends and covers mostly the volcanic shear margin and the COT characterized by a 100-wide transition zone, where Inner SDRs and Landward Flows are observed below a 1-2 km thick sedimentary section. The model includes the upper sedimentary section constrained by seismic reflection and with density values between 1900 and 2150 kg·m<sup>-3</sup>, the upper basaltic crust and SDRs with densities of 2500 and 2550 kg·m<sup>-3</sup>, and middle and lower crust with higher densities between 2850 and 3100 kg·m<sup>-3</sup>.

The Moho is extrapolated from the 3D flexural modelling and was locally readjusted using forward modelling. Along the transect, the forward modelling predicts a Moho between 20-25 km underneath the COT located before C24b, which is somehow deeper than the flexural estimation. Near C23, the Moho reaches 10 km depth.

### 10.5.1 Gravity signature of the Faroes section OF94-97

Along the Faroes section OF94-97, the free air gravity anomalies vary from 0 to 40 mGal with a major positive anomaly high ( $\lambda=80-100$  km) situated in the eastern part of the transect. The gravity field progressively decreases towards the oceanic domain and the Faroes-Shetland Basin (Fig. 10.10). The highest gravity value coincides with the transition between the Landward Flows and the Inner SDRs. The gravity high is explained by a thick transitional crust including the Inner SDRs and underlying high density middle and lower crusts. Beneath the Inner SDRs, shallow and particularly high densities of 3000 kg·m<sup>-3</sup> are required to fit the observed gravity. It is interpreted as shallow mafic to ultramafic complexes emplaced in a narrow zone (40-50 km) during the breakup initiation and SDRs formation. This narrow intruded zone coincides with one of the fault zones developed during the shear volcanic margin development. Densities in the middle crust diminish towards the oceanic domain (2950 to 2850 kg·m<sup>-3</sup>) and underneath the Landward Flows (2900-2810 kg·m<sup>-3</sup>).

### 10.5.2 Magnetic signature of the Faroes section OF94-97

The magnetic amplitude along the Faroes section OF94-97 varies between -400 and 600 nT and the signal is relatively smooth, except at the level of chron C23 where highest values represent a typical oceanic crust magnetic pattern (Fig. 10.11). Before C23, the anomalies are both positive and negative with respect to the base-level; but are generally biased towards positive values. Before C23r, the tilted geometry of the basalt (SDRs) strongly influences the magnetic signature. The positive long wavelength ( $\lambda=60-70$  km) defined by the low-pass filtering of the

magnetic total field characterises the Inner SDRs and decreases toward the Landward Flows. Like the two other transects, the magnetic remanence dominates the susceptibility in our modeling and the geometries of the magnetic bodies are constrained as much as possible by the reflection seismic data.

Like the previous transect, the magnetic signature along the COT does not display any classic layered pattern. As a matter of fact, the atypical tilted and faulted geometry of basalts, with different polarities emplaced along the COTs can explain a broad range of magnetic pattern which can vary from typical oceanic linear signature to weaker signatures usually characteristic of the Norwegian continental domain.

We conclude that the Landward Flows are dominantly characterized by reverse polarity sequences. To the south, the Tertiary Faroes basaltic formations are centered on the Faroe Islands and consist of subaerial lavas, divided into three formations. Based on field revision of the magnetostratigraphy of the lower formation it is tentatively suggested that the lower formation was extruded during chrons C26R to C25N and the two higher formations during C24R. These observations have been used to set the initial model but large uncertainties exist about the presence and eventual thickness of each basaltic formation along this transect. Nevertheless, different tests suggest that reverse polarity should be dominant in this part of the margin. The Inner SDRs have been considered to be emplaced during C24b and C24a and mostly set with normal polarities. This configuration manages to explain the observed magnetic total field. Classic oceanic configuration has been used to model the oceanic domain at C23 level. An off-axis seamount has been observed close to C23 and modelled by means of a positive remanence (+3 A/m) emplaced above an Outer SDRs wedge mixed with reverse polarity (-2 A/m) to explain the negative low anomaly that defines the C23r.

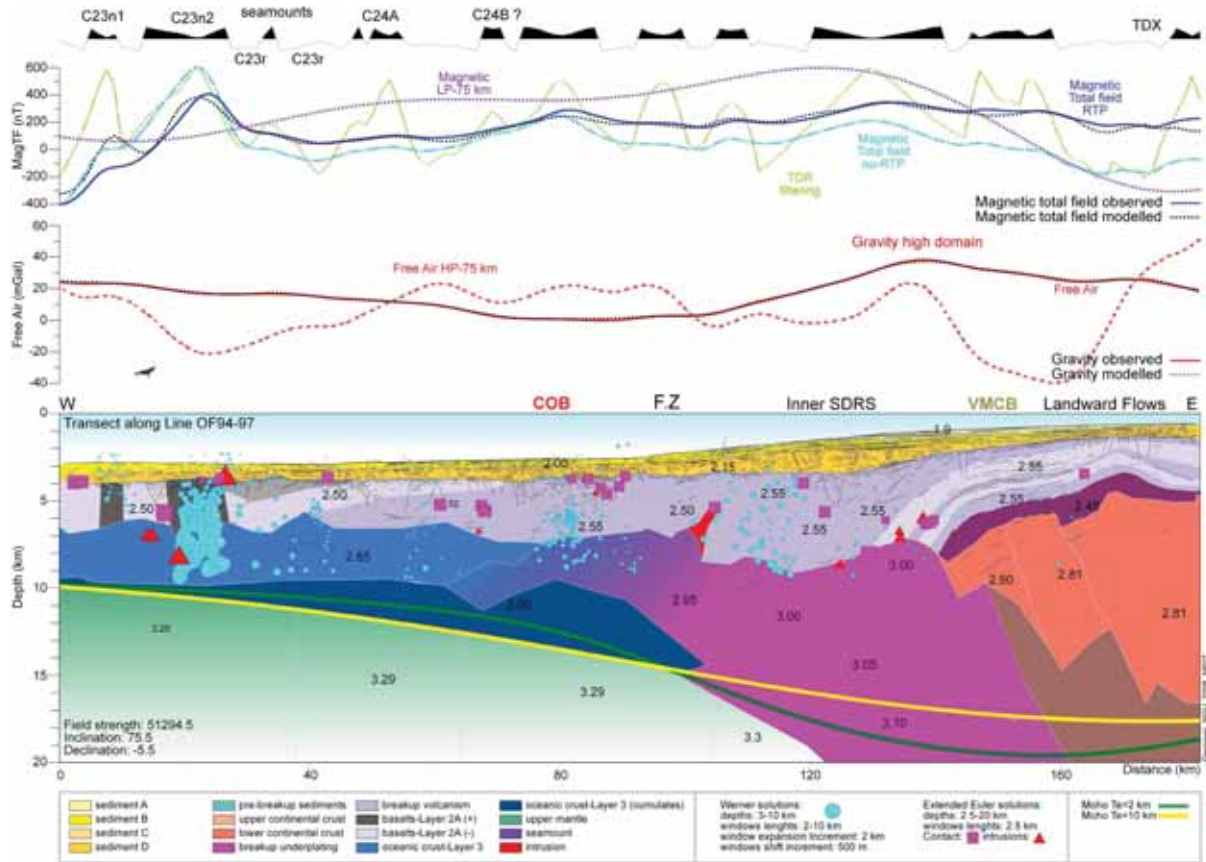


Figure 10.10 Potential field model along the depth-converted line-drawing of the LOS00-13 seismic profile. The detailed geometries of the bodies are controlled by reflection and refraction seismic data and compared with the flexural Mohos deduced assuming different flexural elastic thickness of the plate. The top curve represents the TDX filtering of the magnetic total field. The Middle panel represents the observed and calculated residual IGRF and RTP corrected magnetic anomaly (nT). The upper panel shows the observed and calculated free air gravity anomaly and the 75 km high-pass filtering of the gravity (mGal). Densities (black label) are in 1000×kg·m<sup>-3</sup>.

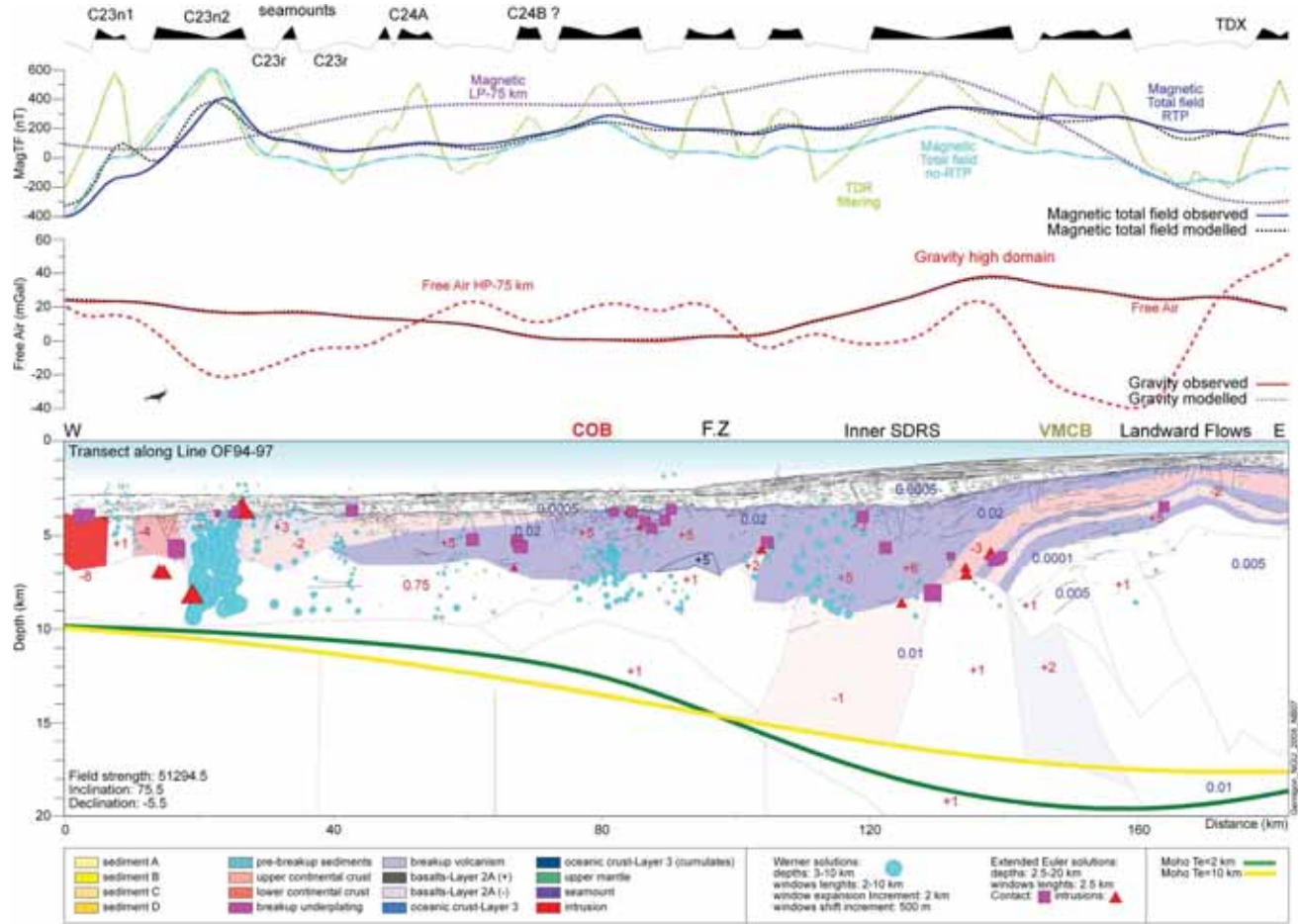


Figure 10.11 Magnetic modelling along the depth converted OF94-97 seismic profile. The detailed geometries of the bodies are controlled by reflection and refraction seismic data and compared with the flexural Mohos deduced assuming different flexural elastic thickness of the plate. The top panel represents the TDX, tilt derivative, low-pass filtering and the observed and calculated residual IGRF and RTP corrected magnetic anomaly (nT). The middle panel represents the observed and calculated free air gravity anomaly and the 75 km high-pass filtering of the free air gravity (mGal). Susceptibilities (blue labels) are in SI units and remanence (red labels) in A/m in the lower panel.

## 11 GEODYNAMIC AND TECTONIC IMPLICATIONS

Laurent Gernigon

### 11.1 Understanding the breakup

Compared to typical magma-poor margins, the COT of the Møre volcanic margin, deduced from the new observations and the modelling is relatively narrow, reaching only a few tens of kilometres in average (40-80 km). This contrasts with the long periods of pre-breakup stretching, perhaps lasting 25 Ma or more, and the great widths of stretched lithosphere, extending across 150 km or more, found on many magma-poor margins (Boillot et al. 1989; Manatschal and Bernoulli 1998; Funck et al. 2004; Manatschal et al. 2007; Peron-Pinvidic et al. 2007). The meaning of the COT and how this transition takes place is poorly understood not only along the mid-Norwegian margin but also for many rifted margins. Much of our present knowledge on the onset of breakup is also based on observations from old and cold passive margins (volcanic or magma poor margins) where the location of the conjugate margin is ambiguous and the basement is buried by thick sediments or voluminous lava flows. Modern and active transition zones between rifting and spreading boundaries are found only in limited world locations. The Red Sea, the Ethiopian Rift and the Gulf of Aden are currently forming as a result of intra-cratonic rifting between the Arabian and Africa plates (Cochran and Martinez 1988; Cochran and Karner 2007; Ebinger and Casey 2001; d'Acremont et al. 2006) and could present some similarity to the Møre volcanic margin. The Woodlark Basin (Taylor et al. 1999; Goodliffe and Taylor 2007) and the Gulf of California (Lizarralde et al. 2007) are also the result of modern continental breakups, but the tectonic history is made more complex by the interaction with recently active subduction systems.

Common issues concerning the COT, including the development of the Møre volcanic margin mostly concern the localization and the lateral expression of crustal extension before and during the breakup. The formation of SDRs is probably a sudden phenomenon associated with a strong lithosphere necking. The paroxysmal phase of breakup magmatism (~55.5-53 Ma event of Saunders et al. 1997) was accompanied by localized deformation and establishment of high volumes of magma that initially formed submarine hyaloclastites and pillow lavas. These rapidly built up to sea level and then became the sites of subaerial lava flows, which flowed both landward and seaward of the breakup axis. Planke et al. (2000) describe well the developmental sequences of the volcanism along the COT including (Fig. 11.1): 1) the initial volcanism in shallow marine environment 2) a large volume effusive volcanism at seaward propagating volcanic centres creating the Landward Flows and hyaloclastics Lava Delta, 3) the emplacement of the Inner SDRs, 4) the progressive subsidence resulting in submergence of the feeder vent system resulting in formation of phreatic eruptions on the Outer Highs and 5) explosive eruptions eventually suppressed by increasing water depths and emplacement of

stacked sheets of pillow lavas or sub-marine flows forming the Outer SDRs. All these features, when correlated with seismic, coincide with specific magnetic signatures.

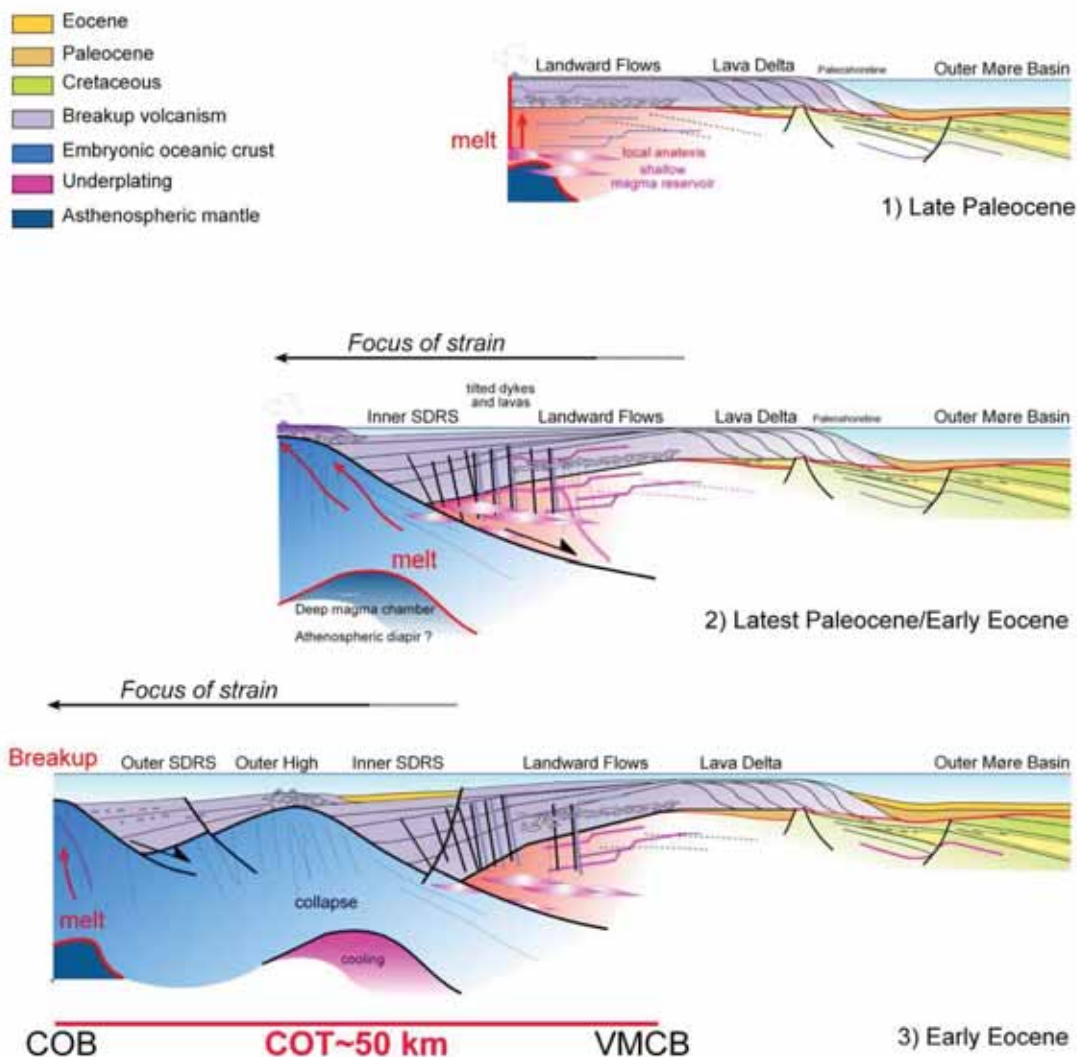


Figure 11.1 Evolution model for the major extrusive seismic facies units formed along the Continent-Ocean Transition (COT) of the Møre volcanic margin in Early Tertiary time. Modified after Planke et al. (2000). COB: Continent-Ocean Boundary; VMCB: Volcanic Margin Continental Boundary.

Field observations from East Greenland where this system is exposed onshore confirm that the continental crust located beneath the Inner SDRs is considerably dilated and intruded by gabbroic to alkali plutons and margin-parallel dykes that feed overlying traps and SDRs (Karson and Brooks 1999; Geoffroy 2005; Klausen 2006). Geoffroy, (2005) and Lenoir (2003) showed that the crustal flexing of the volcanic passive margin is a short-duration event (<2.9 Ma). New dates and estimates of finite extensional strain in the studied areas suggest high extensional strain rates which confirm that the continental lithosphere at volcanic passive margins is softened by high thermal gradients which could explain the flexure of the SDRs

possibly controlled at depth by a possible decollement above a soft and partially molten lower crust (Geoffroy et al., 2005). Evidence of detachment controlling some SDRs along the Møre margin is not so clear and such structural features were not observed on the new seimics used in our study, but some seismic observations seem to agree with such a hypothesis (Gernigon et al. 2006).

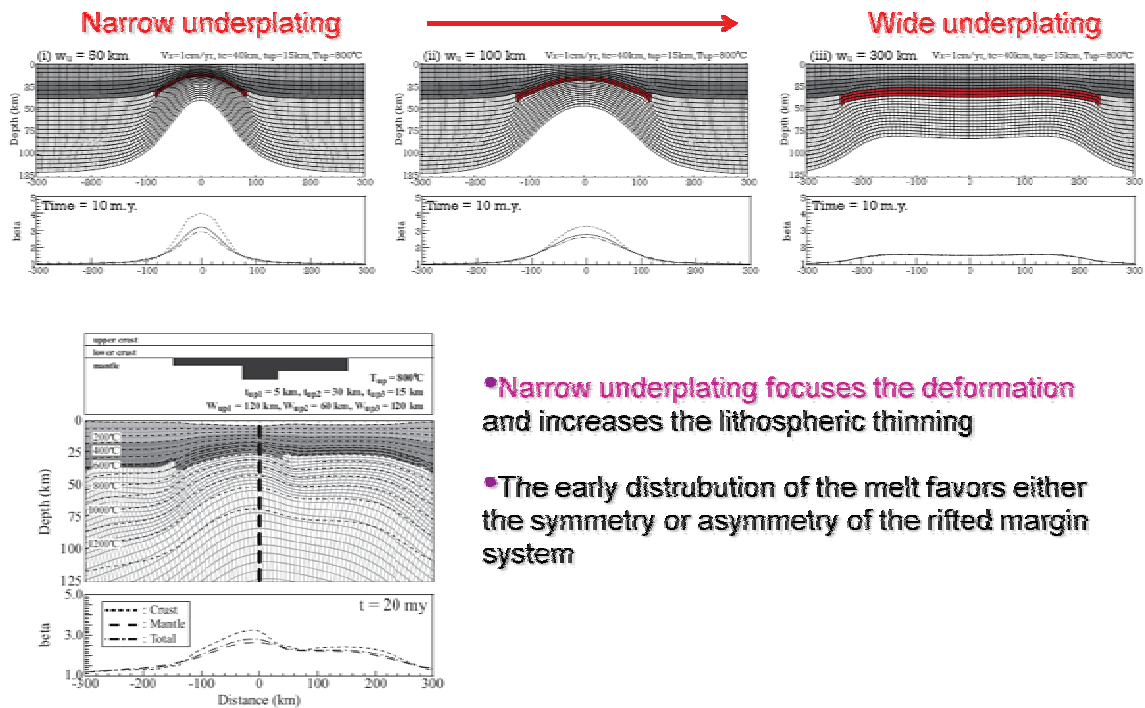
Our gravity modelling also agrees that the Inner SDRs development is accommodated at depth by shallow intrusions and underplating increasing towards the Faroes volcanic margin. High-density ( $3000 \text{ kg.m}^{-3}$ ) bodies underneath the Inner SDRs could witness the presence of mafic to ultramafic material reaching the upper part of the crust. Field evidences on Greenland where similar features are observed show that the maximum finite magma dilatation is met around old magma reservoirs, emplaced during the breakup at a similar level (Callot et al. 2002; Geoffroy 2005). These previous observations conclude that the magma intrusions could focus the deformation and influence the onset of breakup along volcanic margin. This could explain the interpreted narrow COT along the Møre and Faroes margin.

The observations along the NB-07 survey show that the COB itself is unlikely to be a precise line, instead representing a continent-ocean transition from highly stretched and intruded continental crust to dominantly new igneous crust. Identification of earlier seafloor spreading anomalies from lavas erupted subaerially along the Møre volcanic margin, as those on the Faroes area, is likely to be extremely uncertain. Factors leading to uncertainty include: the long flow lengths of lava flows, and their complex interaction with topography, local intrusions and the atypical tilt and stack of the lava flows observed along the SDRs sequences which can reduce the amplitude of the magnetic anomalies.

The COB defined near C24r is usually concordant with abyssal magnetic fabrics, but along the COT linear anomalies prior to C24b and C24r may be either concordant or discordant with continental rift fabric. The new survey suggests that between C24b and C24a, spreading rates vary between  $39.4 \pm 2$  and  $16.2 \pm 2$  mm/year. The distribution is not random and shows that higher spreading rates are observed in the central part of the survey area and decrease progressively both to the northern and southern parts. The spreading rate distribution previously suggested that the onset of breakup initiated between the EJMfz and the Faroes Plateau, probably initiated from unclear initial spreading cells probably initiated along the COT before lateral propagation towards the Jan Mayen Transform margin and the Faroes volcanic shear margin to the south. At least three oceanic segments controlled by individual cells can be proposed in the Norway Basin: 1) One south of the Jan Mayen transform margin, bounded to the south by the Jan Mayen Fracture Zone 2) one south of the Norway Basin pseudofault, west of Domain 1 and 3) a last segment, north of the Faroes volcanic shear margin. Each segment interacts and seems to overlap locally.

Several models have been proposed to explain the spreading centre nucleation and segmentation by varying the amount of extension prior to the initiation of sea-floor spreading

(Vink 1982; Ebinger and Casey 2001; Cochran and Karner 2007). Numerical models have shown that the thickness and composition of the crust, the geotherm, the extension rate, the strength and distribution of pre-existing weak zones and the distribution of mafic underplated material likely contributed to the margin segmentation and onset of breakup (Dunbar and Sawyer 1988; Dunbar and Sawyer 1989; Dunbar and Sawyer 1996; Harry and Bowling 1999; van Wijk and Cloetingh 2002; Corti et al. 2003; Lavier and Manatschal 2006). Recent modelling shows that the initial distribution of mafic intrusions at depth could most likely contribute to margin asymmetry, localization of the deformation and subsequent punctiform initiation of the spreading cells (Fig.11.2) (Yamasaki and Gernigon 2008). The injection of huge volumes of melt into the stretching COT weakened it greatly, allowing localization of the deformation, rapid differential thinning and progress to seafloor spreading (Yamasaki and Gernigon 2008).



•Narrow underplating focuses the deformation and increases the lithospheric thinning

•The early distribution of the melt favors either the symmetry or asymmetry of the rifted margin system

Figure 11.2 Effect of mafic underplating on depth dependent stretching, localization of the deformation and margin asymmetry. After Yamasaki and Gernigon, (2008)

The segmentation and initial distribution of underplated bodies emplaced along the COT from Møre to Faroes probably influenced the breakup and distribution of the second order discontinuities. At the present stage, a complete picture of the melt distribution all along the Møre and Faroes margins is still unclear. Berndt et al. (2001b) already suggested a spatial correspondence of decreased volcanism with the location of the JMFZ influenced by the Jan



Mayen transform margin. According to Berndt et al. (2001b) the Vøring Marginal High locally consists of an up to 16 km thick magmatic column while the maximum amount of magmatic material on the southeastern margin segment is not more than 1 km. Berndt et al. (2001) suggest that heat flow probably decreased the temperature of the magma source region underneath the rifting, continental lithosphere near the incipient Jan Mayen transform margin, and attribute the observed smaller amount of volcanism at the transform margin as compared to the adjacent rifted margins to this process.

The transition zone between the JMFZ and the Norway Basin pseudo-fault could coincide with this relatively amagmatic segment between the Møre and Vøring Marginal Highs, affected by thick SDRs and thicker underplating. The distribution of breakup underplating previously controlled or necessarily not by the preexisting margin heterogeneities could have favour the initiation and subsequent development of such an oceanic discontinuities. South of the Faroes Fracture Zone, the nature of the magnetic anomalies are still unclear and could also reflect local and soft instabilities influenced by the Iceland anomalies. According to Smallwood and White (2002) there is a long history of major ridge jumps in the region close to the core of the Iceland plume (Kristjansson and Jonsson 1998; Garcia et al. 2003; Sigmundsson 2006). It could have been similar during and after the breakup north of Faroes and all along the Greenland-Iceland-Faroes Ridge. Such ridge jumps could explain the complexity of the anomalies observed north of the Faroes, which do not oftent allow a one to one correlation with the anomalies observed in the Norway Basin. However, the tilt of the lava expected between the Faroes and Iceland, possible dike swarms and other lineation due to topography could produce similar ambiguous features.

Observations in the southern Red Sea (Bonatti 1985; Bonatti 1987; Cochran and Karner 2007; d'Acremont et al. 2005) also suggest similar spacing of discontinuities and indicate that a punctiform initiation of spreading may be caused by asthenospheric upwelling, the wavelength of which is controlled by the ratio of the viscosities and the layer thicknesses (Bonatti 1985). Once a diapir reaches the surface at the centre of a segment it continues to grow along strike, eventually merging with its neighbours to create a continuous spreading centre. During rifting, adjacent segments may be offset by accommodation zones that eventually form the site of oceanic transform faults (Cochran and Martinez 1988). In the Woodlark Basin, two models for the initiation of sea-floor spreading have been proposed (Taylor et al. 1999) and could also be applied to the Norwegian system. One involves the propagation of sea-floor spreading into the rifted continental crust; the other includes simultaneous nucleation of sea-floor spreading cells.

Other studies of the geological and dynamic processes by which sea-floor spreading initiates in a continent (Ebinger 2000; Ebinger and Casey 2001) demonstrate that many of the details are highly debated. One shortcoming of all these studies is that uncertainties remain about how the spreading centre first ruptures the surface and how this location is related to the late-stage continental faulting. The early igneous activity is not necessarily associated with only extensional rifting and crustal thinning but could be associated with old crustal zones of

weakness. This observation is consistent with a conclusion of Geoffroy (1998) that even during the extrusive phase of large igneous provinces (LIP) evolution magma is channelled through pinpoint crustal pathways that extend downwards to the mantle and may be associated with reactivated suture zones. It is considered probable that within the NAIP early magmatic activity also affected more outboard zones of weakness, and it is possible that these were sufficiently damaged that they became the focus of subsequent igneous activity and finally became the sites of crustal rupture after localisation of the deformation. In the Møre Marginal High and along the Faroes shear margin, the situation could be similar. A possible prolongation of deep shear zones initially located near the COT could have favoured the melt emplacement at a shallow level and caused the weakening of the lithosphere, allowing the breakup to initiate along this specific area. Analogue and numerical models suggest that subsequent deformation and breakup should focus above such soft and weak lithospheric segments (Callot et al. 2002; Yamasaki and Gernigon 2008).

## **11.2 Early spreading dynamics: hot and warm lithosphere**

When the breakup initiated in the Norway Basin, the early spreading system generates prominent seafloor spreading anomalies, which suggest a NW-SE spreading extension. Except the JMFZ and the Faroes Fracture Zone, the spreading axis was unbroken by any fracture zones other than a 5-50 km dextral offset. Some diffuse magnetic zones suggest, however, the presence of second order discontinuities, overlapping ridges and minor fracture zones. In tectonic style, this interval of spreading most closely resembles fast-spreading ridges such as the present day East Pacific Rise. Most of the instabilities, overlaps and discontinuities seem to focus in the northern part of the survey area above the regional free air gravity high region, which dominates the northern part of the survey.

We suggest that such non-rigid instabilities arise because the enhanced melt production and thicker than normal crust produced in the North Atlantic produce a rheologically weak spreading axis. Oceanic crust was somewhat thicker than normal (10-13 km, compared to c. 6km for normal ocean basins) and is indicative of atypical melt production in the region (e.g., Breivik et al. 2006). The frequent crustal melt injection episodes produced by the fast spreading rate maintain the spreading axis at a hotter temperature, on average, than that of a normal slow-spreading ridge. Fast spreading combined with enhanced melt production may have produced a weak spreading axis. The thick and warm oceanic crust predicted from C24 to C22 infer periods of higher magma supply in that area when plate separation was more dominated by fast spreading rates (e.g., Breivik et al. 2008).

Local round magnetic anomalies can witness off-axis seamounts and high magmatic production along the Norway Basin, still active during Early to mid-Eocene time. Potential and discrete ridge jumps are also expected along the Norway Basin. The alignments of off-axis intrusions with reverse polarity between C24b and C23n and between C23n1 and C22n may eventually

represent some relicts of aborted rift axis formed during discrete spreading reorganisation and rift jumps. Numerical modelling shows that atypical off-axis magmatism can produce such instabilities (Mittelstaedt et al. 2008). Such discrete rifts jumps could explain the slight asymmetry observed on either side of the Aegir Ridge suggested by Jung and Vogt (1997). However, the poor magnetic resolution on the western side of the aborted ridge does not allow us to truly validate this asymmetry (Fig. 11.3). Due to the high magmatic production along the proto-oceanic axis, it is also likely that similar migration and jumps of the deformation could have occurred along the COT. Cluster of anomalies, south of the Norway Basin pseudofault and large seamounts observed on seismic could represent some aborted rift axis.

It may be difficult for an entire oceanic segment to respond instantaneously at the scale of the Norway Basin. Local reduction in melt production and associated thermal cooling may have strengthened the lithosphere, and caused the formation of second order discontinuities such as the Norway Basin pseudofault. In the Norway Basin, the oceanic system reorganised itself according to these complex magmato-tectonic processes. However, the early distribution of the discontinuities is often influenced by the original segmentation of the margin and new fracture zones appear somehow to be influenced by previous heterogeneities, themselves initiated at breakup time (e.g. the Central Fracture Zone). Propagation of competing spreading segments is often observed, especially in the area of the Norway Basin pseudofault. Prior to C22, ridge propagation occurs from the central part towards the northeastern and southwestern flank of the survey. At the same time the oceanic segment located north of the Norway Basin pseudofault propagated to the southwest producing the complex but no-rigid magnetic pattern of the Norway Basin pseudofault. Several mechanisms have also been proposed to cause the propagation and local reorganisation of the spreading ridge segments. Popular hypothesis explaining along-axis migration of some small-offset propagators relate crack length with crack propagation driving force (Macdonald et al. 1991): a longer ridge section should lengthen at the expense of adjacent shorter sections. It has also been proposed that rift propagation may be due to relative motions between the spreading plate boundary and the underlying, fixed asthenosphere and/or the migration of the magma chamber with time (Schouten et al. 1987; Tucholke and Schouten 1988; Gac et al. 2006).

### **11.3 Late spreading dynamics: colder lithosphere and fan-shaped development of the ridge system**

Changes in the direction of sea-floor spreading from NW-SE to NNW-SSE coincide with a significant rift reorganisation and the onset of fan-shaped development in the Norway Basin (Figs. 11.4, 11.5). In contrast with the early spreading system, lower magma supply decrease with the lower spreading rates from C22 to C13 and possibly C10 to the north. Seismic observation and the magnetic pattern show that most of the separation was taken up by faulting and formation of rigid discontinuities like the Central Fracture Zone, north of 64° (Fig. 10.6). Lower spreading rates after C22 coincide with higher faulting of the oceanic crust. The

spreading segments strike approximately perpendicular to the new spreading direction, and the transform faults lay approximately parallel to the spreading direction, although like small offset transforms found elsewhere, they may deviate locally considerably from it. This change in style can be seen in both the gravity and magnetic maps and can also be seen in the structural style observed on modelled transects presented in the previous section (Fig. 10.6).

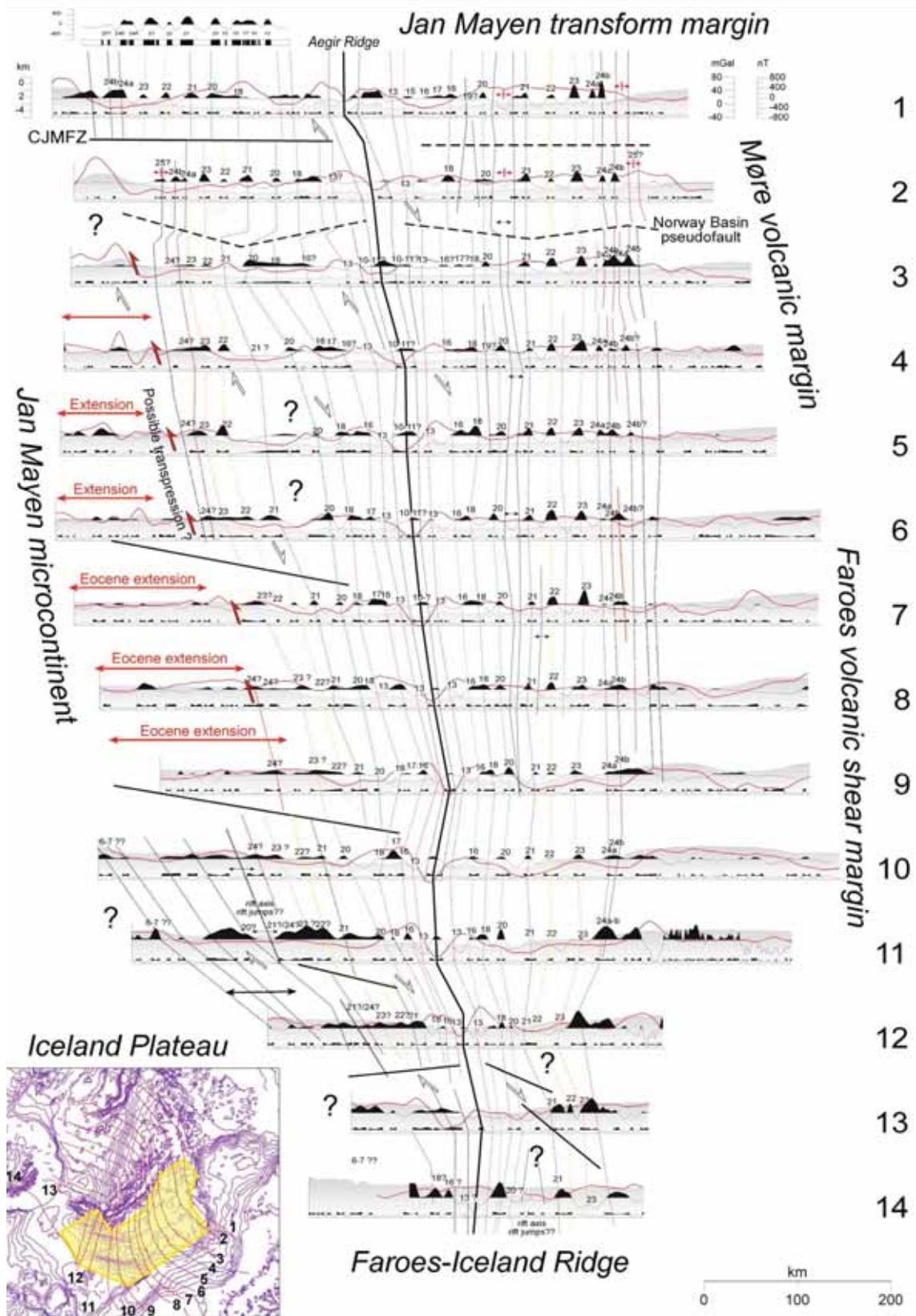


Figure 11.3 Bathymetric, gravity and magnetic profiles along regional flow-lines across the Norway Basin.

This Eocene event after C22n is definitively an important and a new geodynamic observation in the Norway Basin and could reflect a regional reorganisation of the whole Norwegian-Greenland Sea. The new survey illustrates the onset of a fan-shape development of the spreading system after C22n (Fig. 11.3). The onset of propagation and fan-development from north to south suggested between C22 to C13 is clearly associated with a regional change of the spreading direction. The C22-C21 event also coincides with the onset of an atypical magmatic event along the JMFZ (The Vøring Spur overcrusting event) and development of a triple junction in the northern part of the NB-07 survey area (Gernigon et al. 2008). These events are surprisingly concomitant and should have some implications concerning the early Cenozoic development of the margin and the overall plate reconstruction at the scale of the north Atlantic. The NB-07 provides a clear tape recording of this Mid-Eocene tectonic event.

Most of the previous papers have already proposed similar models involving varying degree of fan-shaped development on the Aegir Ridge, with a rotation pole located into the southern end of Aegir Ridge (Talwani and Eldholm 1977; Nunns 1983; Skogseid and Eldholm 1987; Kuvaas and Kodaira 1997; Lundin and Doré 2002; Lundin and Doré 2005; Scott et al. 2005). The previous model often involves the counterclockwise rotation of the Jan Mayen microcontinent splitted away from Greenland by opposite. This idea pre-supposes an opposing fan-shaped spreading along the Kolbeinsey Ridge which is still discussed in many recent papers (e.g., Lundin and Doré 2005; Scott et al. 2005). An onset of the concurrent fan-spreading has been proposed between C18-C17 and C7 by most of the authors. Kuvaas and Kodaira (1997) suggested that the fan-development could not start before C7 time.

Scott et al. (2005) proposed a different model and suggested that spreading from C24 to C18 had a constant NW-SE azimuth and that the Aegir Ridge was parallel to Mohns and Reykjanes ridge (Fig. 11.4). From C18 to C17 time, Scott et al. (2005) suggest a spreading reorganisation from NW-SE to WNW-ESE and a northward propagation of the Kolbeinsey Ridge from C17 to C6. Their model proposed that the Jan Mayen microcontinent was separated from Greenland by a non-rotational model involving a succession of fracture zones which cut the Jan Mayen Ridge and the Chron C24r to C18 oceanic crust to the east. Their model involves a serious segmentation of the central part of the Jan Mayen Ridge during Oligocene time and a stepwise formation of the oceanic crustal offset by numerous fracture zones.

Our interpretation provides new elements for discussion. The new data suggest that normal, almost sub-parallel rift development only occurred from C24 to C22n (Figs 11.3, 11.5). The new data show that the fan-shaped development of the Norway Basin spreading system really exists and developed precisely after C22n and not C18-C17 as previously proposed in the literature. Our observation does not support the model of Scott et al. (2005). Some faults are well observed between C22 to C10 but they represent classic oceanic transforms which accommodated the fan-development of the spreading system. The fracture zones observed from C22 to C13 are trending NNW-SSE and do not agree with the E-W trending fracture zones suggested by the model of Scott et al. (2005).

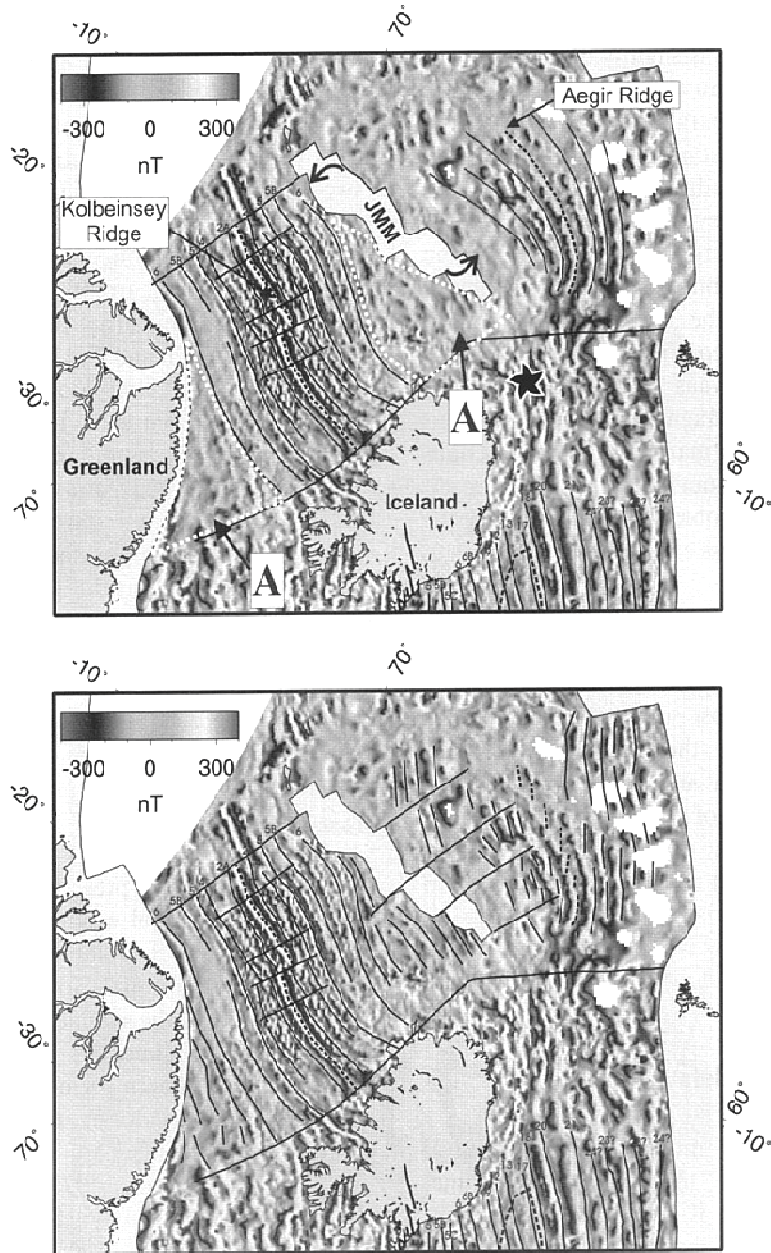


Figure 11.4 Different models for the evolution of the Norway Basin. The upper panel represents the classic fan-shaped spreading interpretation initially suggested by Talwani and Eldholm (1977) and Nunns (1983). The star is the approximate rotation pole for spreading on Aegir ridge. This model involves a compensating triangular system between Greenland and the Jan Mayen microcontinent (A on the cartoon). The lower panel shows an alternative dislocation scenario proposed by Scott et al. (2005).

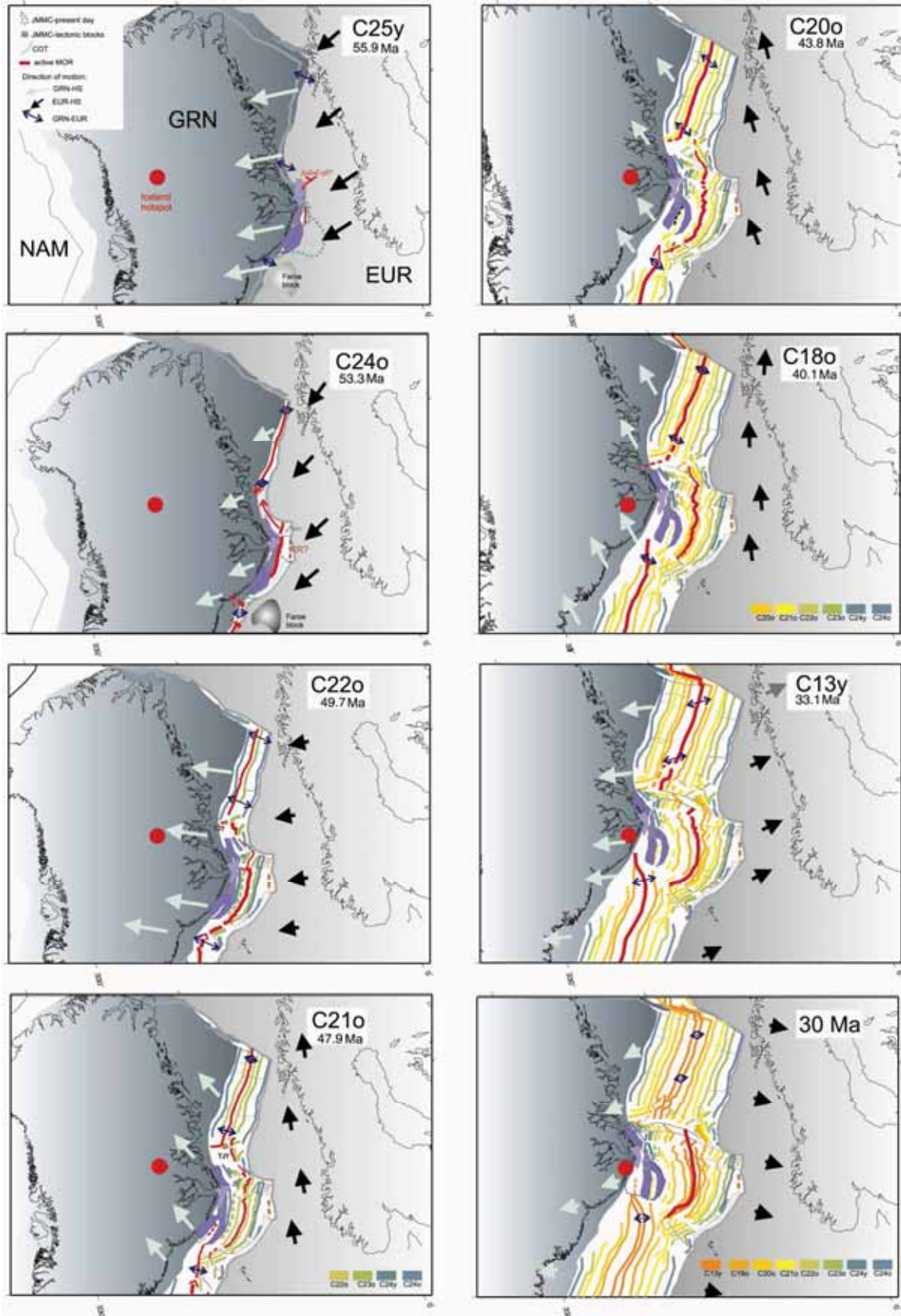


Figure 11.5: Geodynamic evolution of the Norway Basin (Gaina et al., in preparation)



Our model should also involve and supports a compensating geometry on the conjugate part of the Aegir Ridge or between Greenland and Jan Mayen starting at C22n (Fig. 11.5). However, spreading anomalies are only identified at C7-C6 (25.5-20 Ma) on both sides of the Kolbeinsey Ridge and do not easily support such a compensating spreading system to the east of the Jan Mayen microcontinent. Our interpretation suggests that a time gap exists between the onset of the fan-development after C22 (49.7-49.0 Ma) on the eastern side of the Aegir Ridge and the onset of such a propagating spreading system between Jan Mayen and Greenland from C7 (25-26 Ma) to possibly C13 (33.5-33 Ma) according to the propagation model of Lundin and Doré (2005). Our new interpretation suggests that a compensating deformation zone should also exist between C22 and C13, somewhere in the western part of the Aegir Ridge to explain this time gap of ~15-25 Ma (Fig. 11.5). An optional model is to involve possible compression of the oceanic crust between the Jan Mayen Ridge and the Aegir Ridge to compensate and accommodate the conjugate spreading system. An alternative and more reliable option is to involve a progressive continental extension of the southern Jan Mayen area to fully accommodate the fan-shape development of the east Aegir Ridge system or a composite model involving both minor extension in the southern part of Jan Mayen and compression in the central part of the microcontinent (Fig. 11.5)(Gaina et al., in preparation).

## 12 CONCLUSION AND PERSPECTIVES

### 12.1 Main results

- The new survey NB-07 allowed the previous magnetic gaps between the Faroes Plateau and the outer Vøring Basin to be filled and allowed a re-interpretation of the Norway Basin.
- The magnetic anomalies currently observed along the NB-07 reflect the different structure, composition and geodynamic history of the oceanic crust of the Norway Basin and surrounding margins that developed during Eocene-Oligocene time. Several magnetic domains with different magnetic pattern have been observed in the new NB-07 survey and provide new information about the spreading evolution and architecture of the Norway Basin from C24 to C10.
- To illustrate this preliminary interpretation of the NB-07 survey, three geological crustal sections have also been interpreted using forward gravity and magnetic modelling. The forward potential field modelling of the area of the Norway Basin is limited, because of the few constraints available. Gravity and bathymetry data already show that lateral heterogeneities exist in the area, indicating later tectonic events in addition to the general opening of the North Atlantic. However, as only OBS results exist along one line through the northern part of the study area, the interpretations of the density structure remain uncertain and ambiguous to the south. We decided to model only the known topography and adjusted an inner basement horizon to produce intermediate wavelength anomalies and defined a reasonable flexural Moho to constrain the base of the crust.
- The meaning of the COT has been discussed and a proposition of COB has been proposed. The timing of breakup has also been discussed. The COT is extremely narrow (<75 km) and strongly affected by magmatism, which influence the magnetic pattern. The gravity modelling suggests evidences of strong necking and mid to upper crustal intrusions at the level of the Inner SDRs wedges.
- The breakup probably initiated in the central part of the Møre volcanic margin and propagated regionally from north west to southwest from C24 to C22. In the southwestern part, shearing along the COT is observed and coincides with the development of a volcanic shear-margin in the northern part of the Faroes Plateau. During that period, competing oceanic segments have been observed leading to the formation of second and third order unconformities characterised by an overlapping system and a pseudofault development (the Norway Basin pseudofault).

- From C22 to C13 (and possibly C11-10 in the northern part of the Norway Basin, spreading rate decreases and rigid faulting increases, leading to the formation of a new intra-oceanic fracture zone (the Central Fracture Zone), with large displacement increasing from C22 to the level of the Aegir Ridge.
- After C22n, the spreading center accommodated an important geodynamic adjustment. The transition from C22n to C20n reflects a significant change in the Norway Basin. The spreading direction changes from NW-SE between C24 and C22 to NNW-SSE after C22n. At the same time a crudely northward-widening fan-shaped magnetic anomaly pattern developed along the active Aegir Ridge. Compared to the previous models, the new dataset clearly shows that the onset of the fan-shaped evolution definitively starts earlier at C22n (49.7-49.0) instead of C18-C17 (40.1-36.6) as previously proposed.
- Comparison with the conjugate system on the northwestern side of the Aegir Ridge is still unclear due to poor coverage, especially in the southern part of the Jan Mayen Ridge. Our new interpretation suggests, however, that a compensating deformation zone should also exist between C22 to C13, somewhere in the western part of the Aegir Ridge before the onset of breakup between Greenland and the Jan Mayen microcontinent at C7 (or C13 ?). Continental extension of the southern Jan Mayen microcontinent in Eocene time is required to compensate the spreading evolution observed in the eastern part of the Aegir Ridge. This idea should be tested in the future. One scientific problem to solve now is how continental rifting could develop at the same time as spreading occurred in the Norway Basin?

## 12.2 Perspectives

- The NB-07 survey will be better integrated with previous aeromagnetic surveys at the scale of the Norwegian-Greenland Sea to re-evaluate and update the plate tectonic evolution of the whole North Atlantic in light of the new observations. The NB-07 survey provides new kinematic and geodynamic constraints, which can be used to refine the tectonic evolution of the conjugate margin and the development of the Jan Mayen microcontinent. Plate reconstructions could be refined and will allow a better fit of the pre-breakup configuration of the conjugate margins.
- We also suggest to better link the oceanic and continental part in the future. The segmentation of the Norway Basin is most likely controlled by the early rift and breakup history. Potential field modelling and seismic interpretations of the outer Møre Basin and the conjugate Jan Mayen margin, integrated with our new oceanic observations are relevant to better assess the structure and evolution of the adjacent sedimentary basins mostly covered and hidden by Tertiary lava flows. It is also an important point to

understand and document the dynamic processes during the rift to drift transition. The key issues are to understand why and how different portions of the Norway Basin show different stages in the development of the spreading after continental rifting. Two hypotheses have been summarized in our discussion: 1) the structural framework of the pre-breakup rift system could cause differences in the total extension leading to the puctiform initiation of the breakup, 2) the lithosphere of the Møre and Faroes volcanic margins could be locally and rheologically modified and weakened by magmatic processes initiated by local and narrow depth-dependant stretching and puctiform initiation of the breakup. All these points are still unclear but could have serious implications both on the lateral variation of the lithospheric isotherm, plumbing and lateral segmentation and architecture of the Late Cretaceous-Paleocene rift basins expected underneath the lava flows.

- More work is still required to fully constrain the evolution of the Norway Basin. A similar modern aeromagnetic survey between the Jan Mayen microcontinent and the Aegir Ridge will also be an obvious and relevant proposal to fully understand the spreading evolution of the Norway Basin. A remapping of the Faroes-Iceland Ridge will also be relevant to better understand the transition to the southern spreading system initiated to the west of the Rockall and Faroes margins.

### 12.3 Petroleum implications-discussion

Previous contributions already suggested the importance of plate reorganisation in the Norwegian-Greenland Sea and its implications for compressive stress and trap formation on the mid-Norwegian margin.

Doré and Lundin (1996) suggested that the main period of dome formation in the Møre and Vøring Basin could be attributed to the change in spreading from NW-SE to a more E-W trend that took place at the beginning of the Oligocene (Chron 13, 33 Ma). According to this hypothesis, the change in plate motion created a sinistral transpressive regime via possible shear adjustments along the NW-SE lineaments.

However, recent work has led Doré et al. (2008) to re-evaluate this hypothesis because new evidences from drilling and interpretation of 3D seismic data mostly suggest a main Early to Middle Miocene phase of growth of the N-S anticlines along the Jan Mayen Lineament (Ormen Lange Dome, Havsule Dome, and Modgunn Arch). Based on the fact that the main plate reorganisation occurred in Oligocene (C13), Doré et al. (2008) explained the early compressive events of the mid-Norwegian margin by gravitational stress initiated from the proto-Iceland.

Our interpretation provides new elements of discussion and evidences a major Early to Mid. Miocene plate reorganisation phase in the Norway Basin after C22n (49.03-49.71Ma). This

event fits in time with the early phase of growth of the numerous anticlines along the mid-Norwegian margin. Even if more quantitative interpretation and modelling work is required to validate this hypothesis, we propose that the early model of Doré and Lundin (1996) could still be applied in Eocene. Change in spreading direction from NW-SE to a NNW-SSE and local extension south of the Jan Mayen microcontinent could possibly initiate local transpressive stress along pre-existing NW-SE lineaments on the mid-Norwegian margin and initiate dome formation.

Understanding the margin segmentation and location of the transfer systems is also a major issue to constrain basin compartmentalisation and paleogeography. A better assessment and a validation of the oceanic fracture zones can help to detect potential transfer zones along the outer Møre Basin and along the Faroes margin. It can be useful to evaluate or reevaluate conventional paleogeographic models of sand transport via such transfer zones often interpreted as potential sand migration pathways (Fjellanger et al. 2005; Henriksen et al. 2005).

For basin modelling of petroleum systems, a proper description of the margin segmentation and 3D geometry is also important. The narrow COT suggested by the NB-07 survey suggests that a strong differential stretching of the margin occurred during the onset of breakup. Identification of different spreading compartments on the oceanic domain can also help to better quantify or explain the rift dynamic processes involved during the latest Cretaceous-Paleocene phase of rifting in the outer Møre Basin. It can be useful to determine if there is lateral variation of the differential stretching factors coupled or not with the distribution of the magmatism at depth (underplating and plumbing segmentation). This could have implications on the rift architecture, margin asymmetry and temperature evolution in the distal and frontier areas. Furthermore, the thermal history of the Norway Basin likely influenced the basin located near the COT. A new magnetic picture provides new and accurate spreading rates which can be later used to better quantify the thermal evolution of the Norway Basin after breakup.

### **13 ACKNOWLEDGEMENTS**

NGU in collaboration with the Faroes Earth and Energy Directorate (Jardfeingi), Conoco Phillips, Norwegian Petroleum Directorate, Norske Shell, StatoilHydro and Total Norge financed the Norway Basin Aeromagnetic Survey 2007. Rolf Lynum, Eimar Dalsegg and Jomar Gellein participated in the field work. NPD provided seismic, bathymetric and aeromagnetic data from the Norwegian-Greenland Sea area. Thomas Varming initiated the interpretation of the Faroes seismic line OF-97-97 and helped us to get relevant data in the Faroes area. Carmen Gaina kindly provided the plate reconstructions. We express our thanks to these companies, institutions and persons.

## 14 BIBLIOGRAPHY

- Abrahamsen, N. 2006: Palaeomagnetic results from the Lopra-1/1A re-entry well, Faroe Islands. **Geological Survey of Denmark and Greenland Bulletin 9**, 51-65.
- Abrahamsen, N. & Waagstein, R. 2006: Magnetic logs from the Lopra-1/1A and Vestmanna-1 wells, Faroe Islands. **Scientific Results from the Deepened Lopra-1 Borehole, Faroe Islands 9**, 41-49.
- Abrahamsen, N., Schoenharting, G. & Heinesen, M. 1984. Palaeomagnetism of the Vestmanna core and magnetic age and evolution of the Faeroe Islands. In O. Berthelsen, A. Noe-Nygaard and J. Rasmussen (eds.) **The Deep Drilling Project 1980-1981 in the Faeroe Islands**. Annales Societatis Scientiarum Færoensis, Tórshavn, 93-108.
- Allerton, S. & Tivey, M.A. 2001: Magnetic polarity structure of the lower oceanic crust. **Geophysical Research Letters 28(3)**, 423-426.
- Andersen, O.B. & Knudsen, P. 1998: Global marine gravity field from the ERS-1 and Geosat geodetic mission altimetry. **Journal of Geophysical Research-Oceans 103(C4)**, 8129-8137.
- Anderson, D.L. & Natland, J.H., 2005: A brief history of the plume hypothesis and its competitors: Concept and controversy. In G.R. Foulger, J.H. Natland, D.C. Presnall and D.L. Anderson (eds.) **Plates, Plumes & Paradigms**. Geological Society of America Special Paper 388, pp. 119-145.
- Archer, S.G., Bergman, S.C., Iliffe, J., Murphy, C.M. & Thornton, M. 2005: Palaeogene igneous rocks reveal new insights into the geodynamic evolution and petroleum potential of the Rockall Trough, NE Atlantic Margin. **Basin Research 17(1)**, 171-201(31).
- Arkani-Hamed, J. 2007: Differential reduction to the pole: Revisited. **Geophysics 72(1)**, L13-L20.
- Arkani Hamed, J. 1988: Differential reduction to the pole of regional magnetic anomalies. **Geophysics 53**, 1592-1600.
- Bainbridge, G., Musselman, C., Whitehead, N. & McDonald, N., 2002: Euler 3D Deconvolution (v5.1.5). Processing, analysis and visualization system for 3D inversion of potential field. Tutorial and user guide. **Geosoft incorporated**, 66 pp.
- Baranov, V. 1957: A new method for interpretation of aeromagnetic maps:pseudo gravity anomalies. **Geophysics 22**, 359-383.
- Barbosa, V.C.F., Silva, J.B.C. & Medeiros, W.E. 1999: Stability analysis and improvement of structural index estimation in Euler deconvolution. **Geophysics 64(1)**, 48-60.
- Barbosa, V.C.F., Silva, J.B.C. & Medeiros, W.E. 2000: Making Euler deconvolution applicable to small ground magnetic surveys. **Journal of Applied Geophysics 43(1)**, 55-68.
- Behn, M.D. & Lin, J. 2000: Segmentation in gravity and magnetic anomalies along the US East Coast passive margin: Implications for incipient structure of the oceanic lithosphere. **Journal of Geophysical Research-Solid Earth 105(B11)**, 25769-25790.
- Beicip-Franlab 2002: Tutorial - EasyDepth 2.0. The Basin Modeling line. **Beicip-Franlab**, 28 pp.
- Berndt, C., Mjelde, R., Planke, S., Shimamura, H. & Faleide, J.I. 2001b: Controls on the tectono-magmatic evolution of a volcanic transform margin: the Vøring Transform Margin, NE Atlantic. **Marine Geophysical Researches 22(3)**, 133-152.
- Berndt, C., Planke, S., Alvestad, E., Tsikalas, F. & Rasmussen, T. 2001a: Seismic volcanostratigraphy of the Norwegian Margin: constraints on tectonomagmatic break-up processes. **Journal of the Geological Society 158**, 413-426.
- Bhattacharya, B.K. 1966: Continuous spectrum of the total magnetic field anomaly due to rectangular prismatic body. **Geophysics 31**, 97-121.
- Birch, F. 1996. Compressibility, elastic constants. In S.P. Clark (ed.) **Handbook of physical constants**. Geological Society of America, Memoir, 97-174.
- Blakely, R.J. 1995: **Potential Theory in Gravity and Magnetic Applications**. Cambridge University Press, 461 pp.
- Blakely, R.J. & Simpson, R.W. 1986: Approximating edges of source bodies from magnetic or gravity anomalies. **Geophysics 51**, 1494-1498.
- Blakely, R.J., Wells, R.E., Yelin, T.S., Madin, I.P. & Beeson, M.H. 1995: Tectonic Setting of the Portland-Vancouver Area, Oregon and Washington - Constraints from Low-Altitude Aeromagnetic Data. **Geological Society of America Bulletin 107(9)**, 1051-1062.

- Bleil, U. & Petersen, N. 1983: Variation in magnetization intensity and low temperature titanoniagnetite oxidation of oceanic floor basalts. **Nature** **301**, 384.
- Blystad, P., Brekke, H., Færseth, R.B., Larsen, B.T., Skogseid, J. & Tørudbakken, B. 1995: Structural elements of the Norwegian continental shelf, Part II. The Norwegian Sea Region. **Norwegian Petroleum Directorate Bulletin** **8**, 0-45.
- Boillot, G., Mougnot, D., Girardeau, J. & Winterer, E.L. 1989: Rifting Processes on the West Galician Margin, Spain, In Tankard, A. J. & Balkwill, H. R. (eds.) **Extensional Tectonics and Stratigraphy of the North Atlantic Margins**. American Association of Petroleum Geologists, Memoir, 46, 363-377.
- Bonatti, E. 1985: Punctiform initiation of seafloor spreading in the Red Sea during transition from a continental to an oceanic rift. **Nature** **316**, 33-37.
- Bonatti, E. 1987: Oceanic evolution; rifting or drifting in the Red Sea? **Nature** **330**, 692-693.
- Bonatti, E. 1996: Anomalous opening of the Equatorial Atlantic due to an equatorial mantle thermal minimum. **Earth and Planetary Science Letters** **143(1-4)**, 147-160.
- Breivik, A., Faleide, J.I. & Mjelde, R. 2008: Neogene magmatism northeast of the Aegir and Kolbeinsey ridges, NE Atlantic: Spreading ridge mantle plume interaction? **G-Cube. Geochemistry Geophysics Geosystem an electronic journal of the earth sciences** **9(2)**, Q02004, doi:10.1029/2007GC001750.
- Breivik, A.J., Mjelde, R., Faleide, J.I. & Murai, Y. 2006: Rates of continental breakup magmatism and seafloor spreading in the Norway Basin-Iceland plume interaction. **Journal of Geophysical Research-Solid Earth** **111(B7)**, B07102, doi:10.1029/2005JB004004.
- Breivik, A.J., Verhoef, J. & Faleide, J.I. 1999: Effect of thermal contrasts on gravity modeling at passive margins: Results from the western Barents Sea. **Journal of Geophysical Research-Solid Earth** **104(B7)**, 15293-15311.
- Brekke, H., Sjulstad, H.I., Magnus, C. & Williams, R.W. 2001: Sedimentary environments offshore Norway - an overview. In: Martinsen, O. & Dreyer, T. (eds.) **Sedimentary Environments Offshore Norway-Palaeozoic to Recent**. Norsk Petroleums Forening, Special Publication, 10, 1-15.
- Briggs, I.C. 1974: Machine contouring using minimum curvature. **Geophysics** **39**, 39-48.
- Burg, J.P. 1975: Maximum Entropy Spectral Analysis. **Stanford University. PhD thesis, unpublished**.
- Callot, J.P., Geoffroy, L. & Brun, J.P. 2002: Development of volcanic passive margins: Three-dimensional laboratory models. **Tectonics** **21(6)**, 1052, doi:10.1029/2001TC901019, 1-14.
- Cande, S.C. & Kent, D.V. 1995: Revised calibration of the geomagnetic polarity timescale for the Late Cretaceous and Cenozoic. **Journal of Geophysical Research** **100(B4)**, 6093-6095.
- Cannat, M. 1996: How thick is the magmatic crust at slow spreading oceanic ridges? **Journal of Geophysical Research-Solid Earth** **101(B2)**, 2847-2857.
- Cannat, M., Mevel, C., Maia, M., Deplus, C., Durand, C., Gente, P., Agrinier, P., Belarouchi, A., Dubuisson, G., Humler, E. & Reynolds, J. 1995: Thin Crust, Ultramafic Exposures, and Rugged Faulting Patterns at Mid-Atlantic Ridge (22-Degrees 24-Degrees-N). **Geology** **23(1)**, 49-52.
- Carlson, R.L. & Herrick, C.N. 1990: densities and porosities in the oceanic-crust and their variations with depth and Age. **Journal of Geophysical Research-Solid Earth and Planets** **95(B6)**, 9153-9170.
- Christensen, N.I. & Mooney, W.D. 1995: Seismic velocity structure and composition of the continental crust: A global view. **Journal of Geophysical Research - Solid Earth** **100**, 9761-9788.
- Clark, D.A. 1997: Magnetic petrophysics and magnetic petrology: aids to geological interpretation of magnetic surveys. **AGSO Journal of Australian Geology and Geophysics** **17(2)**, 83-103.
- Cochran, J.R. & Karner, G.D. 2007: Constraints on the deformation and rupturing of continental lithosphere of the Red Sea: the transition from rifting to drifting. In G.D. Karner, G. Manatschal and L.M. Pinheiro (eds) **Imaging, Mapping and Modelling Continental Lithosphere Extension and Breakup**. Geological Society, London, Special Publications, 282, 265-289.
- Cooper, G.R.J. & Cowan, D.R. 2006: Enhancing potential field data using filters based on the local phase. **Computers & Geosciences** **32(10)**, 1585-1591.
- Corti, G., van Wijk, J., Bonini, M., Sokoutis, D., Cloetingh, S.A.P.L., Innocenti, F. & Manetti, P. 2003: Transition from continental break-up to punctiform seafloor spreading: How fast, symmetric and magmatic. **Geophysical Research Letters** **30(12)**, 1604, doi:10.1029/2003GL017374, 1-4.

- d'Acremont, E., Leroy, S., Beslier, M.O., Bellahsen, N., Fournier, M., Robin, C., Maia, M. & Gente, P. 2005: Structure and evolution of the eastern Gulf of Aden conjugate margins from seismic reflection data. **Geophysical Journal International** **160(3)**, 869-890.
- d'Acremont, E., Leroy, S., Maia, M., Patriat, P., Beslier, M.O., Bellahsen, N., Fournier, M. & Gente, P. 2006: Structure and evolution of the eastern Gulf of Aden: insights from magnetic and gravity data (Encens-Sheba MD117 cruise). **Geophysical Journal International** **165(3)**, 786-803.
- Direen, N.G., Stagg, H.M.J., Symonds, P.A. & Colwell, J.B. 2008: Architecture of volcanic rifted margins: new insights from the Exmouth - Gascoyne margin, Western Australia. **Australian Journal of Earth Sciences** **55(3)**, 341-366.
- Dobrin, M. & Savit, C. 1988: Introduction to geophysical prospecting. 4th edition. **McGraw-Hill**, 867 pp.
- Doré, A.G., Lundin, E.R., Kuznir, N.J. & Pascal, C. 2008: Potential mechanisms for the genesis of Cenozoic domal structures on the NE Atlantic margin: pros, cons and some new ideas. In H. Johnson (ed.) **The Nature and Origin of Compression in Passive Margins**. The Geological Society, Special Publications, In press.
- Doré, A.G., Lundin, E.R., Fichler, C. & Olesen, O. 1997: Patterns of basement structure and reactivation along the NE Atlantic margin. **Journal of the Geological Society** **154**, 85-92.
- Doré, A.G. & Lundin, E.R. 1996: Cenozoic compressional structures on the NE Atlantic margin: Nature, origin and potential significance for hydrocarbon exploration. **Petroleum Geoscience** **2(4)**, 299-311.
- Dunbar, J.A. & Sawyer, D.S. 1988: Continental rifting at pre-existing lithospheric weaknesses. **Nature** **333(6172)**, 450-452.
- Dunbar, J.A. & Sawyer, D.S. 1989: How preexisting weaknesses control the style of continental Breakup. **Journal of Geophysical Research-Solid Earth and Planets** **94(B6)**, 7278-7292.
- Dunbar, J.A. & Sawyer, D.S. 1996: Three-dimensional dynamical model of continental rift propagation and margin plateau formation. **Journal of Geophysical Research-Solid Earth** **101(B12)**, 27845-27863.
- Dyment, J., ArkaniHamed, J. & Ghods, A. 1997: Contribution of serpentinitized ultramafics to marine magnetic anomalies at slow and intermediate spreading centres: Insights from the shape of the anomalies. **Geophysical Journal International** **129(3)**, 691-701.
- Ebbing, J., Lundin, E., Olesen, O. & Hansen, E.K. 2006: The mid-Norwegian margin: a discussion of crustal lineaments, mafic intrusions, and remnants of the Caledonian root by 3D density modelling and structural interpretation. **Journal of the Geological Society** **163**, 47-59.
- Ebinger, C. 2005: Continental break-up: The East African perspective. **Astronomy & Geophysics** **46(2)**, 16-21.
- Ebinger, C.J. & Casey, M. 2001: Continental breakup in magmatic provinces: An Ethiopian example. **Geology** **29**, 527-530.
- Eldholm, O. & Grue, K. 1994: North-Atlantic volcanic margins - dimensions and production-rates. **Journal of Geophysical Research-Solid Earth** **99(B2)**, 2955-2968.
- Eldholm, O., Thiede, J. & Taylor, B. 1989. Evolution of the Vøring volcanic margin. In O. Eldholm, J. Thiede and E. Taylor (eds.) **Proceedings of the Ocean Drilling Program, Scientific Results, 104. College Station, TX (Ocean Drilling Program)**, 1033-1065.
- Ellis, D., Bell, B.R., Jolley, D.W. & O'Callaghan, M. 2002. The stratigraphy, environment of eruption and age of the Faroes Lava Group, NE Atlantic Ocean. In D.W. Jolley and B.R. Bell (eds.) **The North Atlantic Igneous Province: Stratigraphy, Tectonic, Volcanic and Magmatic Processes**. Geological Society, London, Special Publications, 197. **Geological Society, London**, 253-269.
- Engen, O., Frazer, L.N., Wessel, P. & Faleide, J.I. 2006: Prediction of sediment thickness in the Norwegian-Greenland Sea from gravity inversion. **Journal of Geophysical Research-Solid Earth** **111(B11)**, B11403, doi:10.1029/2005JB003924.
- Fairhead, J.D. & Williams, S.E., 2006: Evaluating normalized magnetic derivatives for structural mapping, SEG 2006 New Orleans Annual meeting, New Orleans, USA.
- Fichler, C., Rundhovde, E., Olesen, O., Sæther, B.M., Rueslåtten, H., Lundin, E. & Doré, A.G. 1999: Regional tectonic interpretation of image enhanced gravity and magnetic data covering the mid-Norwegian shelf and adjacent mainland. **Tectonophysics** **306(2)**, 183-197.



- FitzGerald, D., Reid, A. & McInerney, P. 2004: New discrimination techniques for Euler deconvolution. **Computers & Geosciences** **30(5)**, 461-469.
- Fjellanger, E., Surlyk, F., Wamsteeker, L.C. & Midtun, T. 2005: Upper Cretaceous basin-floor fans in the Vøring Basin, Mid Norway Shelf. In B. Wandas et al. (eds.) **Onshore-Offshore Relationships on the North Atlantic Margin**. Norwegian Petroleum Society, Special Publication, 12, 135-134.
- Florio, G., Fedi, M. & Pasteka, R. 2006: On the application of Euler deconvolution to the analytic signal. **Geophysics** **71(6)**, L87-L93.
- Foulger, G.R., Natland, J.H. & Anderson, D.L. 2005: A source for Icelandic magmas in remelted Iapetus crust. **Journal of Volcanology and Geothermal Research** **141**, 23-44.
- Funck, T., Larsen, H.C., Loudon, K.E. & Ucholke, B.E.a.H.S. 2004: Crustal structure of the ocean-continent transition at Flemish Cap: Seismic refraction results. **Journal of Geophysical Research** **108(B11)**, doi:10.1029/2003JB00.
- Gac, S., Tisseau, C., Dymont, J. & Goslin, J. 2006: Modelling the thermal evolution of slow-spreading ridge segments and their off-axis geophysical signature. **Geophysical Journal International** **164(2)**, 341-358.
- Gaina, C., Gernigon, L. & Ball, P.J. 2008: Paleocene-Recent Plate Boundaries in the NE Atlantic and the formation of the Jan Mayen microcontinent. *Journal of the Geological Society, London in preparation.*
- Garcia, S., Arnaud, N.O., Angelier, J., Bergerat, F. & Homberg, C. 2003: Rift jump process in Northern Iceland since 10 Ma from Ar-40/Ar-39 geochronology. **Earth and Planetary Science Letters** **214(3-4)**, 529-544.
- Gardner, G.H.F., Gardner, L.W. & Gregory, A.R. 1984: Formation velocity and density -The diagnostic basics for stratigraphic traps. **Geophysics** **39**, 770-780.
- Geoffroy, L. 1998: Diapirisme et extension intraplaque : cause ou conséquence ? **Comptes Rendus Geoscience** **326**, 267-273.
- Geoffroy, L. 2005: Volcanic passive margins. **Comptes Rendus Geoscience** **337(16)**, 1395-1408.
- Geosoft 2004: OASIS Montaj v 6.0 Mapping and processing system, The core software platform for working with large volume spatial data. Quick start tutorials. **Geosoft Incorporated**, 258 pp.
- Geosoft 2005a: Montaj grav/mag interpretation, processing, analysis and visualization system for 3D inversion of potential field data for Oasis Montaj v6.1; Tutorial and user guide. **Geosoft Incorporated**, 65 pp.
- Geosoft 2005b: Montaj Geophysics Levelling System, processing and enhancing geophysical data extension for Oasis Montaj v6.2. Tutorial and user guide. **Geosoft Incorporated**, 68 pp.
- Geosoft 2005c: Montaj MAGMAP filtering-2D Frequency Domain Processing of Potential Field Data Extension for Oasis montaj v.6.1. **Geosoft Incorporated**, 66 pp.
- Geosoft 2005d: Montaj GridKnit, Grid extension for OASIS Montaj v6.1, Tutorial and user guide. **Geosoft Incorporated**, 27 pp.
- Gernigon, L., Olesen, O., Ebbing, J., Wienecke, S., Gaina, C., Mogaard, J.O., Sand, M. & Myklebust, R. 2008: Geophysical insights and early spreading history in the vicinity of the Jan Mayen Fracture Zone, Norwegian-Greenland Sea. *Tectonophysics*, in press.
- Gernigon, L., Marello, L., Mogaard, J.O., Werner, S.C. & Skilbrei, J.R. 2007a: Barents Sea Aeromagnetic Survey BAS-06 - Acquisition-processing report and preliminary interpretation. **NGU Report 2007.035, Geological Survey of Norway, Trondheim**. 142 pp.
- Gernigon, L., Olesen, O. & Continental Shelf Geophysics team 2007b: Challenging the Established Truths. *Geoexplor* **4**, 40-44.
- Gernigon, L., Lucazeau, F., Brigaud, F., Ringenbach, J.C., Planke, S. & Le Gall, B. 2006: A moderate melting model for the Vøring margin (Norway) based on structural observations and a thermo-kinematical modelling: Implication for the meaning of the lower crustal bodies. **Tectonophysics** **412(3-4)**, 255-278.
- Gernigon, L., Ringenbach, J.C., Planke, S., Le Gall, B. & Jonquet-Kølstø, H. 2003: Extension, crustal structure and magmatism at the outer Vøring Basin, Norwegian margin. **Journal of the Geological Society** **160**, 197-208.
- Gernigon, L. 2002: Extension et magmatisme en contexte de marge passive volcanique: Déformation et structure crustale de la marge norvégienne externe (Domaine Nord-Est Atlantique) (*Extension*

- and magmatism in a volcanic margin context : deformation and structure of the outer Norwegian margin). **PhD Thesis, "Domaines Océaniques", IUEM/UBO, Brest.** 300 pp.
- Glebovsky, V., Likhachev, A., Kristoffersen, Y., Engen, Ø., Faleide, J.I. & Brekke, H., 2003: Sedimentary thickness estimation from magnetic data in the Nansen Basin, Proceedings of the Fourth International Conference on Arctic Margins, Darmouth, Nova Scotia, Canada.
- Godfrey, N.J., Beaudin, S.L. & Klemperer, S.L. 1997: Ophiolitic basement to the Great Valley forearc basin, California, from seismic and gravity data: Implications for crustal growth at the North American continental margin. *Geological Society American Bulletin* 109, 1536-1562.
- Goll, R.M. 1989. A synthesis of Norwegian Sea biostratigraphies: ODP Leg 104 on the Vøring Plateau. **In O. Eldholm, J. Thiede, B. Taylor et al. (eds.) Proceedings of the Ocean Drilling Program, Scientific Results, 104.** College Station, TX (Ocean Drilling Program), 777-826.
- Goodliffe, A.M. & Taylor, B. 2007: The boundary between continental rifting and sea-floor spreading in the Woodlark Basin, Papua New Guinea. **In G.D. Karner, G. Manatschal and L.M. Pinheiro (eds) Imaging, Mapping and Modelling Continental Lithosphere Extension and Breakup.** Geological Society, London, Special Publications, 282, 217-238.
- Grant, F.S. & Dodds, J. 1972: **MAGMAP FFT processing system development notes.** Paterson Grants and Watson Limited.
- Grauch, V.J.S. & Cordell, L. 1987: Limitations of determining density or magnetic boundaries from the Horizontal Gradient of Gravity or Pseudogravity Data. *Geophysics* 52(1), 118-121.
- Greenhalgh, E.E. & Kuszniir, N.J. 2007: Evidence for thin oceanic crust on the extinct Aegir Ridge, Norwegian Basin, NE Atlantic derived from satellite gravity inversion. *Geophysical Research Letters* 34(6), L06305, doi:10.1029/2007GL029440.
- Gunn, P.G. 1997: Quantitative methods for interpreting aeromagnetic data: a subjective review. *AGSO Journal of Australian Geology and Geophysics* 17(2), 105-113.
- Hagevang, T., Eldholm, O. & Aalstad, I. 1983: Pre-23 magnetic anomalies between Jan Mayen and Greenland-Senja Fracture Zones in the Norwegian Sea. *Marine Geophysical Researches* 5, 345-363.
- Harry, D.L. & Bowling, J.C. 1999: Inhibiting magmatism on nonvolcanic rifted margins. *Geology* 27, 895-898.
- Hathaway, D.H., Wilson, R.M. & Reichmann, E.J. 1999: A synthesis of solar cycle prediction techniques. *Journal of Geophysical Research-Space Physics* 104(A10), 22375-22388.
- Hemant, K., Thebault, E., Manda, M., Ravat, D. & Maus, S. 2007: Magnetic anomaly map of the world: merging satellite, airborne, marine and ground-based magnetic data sets. *Earth and Planetary Science Letters* 260(1-2), 56-71.
- Henriksen, S., Fichler, C., Grønlie, A., Henningsen, T., Laursen, I., Løseth, H., Ottesen, D. & Prince, I., 2005: The Norwegian Sea during the Cenozoic. In: B. Wandas, J.P. Nystuen, E. Eide and F. Gradstein (eds.) **Onshore-Offshore Relationships on the North Atlantic Margin.** Norwegian Petroleum Society (NPF), Special Publication, 12, 111-133.
- Hey, R.N., Menard, H.W., Atwater, T.M. & Caress, D.W. 1988: Changes in direction of seafloor-spreading revisited. *Journal of Geophysical Research* 93, 2803-2811.
- Hey, R.N., Duennebie, F.K. & Morgan, J.M. 1980: Propagating rifts on mid-ocean ridges. *Journal of Geophysical Research* 85, 3647-3658.
- Hsu, S.K. 2002: Imaging magnetic sources using Euler's equation. *Geophysical Prospecting* 50(1), 15-25.
- Johnson, G.L. & Heezen, B.G. 1967: The morphology and evolution of the Norwegian-Greenland Sea. *Deep-Sea Research* 14, 755-771.
- Jolley, D.W. & Bell, B.R. 2002a. The evolution of the North Atlantic Igneous Province and the opening of the NE Atlantic rift. **In D.W. Jolley and B.R. Bell (eds) The North Atlantic Igneous Province: stratigraphy, tectonic, volcanic and magmatic processes.** Geological Society, London, Special Publications, 197, 1-13.
- Jolley, D.W. & Bell, B.R. 2002b. Genesis and age of the Erland Volcano, NE Atlantic Margin. **In D.W. Jolley and B.R. Bell (eds.) The North Atlantic Igneous Province: stratigraphy, tectonic, volcanic and magmatic processes.** Geological Society, London, Special Publications, 197, 95-110.
- Jolley, D.W., Clarke, B. & Kelley, S. 2002c: Paleogene time scale miscalibration: Evidence from the dating of the North Atlantic igneous province. *Geology* 30(1), 7-10.

- Johnson, G.L. & Heezen, B.G. 1967: The morphology and evolution of the Norwegian-Greenland Sea. **Deep-Sea Research** **14**, 755-771.
- Jung, W.Y. & Vogt, P.R. 1997: A gravity and magnetic anomaly study of the extinct Aegir Ridge, Norwegian Sea. **Journal of Geophysical Research-Solid Earth** **102(B3)**, 5065-5089.
- Juteau, T. & Maury, R. (Editors), 1997: **Géologie de la croûte océanique: Pétrologie et dynamique endogènes**. Enseignement des Sciences de la Terre. Masson, Paris, 367 pp.
- Karson, J.A. & Brooks, C.K. 1999: Structural and magmatic segmentation of the Tertiary East Greenland volcanic rifted margin. . In C. Mac Niocaill and P.D. Ryan (eds.) **Continental Tectonics**. Geological Society of London, Special Publications, 164, 313-338.
- Kusznir, N.J. & Karner, G.D. 2007: Continental lithospheric thinning and breakup in response to upwelling divergent mantle flow: application to the Woodlark, Newfoundland and Iberia margins. In G.D. Karner, G. Manatschal and L.M. Pinheiro (eds) **Imaging, Mapping and Modelling Continental Lithosphere Extension and Breakup**. Geological Society, London, Special Publications, 282, 389-419.
- Keating, P. & Pilkington, M. 2004: Euler deconvolution of the analytic signal and its application to magnetic interpretation. **Geophysical Prospecting** **52(3)**, 165-182.
- Kimbell, G.S., Ritchie, J.D., Johnson, H. & Gatliff, R. 2005: Controls on the structure and evolution of the NE Atlantic margin revealed by regional potential field imaging and 3D modelling. In A. Doré and B.A. Vining (eds.) **Petroleum Geology: North-West Europe and Global Perspectives- Proceedings of the 6th Petroleum Geology Conference**. Geological Society, London, 933-945.
- Klausen, M.B. 2006: Similar dyke thickness variation across three volcanic rifts in the North Atlantic region: Implications for intrusion mechanisms. **Lithos** **92(1-2)**, 137-153.
- Korenaga, J., Holbrook, W.S., Detrick, R.S. & Kelemen, P.B. 2001: Gravity anomalies and crustal structure at the southeast Greenland margin. **Journal of Geophysical Research-Solid Earth** **106(B5)**, 8853-8870.
- Kristjansson, L. & Jonsson, G. 1998: Aeromagnetic results and the presence of an extinct rift zone in western Iceland. **Journal of Geodynamics** **25(1-2)**, 99-108.
- Kuvaas, B. & Kodaira, S. 1997: The formation of the Jan Mayen microcontinent: the missing piece in the continental puzzle between the Møre-Vøring Basins and East Greenland. **First Break** **15(7)**, 239-247.
- Larsen, H.C., Saunders, A.D., Clift, P.D. & Schipboard-Scientific-Party 1994: **Proceedings of the Ocean Drilling Program, Initial Reports, 152**. College Station, TX (Ocean Drilling Program), 977 pp.
- Larsen, L.M., Waagstein, R., Pedersen, A.K. & Storey, M. 1999: Trans-Atlantic correlation of the Palaeogene volcanic successions in the Faeroe Islands and East Greenland. **Journal of the Geological Society** **156**, 1081-1095.
- Lavier, L.L. & Manatschal, G. 2006: A mechanism to thin the continental lithosphere at magma-poor margins. **Nature** **440(7082)**, 324-328.
- Laxon, S. & McAdoo, D. 1994: Arctic-Ocean Gravity-Field Derived from Ers-1 Satellite Altimetry. **Science** **265(5172)**, 621-624.
- LeHurray, A.P. & Johnson, E.S. 1989. Rb-Sr systematics of Site 642 volcanic rocks and alteration minerals. In A. Eldholm, J. Thiede and E. Taylor (eds.) **Proceedings of Ocean Drilling Program: Scientific Results, 104**. College Station, TX (Ocean Drilling Program), 437-448.
- Lien, T. 2005: From rifting to drifting: effects on the development of deep-water hydrocarbon reservoirs in a passive margin setting, Norwegian Sea. **Norwegian Journal of Geology** **85(4)**, 319-332.
- Lizarralde, D., Axen, G.J., Brown, H.E., Fletcher, J.M., Gonzalez-Fernandez, A., Harding, A.J., Holbrook, W.S., Kent, G.M., Paramo, P., Sutherland, F. & Umhoefer, P.J. 2007: Variation in styles of rifting in the Gulf of California. **Nature** **448(7152)**, 466-469.
- Lucazeau, F., Brigaud, F. & Leturmy, P. 2003: Dynamic interactions between the Gulf of Guinea passive margin and the Congo River drainage basin: 2. Isostasy and uplift. **Journal of Geophysical Research-Solid Earth** **108(B8)**, doi:10.1029/2002JB001928, 1-13.
- Lundin, E. & Doré, A.G. 2005: NE Atlantic break-up: a re-examination of the Iceland mantle plume model and the Atlantic-Arctic linkage. In A.G. Doré and B.A. Vining (eds) **Petroleum geology: North-West Europe and Global perspectives- Proceedings of the 6th Petroleum Geology Conference**. Geological Society of London, 739-754.

- Lundin, E. & Doré, A.G. 2002: Mid-Cenozoic post-breakup deformation in the 'passive' margins bordering the Norwegian-Greenland Sea. **Marine and Petroleum Geology** **19**(1), 79-93.
- Lundin, E.R. & Doré, A.G. 1997: A tectonic model for the Norwegian passive margin with implications for the NE Atlantic: Early Cretaceous to break-up. **Journal of the Geological Society** **154**, 545-550.
- Luyendyk, A.P.J. 1997: Processing of airborne magnetic data. **AGSO Journal of Australian Geology and Geophysics** **17**(2), 31-38.
- Macdonald, A.H. & Fyfe, W.S. 1985: Rate of serpentinisation in seafloor environments. **Tectonophysics** **116**(1-2), 123-135.
- Macdonald, K.C., Sempere, J.C., Fox, P.J. & Tyce, R. 1987: Tectonic evolution of ridge-axis discontinuities by the meeting, linking, or self-decapitation of neighboring ridge segments. **Geology** **15**(11), 993-997.
- Macdonald, K.C., Scheirer, D.S. & Carbotte, S.M. 1991: Midocean ridges - discontinuities, segments and giant cracks. **Science** **253**(5023), 986-994.
- Manatschal, G. & Bernoulli, D. 1998: Rifting and early evolution of ancient ocean basins: the record of the Mesozoic Tethys and of the Galicia-Newfoundland margins. **Marine Geophysical Researches** **20**(4), 371-381.
- Manatschal, G., Müntener, O., Lavier, L.L., Minshull, T.A. & Péron-Pinvidic, G. 2007. Observations from the Alpine Tethys and Iberia–Newfoundland margins pertinent to the interpretation of continental breakup. In G.D. Karner, G. Manatschal and L.M. Pinheiro (eds) **Imaging, Mapping and Modelling Continental Lithosphere Extension and Breakup**. Geological Society, London, Special Publications, 282, 291-324.
- Mari, J.-L., Glangeaud, F. & Coppens, F. 2001: Traitement du signal pour géologues et géophysiciens-Techniques de base, 2. **Editions Technip**, 268 pp.
- Marson, I. & Klingele, E.E. 1993: Advantages of using the vertical gradient of gravity for 3-D interpretation. **Geophysics** **58**(11), 1588-1595.
- Mauring, E., Beard, L.P., Kihle, O. & Smethurst, M.A. 2002: A comparison of aeromagnetic levelling techniques with an introduction to median levelling. **Geophysical Prospecting** **50**(1), 43-54.
- Mauring, E. & Kihle, A. 2006: Leveling aerogeophysical data using a moving differential median filter. **Geophysics** **71**(1), L5-L11.
- Maus, S., Sazonova, T., Hemant, K., Fairhead, J.D. & Ravat, D. 2007: National Geophysical Data Center candidate for the World Digital Magnetic Anomaly Map. **Geochemistry Geophysics Geosystems** **8**, 10.1029/2007GC001643.
- Mendel, V., Munsch, M. & Sauter, D. 2005: MODMAG, a MATLAB program to model marine magnetic anomalies. **Computers & Geosciences** **31**(5), 589-597.
- Meyer, R., van Wijk, J.W. & Gernigon, L., 2007: An integrated geophysical and geochemical model for North Atlantic Igneous Province magmatism. In G.R. Foulger and D.M. Jurdy (eds.) **Plates, plumes, and planetary processes**. Geological Society of America Special Paper 430, pp. 525-552.
- Miller, H.G. & Singh, V. 1994: Potential-field tilt - a new concept for location of potential-field sources. **Journal of Applied Geophysics** **32**(2-3), 213-217.
- Milligan, P.R. & Gunn, P.J. 1997: Enhancement and presentation of airborne geophysical data. **AGSO Journal of Australian Geology and Geophysics** **17**(2), 63-75.
- Mittelstaedt, E., Ito, G. & Behn, M.D. 2008: Mid-ocean ridge jumps associated with hotspot magmatism. **Earth and Planetary Science Letters** **266**(3-4), 256-270.
- Mjelde, R., Raum, T., Murai, Y. & Takanami, T. 2007: Continent-ocean-transitions: Review, and a new tectono-magmatic model of the Vøring Plateau, NE Atlantic. **Journal of Geodynamics** **43**(3), 374-392.
- Morrissey, T. 2003: Cretaceous and early Tertiary igneous activity and the geological evolution of the North Atlantic region. PhD thesis, University College Dublin, Ireland.
- Mosar, J., Lewis, G. & Torsvik, T.H. 2002: North Atlantic sea-floor spreading rates: implications for the Tertiary development of inversion structures of the Norwegian-Greenland Sea. **Journal of the Geological Society of London** **159**, 503-515.
- Mudge, C. 1991: New developments in resolving details in aeromagnetic data. **Exploration Geophysics** **23**, 277-284.

- Mushayandebvu, M.F., Lesur, V., Reid, A.B. & Fairhead, J.D. 2004: Grid Euler deconvolution with constraints for 2D structures. **Geophysics** **69**(2), 489-496.
- Myhre, A. & Eldholm, A. 1980: Sedimentary and crustal velocities in the Norwegian-Greeland Sea. **Journal of Geophysical Research** **86**(B6), 5012-5022.
- Nabighian, M.N. 1972: The analytic signal of two-dimensional magnetic bodies with polynomial cross-sections ; Its properties and use for automated anomaly interpretation. **Geophysics** **37**, 505-517.
- Nabighian, M.N., Grauch, V.J.S., Hansen, R.O., LaFehr, T.R., Li, Y., Peirce, J.W., Phillips, J.D. & Ruder, M.E. 2005: 75th Anniversary - The historical development of the magnetic method in exploration. **Geophysics** **70**(6), 33nd-61nd.
- Nafe, J.E. & Drake, C. 1957: Variation in depth in shallow and deep water sediments of porosity, density and the velocities of compressional and shear waves. **Geophysics** **22**, 523-552.
- Northwest Geophysical Associates Incorporation 2006: GM-SYS Gravity and Magnetic Modelling software. **Users Guide** v 4.10, 110 pp.
- Nunns, A. 1983: The structure and evolution of the Jan Mayen Ridge and surroundings regions. In J.S. Watkins and C.L. Drake (eds.). **Studies in Continental Margin Geology**. American Association of Petroleum Geologists memoir, 34, 193-208.
- Olesen, O., Ebbing, J., Lundin, E., Muring, E., Skilbrei, J.R., Torsvik, T.H., Hansen, E.K., Henningsen, T., Midbøe, P. & Sand, M. 2007: An improved tectonic model for the Eocene opening of the Norwegian-Greenland Sea: Use of modern magnetic data. **Marine and Petroleum Geology** **24**(1), 53-66.
- Olesen, O., Gernigon, L., Ebbing, J., Mogaard, J.O., Pascal, C. & Wienecke, S. 2006: Interpretation of aeromagnetic data along the Jan Mayen Fracture Zone, JAS-05, NGU Report 2006.018. Geological Survey of Norway, Trondheim. 162 pp.
- Olesen, O., Lundin, E., Nordgulen, O., Osmundsen, P.T., Skilbrei, J.R., Smethurst, M.A., Solli, A., Bugge, T. & Fichler, C. 2002: Bridging the gap between the onshore and offshore geology in Nordland, northern Norway. **Norwegian Journal of Geology** **82**(4), 243-262.
- Osmundsen, P.T., Sommaruga, A., Skilbrei, J.R. & Olesen, O. 2002: Deep structure of the Mid Norway rifted margin. **Norwegian Journal of Geology** **82**, 205-224.
- Pariso, J.E. & Johnson, H.P. 1993: Do lower crustal rocks record reversals of the Earth's magnetic-field - magnetic petrology of oceanic gabbros from ocean drilling program Hole-735b. **Journal of Geophysical Research-Solid Earth** **98**(B9), 16013-16032.
- Parsons, B. & Sclater, J.G. 1977: An analysis of the variation of ocean floor bathymetry and heat flow with age. **Journal of Geophysical Research** **82**, 803-827.
- Péron-Pinvidic, G., Manatschal, G., Minshull, T.A. & Sawyer, D.S. 2007: Tectonosedimentary evolution of the deep Iberia-Newfoundland margins: Evidence for a complex breakup history. **Tectonics** **26**(2), 1-19.
- Pilkington, M., Miles, W.F., Ross, G.M. & Roest, W.R. 2000: Potential-field signatures of buried Precambrian basement in the Western Canada Sedimentary Basin. **Canadian Journal of Earth Sciences** **37**(11), 1453-1471.
- Planke, S. & Eldholm, O. 1994: Seismic Response and Construction of Seaward Dipping Wedges of Flood Basalts - Vøring Volcanic Margin. **Journal of Geophysical Research-Solid Earth** **99**(B5), 9263-9278.
- Planke, S. 1994b: Geophysical response of flood basalts from analysis of wire line logs - Ocean Drilling Program Site-642, Vøring Volcanic Margin. **Journal of Geophysical Research-Solid Earth** **99**(B5), 9279-9296.
- Press, W.H., Teukolsky, S.A., Vetterling, W.T. & Flannery, B.P. (Eds.), 2002: **Numerical recipes in C++**. **The art of Scientific Computing Second Edition**. Cambridge University Press, 972 pp.
- Raum, T. 2000: Crustal structure and Evolution of the Faeroe, Møre and Vøring margins from Wide-angle Seismic and Gravity Data. **PhD thesis, University of Bergen**.
- Raum, T., Mjelde, R., Shimamura, H., Mural, Y., Brastein, E., Karpuz, R.M., Kravlk, K. & Kolsto, H.J. 2006: Crustal structure and evolution of the southern Vøring basin and voring transform margin, NE Atlantic. **Tectonophysics** **415**(1-4), 167-202.
- Ravat, D. 1996: Analysis of the Euler method and its applicability in environmental magnetic investigations. **Journal of Environmental and Engineering Geophysics** **1**, 229-238.

- Ravat, D., Whaler, K.A., Pilkington, M., Sabaka, T. & Purucker, M. 2002: Compatibility of high-altitude aeromagnetic and satellite-altitude magnetic anomalies over Canada. **Geophysics** **67(2)**, 546-554.
- Reid, A.B., Allsop, J.M., Granser, H., Millett, A.J. & Somerton, I.W. 1990a: Magnetic Interpretation in 3 Dimensions Using Euler Deconvolution. **Geophysics** **55(1)**, 80-91.
- Ren, S.C., Skogseid, J. & Eldholm, O. 1998: Late Cretaceous-Paleocene extension on the Vøring Volcanic Margin. **Marine Geophysical Researches** **20(4)**, 343-369.
- Roest, W.R. & Pilkington, M. 1993: Identifying remanent magnetization effects in magnetic data. **Geophysics** **58(5)**, 653-659.
- Roest, W.R., Verhoef, J. & Pilkington, M. 1992: Magnetic interpretation using the 3-D analytic signal. **Geophysics** **5(1)**, 116-125.
- Rumph, B., Reaves, C.M., Orange, V.G. & Robinson, D.L., 1993: Structuring and transfer zones in the Faeroes Basin in a regional context. In J.R. Parker (ed.) *Petroleum Geology of Northwest Europe: Proceedings of the 4th Conference*. **Geological Society, London**, 999-1009.
- Salem, A., Williams, S., Fairchild, D.G., Smith, R. & Ravat, D. 2008: Interpretation of magnetic data using tilt-angle derivatives. **Geophysics** **73(1)**, 1-10.
- Saunders, A.D., Fitton, J.G., Kerr, A.C., Norry, M.J. & Kent, R.W. 1997: The North Atlantic Igneous Provinces. In J.J. Mahoney and M.F. Coffin (eds.) **Large Igneous Provinces: continental, oceanic, and planetary flood volcanism**. American Geophysical Union, Geophysical Monograph, 100, pp. 45-93.
- Scheck-Wenderoth, M., Raum, T., Faleide, J.I., Mjelde, R. & Horsefield, B. 2007: The transition from the continent to the ocean: a deeper view on the Norwegian margin. **Journal of the Geological Society, London** **164**, 8555-868.
- Schouten, H., Dick, H.J.B. & Klitgord, K.D. 1987: Migration of Mid-Ocean-Ridge Volcanic Segments. **Nature** **326(6116)**, 835-839.
- Schreckenberger, B. 1997: Magnetische Anomalien über seawärts einfallenden seismischen reflektorfolgen-eine vergleichende Untersuchung verschiedener vorkommen in Atlantik, Frankfurt, **Thesis**, 117 pp.
- Schönharting, G. & Abrahamsen, N. 1989. Paleomagnetism of the volcanic sequence in Hole 642E, ODP Leg 104, Vøring Basin Plateau, and correlation with Early Tertiary basalts in the North Atlantic. In O. Eldholm, J. Thiede and E. Taylor (eds.). **Proceedings of the Ocean Drilling Program, Scientific Results, Vol. 104**, College Station, TX (Ocean Drilling Program), 912-920.
- Scott, R.A., Ramsey, L.A., Jones, S.M., Sinclair, S. & Pickles, C.S., 2005: Development of the Jan Mayen microcontinent by linked propagation and retreat of spreading ridges. In: B.T.G. Wandås, J.P. Nystuen, E. Eide and F. Gradstein (eds.) **Onshore-Offshore relationships on the North Atlantic Margin**. Norwegian Petroleum Society (NPF), Special Publication, 12, 69-82.
- Sigmundsson, F. 2006: Iceland Geodynamics: crustal Deformation and Divergent Plate Tectonics. **Springer in association with Praxis Publishing, Chichester, UK**, 209 pp.
- Silva, I.A.B.C. & Barbosa, V.C.F. 2003: 3D Euler deconvolution: Theoretical basis for automatically selecting good solutions. **Geophysics** **68(6)**, 1962-1968.
- Sinton, C. & Duncan, R. 1998: <sup>40</sup>Ar/<sup>39</sup>Ar ages of lavas from the southeast Greenland margin, ODP leg 152 and the Rockall Plateau, DSDP Leg 8. In Saunders, A.D., Larsen, H.C., and Wise, S.W. (eds) **Proceedings of the Ocean Drilling Program, Scientific Results, Vol. 152**. College Station, TX (Ocean Drilling Program), 387-402.
- Sirastava, S. & Tapscott, C.R. 1986: Plate Kinematics of the North Atlantic. In P.R. Vogt and B.E. Tucholke (eds.) **The Geology of North America, Volume M, The Western North Atlantic Region**. Geological Society of America, M, 379-404.
- Skilbrei, J.R., Olesen, O., Osmundsen, P.T., Kihle, O., Aaro, S. & Fjellanger, E. 2002: A study of basement structures and onshore-offshore correlations in Central Norway. **Norwegian Journal of Geology** **82(4)**, 263-279.
- Skogseid, J. & Eldholm, O. 1987: Early Cenozoic crust at the Norwegian continental-margin and the conjugate Jan-Mayen Ridge. **Journal of Geophysical Research-Solid Earth and Planets** **92(B11)**, 11471-11491.

- Skogseid, J., Planke, S., Faleide, J.I., Pedersen, T., Eldholm, O. & Neverdal, F., 2000: NE Atlantic continental rifting and volcanic margin formation. In A. Nøttvedt et al. (eds.) **Dynamics of the Norwegian margin. Geological Society Special Publications**, 167, 295-326.
- Smallwood, J.R. & White, R.S. 2002: Ridge-plume interaction in the North Atlantic and its influence on continental breakup and seafloor spreading. In Jolley, D.W. & Bell, B.R. (eds.) **The North Atlantic Igneous Province: stratigraphy, tectonic, volcanic and magmatic processes**. Geological Society of London, Special Publications, 197, 15-37.
- Smith, W.H.F. & Sandwell, D.T. 1997: Global sea floor topography from satellite altimetry and ship depth soundings. **Science** 277, 1957-1962.
- Spector, A. & Grant, F.S. 1970: Statistical models for interpreting aeromagnetic data. **Geophysics** 35(2).
- Stavrev, P. & Reid, A. 2007: Degrees of homogeneity of potential fields and structural indices of Euler deconvolution. **Geophysics** 72(1), L1-L12.
- Storey, M., Duncan, R.A. & Tegner, C. 2007: Timing and duration of volcanism in the North Atlantic Igneous Province: Implications for geodynamics and links to the Iceland hotspot. **Chemical Geology** 241(3-4), 264-281.
- Talwani, M. 1973: Computer Usage in the Computation of Gravity Anomalies. **Methods in Computational Physics** 13, 343-389.
- Talwani, M. & Eldholm, O. 1977: Evolution of the Norwegian-Greenland Sea. **Geological Society of America Bulletin** 88, 969-999.
- Talwani, M., Udintsev, G. & et al. 1976: Initial reports of the Deep Sea Drilling Project, Volume 38, Washington (U.S. Government Printing Office). 38, 1256 p.
- Talwani, M., Udintsev, G., Mirlin, E., Beresnev, A.F., Kanayev, V.F., Chapman, M., Groenlie, G. & Eldholm, O. 1978: Survey at sites 346, 347, 348, 349, and 350, the area of the Jan-Mayen Ridge and the Icelandic Plateau. **Initial reports of the Deep Sea Drilling Project; Supplement to volumes XXXVIII, XXXIX, XL, and XLI. Initial Reports of the Deep Sea Drilling Project 38(Supplement)**, 465-488.
- Taylor, B., Goodliffe, A.M. & Martinez, F. 1999: How continents break up: Insights from Papua New Guinea. **Journal of Geophysical Research-Solid Earth** 104(B4), 7497-7512.
- Taylor, P.N. & Morton, A. 1989. Nd and Pb isotope geochemistry of the upper and lower volcanic series at Site 642. In A. Eldholm, J. Thiede and E. Taylor (eds.) **Proceedings of Ocean Drilling Program: Scientific Results**, 104. College Station, TX (Ocean Drilling Program), 429-435.
- Thompson, D.T. 1982: EULDPH: A new technique for making computer-assisted depth estimates from magnetic data. **Geophysics** 47, 31-37.
- Thurston, J.B. & Brown, R.J. 1994: Automated source-edge location with a new variable pass-band horizontal-gradient operator. **Geophysics** 59(4), 546-554.
- Thurston, J.B. & Smith, R.S. 1997: Automatic conversion of magnetic data to depth, dip, and susceptibility contrast using the SPI (TM) method. **Geophysics** 62(3), 807-813.
- Tisseau, J. & Patriat, P. 1981: Identification des anomalies magnétiques sur les dorsales à faible taux d'expansion: méthode des taux fictifs. **Earth and Planetary Science Letters** 52, 381-396.
- Torsvik, T.H., Mosar, J. & Eide, E. 2001: Cretaceous-Tertiary geodynamics: a North Atlantic exercise. **Geophysical Journal International** 146 (3), 850-866.
- Tsikalas, F., Eldholm, O. & Faleide, J.I. 2005: Crustal structure of the Lofoten-Vesterålen continental margin, off Norway. **Tectonophysics** 404(3-4), 151-174.
- Tucholke, B.E. & Schouten, H. 1988: Kane Fracture Zone. **Marine Geophysical Researches** 10, 1-39.
- Unterneh, P. 1982: Etude structurale et cinématique de la mer de Norvège et du Groenland-Evolution du microcontinent de Jan Mayen, Phd Thesis, Université de Brest, Brest, 227 pp.
- van Wijk, J.W. & Cloetingh, S.A.P.L. 2002: Basin migration caused by slow lithospheric extension. **Earth and Planetary Science Letters** 1998, 275-288.
- Verduzco, B., Fairhead, J.D., Green, C.M. & MacKenzie, C. 2004: The meter reader-New insights into magnetic derivatives for structural mapping. **The Leading Edge** 23, 116-119.
- Verhoef, J., Roest, W.R., Macnab, R., Arkani-Hamed, J. & MembersoftheProjectTeam, 1997: Magnetic anomalies of the Arctic and North Atlantic Oceans and adjacent land areas. **Geological Survey of Canada Open File** 3125
- Vine, F.J. & Matthews, D.H. 1963: Magnetic anomalies over oceanic ridge. **Nature** 199, 947-949.

- Vink, G.E. 1982: Continental rifting and the implications for plate tectonic reconstructions. **Journal of Geophysical Research** **87**, 10677-10688.
- Vogt, D.R., Ostenso, N.A. & Jonhson, G.L. 1970: Magnetic and bathymetric data bearing on sea-floor spreading north of Iceland. **Journal of Geophysical Research** **75**, 903-920.
- Vogt, P.R. 1986. Geophysical and geochemical signatures and plate tectonics. In B. Hurdle (ed.). **The Nordic Seas**. Springer-Verlag, New York, 411-662.
- Vogt, P.R., Johnson, G.L. & Kristjansson, L. 1980: Morphology and magnetic anomalies north of Iceland. **Journal of Geophysics** **47**, 67-80.
- Waagstein, R. 1988: Structure, composition and age of the Faeroe basalt plateau. In Morton, A.C. & Parson, L.M. (eds) **Early Tertiary volcanism and the opening of the northeast Atlantic**. Geological Society, London, Special Publications 39, 225-238.
- Waagstein, R., Guise, P. & Rex, D. 2002. K/Ar and <sup>39</sup>Ar/<sup>40</sup>Ar whole-rock dating of zeolite facies metamorphosed flood basalts: the upper Paleocene basalts of the Faroe Islands, NE Atlantic. In D.W. Jolley and B.R. Bell (eds) **The North Atlantic Igneous Province: stratigraphy, tectonic, volcanic and magmatic processes**. Geological Society, London, Special Publications, 197, 219-252.
- Watts, A.B. 2001: Isostasy and Flexure of the Lithosphere. **Cambridge University Press**, 458 pp.
- Werner, S. 1953: Interpretation of magnetic anomalies of sheet-like bodies. Sveriges Geologiska Årbok, 43, Stockholm.
- White, R.S. & Lovell, B. 1997: Measuring the pulse of a plume with the sedimentary record. **Nature** **387**, 888-891.
- Wienecke, S., Ebbing, J. & Gernigon, L. 2007: 3D gravity modelling, isostasy and elastic thickness calculation in the Barents Sea, **NGU Report 2007.022**. Geological Survey of Norway. 56pp.
- Winograd, S. 1978: On Computing the Discrete Fourier Transform. **Mathematics of Computation** **32**(141), 175-199.
- Xiong, L. 2006: Understanding 3D analytical signal amplitude. **Geophysics** **71**(2), 13-16.
- Yamasaki, T. & Gernigon, L. 2008: Styles of lithospheric extension controlled by underplated mafic bodies. **Tectonophysics in press**.



## 15 LIST OF FIGURES:

Figure 1.1: 3D cartoon and examples of the application of modern NGU aeromagnetic surveys to basin or geodynamic studies. The cartoon illustrates structures and geological units that can cause observable magnetic responses (Gernigon et al. 2007).

Figure 1.2: Geographic location of the NB-07 survey area. Vigra and Vigar represent the two airports used during the survey acquisition.

Figure 1.3: Location of the NB-07 survey area and outline of the previous aeromagnetic surveys surrounding the Norway Basin (Olesen et al. 2006; Olesen et al. 2007). The Norway Basin was mostly covered by sparse magnetic profiles acquired by the U.S. Naval Research Laboratory (NRL) in the 70ies-80ies (Verhoef et al. 1997). The aim of the NB-07 was to fill the profiles gaps between the Faroes and the outer Vøring Basin.

Figure 2.1: Piper Chieftain from Fly Taxi Nord with the docking cradle for the bird containing a Scintrex Cesium Vapour MEP 410 high-sensitivity magnetometer.

Figure 2.2: Flight pattern (blue lines and red tie-lines) of the NB-07 survey.

Figure 2.3: Sensor altitude (plane radar altitude – 70 m). Variation of sensor altitude can partly explain minor variation in the raw magnetic field, later corrected by advanced levelling techniques.

Figure 2.4: Janusz next to the base station magnetometer deployed in the Faroe Islands during the NB-07 acquisition.

Figure 2.5: Sunspot number observations from the US National Oceanic and Asthenospheric Administration (NOOA) compilation and models of prediction after (Hathaway et al. 1999). Monthly averages (updated monthly) of the sunspot numbers show that the number of sunspots visible on the sun waxes and wanes with an approximate 11-year mega cycle. The NB-07 acquisition was acquired during a period of extremely low solar activity, which represented excellent conditions for the NB-07 aeromagnetic acquisition.

Figure 2.6: Diagram of the monthly mean values of the horizontal intensity of the geomagnetic field (H) observed in Tromsø observatory from 1994-2008. This graph illustrates the good correlation between the periodic and semi-periodic evolution of the field and sunspot activity. Similar variation between the Polynomial average of H and its running average illustrate the average good magnetic conditions for aeromagnetic surveying during the two periods in June-July and June-September 2007. Geomagnetic Data from Tromsø Geophysical Observatory (<http://www.tgo.uit.no/aix>). Sunspot numbers from the U.S National Oceanic and Asthenospheric Administration (NOOA) compilation.

Figure 2.7: Magnetic diurnal along profile 210:6 (line with most noise in the NB-07 survey). a) Basemagnetometer reading. b) Basemagnetometer and uncorrected magnetic field from the aeroplane plotted in the same scale.

Figure 2.8: Profiles of intermediate quality (i.e. diurnal variation between 10 and 30 nT per 10 minutes) marked as blue lines. The total length of intermediate quality data is 126 km (i.e. 03 % of the total survey). Both base station and aeroplane readings along line 210:6 are shown in Fig. 2.7.

Figure 3.1: Raw magnetic profiles (without levelling) gridded by means of the minimum curvature algorithm (grid cell size at 500x500 m). Note the artefacts mostly parallel to the line profiles due to diurnals. Projection UTM 30, WGS 84.

Figure 3.2: The IGRF-2006 (formally 2005) model along the NB-07 survey.

Figure 3.3: Example of variation of the geomagnetic field recorded by the base station during the acquisition of Line 600. The standard variation of the total field (in pink) illustrates the diurnal variations observed onshore.

Figure 3.4: Statistical tie levelling of the magnetic profiles, lag corrected and referred to the International Geomagnetic Reference Field (IGRF-2005-06). Gridding of line and tie profiles using the minimum curvature algorithm (grid resolution: 500x500 m). The total magnetic intensity represents the measured magnetic data after removal of the variations due to changes in the magnetic field of the IGRF model. This yields the anomalous total magnetic intensity, which for practical purposes is the component of the anomalous magnetic field along the earth's field direction. With the IGRF removal, the statistical levelling represents the first step of the levelling method.

Figure 3.5: Full levelling magnetic grid of the magnetic profiles, lag corrected and referred to IGRF-2006. The levelling represents the second step of the levelling approach based on least-square technique. Gridding of the line profiles using the minimum curvature algorithm (grid resolution: 500x500 m).

Figure 15.6: Magnetic residual after micro-levelling by decorrugation and subtraction of the total field obtained by statistical levelling (500x500m cell grid spacing). The NW-SE trends represent the micro levelling diurnal variations along the pre-existing tie lines.

Figure 15.7: Total magnetic field after micro-levelling. Results from the FFT decorrugation technique of Geosoft. 500x500m cell grid spacing using the minimum curvature algorithm.

Figure 4.1: 2D power spectrum and distribution of the frequency content of the NB-07 magnetic total field (RTP) gridded after micro-levelling. Red colours correspond to regions of high power, grading to yellow, green and then to blue, which represents the lowest power. The very centre of the frequency spectrum represents the average value in the image, while those frequencies immediately adjacent correspond to low frequency variation. Frequencies gradually increase as we move away from the centre of the frequency spectrum.

Figure 4.2: Magnetic total field produced by a simple prim (left) and power energy spectrum of this magnetic Total field as function of the wavenumbers (k).

Figure 4.3: Frequency content and averaged power spectra computed for different grid size used during the minimum curvature gridding of the NB-07 magnetic total field then reduce to the pole using 2D-FFT. Note that the noise increases with smaller grid cell spacing. Steeper slopes increasing to the left of the plot, coincides with the deep-seated contribution. The depth estimate plot bar is an automatic 5 points slope and depth calculation, derived from the spectrum file (only for the 1000x1000 m grid). The poly-10 curve is an order 10 orthogonal polygonal calculated thought the depth estimation of the spectrum computed for the 1000x1000 grid size. It can be used to highlight the main segment and average statistical magnetic sources. The deepest set of sources along the survey are located at ~19.5 km and two other can be proposed at 4.4 km and 1.74 km in average.

Figure 4.4: Values of inclination (top) and declination (bottom) of the geomagnetic field along the NB-07 survey area. IGRF-model available in 2006.

Figure 4.5: Differences between the 1-D and 2D FFT algorithms used to calculate the reduction to the pole along the NB-07 survey with the mean values of inclination and declination. The result is compared with the original magnetic total field.

Figure 4.6: Differences between the 1-D FFT algorithms using different inclination and declination values. RTP transformation assumes only one value for both Inclination and declination. Since variations of these values along the survey area are small, only the mean value has been considered.

Figure 4.7: Profile map of the Total magnetic field reduced to the pole (I: 75.15; D: -6.05). The RTP was carried out using a 1D-FFT filtering applied to each line profile.

Figure 4.8: Gridded anomaly map of the total magnetic field reduced to the pole (Inc: 75.15; Dec: -6.05). The RTP was carried out using a 2D-FFT filtering along the microlevelled grid (1000x1000 m). The RTP transforms the anomaly into the one that would be observed with vertical magnetization and with a vertical Earth's field, i.e. the anomaly that would be observed if the source were located at the earth's magnetic north pole. As a result, reduction to the pole removes asymmetries caused by the non-vertical inducing field and places the anomalies more directly over their causative bodies, thus facilitating the interpretation of the magnetic dataset. Note that at the Norway Basin latitude, these changes are relatively small.

Figure 4.9: Gridded anomalies map of the Total magnetic field reduced to the pole (I: 75.15; D: -6.05). For better display and to avoid instabilities during 2D-FFT filtering, we finally preferred this grid with a grid size of 1650x1650 m.

Figure 4.10: Upward continuation of the magnetic total field. Upward continuation uses wavelength filtering to simulate the appearance of potential-field maps if the data were recorded at a higher altitude. Large-scale regional anomalies and main crustal patterns are revealed.

Figure 4.11: High-pass filtering (20km) of the magnetic total field, RTP. This filter underlines the distribution of the small wavelengths. Grid cell at 1650x1650m.

Figure 4.12: Low-pass filtering of the magnetic total field at 50km. This filter smoothes the magnetic signal and underlines the distribution of the main magnetic units. These medium anomalies likely reflect mid-crustal sources and already illustrate the basin segmentation and complexity.

Figure 4.13: Band-pass sampling of the magnetic total field. This filter only considers the wavelengths specified in a certain range. This grid illustrate the anomalies sampled using a low wavenumber cutoff of 0.04 (in  $1/k_{\text{unit}}$ ) and a high wavenumber cut-off of 0.6 in  $1/k_{\text{unit}}$ . According to the spectrum analysis, these anomalies should represent sources located in the 3-5 km depth interval.

Figure 4.14: Band-pass filtering of the magnetic total field. This grid illustrates the anomalies sampled using a low wavenumber cutoff of 0 (in  $1/k_{\text{unit}}$ ) and a high wavenumber cut-off of 0.1 in  $1/k_{\text{unit}}$ . According to the spectrum analysis, these anomalies should highlights magnetic sources located at more than 15 km depth if we consider that all the long wavelengths are the results of deep sources.

Figure 4.15: Example and comparison between high-pass, low-pass and upward continuation filters of the magnetic total field.

Figure 5.1: Automatic gain control filtering (AGC) of the NB-07 survey. To highlight the local anomaly details, automatic gain control (AGC) boosts amplitudes in areas with smooth anomalies, without sacrificing the long-wavelength information. Gain is estimated with a sliding square filter window, centred on each grid node in turn.

Figure 5.2: Vertical derivative obtained by convolution along the magnetic total field reduced to the pole and gridded with a cell size of 1650m using minimum curvature. The vertical derivative of an anomaly is related to the depth and geometry of the causative body. The gradient operator attenuates broad, more regional anomalies and enhances local, more subtle magnetic responses and as such is sensitive to shallow magnetic source bodies and contacts.

Figure 5.3: Second vertical derivative obtained by convolution along the magnetic total field reduced to the pole. The second vertical derivative can be seen as a regional-residual separation technique because it suppresses long wavelength anomalies related to regional influences. Due to filtering instability, this filter must be used with some caution in interpreting basement structure.

Figure 5.4: Directional horizontal derivatives along the NB-07 area. The filter enhances the high frequencies along the NW-SE direction.

Figure 5.5: Directional horizontal derivatives along the NB-07 area. The filters enhance the high

frequencies along the NE-SW direction.

Figure 5.6: Directional horizontal derivatives along the NB-07 area. The filters enhance the high frequencies along the N-S direction.

Figure 5.7: Maximum horizontal gradient of the NB-07 dataset, reduced to the pole. After the reduction-to-pole correction, a magnetic body is spatially more directly associated with the related magnetic response. The maximum horizontal gradient (more properly the maxima of the total horizontal gradient) of the anomaly slope is then located near or over the body edge. That is, the horizontal gradient operator in map form produces maximum ridges over edges of magnetic basement blocks and faults or other magnetic bodies. In addition, the horizontal gradient highlights linear and round-shaped features, related to magnetic contacts, in the data set.

Figure 5.8: Analytic signal of the magnetic total field grid, reduced to the pole (1650x1650m cell size). The 3D analytic signal ("3D-Total gradient") is the root-sum square of the vertical and horizontal gradients. Like the horizontal gradient, it is used to delineate the edges of bodies or contacts. It has the advantage over the horizontal gradient that it is independent of the dip of the contact, but the disadvantage that it is somewhat less continuous. It is therefore sometimes advantageous to use the two in parallel.

Figure 5.9: TDR and analytical signal filtering along line 600. The TDR filter is particularly effective in identifying subtle anomalies and their edges.

Figure 5.10: Tilt derivative of the magnetic total field RTP. The tilt derivative (TDR) is an alternative method to derive the maximum gradient anomalies associated with magnetic contacts. The result is strongly peaked along the maxima of the horizontal gradient. This display gives a much sharper definition of the magnetic contacts than the horizontal gradient map. For the NB-07 interpretation, this filter proves to be interesting to map and identify the magnetic chrons.

Figure 5.11: Horizontal derivative of the tilt derivative (HD-TDR) of the magnetic total field grid (1650x1650), reduced to the pole. The different patterns underline major magnetic units and major lineaments.

Figure 5.12: TDX filter of the magnetic total field grid (1650x1650m) reduced to the pole. The different TDX patterns underline major magnetic units and major lineaments.

Figure 5.13: 2D Laplacian filter [0,-1,0,-1,4,-1,0,-1,0] applied to the TDX of the magnetic total field grid (1650x1650m) reduced to the pole. A Hanning filter [0.06, 0.1, 0.06, 0.1, 0.36, 0.1, 0.06, 0.1, 0.06] has subsequently been applied to smooth the edge. This filtering highlights the main inflection points of the TDX grid.

Figure 5.14: Example of different edge detection filters applied to line 600. The TDX filtering highlights the main inflection points of the TDX grid including maximum and minimum for each anomaly. A 3x3 Laplace filter applied to a TDX grid is mostly useful to underline the points of tangency.

Figure 5.15: Pseudogravity of the NB-07 survey. The pseudo gravity was computed using a density contrast of  $1.5\text{g}\cdot\text{cm}^{-3}$  and a magnetization of  $3\text{A}\cdot\text{m}^{-1}$ . Inclination:  $7.5^\circ$  and declination:  $-6.5^\circ$ .

Figure 7.1: Free air gravity and location of the seismic data available around the NB-07 survey.

Figure 8.1: Peak of the Total horizontal gradient (e.g. analytic signal) and location of the discriminated Euler points.

Figure 8.2: Result from Located Euler deconvolution over the NB-07. Result using a structural index of 1.

Figure 8.3: Result from Located Euler deconvolution over the NB-07. Result using a structural index of 2.

Figure 8.4: Result from Located Euler deconvolution over the NB-07, using a structural index of 3.

Figure 8.5: Result from Located Euler deconvolution over the NB-07, using its tilt derivative. Depth

solution using a structural index of 1.

Figure 8.6: Result from Located Euler deconvolution over the NB-07, using its tilt derivative filter. Depth solution using a structural index of 2.

Figure 8.7: Result from Located Euler deconvolution over the NB-07, using its tilt derivative filter. Depth solution using a structural index of 3.

Figure 9.1: Bathymetric map and main physiographic features of the Norwegian-Greenland Sea. Sea-floor spreading led to the formation of Reykjanes, Aegir and Mohns Ridges. Spreading along the Aegir Ridge decreased until ceasing in the Oligocene. A progressive ridge jump along the Kolbeinsey Ridge happened during the same period, connecting the Mohns and Kolbeinsey Ridges and leading to the formation of the Jan Mayen microcontinent. The Jan Mayen Fault Zone (JMFZ) consists of three distinct segments named the western (WJMFZ), eastern (EJMFZ) and central Jan Mayen Fractures zones (CJMFZ), respectively. The polygons represent the outline of the recent JAS-05 and NB-07 aeromagnetic surveys and main study area on the Norway basin. Seaward-dipping reflector sequences (SDRs) represent thick volcanic lava flows extruded during the breakup along the Vøring Marginal High (white outlines). FSB: Faroes-Shetland Basin, FIR: Faroes-Iceland Ridge, MMH: Møre Marginal High, VG: Vicking Graben, VMH: Vøring Marginal High, VS: Vøring Spur.

Figure 9.2: Revised calibration of the geomagnetic polarity time scale for the Late Cretaceous and Cenozoic after Cande and Kent (1995). This chart provides the correlation between the magnetic chrons locally identified in the Norway Basin and their absolute ages in Ma.

Figure 9.3: Magnetic anomaly profiles along the NB-07 survey and surrounding survey tracks (see Chapter 1 for survey descriptions). Correlations and identification of the magnetic chrons on the regional grid were based on the real anomalies peaks. The map also illustrates the data limitation in the westernmost part of the Aegir Ridge and along the Faroes-Iceland Ridge.

Figure 9.4: TDX filter of the magnetic total field combined with the results of an automatic peak detection routine, which highlights both direction and dip of each anomaly. This combination was used to better identify precise edges of each magnetic chrons in order to evaluate the spreading rates of the Norway Basin. The three transects (1,2,3) represents the location of the synthetic models used for correlation and validation of the magnetic chrons. Yellow circles represent the DSDP wells. The black circles show the locations of the explorations wells.

Figure 9.5: Interpretation of the magnetic chrons deduced and correlated with synthetic profiles.

Figure 9.6: TDR filtering of the magnetic total field overlain by the identified and interpreted magnetic chrons (C24 to C13) and magnetic discontinuities.

Figure 9.7: Magnetic total field overlain by the identified and interpreted magnetic chrons (C24 to C13), the magnetic discontinuities and a tentative COB (Continent-Ocean Boundary) and VMCB (Volcanic Margin-Continent Boundary) interpretation.

Figure 9.8: Blended map between the magnetic total field grid overlain by the identified and interpreted magnetic chrons (C24 to C13) and magnetic discontinuities. The TDX filter used to enhance the edges of the magnetic anomalies of the magnetic total field and interpretation of the magnetic chrons and magnetic discontinuities.

Figure 9.9: Low-pass filter of the magnetic total field grid (75 km) overlain by the identified and interpreted magnetic chrons and magnetic discontinuities. This map illustrates the regional segmentation of the magnetic field pattern which coincides with different oceanic domains.

Figure 9.10: Band-pass filtering of the magnetic total field grid (long wavenumbers cutoff of 0 to 0.03 1/k-unit) overlain by the identified and interpreted magnetic chrons and magnetic discontinuities.

This map illustrates the main oceanic anomalies and highlights the trends of the first and second order regional discontinuities observed in the Norway Basin.

Figure 9.11: Map of gridded free air gravity anomalies overlain by the identified and interpreted magnetic chrons and magnetic discontinuities.

Figure 9.12: Map of gridded Bouguer gravity anomalies (reduction 2200 kg.m<sup>-3</sup>) overlain with the identified and interpreted magnetic chrons and magnetic discontinuities.

Figure 9.13: High-pass filtering of the Free-Air anomalies (75 km)) overlain by the identified and interpreted magnetic chrons and magnetic discontinuities.

Figure 9.14: Map of the regional Bathymetry overlain by the identified and interpreted magnetic chrons and magnetic discontinuities.

Figure 9.15: Interpretation of the main volcanic facies observed along the GMNR94-102R. The section also shows the gravity and magnetic signature observed along the volcanic margin. Volcano-stratigraphic monenclature after Planke et al. ( 2001).

Figure 9.16: Seismic observation along the COT near the Jan Mayen transform margin. The red curve represents the Free-air gravity anomalies after high pass filtering at 75 km.

Figure 9.17: Seismic observation along the COT south of the Norway Basin pseudofault. Note that the COB often coincide with fluid escape and mud diapirs. The COB is interpreted east of the C24b anomaly, on the outer edge of the Inner SDRs.

Figure 9.18: Seismic example of large volcanic mounts along COT, west of the Møre Marginal High. Some of the largest seamounts fit with gravity highs and could represent aborted spreading cells emplaced along the proto-breakup axis.

Figure 9.19: Zoom along the domain 2, which characterise the Faroe volcanic shear margin and the complex and unclear transition between the Norway Basin and the the Faroes-Iceland Ridge

Figure 9.20: Bathymetric, gravity and magnetic transects across the COT and the early spreading system of the Norway Basin. Blues labels indicate the magnetic chrons and black labels the spreading rates in mn/year.

Figure 9.21: Examples of round features with opposite polarities compared to their surroundings. They are interpreted as off-axis volcanic mounds or aborted rift features. Dashed lines represent discrete third order (non-rigid) discontinuities.

Figure 9.22: Significant Early-mid Eocene cinematic reorganisation of the Norway Basin between C22n and C21 (49.7-46.2 Ma). The spreading direction changes from NW-SE from C24 to C22 to NNW-SSE/N-S after C22n. Chrons C21n are locally divided by crack propagation of the growing C20r.

Figure 9.23: Detail of the Norway Basin “pseudofault”, located south of the Jan Mayen transform margin. The Norway Basin defines characteristic wavy magnetic pattern pointing in the direction of two propagator features. Between the propagating and the failing rift, the lithosphere is progressively transferred from one plate to another, giving rise to a shear zone with a quite distinctive magnetic fabric. Northern and southern segments are divided by the pseudofault and interacted together.

Figure 9.24: Models of spreading centre reorientation by (A) gradual rotation and (B) propagation. Modified from Hey et al. (1980, 1988).

Figure 10.1: Location of the three seismic lines used for potential modelling.

Figure 10.2: Velocity-density functions for different geologic settings including oceanic sediments and crust. Compilation by courtesy of L. Marelllo, NGU.

Figure 10.3: Compilation of magnetic data from the volcanic sequence of ODP Hole 642E (from Schönharting and Abrahamsen 1989). Flow unit numbers from 1 to 121 represent lava flows. D1 to D7 represent dikes and S4 to S49 numbers represent volcanoclastics). The graph illustrates the

stable inclination in degrees, the median destructive field (MDF), the natural remanent magnetization (NRM) and the Q-ratio. Note that the values used the old nomenclature in Gauss (=  $4\pi$  SI). The boundary between the upper and the lower series is at 1087 mbsf and illustrates a clear polarity change. The reverse upper series is correlated with chron 24r of the magnetic polarity time scale, with an age of ca. 54 Ma. The normal polarity of the lower series is correlated with chron 25, indicating a hiatus between the two series.

Figure 10.4: Compilation of magnetic reversals within the c. 6½ km thick basalt pile of the Faroe Islands, showing stratigraphy and the correlation with the Geomagnetic Polarity Time Scale after Abrahamsen (2006).

Figure 10.5: Example of Flexural Moho computed for an elastic thickness value of 2 km in the Norway Basin area.

Figure 10.6: Potential field modelling along the depth-converted LOS99-02 seismic profile. The detailed geometries of the bodies are controlled by reflection and refraction seismic data and compared with the flexural Mohos deduced assuming different flexural elastic thicknesses of the plate. The top panel represents the TDX, tilt derivative, low-pass filtering and observed and calculated residual IGRF and RTP corrected magnetic anomaly (nT). The middle panel represents the observed and calculated free air gravity anomaly and the 75 km high-pass filtered free air gravity (mGal). Densities (black labels) are in  $1000 \times \text{kg.m}^{-3}$ . Red densities (in  $1000 \times \text{kg.m}^{-3}$ ) represent the mantle densities assuming thermal expansion.

Figure 10.7: Magnetic modelling along the depth converted LOS99-02 seismic profile. The detailed geometries of the bodies are constrained by reflection and refraction seismic data and compared with the flexural Mohos deduced assuming different flexural elastic thicknesses of the plate. The top panel represents the TDX, tilt derivative, low-pass filtering and the observed and calculated residual IGRF and RTP corrected magnetic anomaly (nT). The middle panel represents the observed and calculated free air gravity anomaly and the 75 km high-pass free air gravity (mGal). Along the transect, susceptibilities (blue labels) are in SI units and remanence values (red labels) in A/m.

Figure 10.8: Potential field modelling along the depth converted LOS00-13 seismic profile. The detailed geometries of the bodies are controlled by reflection and refraction seismic data and compared with the flexural Mohos deduced assuming different flexural elastic thickness of the plate. The top panel represents the TDX, tilt derivative, low-pass filtering and the observed and calculated residual IGRF and RTP corrected magnetic anomalies (nT). The middle panel represent the observed and calculated free air gravity anomaly and the 75 km high-pass filtered free air gravity at (mGal). Densities (black labels) are in  $1000 \times \text{kg. m}^{-3}$ .

Figure 10.9: Magnetic modelling along the depth converted LOS00-13 seismic profile. The detailed geometries of the bodies are controlled by reflection and refraction seismic data and compared with the flexural Mohos deduced assuming different flexural elastic thickness of the plate. The top panel represents the TDX, Tilt derivative, low pass filtering and observed and the observed and calculated residual IGRF and RTP corrected magnetic anomalies (nT). The middle panel represents the observed and calculated free air gravity anomaly and the high pass filter of the free air at 75 km (mGal). Susceptibilities (blue labels) are in SI units and remanence (red labels) in A/m in the lower panel.

Figure 10.10: Potential field model along the depth-converted line-drawing of the LOS00-13 seismic profile. The detailed geometries of the bodies are controlled by reflection and refraction seismic data and compared with the flexural Mohos deduced assuming different flexural elastic thickness of the plate. The top curve represents the TDX filtering of the magnetic total field. The Middle

panel represents the observed and calculated residual IGRF and RTP corrected magnetic anomaly (nT). The upper panel shows the observed and calculated free air gravity anomaly and 75 km high-pass filter (mGal). Densities (black label) are in  $1000 \times \text{kg. m}^{-3}$ .

Figure 10.11: Magnetic modelling along the depth converted OF94-97 seismic profile. The detailed geometries of the bodies are controlled by reflection and refraction seismic data and compared with the flexural Mohos deduced assuming different flexural elastic thickness of the plate. The top panel represents the TDX, tilt derivative, low-pass filtering and the observed and calculated residual IGRF and RTP corrected magnetic anomaly (nT). The middle panel represents the observed and calculated free air gravity anomaly and the 75 km high pass filter of the free air gravity (mGal). Susceptibilities (blue labels) are in SI units and remanence (red labels) in A/m in the lower panel.

Figure 11.1: Evolution model for the major extrusive seismic facies units formed along the Continent-Ocean Transition (COT) of the Møre volcanic margin in Early Tertiary time. Modified after Planke et al. (2000). COB: Continent-Ocean Boundary; VMBC: Volcanic Margin Continental Boundary.

Figure 11.2: Effect of mafic underplating on depth dependant stretching, localization of the deformation and margin asymmetry. After Yamasaki and Gernigon, (2008, in press)

Figure 11.3: Bathymetric, gravity and magnetic profiles along regional flow-lines across the Norway Basin.

Figure 11.4: Different models for the evolution of the Norway Basin. The upper panel represent the classic fan-shaped spreading interpretation initially suggested by Talwani and Eldholm (1977) and Nunns (1982). This model involves a compensating triangular system between Greenland and the Jan Mayen microcontinent (A on the cartoon). The lower panel shows an alternative dislocation scenario proposed by Scott et al. (2005).

Figure 11.5: Geodynamic evolution of the Norway Basin (Gaina et al., in preparation).



## 16 APPENDIX 1:

Janus Koziel

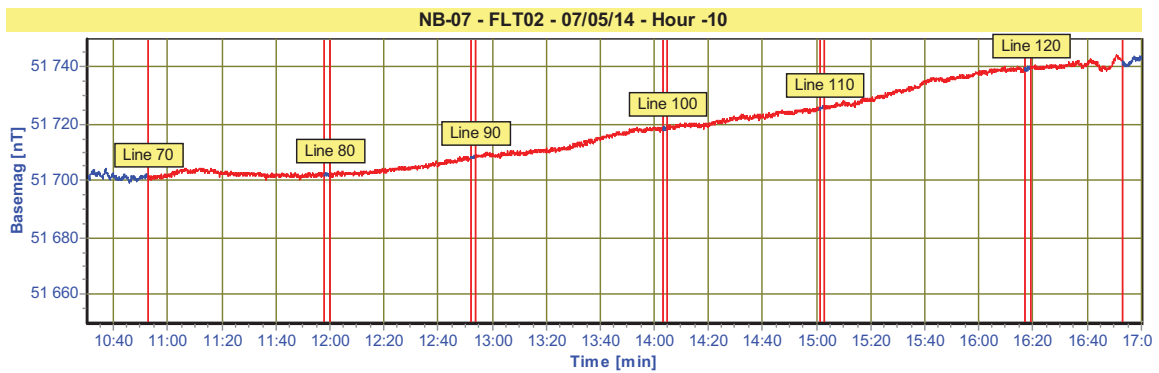
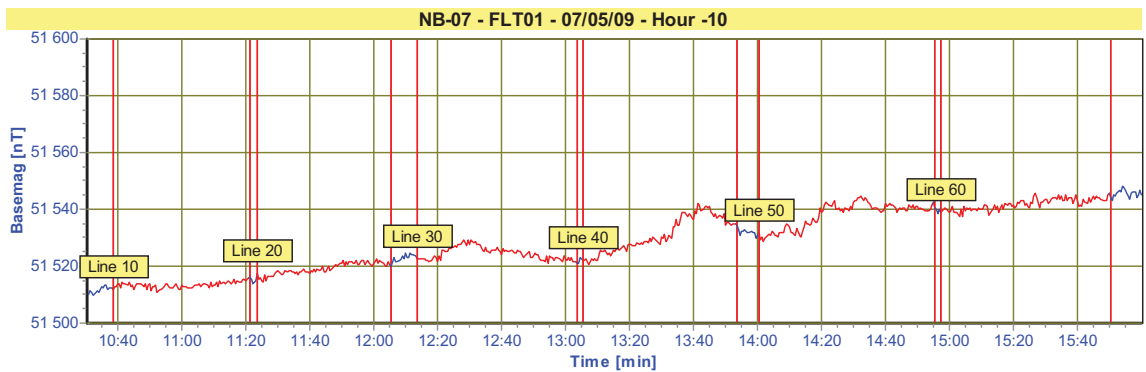
### Recordings from the base magnetometer at Vagar Faroe Islands, Vigra and Rørvik, Norway

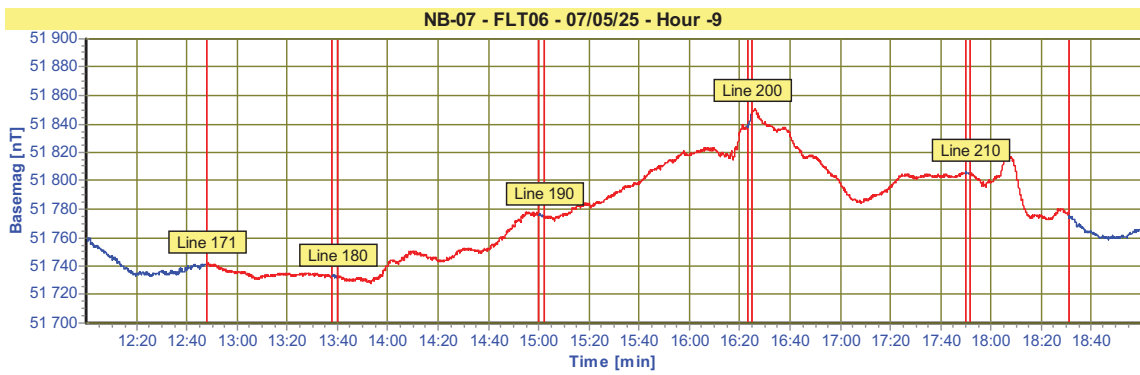
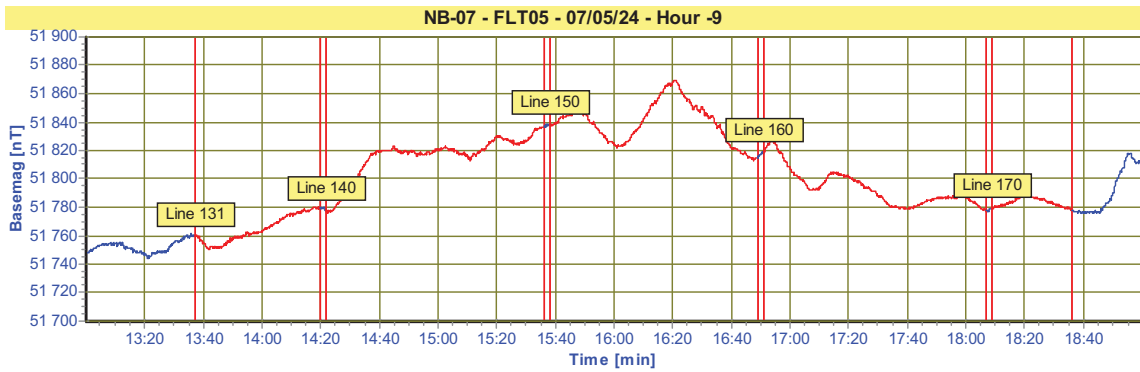
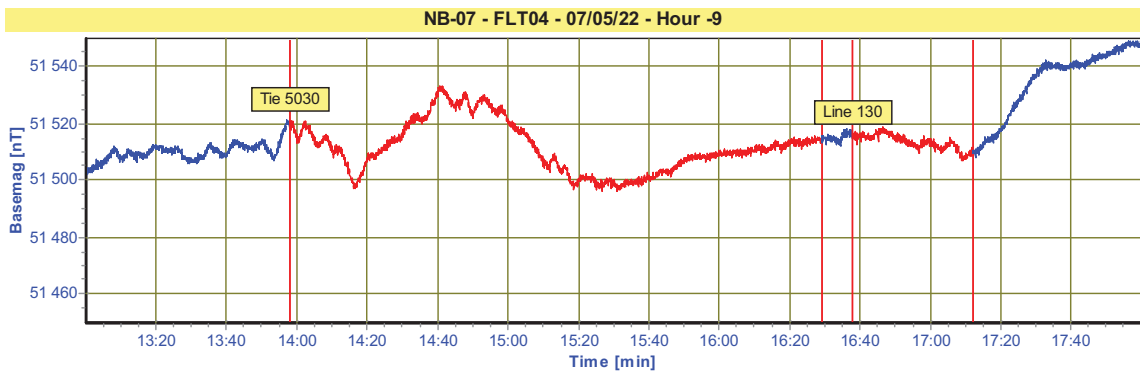
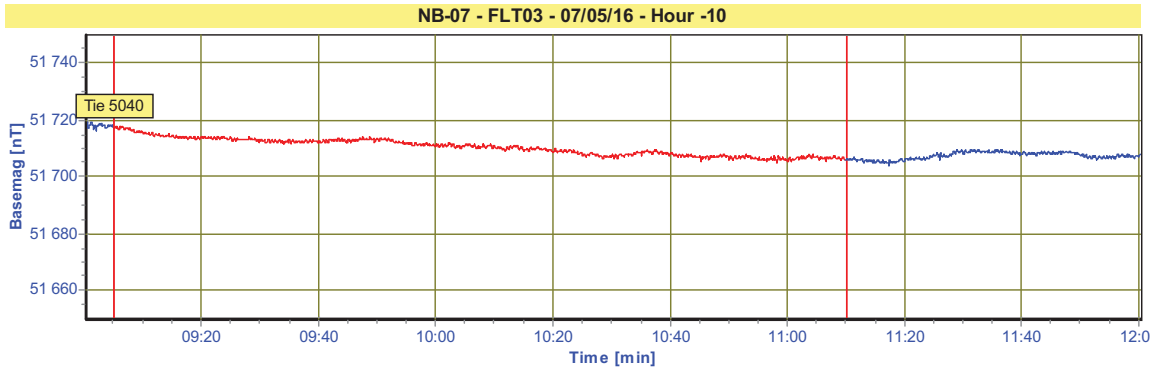
Printout of base magnetic recordings for all flights (1 – 49) acquired during the Norwegian Basin Aeromagnetic Survey 2007 (NB-07).

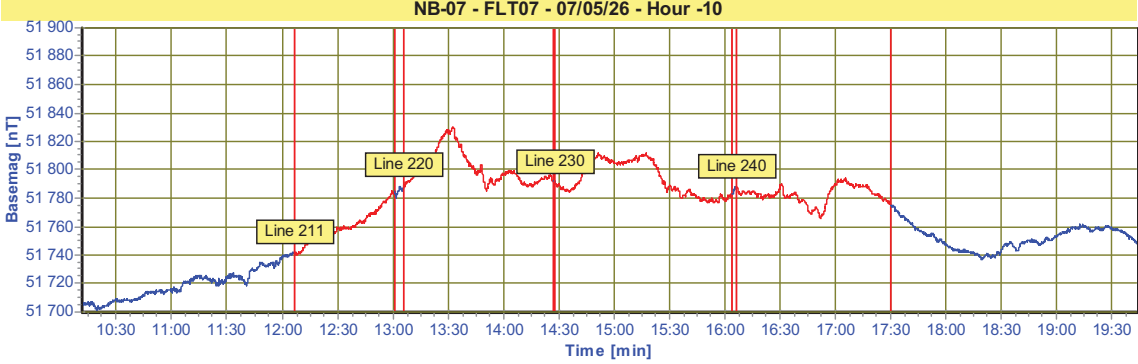
The start and termination times for each profile (both traverse lines and tie lines) are indicated by red, vertical lines (with annotated profile numbers).

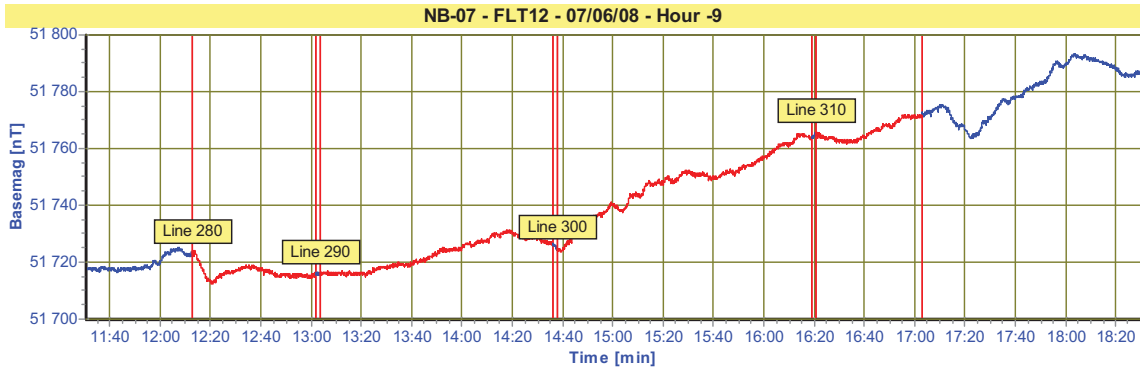
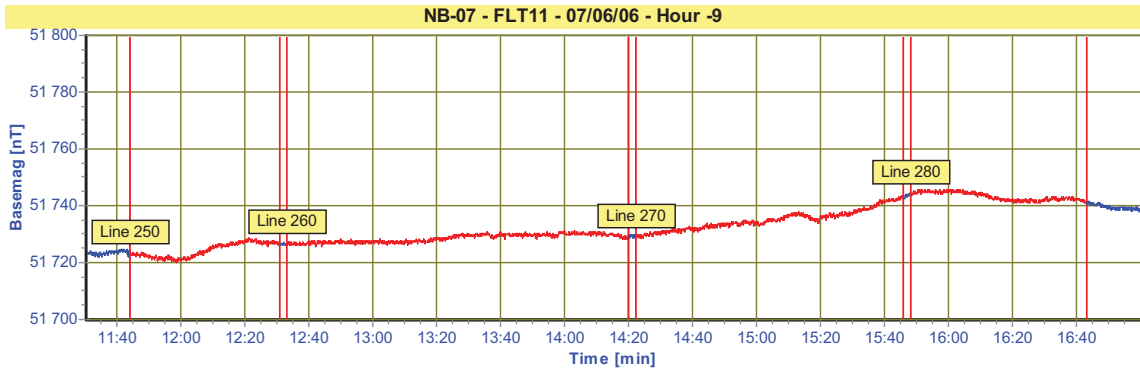
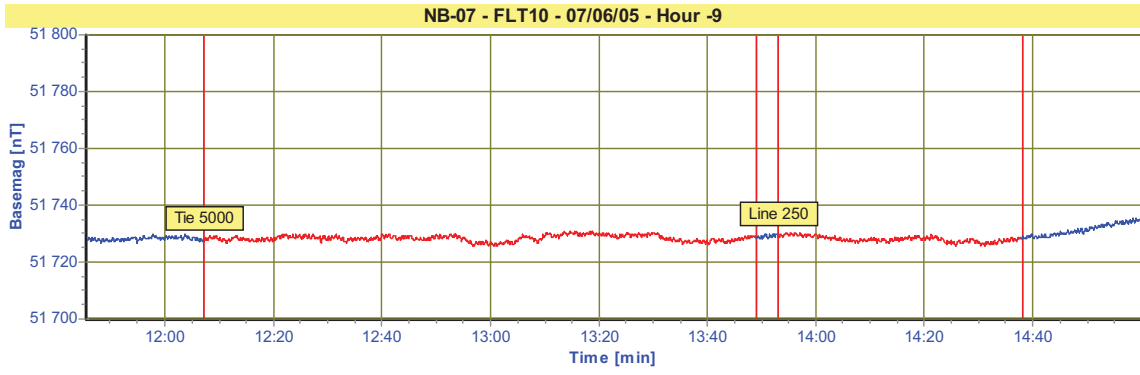
Traverse lines: 10 – 1250 and tie lines: 4990 – 5260.

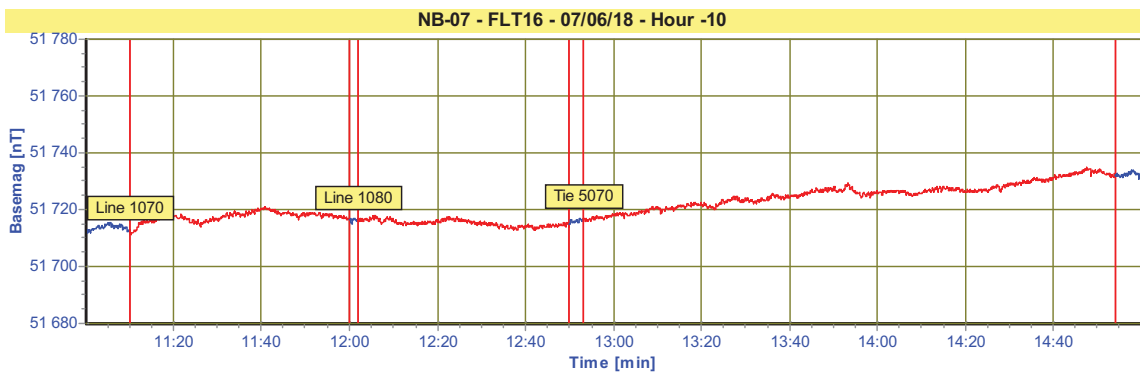
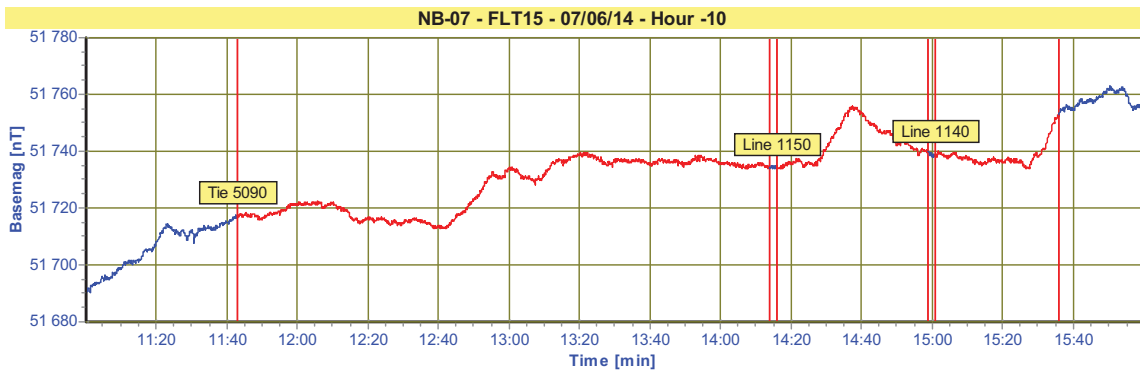
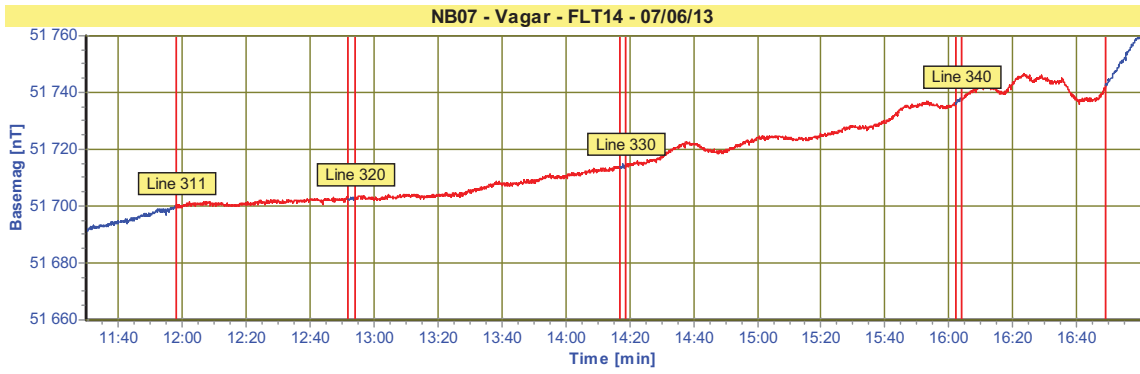
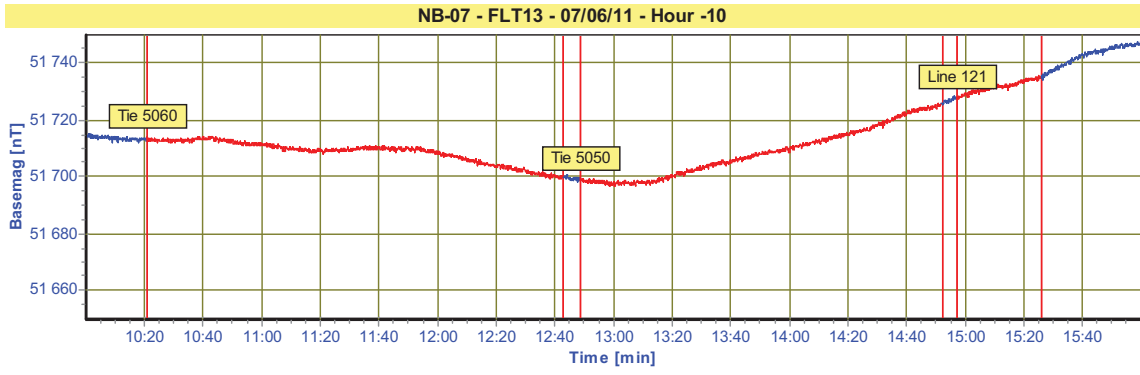
Red curves for lines and tie lines and blue elsewhere.

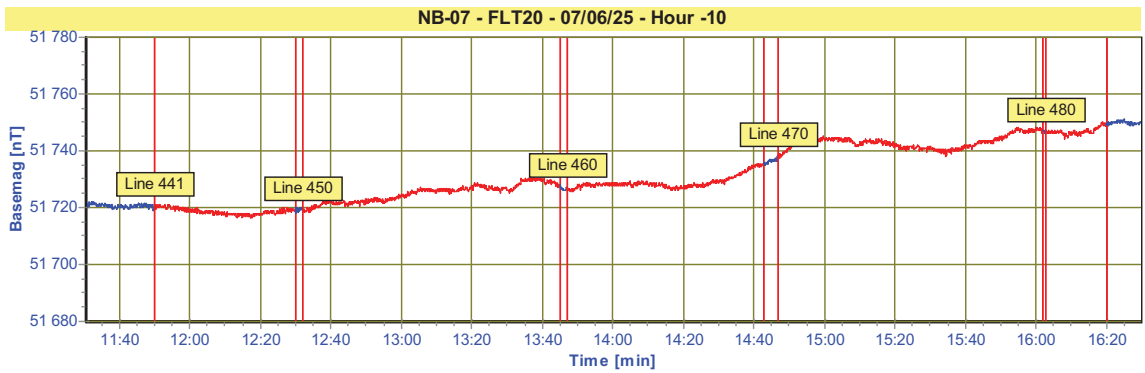
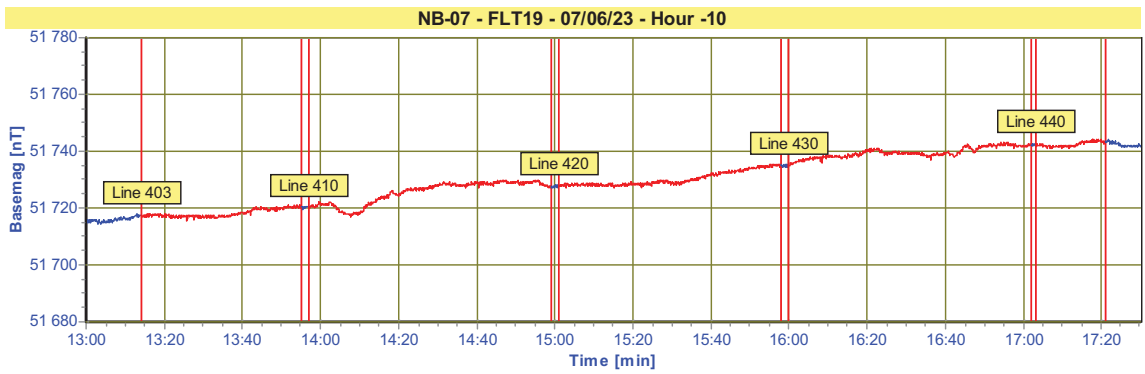
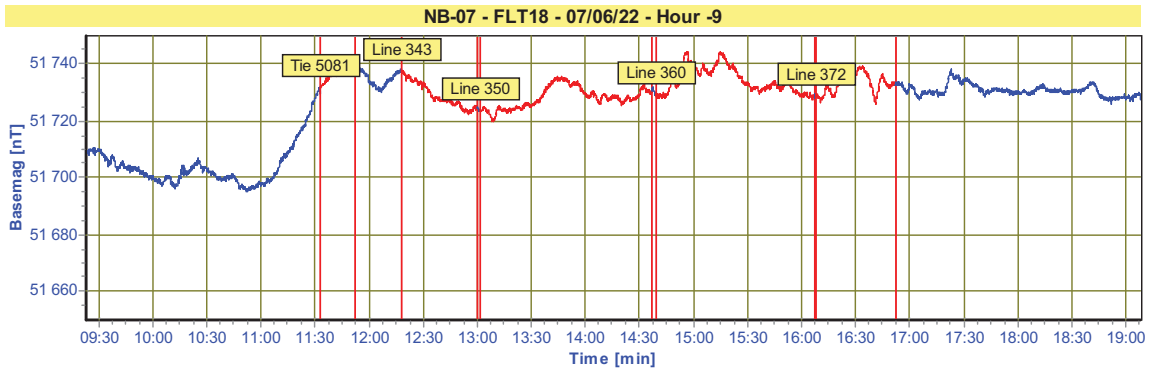
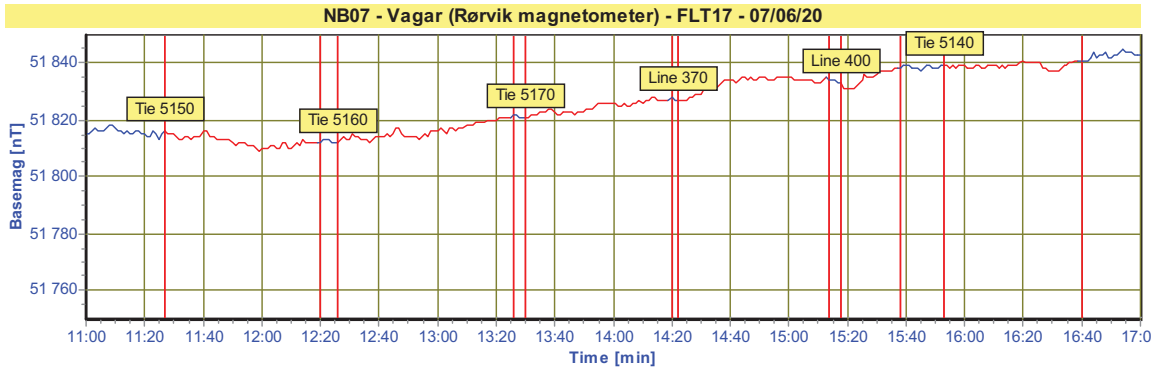


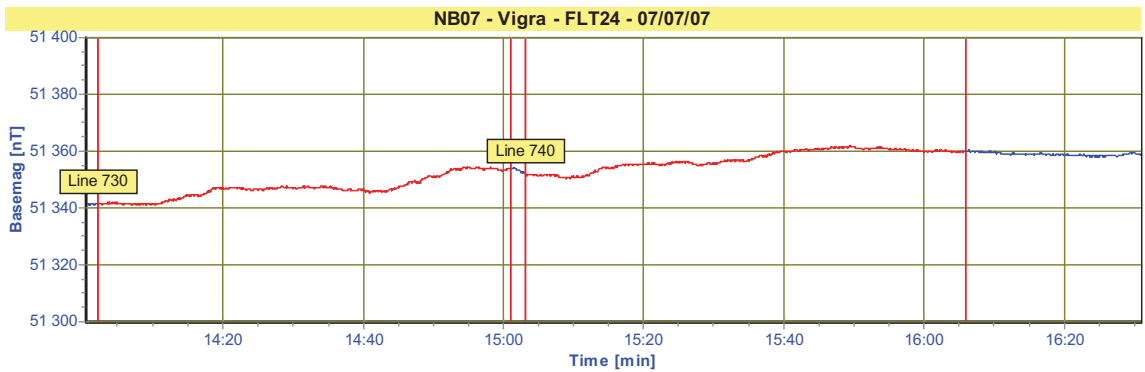
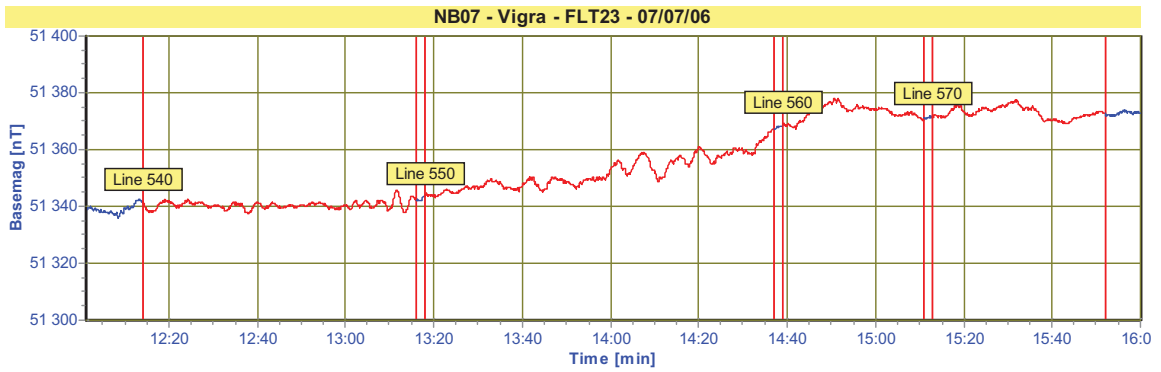
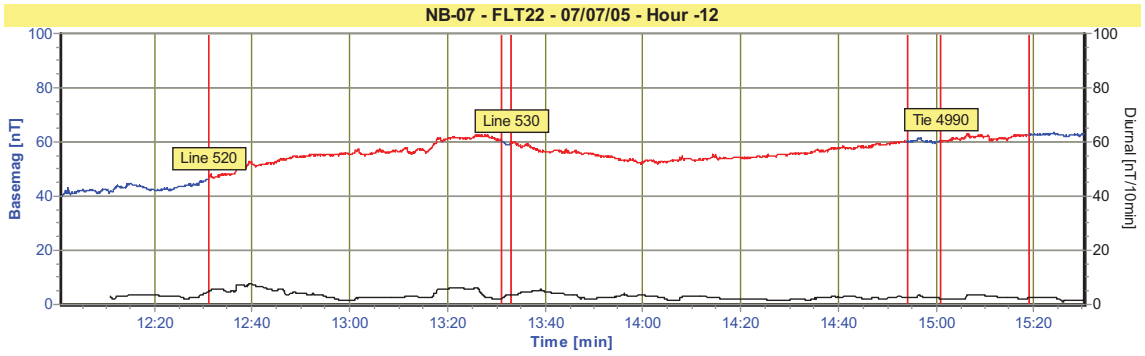
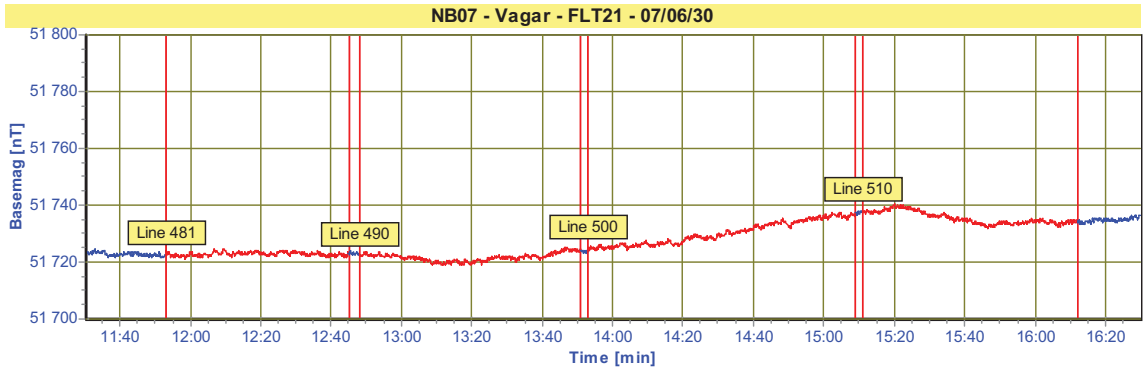


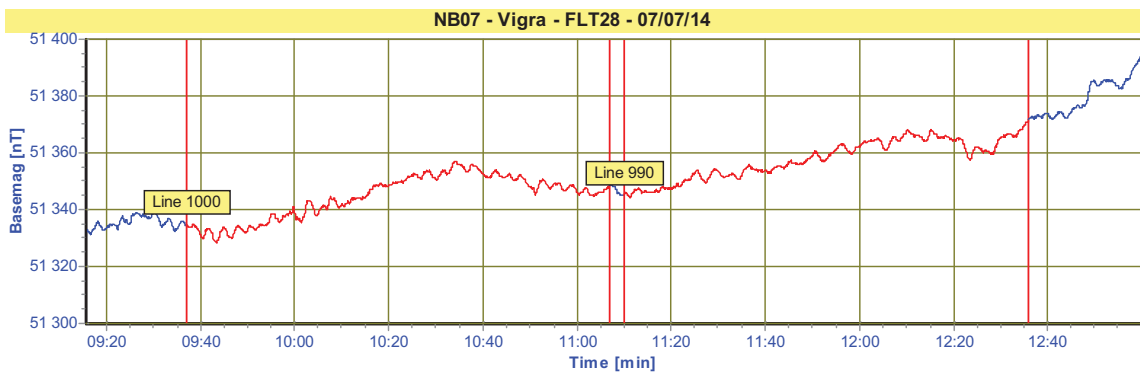
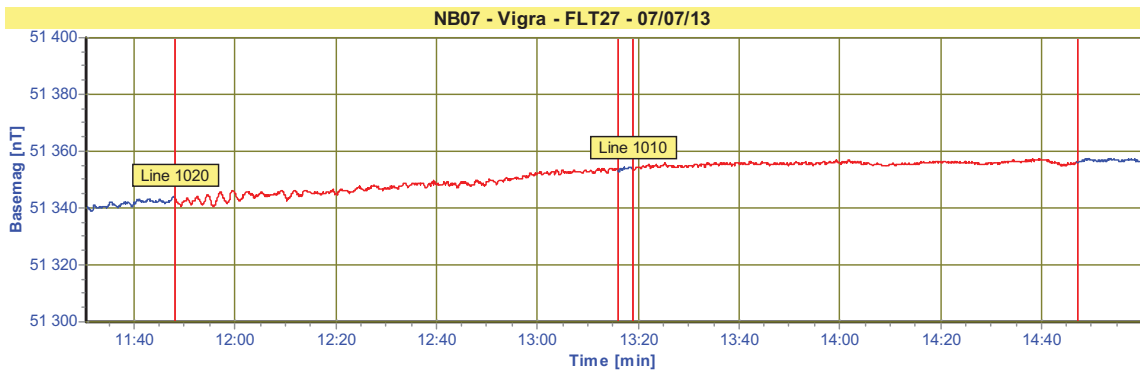
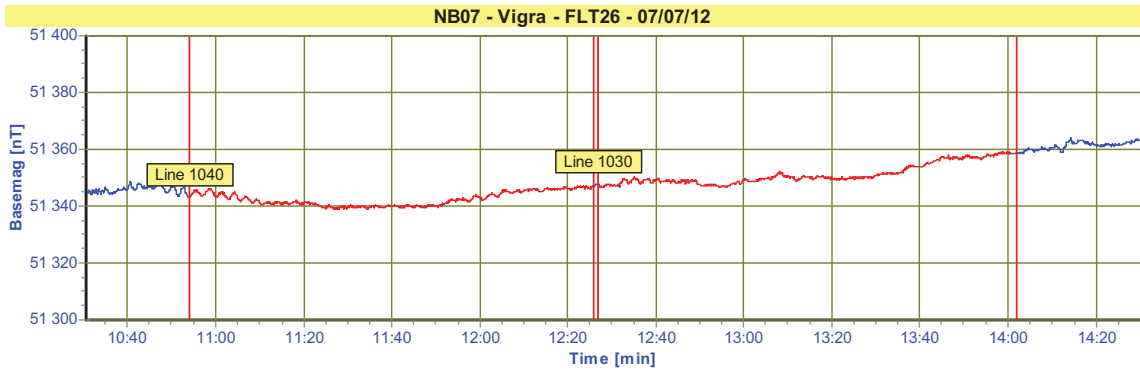
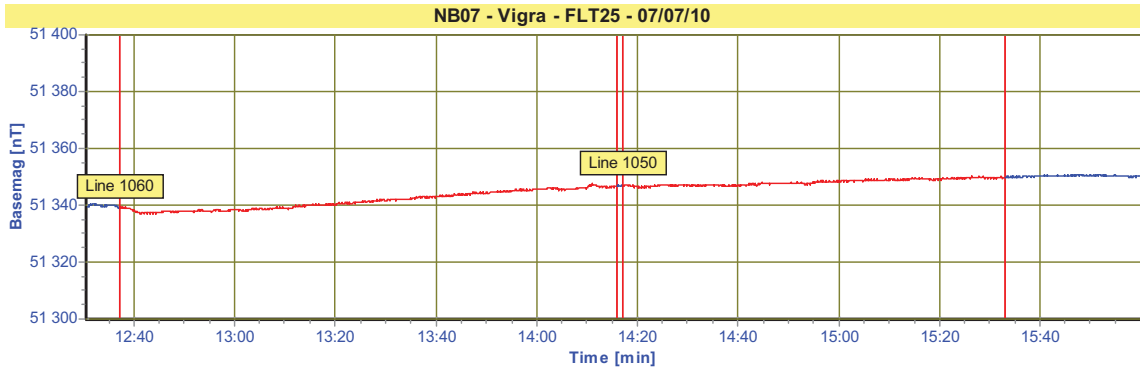




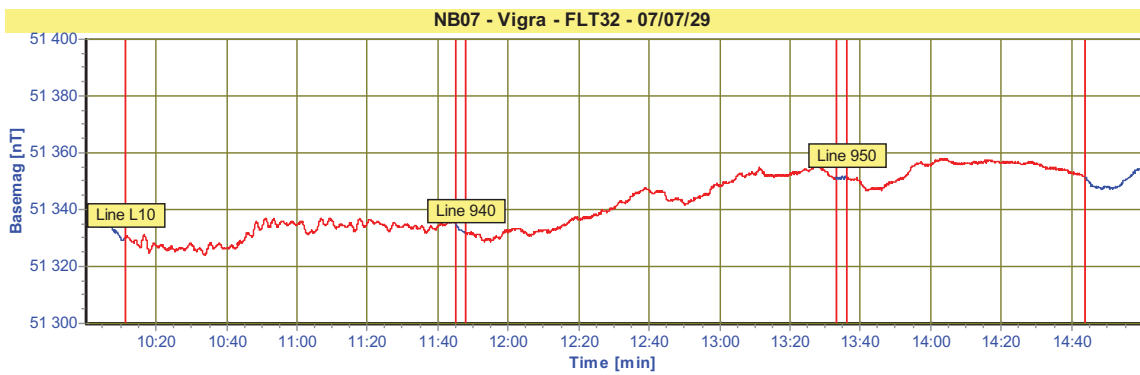
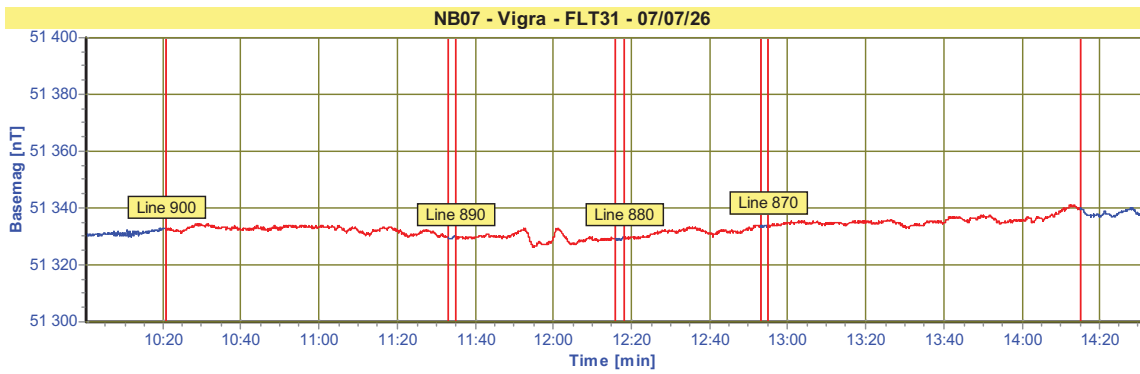
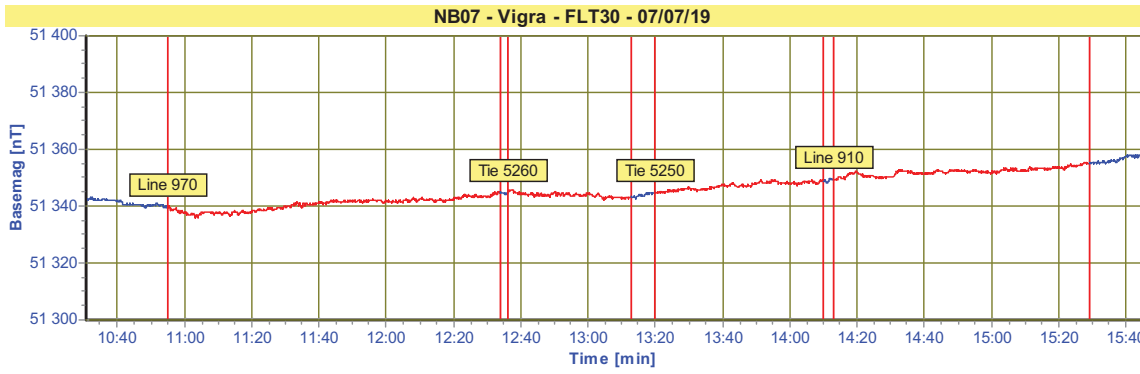
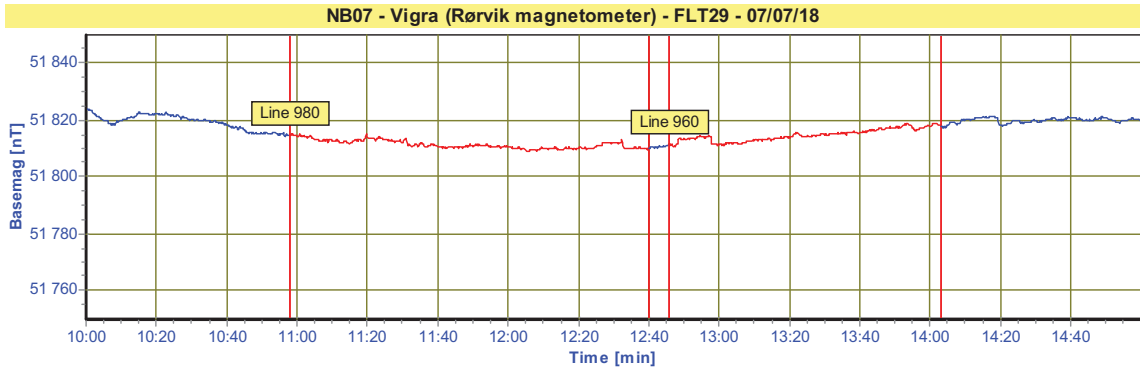


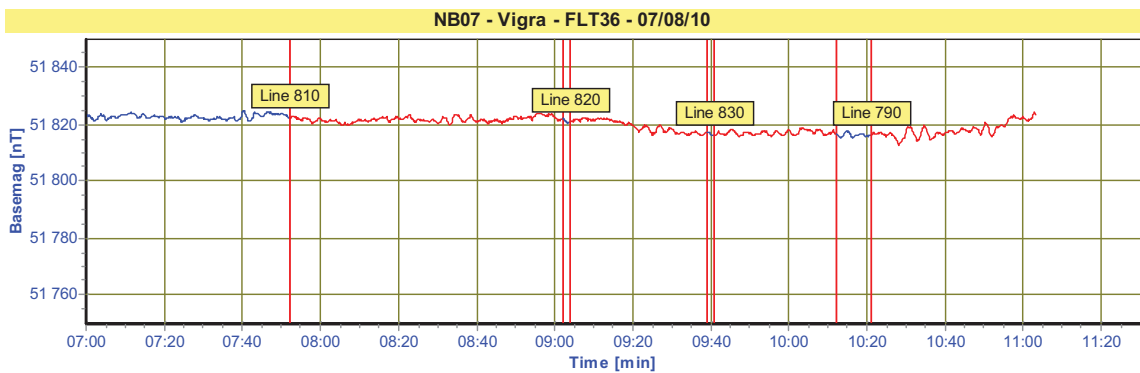
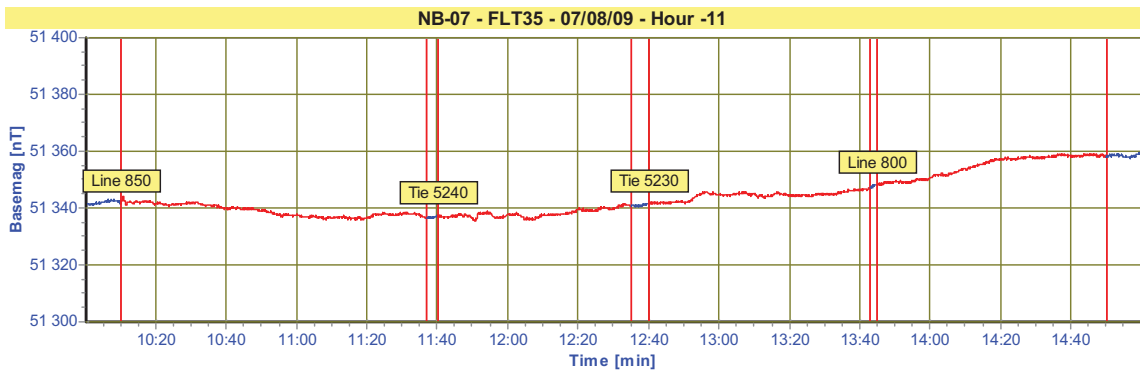
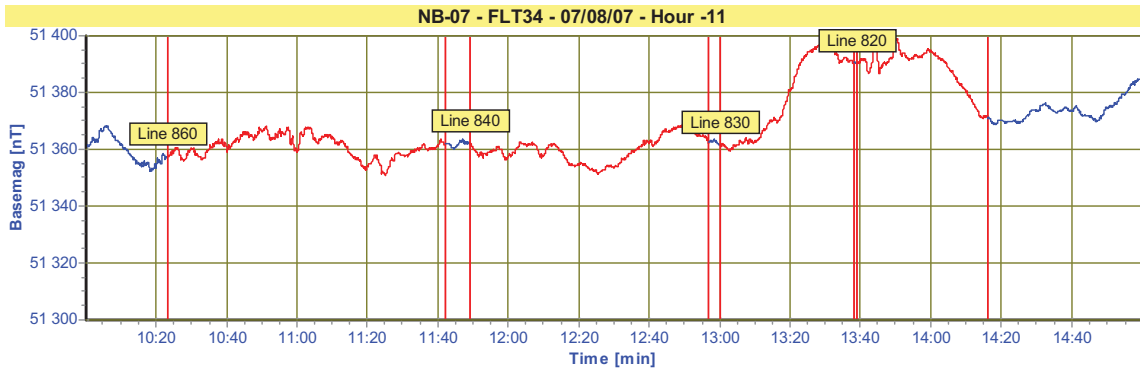
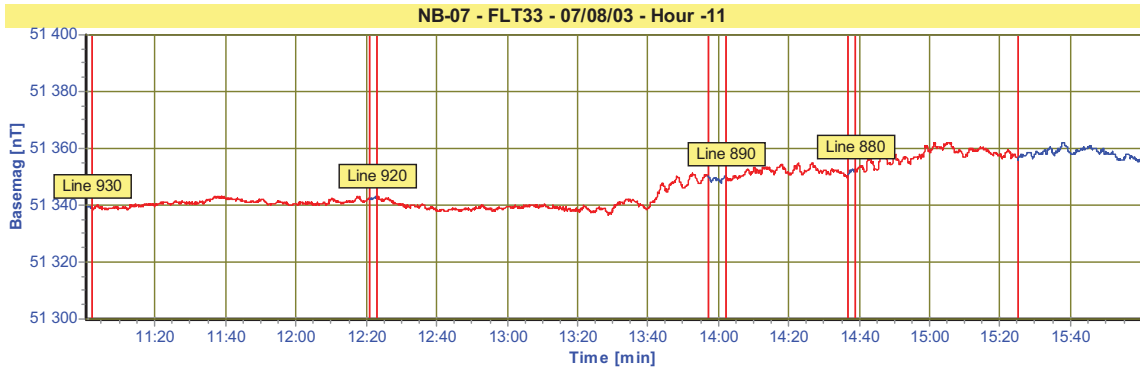


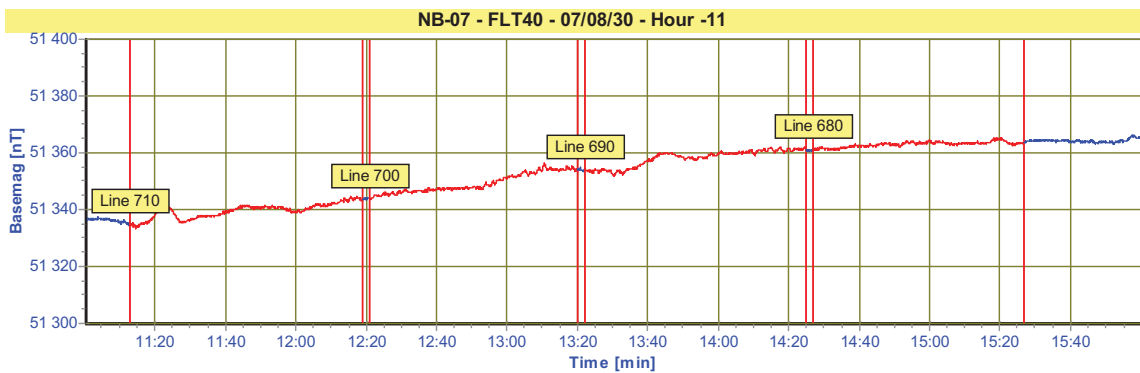
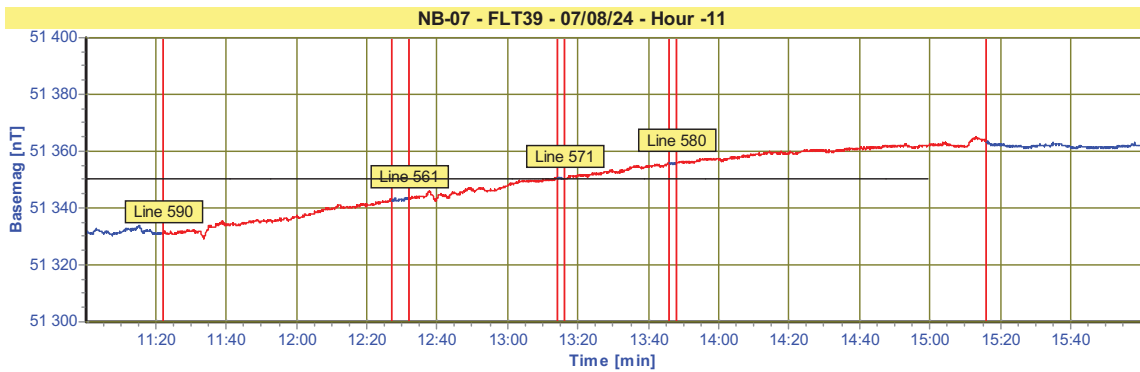
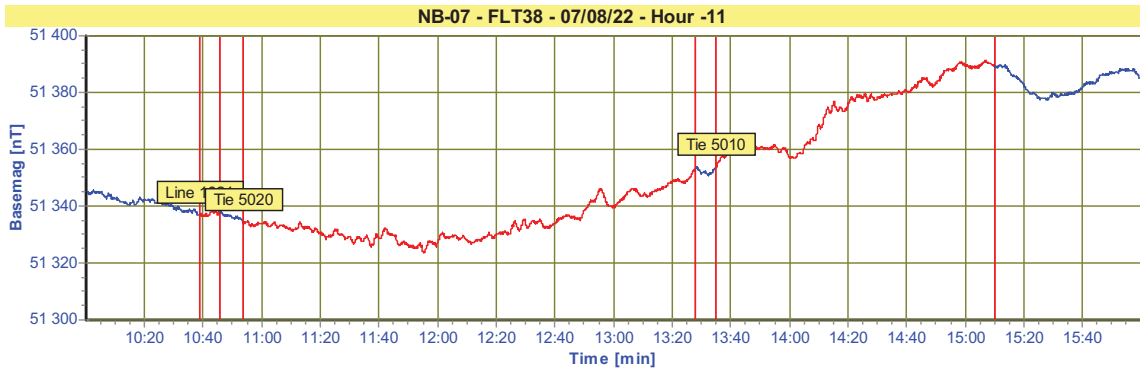
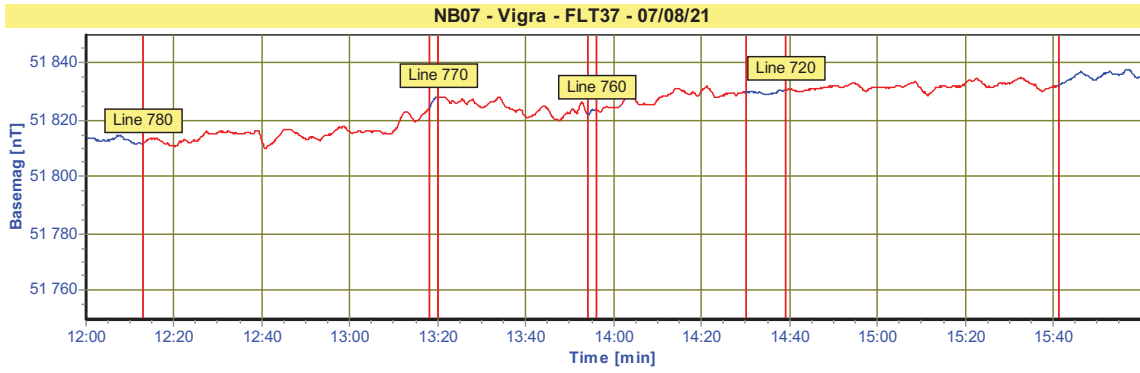


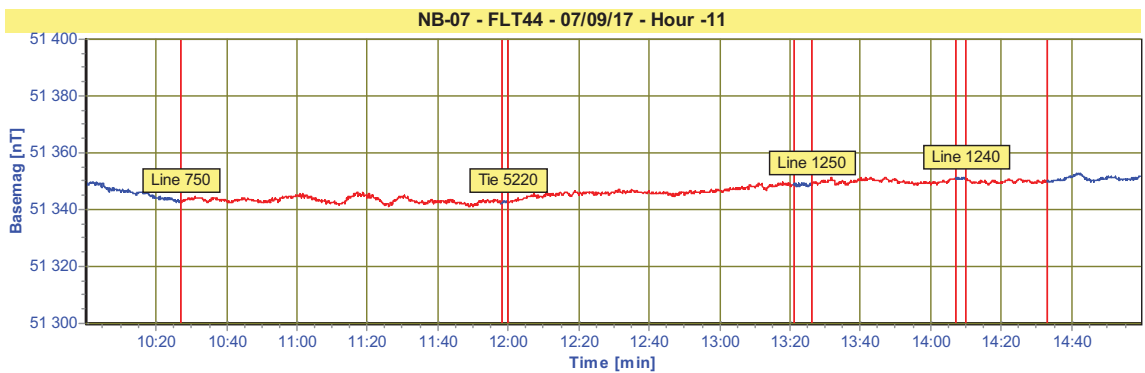
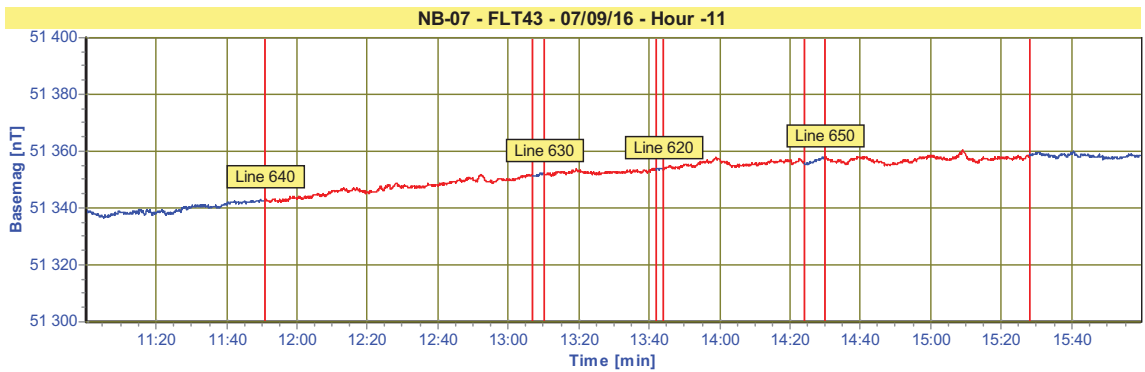
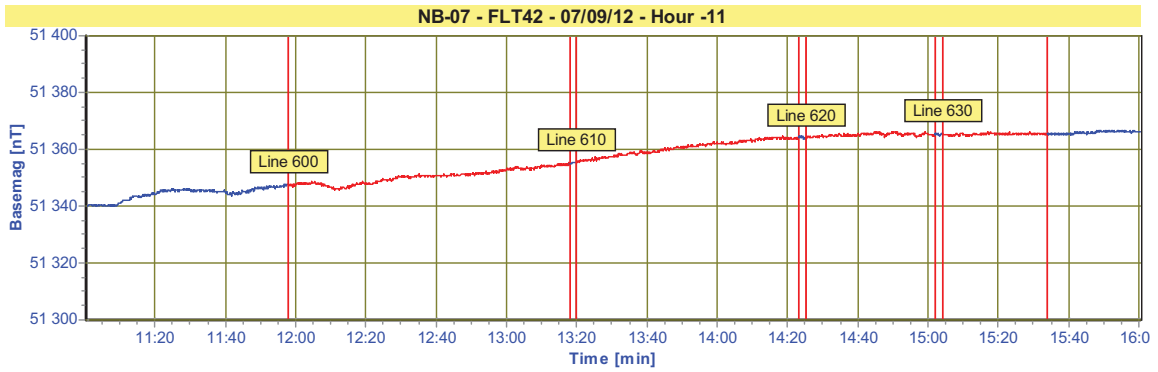
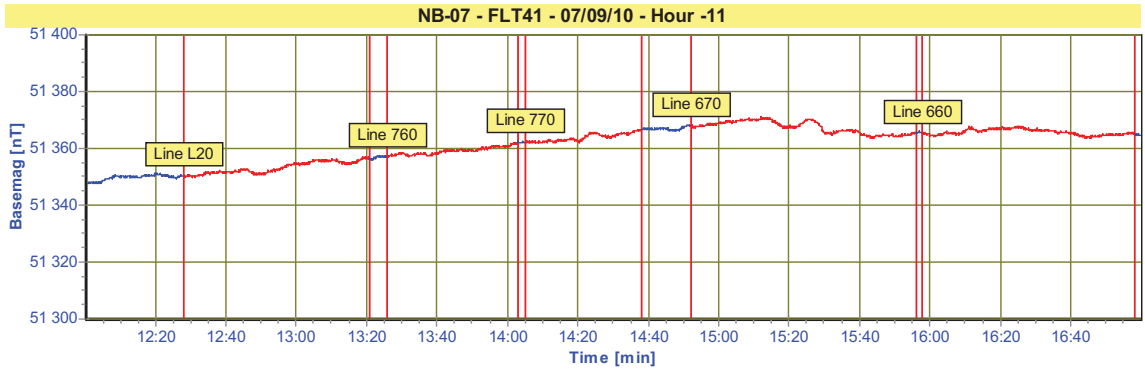


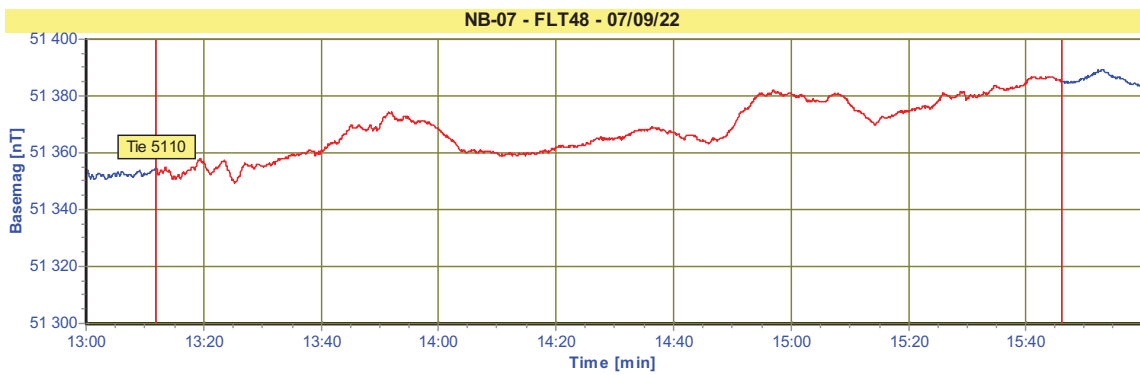
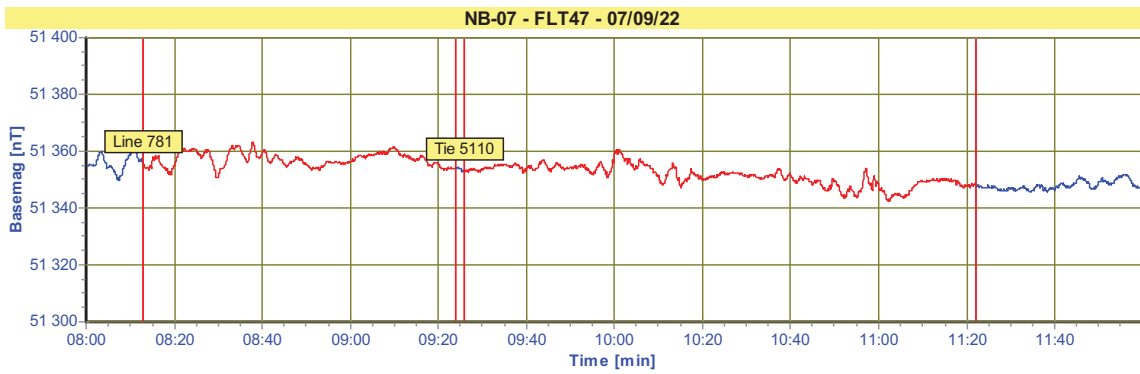
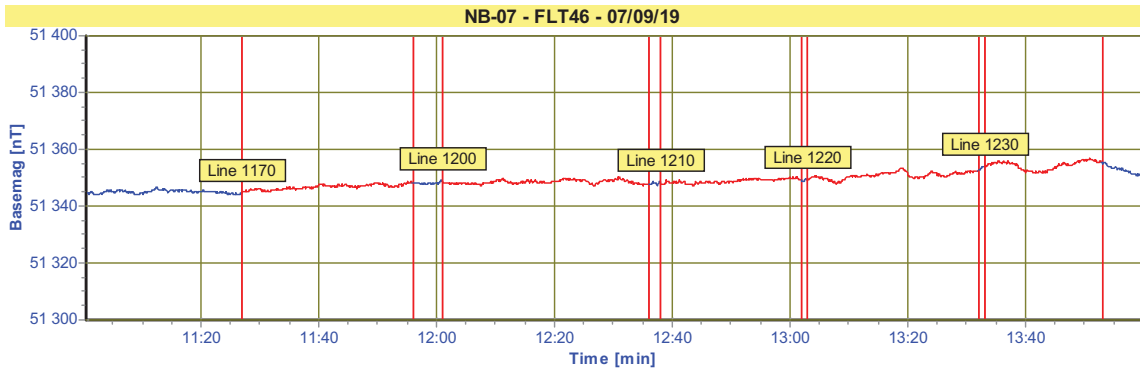
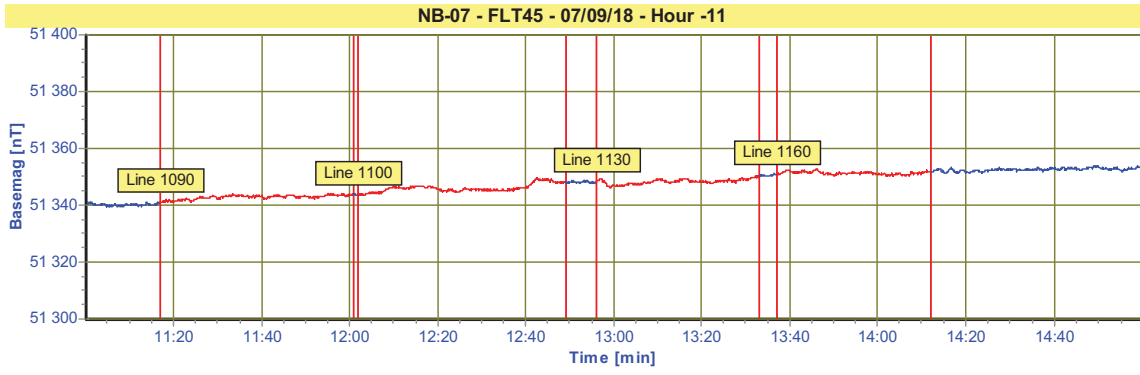


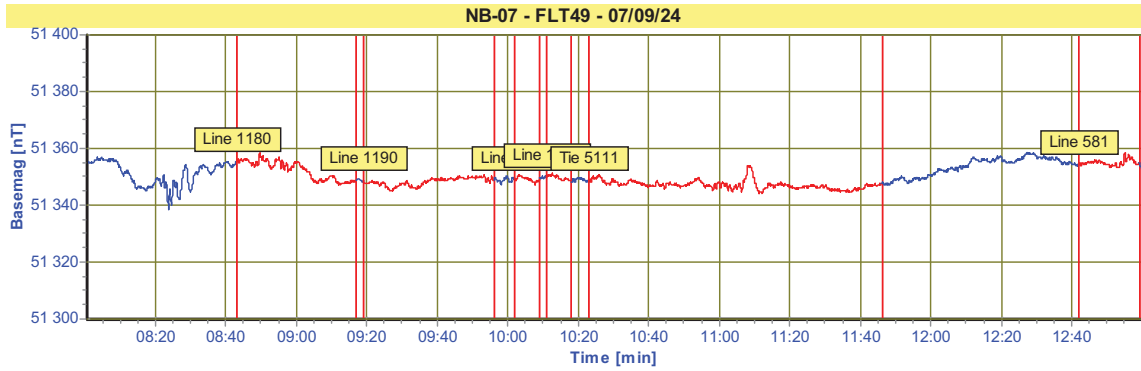












## 17 APPENDIX 2

### GEOLOGICAL SURVEY OF NORWAY DATA LABEL SCHEME

Data item	Channel
<b>INFORMATION ON POSITION</b>	
(Details of the projection used are given in the READ_ME file)	
Projected East (X)	X
Projected North (Y)	Y
UTM East	UTME
UTM North	UTMN
UTM East Masked	UTME_mask
UTM North Masked	UTMN_mask
Mosaic coordinates	(X_mos, Y_mos)
Geographic latitude	Lat
(degrees, minutes, seconds)	(Lat_d, Lat_m, Lat_s)
Geographic longitude	Long
(degrees, minutes, seconds)	(Long_d, Long_m, Long_s)
Altitude	Alt
(radar, GPS, barythmetric)	(Alt_R, Alt_GPS, Alt_Bar)
The radar altimeter height above ground level in meters	Alt_R_m
The radar altimeter height above ground level in feet	Alt_R_ft
Magnetic sensor height above sea level in metres	Alt_asl_m
Terrain elevation	Terr
Shot point	Shot

Navigation point	Nav_p
Flight	
Distance	Distance
Manual fiducials	Fid_manual
Camera fiducials	Fid_camera
Central Meridian	CM
Barometer	Bar
Line Name	Line_Name
Water Depth	W_depth
Adjusted/linked Water Depth	W_depth_adj
Temperature	Temp
Other UTM zones and geoids	_32 (other Zone), _ED50 (other geoid)
<b>DATE AND TIME</b>	
Day	
(day, month, year, julian)	(_d, _m, _y, _j)
Time	
(hour, minute, second, julian)	(_h, _m, _s, _j)
<b>RADIOMETRICS</b>	
Radiometrics	v
Total count	_TC
Potassium channel	_K
Uranium channel	_U
Thorium channel	_Th
Cesium channel	_Cs
Stripped values	_cps
Unstripped cps, no adjustment	_raw
Uranium Up	_Uup
Undefined levelling	_lev
Noise Adjusted Singular Value Decomposition Processed	_NASVD
Elevation for values	_e0 (use zero for ground level, otherwise height in m)
ppm	_ppm (converted to concentration in ppm)
%	_% (converted to concentration in %)
kBq/m2	_kBq/m2 (converted to equivalent surface activity in kBq/m2)
Bq/kg	_Bq/kg (converted to concentration in Bq/kg)

Cosmic	_cosmic
<b>VLF</b>	
VLF-EM	V or VLF
Total	_t
Orthogonal	_o
Inline	_l
Quadrature	_q or _lm
Inphase	_i or _Re
Place	_Rugby (not required)
Volt	volt
Final processed	_anom
<b>ELECTROMAGNETICS</b>	
Electromagnetics	E or EM
Horizontal coplanar	_0i / _0q (inphase / quadrature)
Vertical coaxial	_1i / _1q (inphase / quadrature)
Vertical coplanar	_2i / _2q (inphase / quadrature)
Frequency (kHz)	_7 (specified to the nearest whole kHz)
Resistivity	_res
Conductivity	_con
Volt	_volt
Quadrature	_lm
Inphase	
<b>MAGNETICS</b>	
All magnetics channels begin:	M or Mag
Total Earth field	_tot
Base station magnetics	_base
(name of base station)	(_oslo)
Base station corrected values	_basecorr or _bcorr
IGRF field	_IGRF
(when known IGRF 1997)	(_IGRF97)
Total field anomaly (total magnetic intensity anomaly field, used when IGRF is subtracted from raw)	<b>_anom</b>
Reduced to pole	<b>_rp or _rtp</b>
Left wing sensor	_left
Right wing sensor	_right



Top tail sensor	_top
Bottom tail sensor	_bottom
Magnetics minus culture	_cult
Tie lines only	_tie
Lines only	_line
Magnetization values	_mv
Compu-drape(TM)	_compu
Head corrected values	_head
<b>GRAVITY</b>	
All gravity channels begin:	G
Bouguer corrected	<b>_boug</b>
Free air corrected	<b>_free</b>
Isostatically corrected	<b>_iso</b>
Re-calculated	_recalc
Bouguer gravity at 2.0 g/cc	<b>G_boug_20</b>
2D_Bouguer gravity at 2.0 g/cc	<b>G_2D_boug_20</b>
Mapped	_Map
Bouguer correction value	_bougvalue
3D Bouguer correction value	_3D_bougvalue
Eotvos values	_eotvos
Corrected for Eotvos values	_eotvoscorr
Isostatic residual gravity	_res_iso
Vertical motion monitor	_vmon
Density values	_dv
<b>COMMON TO MAGNETICS AND GRAVITY</b>	
Raw data (from instrument)	<b>_raw</b>
Undefined edit	_edit
Undefined numerical correction	_corr
Corrected according to _corr	_corred
Basement surface	_bs
Basement thickness	_bt
Network adjusted/linked	_adj
Controlled	_ctrl
Offset corrected	_offcorred
<b>FILTERS</b>	
Bandpass	_bp (details may follow)
High-pass	_h (details may follow)
Low-pass	_l (details)

De-corrugation	_d (details)
Unknown filter	_f or -filt
Vertical gradient	_v or _vg
Horizontal gradient	_hg
2nd horizontal gradient	_2hg
Horizontal gradient X	_hgx
Horizontal gradient Y	_hgy
Longitudinal gradient	_hgl
Transverse gradient	_hgt
Total horizontal gradient azimuth $<^{\circ}$	_thg
With horizontal gradient enhancement	_whge
Second vertical derivative	_2v
Upward continuation	<b>_u (details)</b>
Upward continuation	<b>_d (details)</b>
Analytic signal (1D)	<b>_a</b>
3D analytic signal (total magnetic gradient)	<b>_as</b>
Shaded	_s
Pseudo depth slice 1	_pds1
Pseudo-gravity	_pg
Residual	_res
10km residual	_res_10
15km residual	_res_15
Regional field	<b>_reg</b>
Spike removal/despiked	_sr
Akima filter	_AKIMA
Tilt derivative	<b>_tdr</b>
TDX-filter	<b>_tdx</b>
1D or 2D FFT filtering	_1D or _2D
<b>LEVELLING</b>	
2D level	_2D (if no better details)
Amarok '3D' level	_3D
Full level (miss-ties to zero)	<b>_full</b>
statistical level	_ord2 (e.g. second order)
Unspecified final adjustment, usually for mapping	<b>_Final</b>
Micro levelled	<b>_Mic</b>
Grid levelling	<b>_glev</b>
Undefined levelling	<b>_lev</b>
Tie levelling	<b>-tlev</b>
NGU moving differential median	
Micro-levelling filter	<b>_MicNGU</b>

<b>ORIGINAL INFORMATION PRESERVED IN THE NEW ARCHIVE</b>	
Original data channel name	O_name
Original line name(from which the NGU line number is extracted)	O_line
Original line number	O_num
<b>UNKNOWN DATA CHANNELS</b>	
Unknown data The unknown data channels are labelled with 'Z' followed by a number. The number indicates the position of the data column in the original data file. This number is usually the original column number take away 3.	Z1 to Zn
<b>GENERAL PROCESSING</b>	
Lag corrected values	_lag
Gridded data	_grid